Détermination d'un critère prédisant l'efficacité du procédé d'électrocoalescance sur la destabilisation d'émulsions eau-pétrole brut

Jonathan Raisin

UNIVERSITÉ DE GRENOBLE

THÈSE

Pour obtenir le grade de

DOCTEUR DE L'UNIVERSITÉ DE GRENOBLE

Spécialité : **Mécanique des fluides, Energétique, Procédés**

Arrêté ministérial : 7 Août 2006

Présentée par

Jonathan RAISIN

Thèse dirigée par **Jean-Luc REBOUD**
et codirigée par **Pierre ATTEN**

préparée au sein du laboratoire **G2ELab**
et de l'École Doctorale **I-MEP2**

Electrocoalescence in Water-in-Oil Emulsions: Toward an Efficiency Criterion

Thèse soutenue publiquement le **8 Avril 2011**,
devant le jury composé de :

Mr Laurent DAVOUST
Professeur à Grenoble-INP, Président
Mr Jérôme BELLETTRE
Professeur à Polytech'Nantes, Rapporteur
Mr Antonio CASTELLANOS
Professeur à l'Université de Séville, Rapporteur
Mr Svend Tollak MUNKEJORD
Docteur à SINTEF Energy Research, Examinateur
Mr Jean-Luc REBOUD
Professeur à l'Université Joseph-Fourier, Directeur de thèse
Mr Pierre ATTEN
Docteur ès sciences au CNRS, Co-Directeur de thèse

Preface

This thesis is based on work performed at the G2ELab/French CNRS as a part of the collaborative research project “Electrocoalescence – Criteria for an efficient process in real crude oil systems”; coordinated by SINTEF Energy Research. The project was supported by The Research Council of Norway, under the contract no: 169466/S30, and by the following industrial partners: Aker Solutions AS, BP Exploration Operating Company Ltd, Hamworthy Technology & Products AS, Petrobras, Saudi Aramco, Shell Technology Norway AS and Statoil ASA.

Within these organizations, I first want to express my gratitude to Mr Lars Lundgaard and Dr Petter E. Røkke for enabling such an interesting joint research work as well as for their kindness and warm welcome at every meeting. All the other project colleagues and especially Dr Svend T. Munkejord, Dr Knut E. Teigen, Dr Simone Less and Pr Gunnar Berg are also acknowledged for the invaluable contribution they brought to my final manuscript by sharing their ideas and results.

Most of all, my thanks go to my supervisors, Pr Jean-Luc Reboud and Dr Pierre Atten, the inputs of which spread way beyond simple guidance. Through their complementary efforts, they not only filled me with their scientific knowledge and skills but also gave me the urge to surpass myself. These four years spent on their side were extremely enjoyable both from a personal and a professional perspective and will never be forgotten.

Thanks to the jury members of my PhD defense, Pr Laurent Davoust, Pr Jérôme Bellettre, Pr Antonio Castellanos and Dr Svend T. Munkejord for their thorough review of my work and for all their encouraging comments and insightful remarks.

In addition, I am grateful to all those who, with their unswerving help and support, made this thesis possible. In particular, my parents Michel Raisin and Roselyne Mercier, my dear friends, Quentin “software master” Gueguan, Lucian “wannabe photographer” Caliap, Tristan “jukebox” Déléonibus, Vincent “encyclopedia of hazardous chemistry” Boucher, Emilie “Godmother” Brun, Alexandre “gtalk” Capecci, Julien “Big Daddy” Selva, Hugo “Mr Slave” Barrionuevo, and many others, my fellow employees of the G2ELab, Christophe Pollet, Alain Tisserand, Jean-Luc Palenzuela, Daniel Ogier, Julien

Bamberger, Corine Marcon, Claire Roux, Geneviève Teissèdre, Pascal Rain and Olivier Lesaint.

Lastly, words fail me to express my appreciation to Christelle Dubois whose dedication, love and persistent confidence in me, has taken the load off my shoulder. I owe her for being unselfishly let her intelligence, passions, and ambitions collide with mine and for turning these three years into such an amazing experience.

Contents

Introduction

"The word *petroleum*, derived from the Latin *petra* and *oleum*, means literally rock oil and refers to hydrocarbons that occur widely in the sedimentary rocks in the form of gases, liquids, semisolids, or solids" (Speight, 2006). Although its first use is lost in the darkness of antiquity, it is known that the builders of Babylon used *asphaltum* (a natural tar-like substance that washes ashore from oil seepages beneath the water surface) to bind together the rocks from which the city was built. The Greek historian Descorides Pedaners recorded that citizens of Agrigentum in Sicily burned petroleum in lamps long before the birth of Christ. Oil was also used for various purposes by Persians, Hindus, Incas, Aztecs, and Indians.

In modern societies, petroleum has become one of the most important substance, providing not only raw materials for the ubiquitous plastics and other products, but also fuel for energy, industry, heating, and transportation. Though, with the fields output declining (at an average rate of 4.5 % according to the International Energy Agency (IEA, 2011)) and the energy consumption increasing all over the world, there has been a gradual acceptance that petroleum will, at some time within the foreseeable future, be in very short supply. As a result, industry's approach has evolved to such an extent that wells that were previously regarded as nonprofitable because of their inability to produce oil without considerable external stimulation are now reexamined with the object of, literally, recovering every last possible drop (Speight, 2006). In the mean time, the world reserves of light, easily processable, crude oils being almost depleted, there has been a growing interest for the extraction of heavy and extra heavy crude oils. Because of this progressive transition in oil quality, industrials have and will continue to face extremely complex challenges that often require strong scientific supports to be adressed.

The present thesis fell within the framework of an international project focusing on one of these challenges, i.e. the removal of water coproduced with crude oil in the form of stable emulsions during recovery and desalting operations. In the early age of petroleum processing, the dehydration step was limited to the exploitation of the natural density difference between both phase. Extracted crude oil was thus put to rest for days in

large settling tanks, particularly cumbersome on offshore platforms, to allow the gravitational sedimentation of water droplets (with a mean diameter on the order of tens of microns). In order to take full advantage of Stokes' law (Noik et al., 2006) (through the quadratic dependence of the settling velocity on the droplets radius) and speed up the overall separation stage, different techniques promoting droplet growth have been developed. Among those, electrostatically induced attraction and merging, a.k.a. *electrocoalescence*, has demonstrated unmatched capabilities. Over the years, it has proven able to drastically reduce the use of heat and of chemical emulsion breakers, respectively detrimental from an energy and environmental viewpoint, and has consequently become a standard of most of the state-of-the-art separators.

Yet, although the beneficial effect of electric forces to the separation of water-in-crude oil emulsions has been known for a century, a lot of gray areas remain, particularly on the question of efficiency. Most of the earlier studies were devoted to its improvement through the identification of optimal operating conditions (electric field intensity, waveform, frequency). Though, since those are often closely related to the nature of the crude oil being processed, strong variations in dehydration efficiency were frequently observed between different wells or simply with time and the maturing of the oil inside a given well. Works conducted at the Grenoble Electrical Engineering Laboratory (G2ELab) and summarized in this manuscript aimed at addressing this shortcoming, by providing a criterion that predicts the probability of electrocoalescence of water droplet pairs as a function of the different key parameters. Emphasis was placed on the understanding and modeling of the hydrodynamic and electrostatic interactions, leaving most of the chemical aspects in the hands of expert project coworkers at the Norwegian University of Technology (NTNU) - Ugelstad Laboratory.

The first chapter is a brief introduction to the formation, stabilization and separation of water-in-crude oil emulsions. A special attention is paid to the characterization of the electrocoalescence process through the description of the physical mechanisms involved and their associated forces. Some of the marketed technologies are then presented and the shortcomings that prevents an accurate estimation of their efficiency are finally underlined.

As a preliminary for the study of electrocoalescence, the second chapter deals with the deformation and stability of electrostatically stimulated water-oil interfaces. A numerical scheme, implemented to simulate electrohydrodynamic problems with moving boundaries, is first detailed and then used in combination with experiments to extend asymptotic results previously obtained, in model configurations, through analytical treatments.

The third chapter is divided in two parts. Firstly, numerical simulations are used to investigate the thinning of the oil film in between droplets approaching under electrostatic

attraction forces. An order of magnitude estimate for the drainage time is widely validated and balanced with the time of proximity to deduce a criterion predicting the probability of electrocoalescence resulting from a flow induced collision. Secondly, the assembly of an experimental setup designed to ultimatelty improve the relevance of the former criterion is described.

The fourth and last chapter is an answer to an otherwise unfulfilled requirement defined in the design of the "water droplets electrocoalescence in an oil shear flow" experiment. It presents the development of a new actuation method for the injection of uncharged conductive drops in a viscous dielectric liquid based on the application of an electric field pulse.

Chapter 1

Separation of water-in-crude oil emulsions: physical aspects, chemistry and technology

1.1 Introduction

In the petroleum industry, the co-production of water and crude oil in the form of stable emulsions is highly undesirable from a process and product quality point of view. Corrosion of equipments (pipes, casings, valves, etc.), deactivation of catalysts, higher operational costs due to significant increase of viscous losses and transportation of water are among the detrimental consequences that make a dehydration step compulsory. After a basic introduction to the nature of petroleum, this chapter highlights the processes and mechanisms that generates such emulsions. Brief discussions on the stabilizing effect of chemically active species, naturally present in crude oils, and on the techniques commonly employed to remove the emulsified water are then presented. A particular focus is placed on the one, known as *electrocoalescence*, that has proven to be the most efficient. Both the physical mechanisms at work and forces acting on water droplets during the process are reviewed. Finally, the historical evolution of the associated technology, from conventional to state-of-the-art devices, is recounted and used to introduce a discussion on the main objective of the thesis: the modeling of electrocoalescence efficiency.

1.2 Crude oil

1.2.1 Origin

Petroleum, also referred to as conventional crude oil, is a brownish green to black liquid substance scattered at different depths throughout the earth's crust. Though its origin has long been debated and yet not conclusively assessed, most geologists view crude oil and natural gas as the products of compression and heating of ancient vegetation over geological time scales (Speight, 2006). According to this biogenic theory, it is formed from the decayed remains of prehistoric marine animals, terrestrial plants and predominantly from microscopic plankton organisms. Over many centuries this organic matter, mixed with mud, is buried under thick sedimentary layers of material. The resulting high levels of heat and pressure cause the remains to metamorphose, first into a waxy material known as kerogen, and then into liquid and gaseous hydrocarbons in a process known as catagenesis. These then migrate through adjacent rock layers until they become trapped in porous underground rock formations (typically sandstone) called reservoirs, forming an oil field.

1.2.2 Ultimate (elemental) composition

The composition of petroleum obtained from a well is variable and depends not only on the original composition of the oil in situ but also on the manner of production and the stage reached in the life of the well or reservoir. With few exceptions, the proportions of the main elements (carbon, hydrogen, nitrogen, oxygen, sulfur, and metals) in crude oils vary over fairly narrow limits (Table 1.1). Such small differences are quite surprising considering the great diversity in physical properties and render any elemental based classification, such as for coils, quite irrelevant. Instead, hydrocarbon group type analysis is commonly employed (Sjöblom et al., 2003).

Table 1.1: *Elemental composition of crude oils.*

Carbon	83.0% to 87.0%	Oxygen	0.05% to 1.5%
Hydrogen	10.0% to 14.0%	Sulfur	0.05% to 6.0%
Nitrogen	0.1% to 2.0%	Metals (Ni and V)	<1000 ppm

1.2.3 The SARA classification and Petroleomics

The *Saturates*, *Aromatics*, *Resins* and *Asphaltenes* (SARA) classification is one among the two main examples of such group type analysis, separating the crude oils in four main

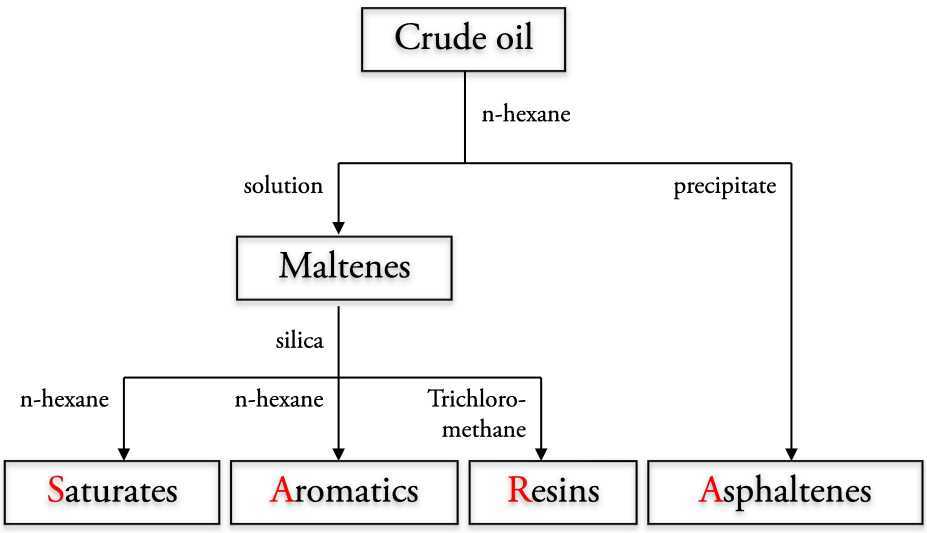

Figure 1.1: *SARA-separation scheme. Reproduced from Aske et al. (2001).*

chemical classes based on differences in solubility and polarity (Figure 1.1). Saturates (or aliphatics) are non polar compounds, whose structure is free from any double bond and includes alkanes, cycloalkanes and wax (all paraffins from straight-chained paraffins to cycloparaffins) (Sjöblom et al., 2003). Aromatics are hydrocarbons containing one or more aromatic nuclei such as benzene, naphthalene, and phenanthrene ring systems that may be linked up (substituted) with naphthalene rings or paraffin side-chains. Resins and asphaltenes are polar molecules that are operationally defined as solubility classes, namely the fraction of the crude oil respectively soluble and precipitating in light alkanes like pentane, heptane or hexane (see Figure 1.1). Asphaltenes can be regarded as similar to the resins, but with higher molecular weights, typically $500 - 1500\ g.mole^{-1}$. They also contain heteroatoms such as nitrogen, oxygen or sulfur (Figure 1.2a), though in larger proportions, as well as organometallic constituents (Ni, V, Fe). The structure of asphaltene molecules is believed to consist of polycyclic aromatic clusters, substituted with varying alkyl side chains. In the last century, asphaltenes have concentrated most of the attention and been the topics of many studies because of their tendency to precipitate, causing a large variety of problems spanning from reservoir damage to equipment plugging, catalyst deactivation, etc (Figure 1.2b). Furthermore, even though a clear picture of the mechanism is still missing, asphaltenes aggregation was proven to greatly influence the stability of water-in-crude oil emulsions (see section 1.4 and Hannisdal et al. (2006)). With the world production progressively shifting towards heavy oils which have particularly high contents of resins and asphaltenes, the latter phenomenon is becoming more and more important.

Petroleomics refers to the characterization of petroleum at the molecular level (Marshall and Rodgers, 2008). Basically, with sufficiently high mass resolving and mass ac-

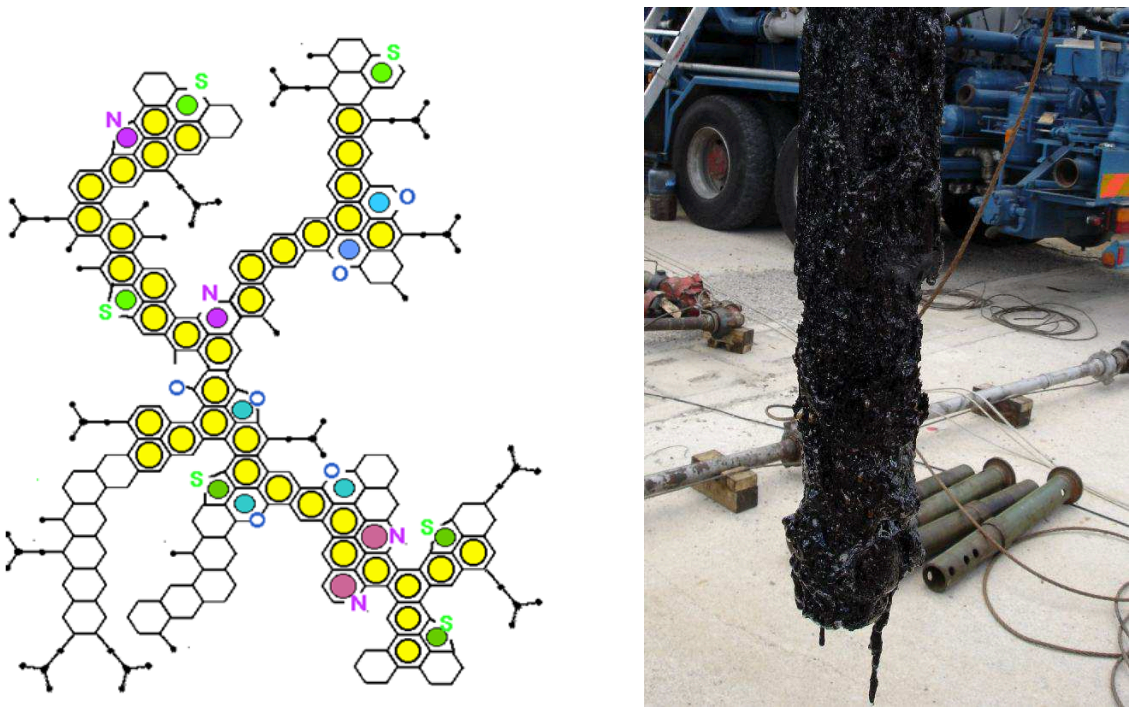

(*a*) (*b*)

Figure 1.2: *(a) Molecular structure of asphaltenes proposed for Maya crude (Mexico) by Altamirano et al. (1986). (b) Asphaltene deposition on tools extracted from a well in Italy (Lightford et al., 2008).*

curacy power, now routinely available from high magnetic field ion cyclotron resonance mass spectrometry, it becomes possible to resolve and identify uniquely and simultaneously each of the thousands of elemental compositions $C_cH_hN_nO_oS_s$ from which any crude oil is composed of. Petroleomics opens up for extraordinary new opportunities in the understanding of petroleum nature and is expected to ultimately allow correlation between chemical structure and properties.

1.2.4 Characteristic properties

As briefly introduced in the previous sections, crude oils are very complex mixtures exhibiting a wide range of physical behaviors. In order to cope for the absence of a universal chemical classification and still be able to anticipate processing conditions, industrials have relied on characteristic properties. There exist many but within the scope of this thesis, four are of particular interest.

Specific gravity (Sg), i.e. density with respect to water, is a property that has found wide use in the industry for preliminary assessment of the character and quality of crude oils. Although it can still be found in numbers of scientific papers, the (Ameri-

can Petroleum Institute) *API gravity* defined, at a standard temperature of $60°F$, by

$$Degrees\ API = \frac{141.5}{Sg} - 131.5 \tag{1.1}$$

has become more common. Encountered API gravities usually range from about 45.3° ($Sg = 0.8$) for the lighter crude oils down to below 10° for heavier ones and bitumen.

Viscosity measures the crude oils' internal resistance to flow and is commonly expressed in poise (p) or centipoise (cp). The extremely wide reported variations (from tens to many thousands of centipoise) make it by far the most determinant property regarding the choice of processing conditions (from extraction and transportation to refining). Crude oils viscosity strongly depends on temperature, pressure and on the presence of emulsified water.

Interfacial tension (IFT) originates from the difference in attractive intermolecular forces acting in two liquid phases. In the present context, it provides an estimate of the intensity of capillary forces that tend to maintain the sphericity of water droplets by counteracting any source of deformation. Because crude oils contain interfacially active species (such as asphaltenes), a distinction is often made between *dynamic* and *static* tension. The first concerns droplets either freshly exposed to "contamination" (section 1.3.2) or experiencing fast transient stimulation[1]. The static tension is that existing after static equilibrium concentrations have been reached at the interface. Typical values in the latter case are in the range $10 - 25\ N.m^{-1}$ (Less, 2008).

Conductivity in crude oils results from the motion of conductive solids, polar organic and inorganic constituents (predominantly asphaltenes (Lesaint et al., 2010)). Measured values depend on the crude oils viscosity (and therefore on other parameters such as temperature and pressure) but are generally comprised between $10^{-9} - 10^{-7}\ S.m^{-1}$. Such relatively high conductivities (for a dielectric liquid) have practical consequences on the effectiveness of certain types of electric forces (see section 1.5.1.3).

1.3 Birth of water-in-crude oil emulsions

1.3.1 Recovery and transportation

The history of the emulsification starts with the recovery of oil from the reservoir, where it resides together with salt water and gas in small pores and fractures. The course of the process is often divided into three successive stages: *primary recovery* , *secondary recovery*

[1] More precisely, when interfacial convection or deformation rates exceed that of adsorption/desorption and interfacial diffusion of the species (section 4.4.3).

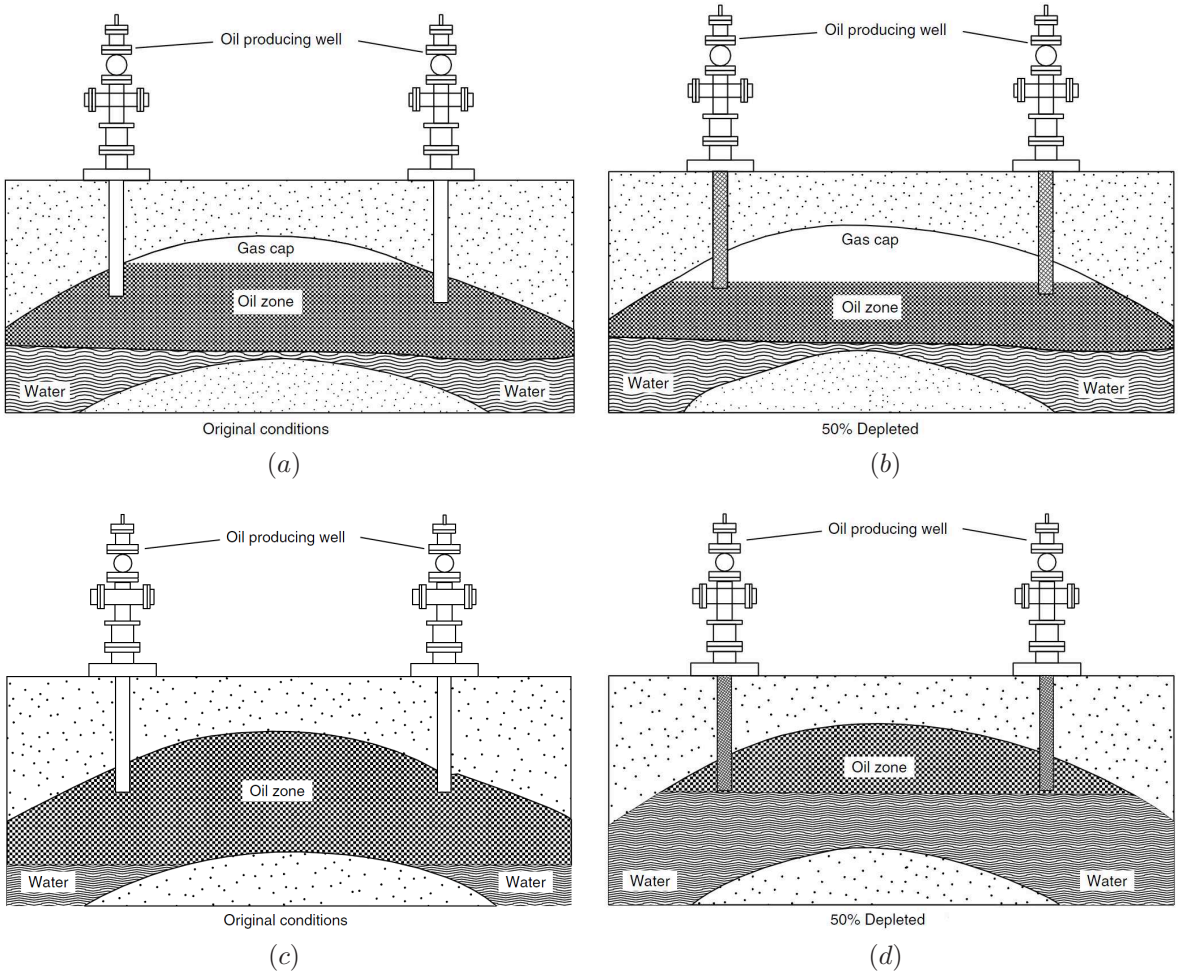

Figure 1.3: *The two most efficient oil primary recovery mechanisms (Speight, 2006). The* gas cap drive *(a,b): if gas has accumulated beneath the top of the reservoir, its decompression forces the oil into wells situated at the bottom of the oil-bearing phase. The* water drive *(c,d): separately or concurrently, the water pressure drives the lighter oil out in the producing wells.*

and *enhanced (tertiary) oil recovery (EOR)*. The former denotes the natural flow of oil inside the well and up to the surface due to the underground pressure (reservoir energy) and can basically be driven by six mechanisms. Those were thoroughly described by Ahmed (2001) as rock and liquid expansion drive, depletion drive, gas cap drive (Figures 1.3a and 1.3b), water drive (Figures 1.3c and 1.3d), gravity drainage drive, and combination drive. Over the lifetime of the well, the underground pressure is likely to fall, and, at some point, to become insufficient to maintain the extraction rate. Secondary recovery consists in supplementing the natural reservoir energy by introducing some form of artificial drive, the most basic and employed method being the injection of gas (*gasflooding*) or water (*waterflooding*) through a separate well. Usually, the selected process follows the primary recovery but it can also be conducted concurrently (Ahmed, 2001). In both cases, successful reservoir management requires early recognition of the type of natural

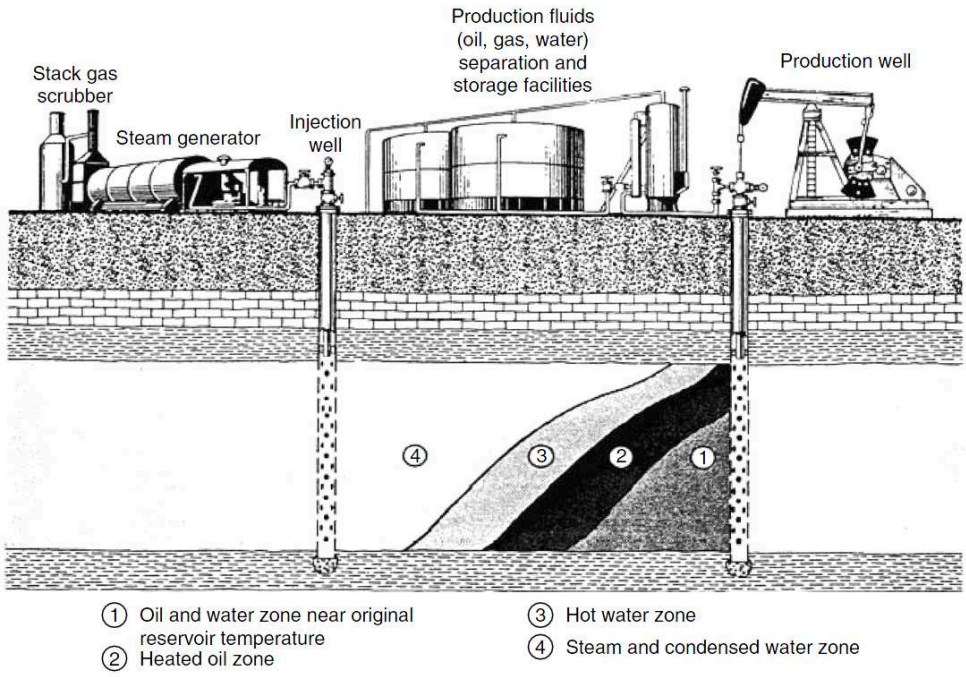

Figure 1.4: *Oil recovery by steam stimulation. Reproduced from Speight (2006) (originally from the United States Department of Energy, Washington DC).*

drive mechanism present. Together, primary and secondary recovery allow an average of 25 % to 35 % of the oil to be extracted (Speight, 2006). Such low efficiency is often linked to the porous rock heterogeneity, the location of wells, and the effect of viscous, gravitational and capillary forces (see section 1.5.1.2) which act simultaneously in the reservoir. For instance, in waterflooding, the latter will cause water to flow more rapidly through the smaller pores or fractures. This may result in bypassing and entrapment of consequent amounts of oil. Enhanced recovery processes aim at counteracting this phenomenon by thermally or chemically altering the residual oil. Although a complete review of the methods is beyond scope[2], it is noteworthy that the two most extensively used ones (Speight, 2006, Alvarado and Manrique, 2010), namely *steam stimulation* (see Figure 1.4) and *microemulsion flooding*, involve again injection of water. As a consequence, the recovery process usually coproduces crude oil and emulsified (because of the phase immiscibility) water in large proportions. Under certain circumstances, amounts of water approaching 80 % to 90 % may even be reached. Furthermore, during the transfer from the wellhead to the manifold, the necessity to release part of the gas results in substantial pressure reductions through chokes and valves. Intense mixing of oil and water occur, possibly decreasing the size of the droplets through flow induced break-ups down to diameters averaging around ten microns[3] (Kokal, 2006).

[2]Any reader willing to learn more about the extraordinarily interesting topic of petroleum is greatly advised to read the book from Speight (2006).

[3]The droplet-size distribution in an emulsion depends on several factors including the IFT, shear, nature and amount of emulsifying agents, presence of solids, and bulk properties of oil and water (Kokal,

1.3.2 Desalting

Desalting is a washing operation, performed at the production site or at refineries, which rely on the injection of fresh (clean) water to remove crude oil contaminants such as dirt, inorganic salts (mainly chlorides and sulfates of sodium, potassium, magnesium and calcium) and solids (Speight, 2006). Formation of very small water droplets is usually favored as it increases the interfacial area available for adsorption, though leading to formation of very stable emulsions that ultimately need to be disposed of.

1.4 Destabilization of emulsions

Due to the extremely wide variety of constituents found in crude oils (more than 60,000 according to Marshall and Rodgers (2008) (see also section 1.2)), the stability of emulsions is a very complex problem. From the chemical standpoint, it seems to be predominantly governed by the interplay between asphaltenes and resins (Sjöblom et al., 2003) and the presence of fine solids, either organic or inorganic (Hannisdal et al., 2006). Insofar model oils were used in the thesis[4], only a simplified picture of the destabilization mechanism is given hereafter. Any reader searching for additional details on the chemical aspects should have a look at the works from Sjöblom (2006) and Sanfeld and Steinchen (2008).

1.4.1 Sedimentation

Physically, stability can be viewed as the ability of an emulsion to prevent the separation of its *disperse phase* from its *continuous phase*, under any external stimulation. Owing to the density difference, destabilization naturally arises from the gravitational sedimentation of water droplets through the lighter crude oil, but can also be accelerated by centrifugation. In both events, a typical order of magnitude[5] of the settling velocity (for a sphere of radius R_d) is given by Stokes' law:

$$U_T = \frac{2R_d^2|\Delta\rho|g}{9\mu_o} \tag{1.2}$$

where $\Delta\rho$ is the density difference between both liquids, g the gravitational/centrifugal acceleration and μ_o the continuous phase dynamic viscosity. The adsorption of *surfactants* (e.g. asphaltenes) from the bulk to the water-oil interface may considerably delay the phase separation. Indeed, while flowing through the viscous oil, water droplets experience shear stresses that convect these surfactants toward zones with lower velocity gradients

2006).

[4] And, as a matter of fact, because of the limited knowledge of the author on this particular topic.

[5] As mentioned by Eow et al. (2001), equation (1.2) is, in fact, only valid for a single solid particle, away from any wall.

where they accumulate. This gives rise to local differences in concentrations which, in turn, induce reverse interfacial flows, referred to as *Marangoni flows*, that slow the overall motion. Still, from equation (1.2), it is clear that intensification of sedimentation results from increasing the density difference between the phases and decreasing the continuous phase viscosity (Eow et al., 2001). Those two can be varied, to some extent, by the addition of diluents and heating, respectively, though at a high economical cost. Moreover, due to the quadratic dependence of U_T on R_d, any mechanism that would lead to an increase in the droplets size would have a much significant impact on the phase separation.

1.4.2 Coalescence

Coalescence refers to the process in which two or more droplets merge together to form a single larger drop in a thermodynamically irreversible way. In modern theories, it is generally described as the successive completion of three individually manageable sub-processes (Chesters, 1991, Zdravkov et al., 2003). First, external forces, such as gravity, play an important role in bringing droplets into collision. The second stage then consists in the thinning of the interstitial film of liquid (continuous phase), trapped in between the approaching droplets, by suction at the Plateau borders. As the interfacial separation goes down below about 1000 Å(Atten, 1993, Lundgaard et al., 2006), other surface forces, namely van der Waals attraction and electric double layer repulsion (DLVO[6] theory, (Sanfeld and Steinchen, 2008)) start to influence the drainage mechanism. The rate of thinning, often determining the outcome of a collision, strongly decreases with the augmentation of the bulk phase viscosity (Stein, 1993) and also with the presence of surfactants. Experimental and numerical studies (Nierstrasz and Frens, 1998) showed, e.g., that Marangoni flows and marginal regeneration processes counteract the lateral expel of liquid inside the film and may lead to metastable configurations. Finally, if at some point, the film reaches its critical thickness (experimentally reported on the order of tens of nanometers (Stein, 1993)), any significant mechanical or thermal disturbances will cause it to become unstable and break, possibly resulting in droplets coalescence.

1.4.3 Enhancement techniques

Along with the addition of diluents and heating, there exist several techniques to enhance the natural separation of water-in-crude oil emulsions (Eow and Ghadiri, 2002). Laminar or turbulent flows can be used to increase the collision rate[7] (see section 1.5.2 and chapter

[6]Named after B. Derjaguin, L. D. Landau, E. J. W. Verway and T. Overbeek.

[7]Brownian motion is also a phenomenon susceptible to induce collisions of very small droplets. Though, in most cases and particularly in state-of-the-art electrocoalescence technologies, its effect is largely

3). Chemical demulsifiers can be injected to neutralize the stabilizing effect of surfactants. When added, they migrate to the water-oil interface, causing rupture or weakening of the protective film around the droplets (i.e by displacement of the originally absorbed crude oil components or by locally changing the solubility conditions (Less, 2008)). Besides, the selection of the right demulsifier is of crucial importance since its effectiveness depends on the composition of the oil as well as the water pH value[8], content of salts and temperature of the emulsion. Other techniques involve centrifugation, filtration, membrane separation as well as the use of microwave radiation and ultrasonic vibration. Yet, from the environmental and energy efficiency points of view[9], none of the above compares to electrostatic demulsification (Noik et al., 2006).

1.5 Electrocoalescence

Historically, the beneficial contribution of electric forces to the separation of water-in-oil emulsions was discovered by Cottrel (Cottrell, 1911, Cottrell and Speed, 1911) about a century ago. After inducing a high potential difference between two metallic wires immersed in an water-in-crude oil emulsion, the authors started to observe arrangement of droplets in chains extending from one electrode to the other. Coalescence of adjacent droplets then rapidly occurred, increasing their size until the point where they became large enough to sediment. Several studies followed, investigating the influence of AC (Taylor, 1988), DC (Charles and Mason, 1960) and pulsed DC fields (Bailes and Larkai, 1981, Bailes and Stitt, 1987) on different types of water-in-oil emulsions (Eow et al., 2001). Although the electrocoalescence phenomenon is still far from being fully understood, partly because of the complex electric and hydrodynamic interactions, a certain consensus has been reached on its basics (Figure 1.5). In the first stage, the fluid motion plays the dominant role in bringing two droplets in close proximity. Then, the coalescence which would not occur naturally in most cases without applied field (see Figure 1.12 in section 1.5.2) is promoted by the field induced attraction force, deformation and interfacial instability (Lundgaard et al., 2006). The following sections review succinctly the physical mechanisms at work and their associated forces.

negligible compared, e.g., to turbulent shear.

[8] Because of its influence on the ionization of the crude oil interfacially active components (Kokal, 2005).

[9] Respectively in terms of amounts of chemical demulsifiers used and power consumed.

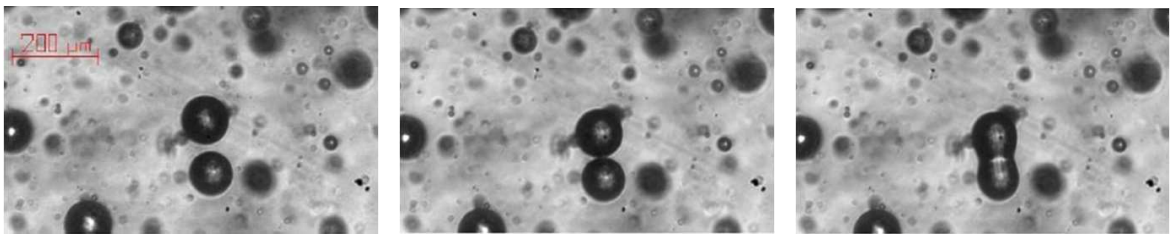

Figure 1.5: *Electrocoalescence of two droplets in a 1.5 % water-in-oil emulsion of Nytro 10XN induced by an applied vertical AC field (1 $kV.cm^{-1}$, 100 Hz). Reproduced from Hølto (2009).*

1.5.1 Theoretical background

According to Coulomb, any charge q placed in an electric field $\mathbf{E}$ experiences a force

$$\mathbf{F} = q\mathbf{E}. \tag{1.3}$$

Though seemingly simple, this law has many practical consequences for complex systems such as water-in-oil emulsions. For the sake of clarity, emphasis is, for now, placed on the case of a single perfectly conductive[10] droplet of radius R_d suspended in a perfect dielectric liquid. More intricate configurations are further addressed in section 1.5.1.4, chapters 2, 3, 4 and appendix A.

1.5.1.1 Polarization/Conduction

Polarization of water droplets can be viewed as an instantaneous phenomenon that arises from two different mechanisms. *Electronic polarization* is universal and results from the field induced rearrangement of the electronic clouds. *Orientation polarization* is specific of the so-called polar materials and consists in the alignment of all the molecular dipole moment with the electric field direction (Lundgaard et al., 2006). Interfacial charge distributions of opposite polarity thus form on the sides of the droplet, turning it into a "dipole". If, in addition, a DC field (or an AC field with a period much longer than the relaxation time of space charge $\tau_E = \epsilon_w/\sigma_w$, i.e. the ratio of the water permittivity to its conductivity) is used, conduction strengthens the polarization. As a result, the background electric field completely vanishes inside the droplet and is amplified by a factor 3 at its poles.

[10]Perfect conductivity is usually assumed when ionic species resulting from the dissociation of dissolved electrolytes (here mostly salts) are present in high concentrations (Atten, 1993, Lundgaard et al., 2006).

1.5.1.2 Deformation

Depending on its intensity, an electric field can dramatically modify the shape of a water droplet suspended in an immiscible insulating liquid. Early observations of this phenomenon dates back to Macky (1931) and led to numerous subsequent investigations on, e.g., the equilibrium shapes, instability conditions, deformation dynamics and the influence of surfactants (Taylor, 1964, Miksis, 1981, Berg et al., 2002, Eow and Ghadiri, 2003b, Berg et al., 2005, Dubash and Mestel, 2007). Basically, the same forces that drive the polarization also induce mechanical stresses at the water-oil interface. Those are expressed through the Maxwell stress tensor, defined as:

$$\mathbf{M} = \epsilon_0 \epsilon_{r_o} \left[\mathbf{E}\mathbf{E} - \frac{1}{2} \left(\mathbf{E} \cdot \mathbf{E} \right) \mathbf{I} \right] \tag{1.4}$$

where ϵ_0 is the absolute permittivity of vacuum, ϵ_{r_o} the relative permittivity of the continuous phase and $\mathbf{I}$ the identity tensor. Diagonal and off-diagonal terms in equation (1.4) correspond to pressures and shear stresses, respectively. For a perfectly conductive droplet, the electric field only acts normal to the interface (along $\mathbf{n}$). Hence, only the diagonal terms remain, yielding the well-known *electrostatic pressure*

$$p_E = \frac{1}{2} \epsilon_0 \epsilon_{r_o} (\mathbf{n} \cdot \mathbf{E})^2. \tag{1.5}$$

In light of equation (1.5), elongation of the droplet is likely to occur along the direction of the electric field, i.e. where p_E is maximum. For weak fields, stable deformed shapes may exist as interfacial tension tries to resist the creation of additional interfacial area by opposing a restoring pressure, referred to as the *capillary pressure*. Its intensity is given by Laplace's law

$$p_{Cap} = -2\gamma H \tag{1.6}$$

where γ denotes the interfacial tension (IFT) coefficient and H the mean curvature of the interface. For higher fields, though, interfacial tension may not be able to compensate for the increased electric stresses and the droplet may elongate until it undergoes some form of break-up (see Figure 1.6). Assuming an ellipsoidal shape for the deformed interface, Taylor (1964) derived an estimate for the critical background electric field writing

$$E_{0_{Crit}} = 0.648 \sqrt{\frac{\gamma}{2 R_d \epsilon_0 \epsilon_{r_o}}}. \tag{1.7}$$

and corresponding to an aspect ratio of 1.9 (in practice, those two values are slightly overestimated by the author's model, see appendix A). Due to their very small radius,

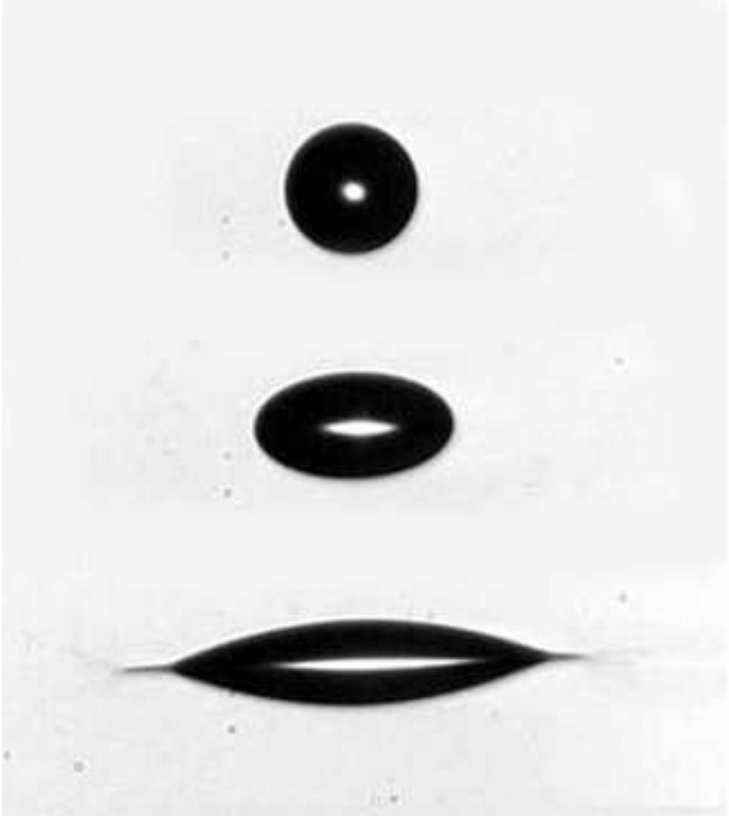

Figure 1.6: *Deformation and disruption of a conducting water drop freely suspended in a dielectric oil (Nitro 10X) and subjected to an increasing electric field (from top to bottom). Reproduced with the courtesy of G. Berg.*

single drops in the size range of interest ($10-20\ \mu m$) can usually sustain relatively strong electrostatic stimulation. Though, as presented in the upcoming section, this picture becomes considerably altered in emulsions.

1.5.1.3 Motion/Attraction

From a physical point of view, two different but not necessarily exclusive mechanisms can cause water droplets to approach or drift when subjected to an electric field. In the literature, those are referred to as *electrophoresis* and *dielectrophoresis*. The former is mainly encountered in homogeneous/uniform DC fields[11] and describes the motion resulting from the action of Coulombic forces (see equation (1.3)) on a droplet carrying a net charge. In electrocoalescers, such droplets can be produced through the electrostatic destabilization of larger drops, adsorption of chemical additives or through direct contact with bare electrodes. In the latter event, the amount of charge acquired by the droplet is proportional to the square of its radius R_d and to the electric field strength E (Cho,

[11] In AC fields, the droplet may deform and oscillate, but over time no net displacement is generally observed.

1964). Strictly speaking, *dielectrophoresis* only arises in inhomogeneous electric fields, either DC or AC. Schematically, both charged and neutral droplets will experience stronger Coulombic forces on the side where the field is higher and move accordingly.

Yet, neither of these mechanisms plays a predominant role in the attraction stage preceding electrocoalescence, at least not in the present problem. Indeed, most crude oils being slightly conductive ($\sigma_o \sim 10^{-9} - 10^{-7}\ S.m^{-1}$), any excess of charge within emulsion droplets will leak away in the surrounding oil (Bailes and Larkai, 1981) at a rate given by the relaxation time $\tau_E = \epsilon_o/\sigma_o$ (here on the order of 2.7 10^{-4} s to 1.8 10^{-2} s, (Lundgaard et al., 2006)). Electrophoretic attraction is therefore restricted to adjacent charged droplets of opposite polarity, and so is disregarded in this thesis. Moreover, dielectrophoretic forces resulting from an applied divergent field are generally very weak. Droplets approach may be achieved, providing they have different sizes, though at very slow rates.

A "third" mechanism is actually responsible for the occurrence of electrocoalescence. Because of their polarization in any given electric field, two water droplets interact and mutually attract each other. The resulting interaction force, negligible at long distance, considerably increases when the droplets are brought in close proximity and become affected by each others' inhomogeneous field created by their own dipolar moment. Note that for this reason, this mechanism is often regarded as dielectrophoretic in nature. The evolution of the force magnitude with the droplets spacing is discussed hereafter.

1.5.1.4 Electrostatic interaction force

Point-Dipole approximation

At a long separation distance, s, the electrostatic interaction between two droplets of radii R_1 and R_2 can be approximated by the force acting in between two dipoles located at their centers. In this so-called *point-dipole approximation*, the force decomposes into a radial F_r and a tangential F_θ component expressed respectively as

$$F_r = -12\pi\epsilon_0\epsilon_r R_2^3 E_0^2 \frac{R_2^3}{(s+R_1+R_2)^4}\left(3K_1 cos^2\theta - 1\right) \tag{1.8}$$

$$F_\theta = -12\pi\epsilon_0\epsilon_r R_2^3 E_0^2 \frac{R_2^3}{(s+R_1+R_2)^4} K_2 sin2\theta \tag{1.9}$$

where K_1 and K_2 are coefficients equal to 1. Depending on the skew angle θ ($\neq 0$), the force may either be attractive or repulsive and tends to align the droplets with the direction of the field (Figure 1.7). For two droplets of even radii R_0 and $\theta = 0 + k\pi$,

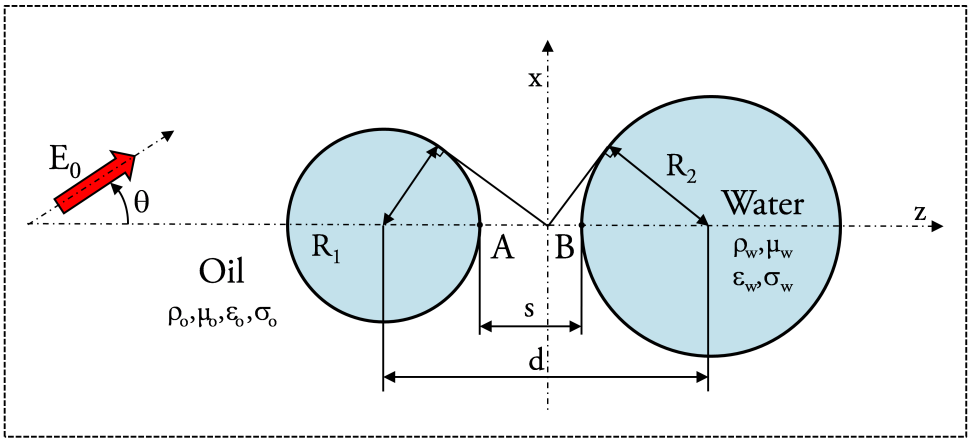

Figure 1.7: *Conductive water drops of different sizes suspended in oil and influenced by a homogeneous electric field. θ characterizes the angle formed between the droplets axis and the electric field.*

$F_\theta = 0$ and the classical formulation of Waterman (1965) is recovered:

$$F_r = -24\pi\epsilon_0\epsilon_r E_0^2 \frac{R_0^6}{(s+2R_0)^4}. \tag{1.10}$$

Dipole-Induced Dipole model

When the separation distance is reduced below about one radius ($s/R_1 \sim 1$), (see appendix A), displacement of the dipole moments arise with the mutual inductions between the droplets. The previous approximation, neglecting this effect, is thus no longer valid. A multiple image method, relying on the assumption that a point-dipole in one droplet induces a new dipole in the other and reciprocally, was developed by Yu and Wan (2000). The first two terms of the method give the *Dipole-Induced Dipole model* corresponding to equations (1.8) and (1.9) with coefficients K_1 and K_2 defined as:

$$K_1 = 1 + \frac{R_1^3 d^5}{(d^2-R_2^2)^4} + \frac{R_2^3 d^5}{(d^2-R_1^2)^4} + \frac{3R_1^3R_2^3\,(3d^2-R_1^2R_2^2)}{(d^2-R_1^2-R_2^2)^4}, \tag{1.11}$$

$$K_2 = 1 + \frac{R_1^3 d^3}{2\,(d^2-R_2^2)^3} + \frac{R_2^3 d^3}{2\,(d^2-R_1^2)^3} + \frac{3R_1^3R_2^3}{(d^2-R_1^2-R_2^2)^3}. \tag{1.12}$$

where d is the distance between droplets center. As shown by Pedersen (2008), the DID model offers a fair amount of accuracy, down to $s/R \sim 0.1$ (appendix A) at a relatively low computational cost.

Analytical solution

At even smaller separation distances, more sophisticated expressions are required. In the configuration illustrated on Figure 1.7, Davis (1964) gave analytical solutions for the potential, electric field and attraction force for two arbitrary sized spheres carrying

any net charge, using bispherical coordinates. For neutral rigid water droplets, the force components on the smaller one (#1) writes

$$(F_r)_1 = 4\pi\epsilon_0\epsilon_{r_o}R_1^2E_0^2\left(F_1 cos^2\theta + F_2 sin^2\theta\right) \tag{1.13}$$

$$(F_\theta)_1 = 4\pi\epsilon_0\epsilon_{r_o}R_1^2E_0^2F_3 sin2\theta \tag{1.14}$$

where F_1, F_2 and F_3 are highly intricate series depending on the drop size ratio R_1/R_2 and on the relative interfaces spacing s/R_1. Furthermore, based on these two variables, Davis (1964) also introduced a very convenient parameter, denoted E_3, allowing to relate the maximum electric field intensity E_A, reached at the droplet pole A, to the imposed value E_0 according to

$$E_A = E_3E_0 cos\theta. \tag{1.15}$$

All the above equations implicitly consider that the droplet maintain a spherical shape during the approach process. In practice, due to the electric field enhancement occurring in between the droplets (e.g. $E_3 \sim 14.2$ for $R_1/R_2 = 1$ and $s/R_1 = 0.1$), electric stresses may become strong enough to deform the water-oil interface. The subsequent increase in curvature at the facing poles leads, in turn, to a reinforcement of the attraction forces which is most often only taken into account through numerical simulation.

1.5.1.5 Mechanical forces

In addition to electrostatic interactions, other forces transferred from the conveying liquid to the droplets through friction and pressure difference also play a major part in the electrocoalescence process (Lundgaard et al., 2006). Neglecting gravity (in general, it only becomes significant after successive merging events and substantial droplets growth) and virtual mass effects (small average relative acceleration), three different contributions either favorable or detrimental have been distinguished in the literature.

Drag force

Basically, *drag* opposes the relative motion of a water droplet through its conveying liquid. At "steady state" the resulting force takes the form

$$\mathbf{F_d} = -\frac{1}{2}\rho_o C_d A(\mathbf{u}\cdot\mathbf{u})\frac{\mathbf{u}}{\|\mathbf{u}\|} \tag{1.16}$$

where ρ_o is the continuous phase density, $A = \pi R_d^2$ the frontal area of the droplet and $\mathbf{u}$ the relative phase velocity. At low particle Reynolds number $Re_d = 2\rho_o R_d\|\mathbf{u}\|/\mu_o$, the

drag coefficient C_d for a spherical liquid droplet is an empirical function expressed as

$$C_d = \frac{24}{Re_d}\frac{\lambda + \frac{2}{3}}{\lambda + 1}, \tag{1.17}$$

$\lambda = \mu_w/\mu_o$ being the disperse to continuous phase viscosity ratio. It is noteworthy, that the right hand side term of equation (1.17) accounts for the reduction of the viscous part of the drag generated by internal circulation.

Film thinning force

The *film thinning force* reflects the hydrodynamic resistance to the drainage of the liquid trapped in between two approaching droplets. Depending on the bulk phase and interface properties, a few different expressions can be found, the relevance of which is investigated in chapter 3 (see section 3.3.2). Generally, a very rough order of magnitude, calculated for two rigid spheres of either even or uneven radii, is given by

$$\mathbf{F_f} = -\frac{6\pi\mu_o}{s}\left(\frac{R_1 R_2}{R_1 + R_2}\right)^2 (\mathbf{u_1} - \mathbf{u_2}) \tag{1.18}$$

where $\mathbf{u_1}$ and $\mathbf{u_2}$ are the droplets respective velocity (Jeffrey, 1982).

Compressional force

During flow induced collisions, the carrier liquid exerts a *compressional force* on the water droplets which drives, at least partly, the drainage process in the absence of an applied electric field. In turbulent conditions, this force is usually assumed to be proportional to the mean-square velocity difference at either ends of the eddy with a size of the equivalent diameter

$$\mathbf{F_c} = \rho_o \zeta^{2/3} (2(R_1 + R_2))^{2/3} \left(\frac{2R_1 R_2}{R_1 + R_2}\right)^2 \frac{\mathbf{u_1} - \mathbf{u_2}}{\|\mathbf{u_1} - \mathbf{u_2}\|} \tag{1.19}$$

where ζ stands for the turbulent eddy dissipation rate (Coulaloglou and Tavlarides, 1977).

1.5.2 Historical evolution of the electrostatic separators

Early, also referred to as conventional, electrocoalescers were large vessels containing electrodes, between which a "treating space" exists where dispersed water droplets grow mainly by electrocoalescence, and a "settling zone" where phase separation takes place under laminar-flow conditions (Urdahl et al., 2001). A considerable residence time, typically $30 - 40$ min, was required, hence the need for large vessels. This led to problems offshore where, in order to economize on platform structure, an important issue is the reduction of weight and size of topside equipment. Among the marketed innovative solutions, three

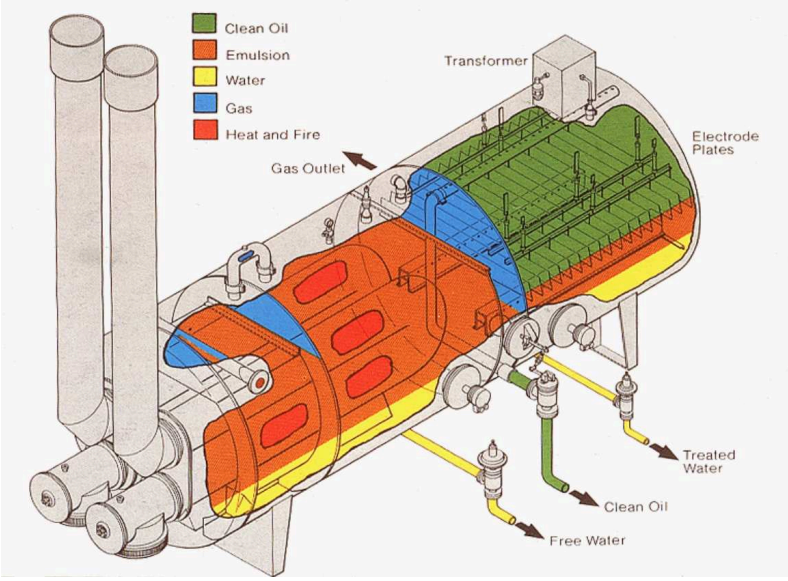

Figure 1.8: *Schematic drawing of the NATCO Dual Polarity® Electrostatic Treater Cameron (2011).*

particularly remarkable ones drawn the author's attention.

With its nearly thirty years of existence[12], NATCO's Dual Polarity® Electrostatic Treater reflects, on its own, the evolution of the understanding of the electrocoalescence phenomenon. The crude oil emulsion enters the Dual Polarity® Treater and flows downward over a hood baffle (Cameron, 2011). "Free water"[13] separates immediately and therefore does not need to be heated. The hood baffle also helps to eliminate firetube scaling by keeping the free water from coming directly into contact with the firetube. The oil emulsion is heated as it flows up after the firetube. Due to the reduction in continuous phase viscosity, larger water droplets settle to the bottom of the vessel, while smaller ones remain in the emulsion as it flows into the electrostatic field region. The "main improvement" of the NATCO's Treater lies in the combined use of AC and DC fields to accelerate coalescence and thus sedimentation. As seen on Figure 1.9, when entering the coalescence section, water droplets may acquire net charges after contacting vertical pairs of steel electrodes of opposite polarity. Induced electrophoretic forces hence promote long distance attraction and assist dipolar coalescence for an "optimum" growth of the droplets. Once they become large enough to be significantly affected by gravity, they fall towards the planar water-oil interface. An AC electric field, most effective in water-rich zones (due to the lower interfacial separation), keeps favoring the coalescence process and mitigates against corrosion (Less, 2008) occurring through ionic conduction in the sedimented water. In order to avoid arcing and discharges resulting from the formation of water drops chains

[12]It was first introduced in the 1970s and upgraded to Dual Frequency® Electrostatic Treater in the beginning of the 21st century.

[13]Denoting drops that settle on their own within $3 - 10$ minutes (Stewart and Arnold, 2008).

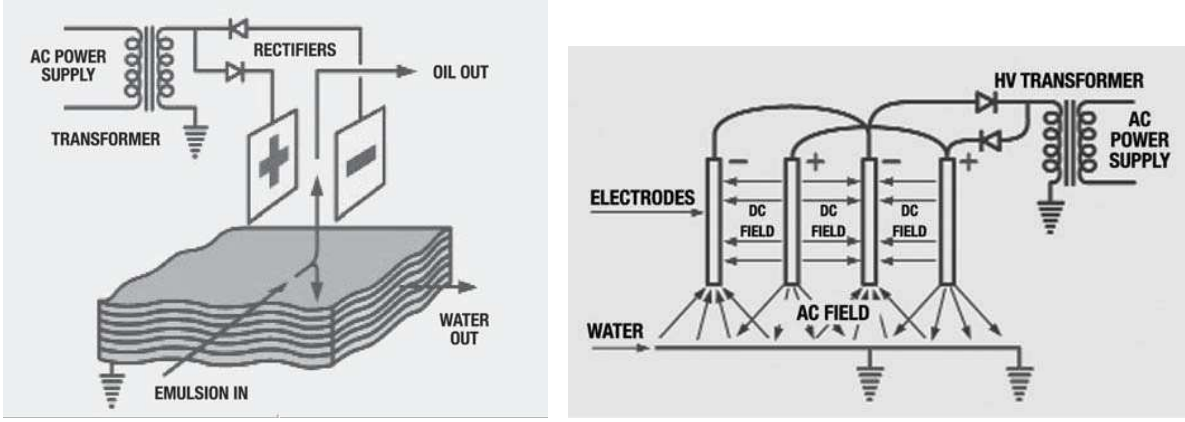

(*a*) (*b*)

Figure 1.9: *Combined AC/DC electric field configuration in the coalescence section of the NATCO Dual Polarity® Electrostatic Treater. Reproduced from Cameron (2011).*

(Cottrell, 1911) in "wet" crude oils, NATCO has implemented vertical coated electrodes since 1982. Those consist of plates of composite (fiber reinforced plastic) construction with graphite or carbon embedded in the central portion to impart conductivity along its length. The remainder of the plate contains filler materials that lead to the adsorption, on its surface, of a water layer, which then becomes the conductive medium. As a result, only the area in the immediate vicinity of an arc will discharge, almost eliminating decline of performance. Despite voltage decays due to the non-negligible conductivity of crude oils (see section 1.5.1.3), NATCO claimed "considerable gain" in terms of heating temperature (reduction of about $8°C$), mass loss and throughput (increase of about 29 % at 10,000 bopd (barrels of oil per day) of a 32.5° API gravity crude) compared to conventional electrostatic dehydrators. In 2002, NATCO commercialized a new patented technology, known as Dual Frequency®, allowing additional modulations of the AC/DC electric fields to both limitate the voltage decay and optimize the process with regards to the crude properties. For instance, units installed at a South American oil facility demonstrated able to operate a 27.1° API gravity oil at flows between 45,000 and 60,000 bopd with inlet water cuts (WC) typically ranging from 20 to 30 % and reduce the BS&W (Basic Sediment and Water) below 1 % (Armstrong and Sams, 2008).

More recent electrocoalescers rely on both strong hydrodynamic and electrostatic stimulations. Typical examples are the Vessel Internal Electrostatic Coalescer (VIEC®) and the Compact Electrocostatic Coalescer (CEC™). The VIEC® is, along with its high temperature declination (up to $150°C$) the HTVIEC® and the Low Water Content Coalescer (LOWACC), part of a oil-water separation product line supplied by Aibel AS, now Hamworthy (Figure 1.10). A full VIEC® system (Figure 1.11a) is usually constituted of

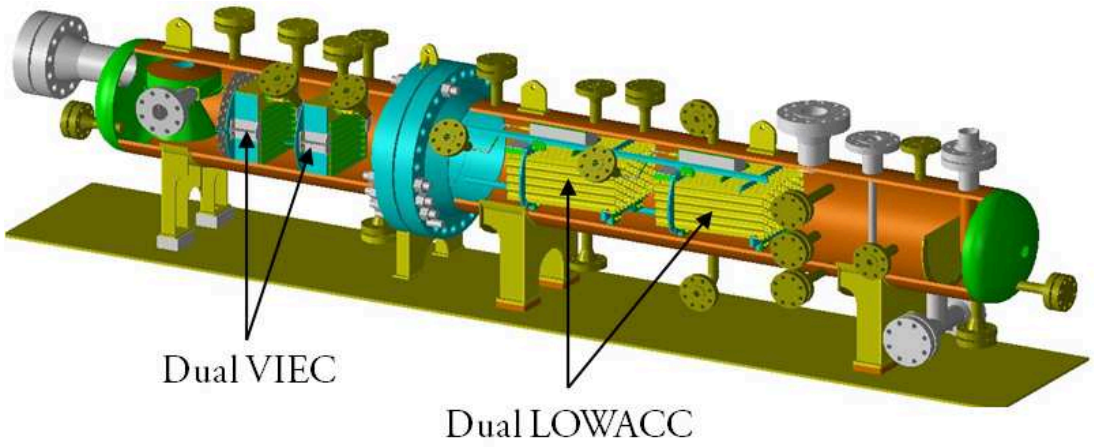

Figure 1.10: *3D CAD model of a test separator containing two Version 2 VIEC® units and two LOWACC prototypes implemented at Vetco Aibel (now Hamworthy (2011)) in 2004.*

an arrangement of single, humanly replaceable, modules (Figure 1.11b), each constituted by sets of electrodes molded into a perforated epoxy (or ceramic for the HTVIEC®)) wall (Piasecki et al., 2004). Rectangular holes act as mechanical flow straighteners that increase turbulence within the crude oil and favor to some extent, the frequency of water drop collisions (chapter 3). In addition, each module is powered by an AC high voltage, the operating frequency of which is controlled in the kHz region to overcome the voltage drop across the insulation layer. Being secured from electrical breakdown, VIEC® systems can withstand large inlet water cuts and perfectly adapt to the harsh first stage separator conditions. Since 2003, VIEC® units have been installed in at least 15 different fields all over the world, treating crudes ranging between API $11° - 40°$. When turned on, achieved BS&W drops below $5 - 6$ %, even at reduced heating temperatures and amount of injected demulsifiers (Figure 1.12). The LOWACC is designed to operate downstream of the VIEC® to knock out the last trace of water, possibly reaching export qualities ($BS\&W < 0.5$ %) and enabling one-stage separation[14]. With its robust design and fully insulated electrodes, the LOWACC can also be used to enhance heavy oil separation (Figure 1.10).

The CEC™ is a small lightweight vertical flow-through unit (with a typical height of 5.5 m and an outside diameter of 1.2 m) that can easily be retrofitted upstream of an existing gravity separator to enhance its performance without much other modifications (Figure 1.13). The idea behind the CEC™ was originally patented by an oil company, Statoil, in the mid 1990s, following research that had been performed at the Southampton University since the 1980s (Statoil, 2011). It has been further developed through a cooperation with British Petroleum (BP) and is now distributed by AkerSolutions™

[14]Understand "in one separator vessel".

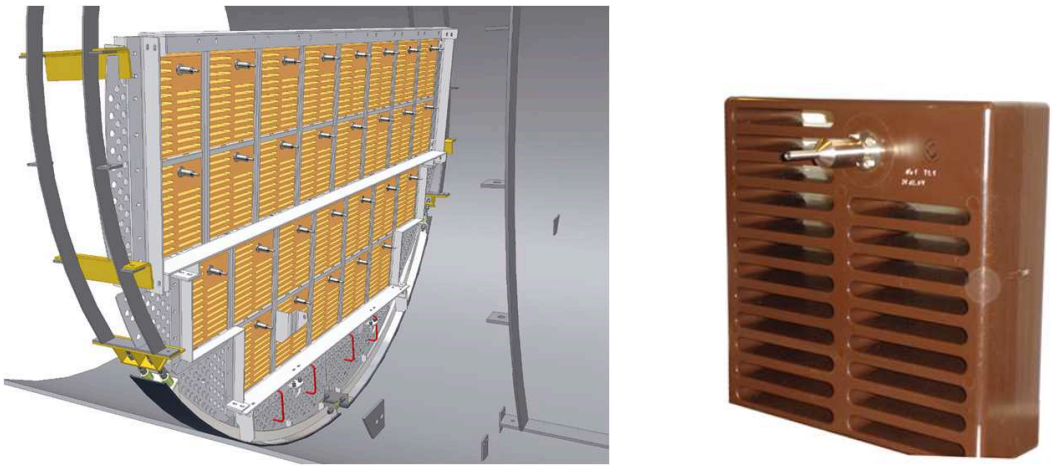

(*a*) (*b*)

Figure 1.11: *3D CAD model of a large separator equipped with a VIEC® system (a) and photograph of one of its 26 modules (b) (Hamworthy, 2011).*

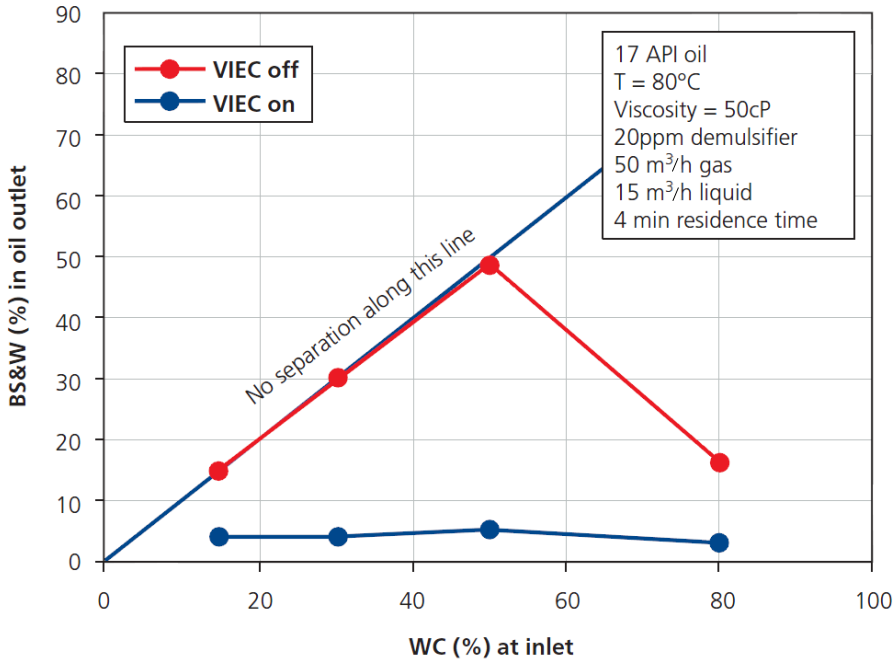

Figure 1.12: *Dewatering efficiency of a high pressure test separator equipped with the VIEC system as a function of the crude water cut at inlet. Reproduced from Hamworthy (2011).*

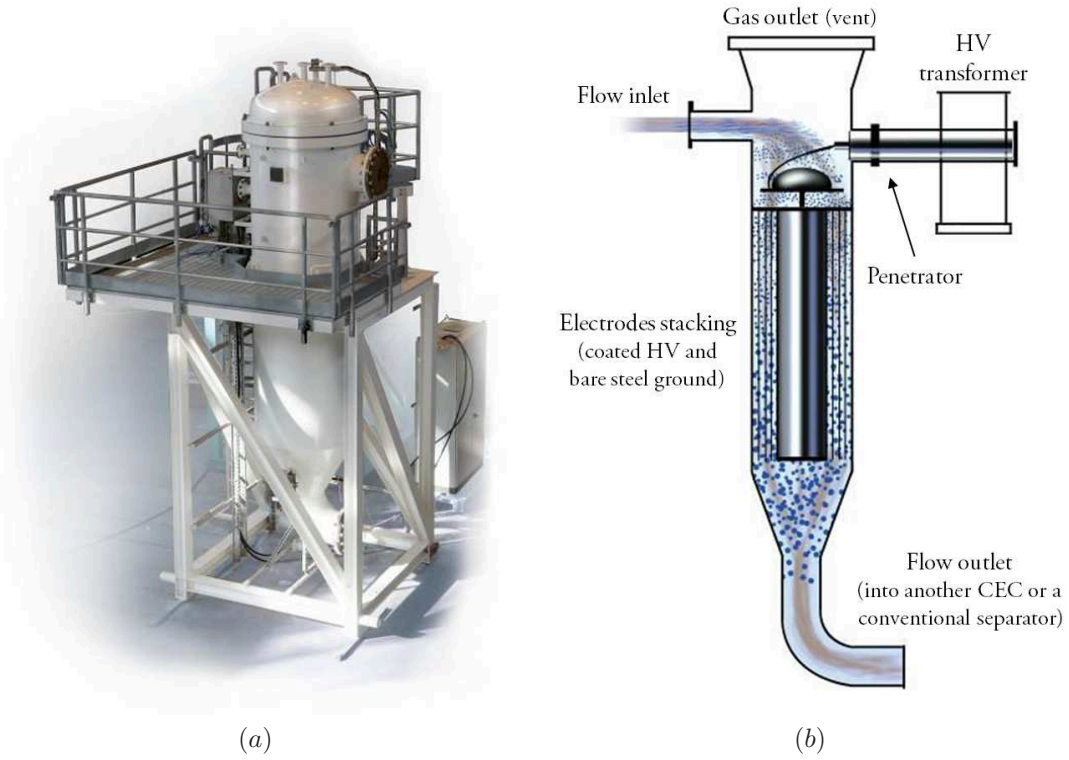

Figure 1.13: *Actual CEC^{TM}unit (a) and schematic drawing of its internal components (b) (AkerSolutions, 2011).*

who exclusively owns the commercial rights. Technically speaking, the CEC^{TM} consists of an entanglement of concentric annular (bare ground and insulated HV) electrodes, in between which a turbulent crude oil flow is subjected to strong AC fields (on the order of $kV.cm^{-1}$). Water droplets merge several times within a matter of seconds, resulting in a mean diameter growth of about an order of magnitude. As the VIEC®, it is tolerant to extreme inlet water contents (up to 100 %), though its best implementation is usually after the second or third stage separator. For instance, the separation system, combining a CEC^{TM} unit and a sedimentation tank, operating at Statoil's Glitne field (North Sea) since 2002 has proven able to produce 65,000 bopd with less than 0.3 % BS&W[15] of a 32° API crude having 20 % WC and that, at a heating temperature of 70°C and without any chemical demulsifiers. Other such systems were also installed in Mærsk's Al Shaheen, Marathon's Alvheim and Petrobras' Jubarte fields[16], treating up to 130,000 bopd at API ranging from 14° to 36°.

[15]That is to say below the export quality target of 0.5% BS&W.

[16]Here, data dates back to 2008. The author would not be surprised if a market breakthrough was accomplished during the last two years.

1.5.3 Towards a criterion of electrocoalescence

Since their first industrial implementation, the control and improvement of electrostatic coalescers efficiency has always been a central concern. In order to overcome the tremendous complexity of the electrocoalescence mechanism when applied to water-in-crude oil emulsions, the widely acclaimed approach was to investigate separately the various phenomena — which additionally might occur at different length and time scales — and converge progressively by evaluating their respective contribution. Early works were devoted to the identification of optimum operating conditions, i.e. electric field type (Waterman, 1965, Bailes and Larkai, 1981), frequency, and to the determination of relatively simple, either empirical or theoretical, models. Wang et al. (1994) expressed, e.g., the demulsification rate as a function of the electric field strength and initial drop size. Atten (1993) proposed another formulation using the water hold-up and shear rate. Research on electrocoalescence later spread over an extensive number of scientific domains, including among others, studies regarding interfacial chemistry (Mohammed et al., 1993, Førdedal et al., 1996) and emulsions behavior under electric and/or hydraulic (Harpur et al., 1997, Lesaint et al., 2009) stimulation. Benefiting from the gained understanding, especially on the multi-stage nature (see section 1.5) of the mechanism, an ongoing approach undertaken to progress towards the estimation of the electrocoalescence efficiency in actual devices consisted in considering the probability of its three sub-processes to occur. These are recalled as the hydrodynamically induced collision of two drops, the critical thinning of the interstitial fluid film promoted by electric forces and the final bridging of the interfaces, respectively[17]. Nevertheless, while several expressions describing the former and its dependency on the flow had already been established (see for instance the review by Liao and Lucas (2010)), very few was available on the two latter back in 2007, particularly as some physical aspects, e.g. the role of asphaltenes, were far from being fully understood and as the collection of experimental data was limited by the poor crude oil transparency to visible and IR lights[18]. Consequently, addressing these shortcomings which had severely hindered the modeling of state-of-the-art compact electrostatic coalescers operation, either theoretically or by numerical simulation[19] became of primary interest. With regards to the laboratory knowledge, emphasis was rather placed on the fluid drainage process

[17] To be even more exhaustive, a probability of "full merging" should also be included to account, for instance, for partial coalescence phenomenon (Hellesø et al., 2009) or break-up at high Capillary numbers Ca following the interface recombination.

[18] Prior to the recent development of high-speed NIR infrared cameras (Aakre et al., 2005), experimental studies on the electrocoalescence of water-in-crude oil emulsions relied mostly on the analysis of changes in the mixture refractive index, i.e. indirect and relatively large scale techniques.

[19] Use of the latter has growingly extended over the last decade following the tremendous increase in computational power.

and particularly on the establishment of a criterion predicting the conditions required for the film to reach its critical thickness.

First efforts spent in that direction are attributed to Charles and Mason (1960) and Allan and Mason (1961). The authors led the way by studying the effects of electric fields on the stability and partial coalescence of conductive liquid drops at a flat interface between a dielectric liquid and their own bulk phase. They gave, for instance, asymptotic expressions linking the dielectric film thinning rate and the corresponding resting time to the applied electric field, using the electrostatic attraction force acting on an undistorted conducting sphere near a conducting plane in a macroscopically uniform field, formulated by Sartor (1959). About forty years later, Eow and Ghadiri (2003a) and Aryafar and Kavehpour (2009) performed experiments in a similar configuration to identify conditions producing instantaneous and single-staged electrocoalescence respectively. Despite giving insights into the optimal operating parameters, neither provided a complete characterization of the mechanisms. With the assumption of a very low viscous surrounding medium, Taylor (1968) improved the previous approach of Latham and Roxburgh (1966) and proposed, based on experimental results, relations to calculate the critical potential difference and interfacial spacing between two very close drops, leading to interfacial instability, as a function of their initial configuration. A physical picture and a justification of those "empirical laws" were given, decades later, in Atten et al. (2006) along with an extent to the case — more relevant to electrocoalescence in water-in-crude oil emulsions — of charge free conducting drops, suspended in a insulating medium under the influence of a uniform applied electric field. Recently, Ristenpart et al. (2009) observed and characterized the non-coalescence of millimeter sized and oppositely charged water drops in light Louisiana Gulf sweet crude oil over a threshold applied electric field, in terms of a critical angle of the facing interfaces. This phenomenon was also reported by Hellesø et al. (2009) in the electrocoalescence of charge free water drops falling through different crude oils onto resting water drops and also implies the existence of electric field limitations over which the process efficiency might be degraded. However, in its current form, i.e. without being expressed in terms of easily monitorable parameters (drop radii, interfacial tension coefficient, surfactant types and concentrations, initial separation distance, applied electric field, etc.), the criterion appears hardly applicable to the enhancement of dewatering technologies. Furthermore, and as all the others, it still does not take into account the finite time available for the drop to coalesce and explain failed electrocoalescence events happening at low interfacial deformation.

1.6 Conclusion

The literature review presented in this first chapter has highlighted various aspects of water-in-crude oils emulsions, from their almost inevitable formation to their complex but necessary resolution. In this latter perspective, the most environmentally friendly and energy efficient technique, referred to as electrocoalescence, was introduced. In order to provide a clear picture of the involved phenomenon, a particular attention was paid to the characterization of its successive stages and of the hydrodynamic and electrostatic interactions. Concerning other important mechanisms at work, such as those explaining emulsions stability and related to the chemistry of petroleum, brief descriptions were formulated and references to more comprehensive studies were given. Then, progresses accomplished in the electrocoalescers technology over the last decades were illustrated through a few remarkable examples, including state-of-the-art marketed devices. Finally, the lack of adequate tools available for the estimation of their efficiency in operating conditions was underlined, and the approach undertaken in the following chapters to address this matter was clarified.

Chapter 2

Deformation and stability of electrically influenced water-oil interfaces

2.1 Introduction

The difficulty in building a criterion predicting the probability of electrocoalescence of colliding drops lies, aside from the mechanism complexity, in the "deficiencies" of the techniques available for its study. On the one hand, the spatial and temporal resolution of up-to-date optical cameras remain, despite continuous improvements, too low to accurately track the interface evolution in experimental investigations, especially during the last steps of the process. On the other hand, numerical simulation allows very fine discretization but is inherently restricted by the existence of laws describing the different physical phenomena involved and hardly represents actual situations. Combining both might appear time consuming but truly helps to overcome these limitations and identify the dominant, sometimes underlying, factors influencing the overall mechanism. This chapter first presents the development of a general numerical scheme implemented — in a commercial multi-physics software — to simulate both quasistatic and transient behaviors of interfaces between perfectly conductive and dielectric liquids subjected to electrostatic forces and used throughout the thesis. Then, the interest of the approach is illustrated by the validation and extension of asymptotic analytical criteria predicting the quasistatic instability of such interfaces in configurations relevant to the electrocoalescence of water drops in oil.

2.2 A numerical scheme for solving EHD problems with moving boundaries

2.2.1 Choice of the method

Quite a few numerical methods used to solve EHD problems involving deformations of interfaces between non miscible fluids are reported in the literature. Selecting one among them thus requires special care and is most often dependent on the intrinsic nature of the phenomenon to be modeled. A first important criterion concerns the distinction between static and time-dependent problems. The former case correspond to a classic bifurcation problem and is governed by the "augmented Young-Laplace equation" (as, e.g. in the studies of Rayleigh (1882), Taylor (1964, 1966), Miksis (1981), Joffre et al. (1982), Basaran and Scriven (1989), Harris and Basaran (1993, 1995)). For the latter, i.e when emphasis is placed on the dynamical evolution of the interfaces, determining the motion of the fluids and therefore solving the Navier-Stokes equations (or Euler equations for inviscid fluids) becomes compulsory. After the initial approaches based on the ellipsoidal approximation and on the computation of electric field around elongated single drop or drops pair (Taylor, 1964), different numerical methods were proposed and further classified in two groups, each having its own strengths and weaknesses.

Interface tracking methods use markers (front tracking) or a separate grid to locate the interface. For instance, Boundary Integral techniques or Boundary Element methods (BEM) (Brazier-Smith, 1971, Miksis, 1981, Sherwood, 1988, Mansour and Lundgren, 1990, Schulkes, 1994, Setiawan and Heister, 1997) are very efficient in problems where there is a small surface to volume ratio. Indeed, avoiding volume discretization saves a considerable amount of computational resources and allows finer description of the interfaces. However, this strongly constrains the applicability range of the method which is, in practice, mainly devoted to the resolution of Laplace equations, i.e. electric field in a perfect dielectric medium and potential or Stokes flow. Finite Element coupled with Arbitrary Lagrangian-Eulerian (ALE) methods associate displacement of interfaces and resolution of electrostatics and fluid dynamics equations in deforming meshes (Basaran and Scriven, 1989, Feng, 1999, Notz and Basaran, 1999) and are interesting to treat more general problems. Leaky dielectric models or Navier-Stokes equations can be taken into account (Supeene et al., 2008). These methods offer high accuracy and "perfect" mass conservation at relatively low computational cost but can not handle topological changes such as coalescing or splitting interfaces.

Interface capturing methods can get over this difficulty as the interface is not tracked

explicitly but rather obtained by geometrical reconstruction. Simulations of complete sequence including topological changes using the Volume of Fluid (VOF), the Level Set or even more recently the Phase-Field methods have been developed in Richards et al. (1995), Zhang (1999), Tomar et al. (2007). Interfacial forces are transformed in volume terms through a continuum surface force model (CSF) (Brackbill et al., 1992). However, accuracy of interfaces location and curvature strongly depends on the initial mesh size and, therefore, adaptive grids and/or segregated solver are often required to decrease the computational load. Moreover, numerical treatment of very thin liquid films remains challenging.

The location of the water-dielectric fluid interface, and mainly the resulting curvature, has a major influence on the local electric field, the electrostatic and capillary pressures and thus must be tracked very accurately at each time step. Furthermore, as, in the thesis, emphasis was placed on the deformation and instability of the interfaces rather than on its breakup or on the possible merging of the drops, the choice of a Finite Element - Arbitrary Lagrangian-Eulerian seemed most appropriate.

2.2.2 Governing equations and boundary conditions

The developed model aims at computing the transient deformation generated by the action of an electric field on any interface between a perfectly conducting liquid (water - domain D_1) and a perfectly dielectric fluid (air or oil - domain D_2), as presented on Figure 2.1. Assuming that both fluids, characterized by their mass density ρ_i and viscosity μ_i, are incompressible, the velocity fields $\mathbf{u_i}$ and pressures p_i, in water and in the dielectric fluid, can be calculated by solving separately the time-dependent Navier-Stokes equations in each medium i:

$$\rho_i \frac{\partial \mathbf{u_i}}{\partial t} - \nabla \cdot \left[\mu_i \left(\nabla \mathbf{u_i} + (\nabla \mathbf{u_i})^T \right) \right] + \rho_i \left(\mathbf{u_i} \cdot \nabla \right) \mathbf{u_i} + \nabla p_i = \mathbf{F_i}, \tag{2.1}$$

$$\nabla \cdot \mathbf{u_i} = 0. \tag{2.2}$$

This also ensures, through the resolution of the continuity equation (2.2), the volume conservation of closed domains such as drops. In the absence of space charges in the dielectric fluid, the volume force field $\mathbf{F_i}$ stands for the gravitational force ($\mathbf{F_i} = \rho \mathbf{g}$). Depending on the scale of the experimental configuration studied, it will either be considered or neglected. When air is chosen as the dielectric fluid, its dynamics can be neglected and the pressure inside the domain 2, p_2, can be considered as uniform. In that case, the calculation of the fluid dynamics equations inside the dielectric domain D_2 is avoided. Brownian motion and any effects due to temperature gradients inside the fluids are neglected.

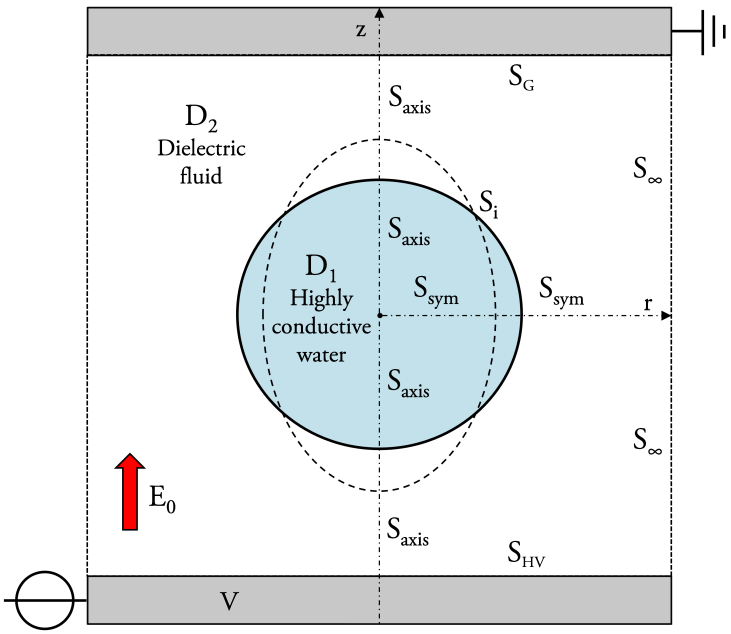

Figure 2.1: Geometry and associated boundaries S of a typical axisymmetric problem involving an electrically influenced fluid-fluid interface. Subscripts *axis*, G, HV, i, *sym* and ∞ stand respectively for *axisymmetry*, *ground*, *high-voltage*, *interface*, *planar symmetry* and *infinity*.

From an electrostatics point of view, the electric potential V, constant inside the water phase due to the assumption of perfect conductivity[1], is obtained in the dielectric fluid domain of relative permittivity ϵ_{r_o} by solving the Laplace equation

$$\nabla \cdot (\epsilon_0 \epsilon_{r_o} \nabla V) = 0. \tag{2.3}$$

The electric field $\mathbf{E}$ is then given by

$$\mathbf{E} = -\nabla V. \tag{2.4}$$

The electrohydrodynamic (EHD) coupling arises from the action of the capillary p_{Cap} and electrostatic p_E pressures at S_i and intervene in the normal component of the interfacial stress boundary condition for the Navier-Stokes equations:

$$\begin{aligned}(p_1 - p_2) + \left[\mu_2 \left(\nabla \mathbf{u_2} + (\nabla \mathbf{u_2})^T\right) \cdot \mathbf{n} - \mu_1 \left(\nabla \mathbf{u_1} + (\nabla \mathbf{u_1})^T\right) \cdot \mathbf{n}\right] \cdot \mathbf{n} \\ - 2\gamma H + \frac{1}{2}\epsilon_0 \epsilon_{r_o} E_n^2 = 0\end{aligned} \tag{2.5}$$

where H denotes the mean curvature of the interface and $E_n = \mathbf{n} \cdot \mathbf{E}$ is the normal com-

[1]The validity condition (Woodson and Melcher, 1968), i.e. a ratio of the charge relaxation time scale τ_E to the other mechanical time scales (capillary $t_{Cap} = \sqrt{\rho_w R_d^3/\gamma}$ and viscous $t_\mu = \rho_w R_d^2/m u_w$ much smaller than unity, is widely fulfilled either with salted water in actual crude treatment technologies or with tap water in the experiments (see Table 2.2 for liquid properties).

ponent of the dimensional electric field $\mathbf{E}$ on the interface with $\mathbf{n}$ taken as the outward pointing unit vector normal to the interface, at the point considered. The interfacial tension coefficient γ is prescribed constant along the interface as the surfactants concentration is supposed to be at constant equilibrium. Equations describing the adsorption/desorption as well as bulk and interfacial transport of surfactants were not implemented during the course of the thesis. Still, the assumption should well represent quasistatic cases, i.e. where surfactant dynamics are dominant compared to the interface evolution, and deviations that are to occur in transient problems as in chapters 3 and 4 will be discussed. The continuity of tangential stresses and of the velocity fields at S_i forms the remaining interfacial boundary conditions for the Navier-Stokes equations and are respectively expressed as:

$$\left[\mu_2 \left(\nabla \mathbf{u_2} + (\nabla \mathbf{u_2})^T\right) \cdot \mathbf{n} - \mu_1 \left(\nabla \mathbf{u_1} + (\nabla \mathbf{u_1})^T\right) \cdot \mathbf{n}\right] \cdot \mathbf{t} = 0 \tag{2.6}$$

and

$$\mathbf{u_1} = \mathbf{u_2}. \tag{2.7}$$

Other boundary conditions for the fluid dynamics and electrostatics problems, used in the different configurations, are more trivial and are summarized in Table 2.1.

2.2.3 Interface evolution and mesh regularization

As explained in section 2.2.1, the evolution of interfaces is tracked and performed through an Arbitrary Lagrangian-Eulerian method. A brief description of its principle is given hereafter and interested readers are advised to read the book of Donea et al. (2004) and articles from Hughes et al. (1981), Souli and Zolesio (2001). The ALE approach combines the advantages of both the Lagrangian and the Eulerian descriptions while minimizing their respective drawbacks (Donea et al., 2004). A third domain, the "referential domain" Ω_χ where reference coordinates χ are introduced to identify the grid points, is added and used to track the movement of both the spatial domain Ω_x (Eulerian description) and the material domain Ω_X (Lagrangian description) by introducing invertible mappings. The fundamental relation between the material time derivatives, referential time derivatives and spatial gradient is used to adapt the conservation equations (thus the Navier Stokes equations) to the ALE formulation. Its expression is

$$\left.\frac{\partial f}{\partial t}\right|_X = \left.\frac{\partial f}{\partial t}\right|_\chi + \mathbf{c} \cdot \nabla f \tag{2.8}$$

where $\mathbf{c}$ is the relative velocity between the material and reference system. At each time step, the fluid-fluid interface is moved in a Lagrangian way, using the computed velocity

Table 2.1: *Other boundary conditions found in the different simulations*

Boundary	Abbreviation	Mathematical form
Navier-Stokes		
Axisymmetry Planar symmetry	S_{axis} S_{sym}	$\mathbf{t}\cdot\left[\mu_i\left(\nabla\mathbf{u_i}+(\nabla\mathbf{u_i})^T\right)\right]\cdot\mathbf{n}=0,\ \mathbf{n}\cdot\mathbf{u_i}=0$
Infinity	S_∞	$\left[-p_2\mathbf{I}+\mu_2\left(\nabla\mathbf{u_2}+(\nabla\mathbf{u_2})^T\right)\right]\cdot\mathbf{n}=0$[a]
Walls	$S_{HV,G}$	$\mathbf{u_i}=\mathbf{0}$
Capillary Inlet	S_e	$\mathbf{u_i}=-u_0\mathbf{n}$[b]
Electrostatics		
Interface	S_i	$\int_{S_i}\rho_s=0$[c]
HV Electrode	S_{HV}	$V=V_0$
Planar symmetries	S_{sym}	$V=V_0/2$
Ground	S_G	$V=0$
Axisymmetry Infinity[d]	S_{axis} S_∞	$\mathbf{n}\cdot\epsilon_0\epsilon_{r_o}\mathbf{E}=0$

[a] In configurations where gravity effects are considered (see section 2.3.1), the pressure term in the equation is removed giving a no viscous stress boundary condition.

[b] The equation is a general form used, in sections 2.3.2 and 4.3 to constrain the flow rate at the inlet of capillaries. In studies where the volume of liquid must remain constant during the electrostatic stimulation, u_0 is set to zero leading to a wall boundary condition. However, the former was kept as it more physically accounts for the behavior of the actual surface in experiments.

[c] Only applies for neutral drops freely suspended between electrodes. Since in that case, the potential evolves with the drop motion, the equation calculates V so that the total charge on the boundary is equal to zero.

[d] The equation specifies that the normal component of the electric displacement equals zero at the boundary. Here, it results from the approximation of non-disturbance of potential, whose distribution is not known a priori, far from the water-dielectric interface. Computational domains of numerical models have been defined such that this approximation is valid at S_∞ but have willingly been reduced in Figures 2.2, 2.6 and 3.2, for clarity purposes.

u. The mesh velocities inside the computational domain are then prescribed by solving

$$\begin{aligned}\frac{\partial^2}{\partial r^2}\left(\frac{\partial R}{\partial t}\right)+\frac{\partial^2}{\partial z^2}\left(\frac{\partial R}{\partial t}\right)&=0,\\ \frac{\partial^2}{\partial r^2}\left(\frac{\partial Z}{\partial t}\right)+\frac{\partial^2}{\partial z^2}\left(\frac{\partial Z}{\partial t}\right)&=0,\end{aligned}\tag{2.9}$$

where (R,Z) and (r,z) denotes, respectively, the 2D axisymmetric coordinates in the referential and in the spatial frames. Boundary conditions, involved in the resolution of the system of partial differential equations (PDE) (2.9) are either deduced from the computed velocity **u**, along the interface, or such that the normal component of the displacement equals zero, along all other boundaries. This mesh regularization technique referred to as a "Winslow Smoothing Method" offers more stability and faster convergence in 2D calculations than those based on Laplace smoothing (Knupp, 1998).

2.2.4 Computations and software

The simulations were performed with the commercial software COMSOL MULTIPHYSICS^{TM} version 3.4 through the following steps. A computational domain is first defined and discretized, using the finite element method (FEM), into triangular Lagrange elements: P_2-P_1 for fluid dynamics (second order for the velocity field and first order for the pressure) and quadratic for electrostatics and moving mesh. The software then converts all the equations and boundary conditions formulated by the user, through the so-called "application modes", to the weak form and collects them into one large system of PDEs and boundary conditions (FEMLAB, 2006). The fully coupled, transient/quasistatic and non linear problem is solved using the method of lines with calls to the differential-algebraic system solver DASPK (Brown et al., 1994) and to the linear system solver UMFPACK (Davis, 2004). In conjunction with the regularization technique, a semi-automatic remeshing procedure (see appendix A.3) was used to prevent the strongly non-uniform stretching of the mesh elements which tends to degrade accuracy of the approximations.

The main modification of the software concerned the implementation of the interfacial forces into the corresponding boundary condition (2.5). Electrostatic pressure $p_E = \frac{1}{2}\epsilon_0\epsilon_{r_o}E_n^2$ is directly computed from the Laplace equation (2.3) and (2.4), while the capillary pressure $-2\gamma H$ is expressed through a weak formulation (Saksono and Peric, 2006) adapted to the axial symmetry condition. Introducing the surface divergence operator ∇_s, the mean curvature writes $H = -\frac{1}{2}\nabla_s \cdot \mathbf{n}$ and the weak term accounting for the action of interfacial tension forces becomes $\gamma\nabla_s \cdot \mathbf{n}$. Such a formulation allows to avoid the explicit calculation of both the normal vector $\mathbf{n}$ and the local curvature H which is, as a matter of fact, not readily available.

The retained numerical scheme being purely dynamic in nature to enable investigations on the electrocoalescence of free droplets in stagnant fluids or shear flows, artifacts were used to treat quasistatic problems. Three different methods ensuring that the inertial and viscous terms of the hydrodynamics problems remain negligibly small were tested and compared in the thesis. They respectively consist in: i) removing the time derivatives in the Navier-Stokes equations (equation (2.1)), which will be referred to as the quasistatic method; ii) greatly artificially increasing the liquids viscosity; iii) applying a very slow rise of the potential difference. Unless otherwise mentioned, simulations feature axisymmetric geometries, and, in the particular case of two droplets of same radius, take advantage of the plane of symmetry. Computing more than one drop on the same axis is possible by solving the Navier-Stokes equations in each supplementary domain. Finally, as COMSOL MULTIPHYSICS^{TM} 3.4 handles multi-core processing, the simulations with degrees of freedom varying approximately from 27000 up to 200000, were run on a double Intel

Quad-Core Xeon E5430, 2.66 GHz processor.

2.3 Criteria of quasistatic water-dielectric fluid interfaces instability

As mentioned in section 1.5.3, the first investigation on the conditions leading to the instability of drop pairs subjected to a potential difference dates back to Latham and Roxburgh (1966) and their study on cloud electrification. By assuming an ellipsoidal shape for the deformed interfaces (based on the work from Taylor (1964) on the disintegration of a single conducting drop in a uniform electric field) and by using Davis' coefficient (obtained for two conducting sphere in a uniform electric field) for the field magnification at the facing poles, authors were able to relate the critical disrupting field to the initial geometrical configuration. However, Taylor (1968) highlighted a few flaws in their approach, that cruelly limit its domain of validity. Indeed, firstly, the former retained hypothesis is highly unrealistic for drops initially in close proximity since, in that case, elongation is mostly concentrated on their facing side. Moreover, even at higher initial spacing, a static criterion is not strictly applicable to the problem of freely suspended drops as it does not take their relative motion, accompanying their deformation, into account. Taylor (1968) therefore considered a real instability problem by anchoring the two drops of same radius R_0 on coaxial rings of radius a with $a \ll R_0$. Doing so, he constrained the interface elongation to a region matching roughly that where the electrostatic pressure effects ($\sqrt{R_0 s_0}$, s_0 standing for the drops initial separation along the axis of symmetry (Atten et al., 2006)) and neglected variations of the drop internal pressure. Further simplifications were achieved by restricting the study to very small s_0 ($s_0/R_0 \ll 1$) so that the electric field between them could be approximated by $E = V/\Delta z$, Δz being the interfaces distance, at any point. His most important results concern the asymptotic behaviors found for the critical distance and potential difference between the interfaces respectively taking the expressions $s_{Crit} \cong 0.5 s_0$ and $V_{Crit} \cong 0.38 s_0 \sqrt{\gamma/(\epsilon_0 \epsilon_{r_o} R_0)}$. The theoretical approaches resumed hereafter stemmed from his work and were developed by Atten and colleagues[2] to characterize the full quasistatic deformation of the drops. In practice, the typical time associated with the slow motion of the drops under the action of the mutual attraction force is several orders of magnitude higher than that of the interfaces disruption leading to coalescence, thus allowing to seek for quasistatic solutions (Atten and Aitken, 2007).

[2]Readers should be aware that different notations have been adopted here in order to fit with the overall manuscript consistency.

2.3.1 Rigid sphere-deformable interface

2.3.1.1 Background and asymptotic analytical approach

The problem of deformation and instability of a horizontal interface between water and an insulating fluid, electrically influenced by a metallic sphere located just above it, was considered in Atten et al. (2005), Atten and Aitken (2006), Atten et al. (2008b) as the most simple configuration to investigate the basic electrocoalescence phenomenon of two water droplets. Indeed, in the case of highly uneven droplets, the deformation of the small one is negligible compared to that of the large one. The retained arrangement is presented on Figure 2.2 and corresponds to the experimental setup described in Atten et al. (2005).

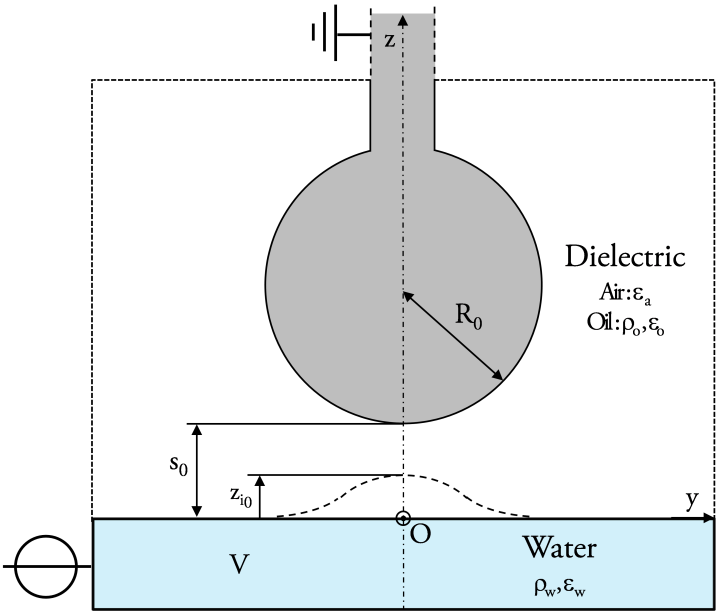

Figure 2.2: *Water interface electrically influenced by a metallic sphere. Geometry of the axisymmetric problem and associated parameters.*

The two problems are not perfectly similar though: gravity effects can not be neglected here because the spatial scale of the experiment is at least two orders of magnitude greater than that of droplets in water-in-oil emulsions (see section 1.3.1). However, the restoring force due to gravity adds to capillary forces and does not qualitatively modify the interplay between electrostatic and capillary effects. In their study, Atten et al. (2005) started by formulating an equilibrium condition from the balance of all forces acting at the interface:

$$\frac{1}{2}\epsilon_0 \epsilon r_o E_n^2 - \gamma\left(\frac{1}{R_1}+\frac{1}{R_2}\right) - \Delta\rho g z_i = 0 \tag{2.10}$$

where R_1 and R_2 are the principal radii of curvature and $z_i = z_i(r)$ is the elevation of the interface in cylindrical coordinates (the φ dependence being discarded due to the axisymmetry of the configuration). Then, assuming, as in the reference study, the asymptotic

case of very small separation ($s_0 \ll R_0$) allowed them to approximate both the sphere ordinate as $z_s = s_0 + r^2/(2R_0)$ and the electric field as $E_n = V/(z_s - zi)$. By further expressing the gravitational and capillary components as a function of $z_i(r)$, and, finally, by introducing the dimensionless variables:

$$f = \frac{z_i}{s_0}, \qquad r^* = \frac{r}{\sqrt{s_0 R_0}} \tag{2.11}$$

the authors deduced, from 2.10, the equation governing the deformation of the interface:

$$\frac{f''}{(1+\psi f'^2)^{3/2}} + \frac{1}{r^*}\frac{f'}{\sqrt{1+\psi f'^2}} - Bo\, f = -\frac{Be}{\left[1 + \frac{r^{*2}}{2} - f\,(r^*)\right]^2} \tag{2.12}$$

which involves the non-dimensional parameters Bo, Be and ψ respectively defined here by:

$$Bo = \frac{\Delta\rho g s_0 R_0}{\gamma}, \qquad Be = \frac{1}{2}\frac{\epsilon_0 \epsilon_{r_o} V^2 R_0}{s_0^2 \gamma}, \qquad \psi = \frac{s_0}{R_0}. \tag{2.13}$$

Equation (2.12) was solved numerically using the classical Runge-Kutta integration scheme with boundary conditions $f' = 0$ at $r = 0$ and $f \to 0$ when $r \to \infty$ in order to obtain the electric Bond number Be as a function of the relative interface elevation at the axis $f_0 = z_{i_0}/s_0$ for different values of the gravitational Bond number Bo (Figure 2.3). Static

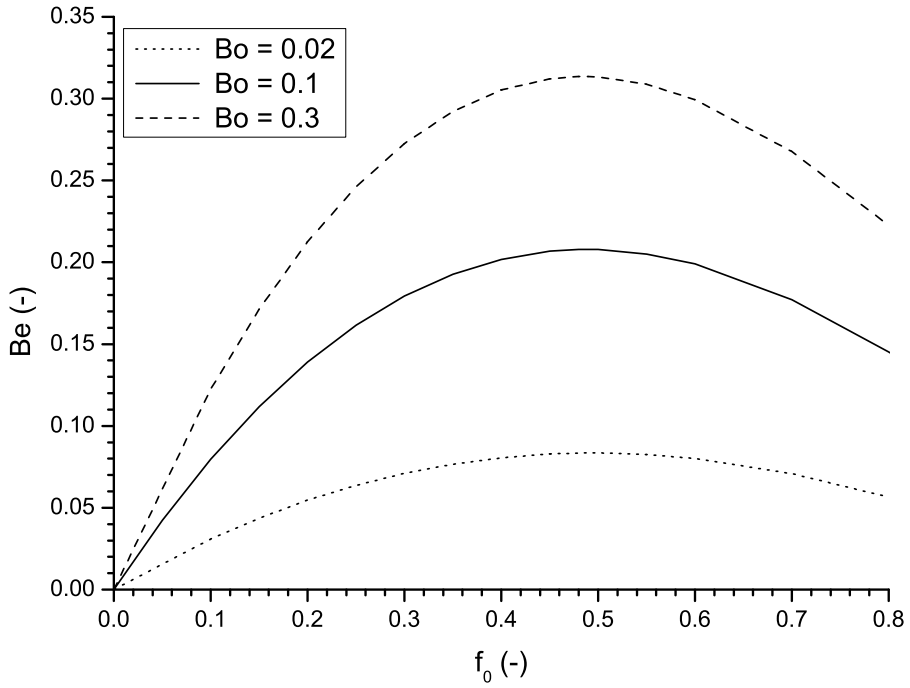

Figure 2.3: *Variation of the electric Bond number Be as a function of the relative interface elevation at the axis f_0 for three values of the Bond number Bo. Reproduced from Atten and Aitken (2006).*

solutions correspond to the left side of the curves, i.e. where the deformation of the inter-

face increases with Be up to a critical value close to $f_0 = 0.5$ scarcely dependent on Bo. From there, critical values of the electric Bond number Be_{Crit} were extracted to build a criterion predicting the appearance of an interfacial instability, roughly approximated in the interval $[0.05, 0.34]$ by:

$$Be_{Crit} \cong 0.48 Bo^{\alpha} \qquad \text{with} \qquad \alpha \cong 0.36. \tag{2.14}$$

2.3.1.2 Simulation results

Numerical simulations of the interface rise induced, in the configuration schematized in Figure 2.2, by the application of a potential difference between the sphere and the High-Voltage electrode were performed with dimensions ($R_0 = 4\ mm$) corresponding to the experimental setup (Atten and Aitken, 2006). Both air and Indopol polybutene oil grade L-6 (which properties can be found in Table 2.2) were used as insulating fluids and initial spacing s_0 between the sphere and the interface was varied in the range 0.045 to 3 mm.

Table 2.2: *Typical liquids properties at* $20°C$

	Tap water	**Polybutene oil**
Density $(kg.m^{-3})$ ρ_i	1000	824
Viscosity $(Pa.s)$ μ_i	0.001	0.0102[a]
IFT $(N.m^{-1})$ γ	0.025-0.013[b]	
Relative permittivity (-) ϵ_{r_i}	80.1	2.2-2.3
Conductivity $(S.m^{-1})$ σ_i	0.05-0.08	$\leq 6.7\ 10^{-13}$

[a] The evolution of the oil dynamic viscosity as a function of temperature for a polybutene oil (Ineos Oligomers - Indopol Grade L-6), calculated using a viscometer, is available in appendix B.1.

[b] The static surface tension coefficient (oil/air) of the L-6 grade lies, according to the supplier, in the range $0.022 - 0.027\ N.m^{-1}$. However, no data were available for the static interfacial tension of a water/polybutene oil interface. Tensiometer measurements performed in the lab and corroborated by experiments with a pendant drop apparatus at NTNU's Ugelstad Lab. gave initial value close to about $0.035\ N.m^{-1}$. The IFT coefficient was found to decrease slowly with time most probably due to the adsorption of surfactant from the bulk. As oil was stored under atmospheric conditions, those are expected to come from the oxidation of the olefinic bond at the chain ends of the polybutene molecules and to consist in ketones, aldehydes and carboxylic acids which are all somewhat polar groups (Decroocq and Casserino, 2005). Reported IFT values correspond to the range in which it was used in experiments (further specifications are available in figure captions).

Typical results are illustrated on Figure 2.4 in the form of the relative rise of a water-air interface at the axis of symmetry $f_0 = z_{i_0}/s_0$ as a function of the square of the applied voltage V^2 for different values of s_0. In this first configuration, the ability of a single calculation (for each s_0) to accurately determine the static limit of stability was tested. Curves

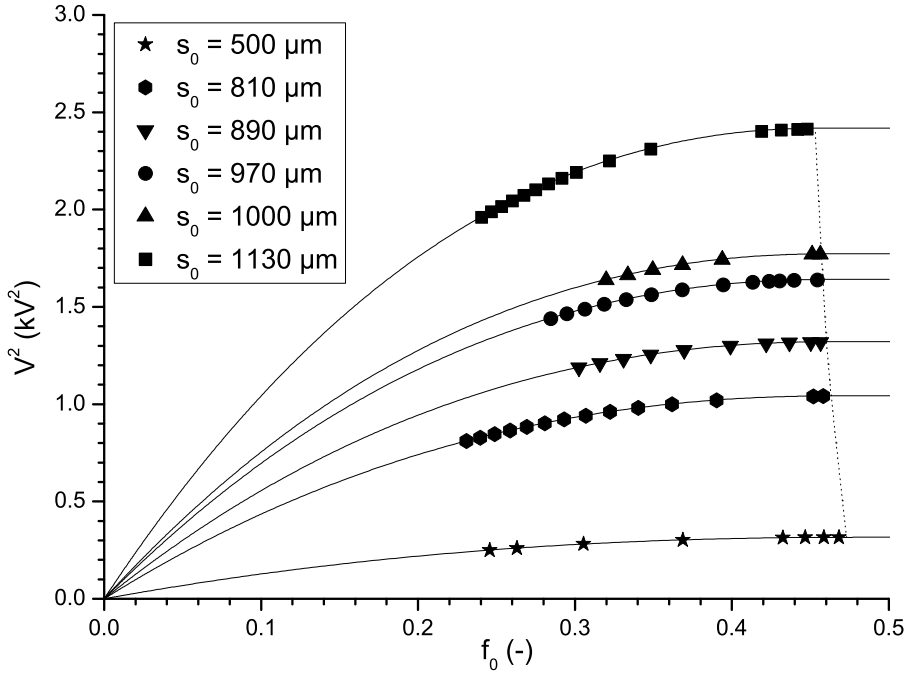

Figure 2.4: *Relative level rise of a water-air interface as a function of the sphere potential squared V^2 for different values of the initial spacing s_0. Marks and curves represent stabilized transient and quasistatic solutions respectively. Dotted line shows the quasistatic limit of stability deduced from the computations. Simulation parameters are:* $\gamma = 0.070\ N.m^{-1}$, $\epsilon_{r_a} = 1$.

produced with the quasistatic method (see section 2.2.4) and a growing applied voltage are compared with data points representing stabilized solution computed with a transient formulation and an artificially increased water viscosity to overdamp the free surface oscillation. Both methods agree very well, especially in the prediction of the critical applied potential difference V_{Crit} above which instability occurs corresponding to an extremely fast increase of f_0 (i.e. the horizontal asymptotes at the right hand side of the graph). Experimentally, an upward flowing water jet issuing from the interface quickly impinges the sphere. Stable deformation of the free surface is obtained up to a relative level rise a little smaller than 50 %, deviations on the estimation of the static limit of stability $f_{0_{Crit}}$ between both methods being less than 1.5 %. Figure 2.4 additionally shows that $f_{0_{Crit}}$ tends to slightly decrease with the augmentation of the initial spacing s_0 (from 0.473 to 0.453). In a manner similar to that presented in the asymptotic approach, s_0 and associated V_{Crit} were used to calculate a critical electric Bond number Be_{Crit} plotted in Figure 2.5, for both water-air and water-polybutene interfaces, as a function of Bo. Asymptotic analytical results from Atten et al. (2005) and unpublished experimental measurements[3]

[3]Those were conducted, both by another student in the framework of a Master's thesis and by Pierre Atten, in parallel to this thesis. No technique was available to estimate IFT coefficients, in the lab, at that time. Therefore, extra precautions, illustrated by the error bars in Figure 2.5, were taken on the calculation of Be_{Crit}, particularly for the water-polybutene oil interfaces which were, in general subjected to longer aging due to their more challenging experimental implementation.

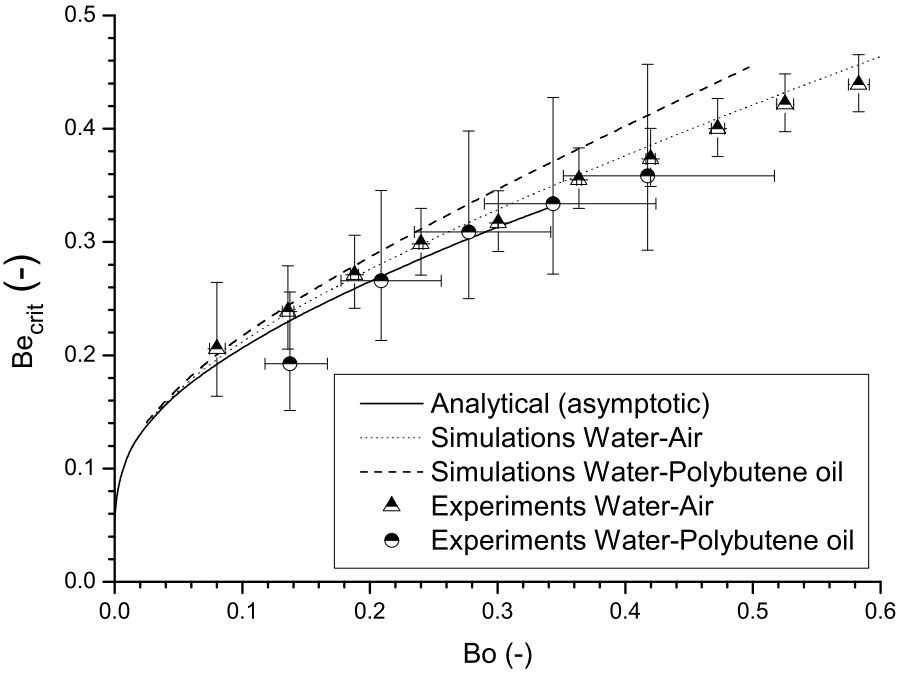

Figure 2.5: *Variation of the critical electric Bond number Be_{Crit} as a function of the Bond number Bo for water-air and water-polybutene oil interfaces. Comparison between asymptotic analytical, numerical and experimental results. Retained IFT coefficients, in the two latter approaches, are $\gamma = 0.07$ $N.m^{-1}$ and $\gamma = 0.025$ $N.m^{-1}$ for water-air and water-polybutene oil interfaces respectively. Error bars account for an uncertainty of 0.02 and 0.05 $N.m^{-1}$ on those values cumulated with an indeterminacy of 15 μm on the determination of the initial separation distance s_0.*

are also reported. A general good agreement is found in a large range of Bond number Bo independently of the dielectric fluid. Quite expectedly, numerical and analytical values coincide well for low Bond numbers, i.e. in the validity range of the asymptotic treatment, and progressively shift from each other as Bo increases. Deviations, that become significant at relatively large Bond numbers, can be attributed to the approximations made in the derivation of equation (2.10) which led to the dimensionless form (2.12). Both have actually opposite influence on Be_{Crit}: the expression $V/\Delta z$ does not account for the field reinforcement produced by the curvature of the interface that increases along with ψ but is here overcompensated for by the clear underestimation of the actual z_s due to the paraboloid equation retained for the sphere surface. Their combined effects thus overestimate the actual electric field between the sphere and the interface and so lower the applied voltage required to reach instability which is consistent with the smaller Be_{crit} predicted by the theoretical approach. Moreover, they stipulate the existence of a unique solution linking Bo and Be_{Crit} for equation (2.10) which is obviously not representative of the actual case. Indeed, in order to obtain similar Bond numbers in the water-polybutene oil configuration ($\gamma = 0.025$ $N.m^{-1}$ and $\Delta\rho = 176$ $kg.m^3$ instead of $\gamma = 0.070$ $N.m^{-1}$ and $\Delta\rho = 1000$ $kg.m^3$), about two times larger initial spacings s_0 must be used and small

non-linear influence of the ψ ratio can be seen. Still, for moderate changes in the liquid properties, the following laws should give fair approximations for the variation of Be_{Crit} as a function of Bo in the interval $Bo \in [0.025, 0.5]$ for water-air and water-oil interfaces respectively:

$$Be_{Crit} \cong 0.489\,(Bo - 0.022)^{0.707} + 0.131 \qquad \text{with} \qquad R^2 = 0.99998 \tag{2.15}$$

$$Be_{Crit} \cong 0.555\,(Bo - 0.025)^{0.760} + 0.140 \qquad \text{with} \qquad R^2 = 0.99996 \tag{2.16}$$

Experimental results compare well with those of simulations, especially for the water-air configurations where the IFT coefficient was more accurately known (see footnote 3).

2.3.2 Anchored facing drops

2.3.2.1 Background and asymptotic analytical approach

Following the aforementioned asymptotic study, Atten and Aitken (2007) took one step forward toward the establishment of an electrocoalescence criterion by investigating theoretically the critical conditions for the electrically induced instability and coalescence of two closely spaced even conducting droplets, anchored at the tip of capillary tubes and immersed in a dielectric liquid. The problem was again to determine both the deformation of the drops, particularly at the facing zones of the interfaces and the threshold applied potential difference above which the system gets unstable as a function of the different geometrical parameters, i.e. R_0, s_0 and the angle θ_m depicted on Figure 2.6. The latter, formed between the nozzle axis and the anchorage/triple point of the menisci, characterizes the initial shape of the "drops": θ_m equals 90° for hemispherical drops and θ_m is larger than 90° when the drops radius exceeds that of the capillary. The authors

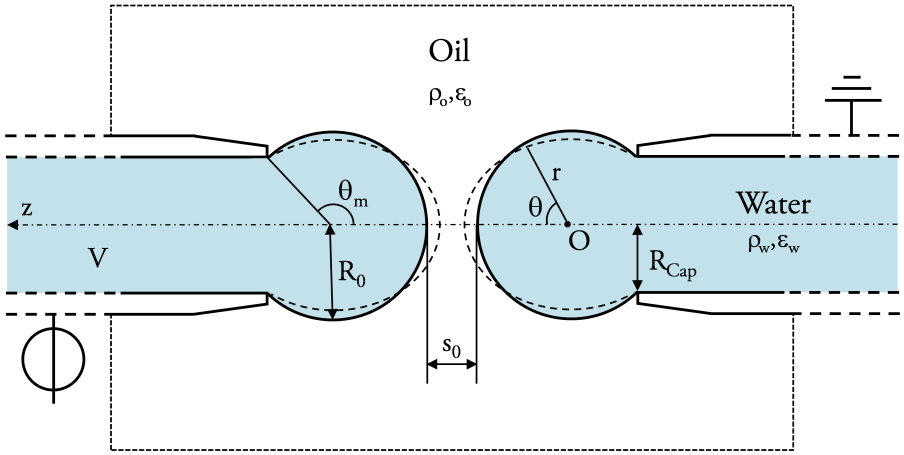

Figure 2.6: *Anchored water menisci suspended in an insulating liquid and subjected to a potential difference. Geometry of the axisymmetric problem and associated parameters.*

considered here the case of small droplets immersed in a quiescent liquid so that gravitational effects could be neglected (Bond numbers $Bo = \Delta\rho g R_0^2/\gamma$ for droplet radius in the hundreds of micrometer range are typically < 0.01) to improve the criterion relevance to practical electrocoalescence problems. Therefore, the static equilibrium condition, at any point of the interface, imposes that the pressure difference between water and the outer liquid is compensated for by the electrostatic and capillary pressures, p_E and p_{Cap}, and is formulated as:

$$p_w - p_o = \gamma\left(\frac{1}{R_1} + \frac{1}{R_2}\right) - \frac{1}{2}\epsilon_0\epsilon_{r_o}E_n^2 \tag{2.17}$$

Using a spherical coordinates system $r,\ \theta,\ \varphi$ in place of a classical cylindrical one $r,\ \varphi,\ z$ adopted in many studies involving drop deformed by the gravitational force (including the former) they expressed the equation describing the axisymmetric interface location of one drop as $r = g(\theta)$. Normalizing the spatial coordinates by the radius of non deformed drops R_0 and introducing the deformation f scaled with the initial spacing between those drops, s_0, it becomes:

$$g\left(\theta\right) = R_0\left[1 + \psi f\left(\theta\right)\right] \tag{2.18}$$

By further stating the surface curvature as the divergence of the unit vector normal to the interface and assuming, again, the asymptotic case of $\psi \ll 1$ thus approximating the electric field by $V/\Delta z$ (where $\Delta z = s_0[1 - 2fcos\theta + 2(1 - cos\theta)/\psi]$ is the distance between facing points of the interfaces), the authors obtained the equation governing the deformation profile f:

$$\begin{aligned}\left(1+\psi f\right)f'' + \frac{cos\theta}{sin\theta}f'\left[\left(1+\psi f\right)^2 + \psi^2 f'^2\right] - \psi f'^2 = -\frac{\left[\left(1+\psi f\right)^2 + \psi^2 f'^2\right]^{3/2}}{\psi}\left\{2\right.\\ \left. -\frac{2}{\sqrt{\left(1+\psi f\right)^2 + \psi^2 f'^2}} + \partial p_w + \frac{Be}{\left[1 - 2fcos\theta + \frac{2}{\psi}\left(1 - cos\theta\right)\right]^2}\right\}\end{aligned} \tag{2.19}$$

which involves the non-dimensional change in the inner drop pressure ∂p_w and the electric Bond number Be. Solutions of equation (2.19) were calculated by numerical integration using the embedded Runge-Kuttta-Fehlberg method with boundary conditions $f' = 0$ at $\theta = 0$, $f = 0$ at $\theta = \theta_m$ and drop volume conservation $\partial_{Vol} = 0$ in conjunction with a double shooting method. Indeed, given a value f_0 for the deformation at the axis ($\theta = 0$), appropriate values of Be and ∂p_w must be found to satisfy the volume conservation and boundary conditions. Results are presented and compared with numerical simulation and experimental values in section 2.3.2.3

2.3.2.2 Numerical and experimental procedures

Experiments were conducted in a cell manufactured out of PVC (#6,#10) and PMMA (#9), represented on Figure 2.7, filled with synthetic polybutene oil[4]. Tap water menisci

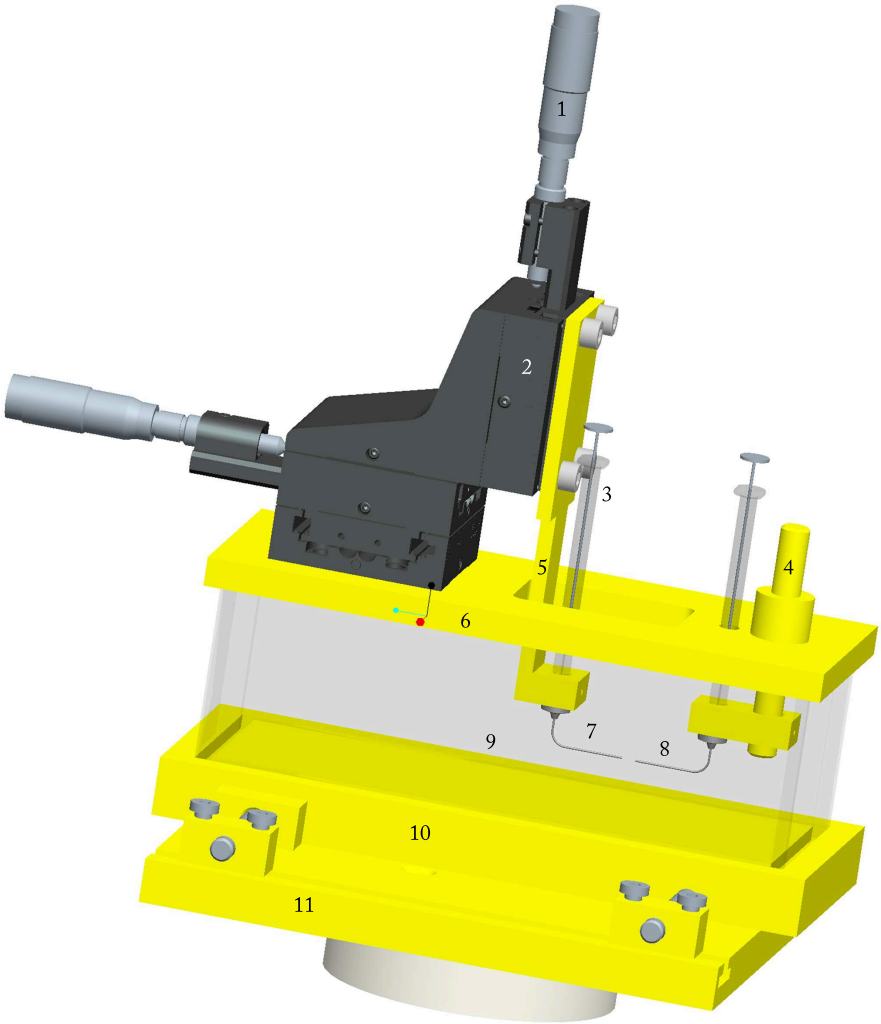

Figure 2.7: *3D CAD model of the anchored facing drops experimental cell. Nomenclature: 1, Micrometer - 2, XYZ linear stage - 3,* 10 μL *syringe - 4, HV needle holder - 5, Grounded needle holder - 6, PVC cell lid - 7, Grounded metallic needle - 8, HV metallic needle - 9, PMMA walls, 10, - 11, Cell holder.*

are formed (Figure 2.8a) at the tip of two curved metallic needles (#7,#8) of inner radius $R_{Cap} = 294\ \mu m$ linked to 10 μl syringes (#3) and held in place by different articulated supports: one (#5) features a XYZ linear stage (Newport - M-460P-XYZ) (#2) to set and vary the initial interface spacing while the other (#4) is mounted on pivot to easily correct angular misalignments and ensure the axisymmetry of the configuration. The designed cell provides an independent control of the menisci volume[5], allowing to work

[4]Additional details on the choice of materials and liquids, assembly, cleaning procedures are available in section 3.4.2.

[5]The use of syringes additionally enables to keep the menisci volume constant during the potential raise which is compulsory to obtain quasistatic solutions for the deformation of electrostatically stressed water-

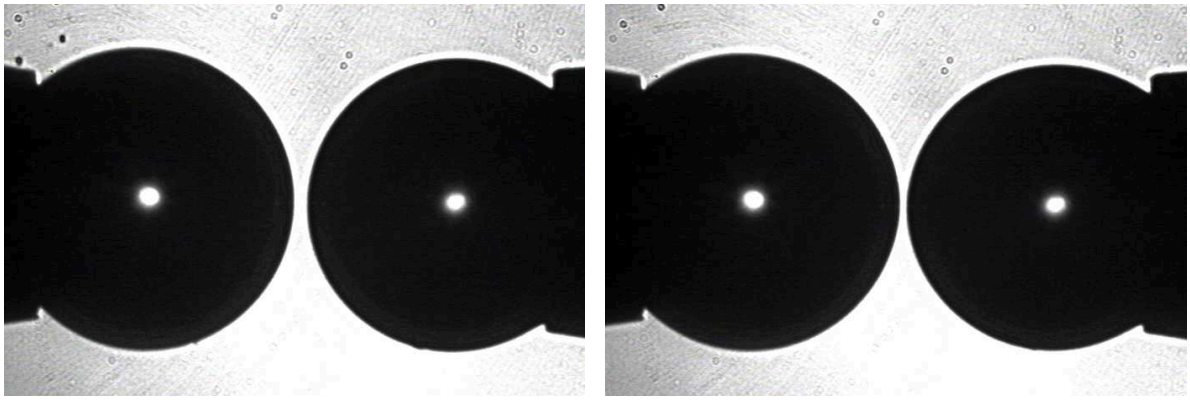

(a) (b)

Figure 2.8: *Photographs of the electrically induced deformation of two anchored water meniscus immersed in polybutene oil. (a) represents the initial configuration with no electric field while (b) shows the critical configuration, i.e. the last stable deformation before coalescence. Average drop radius and anchorage angle, initial spacing, critical applied voltage and measured IFT coefficient are respectively* $R_0 = 395.1 \pm 7\ \mu m$, $\theta_m = 132°$, $s_0 = 30.4 \pm 4.6\ \mu m$, $s_{Crit} = 17 \pm 4.6\ \mu m$, $V_{Crit} = 30.9\ V$ *and* $\gamma = 0.014\ N.m^{-1}$.

both with even "drops" as in the asymptotic analytical approach or with uneven "drops". An AC sine voltage of frequency around $900Hz$[6], produced by an arbitrary wave generator (Wavetek - 395) and magnified by a High Voltage amplifier (Trek - 20/20), is applied to one of the needle (#8), the other being grounded (#7). The resulting potential difference V between the menisci is raised very slowly until reaching the quasistatic stability limit at V_{Crit} (Figure 2.8b) beyond which disruption of the interfaces occurs leading to coalescence. Menisci deformation was visualized, in a direction perpendicular to the PMMA walls, and captured, on a PC using a 25 fps analog CCD camera (Bosh - LTC0335/50) coupled with a LED light source functioning as a focused back illuminator and a frame grabbing package (Data Translation, Inc - FGSDK32 & DT-Acquire 3.3.0). Acquired photographs of resolution 512x582 pixels were then post-treated thanks to an in-house developed[7] software suite programmed with OpenCV (Bradski and Kaehler, 2008) and based on Hough transform for circle detection (Yuen et al., 1990), to deduce the key geometrical parameters. An overall error of 2 pixels, i.e. 4.6 μm, was systematically applied to the value of the initial and critical separation distance in order to account for the algorithm accuracy and the possible influence of light reflections between menisci interface.

Numerical simulations were performed in the case of two even menisci, thus by taking

dielectric interfaces. Numerically, it was accomplished by prescribing a zero flow boundary condition at the capillary inlet, i.e. $u_0 = 0$ (see Table 2.1).

[6]Mainly to prevent oscillations of the interface that can lead to transient disruption. Moreover, since the electrostatic pressure is quadratic in field strength, the r.m.s critical value of the AC voltage retained for the experimental V_{Crit} is equal to that of a DC voltage.

[7]In the course of this thesis by a fellow PhD student.

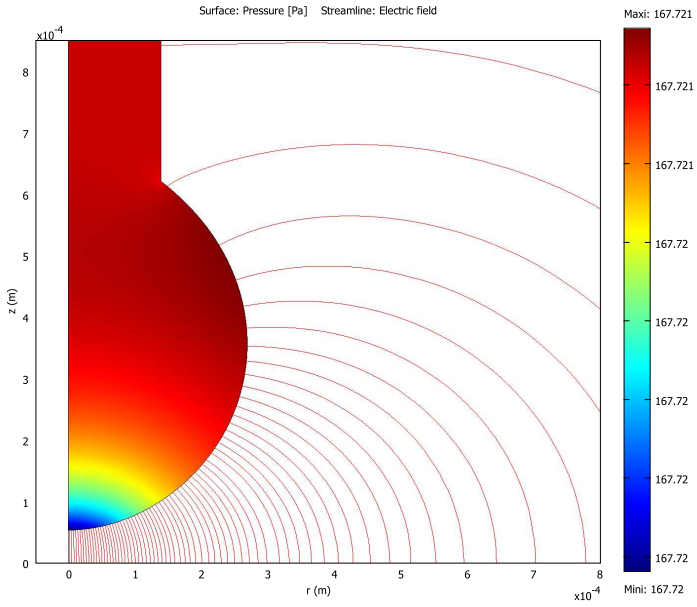

Figure 2.9: *Electrically induced transient deformation of anchored facing droplets in conditions very slowly approaching the critical ones. The pressure field in the water domain shows the very small gradient, resulting from the increase in electrostatic pressure, that drives the interface deformation and flow of liquids. Simulation parameters:* $\theta_m = 150°$, $R_0 = 279\ \mu m$, $\psi = s_0/R_0 = 0.717$, $\gamma = 0.025\ N.m^{-1}$, $\epsilon_{r_o} = 2.3$, $V_{Crit} = 246\ V$, $s_{Crit}/s_0 = 0.55$.

the plane of symmetry located between them into account, and with different R_0, s_0 and θ_m. As the equilibrium shape of the "drops" is mostly governed by the action of forces in the facing zone, influence of the needles wall thickness on the local electric field, in the vicinity of the anchorage point, was neglected. In view of the results obtained in the former configuration, the complete evolution of the interface for varying ψ were computed through single calculations using both the quasistatic method and a transient formulation with a rising applied voltage. In the latter case, a very slow variation ($V(t) = 0.1\ V.s^{-1}$) was employed in order to avoid interfacial oscillations possibly caused by the unsteady acceleration term in the Navier-Stokes equations. An example of such simulations is illustrated on Figure 2.9 in a configuration where the non-dimensional parameter ψ is much higher than the limit of validity of the asymptotic approach (the shape of the electric field streamlines drawn in the oil domain confirm, for instance, the irrelevance of the approximation $E = V/\Delta z$) and with an applied voltage very close to V_{Crit}. Outputs of the simulations, i.e. s_{Crit} and V_{Crit}, are deduced from plots representing the variation of the relative droplets spacing as a function of the applied voltage (Figure 2.10). Indeed, the appearance of the interfacial instability corresponds to a very steep drop of those curves which provides an accurate evaluation of both values independently of the formulation considered (deviations between the quasistatic and transient methods being smaller than 0.1%).

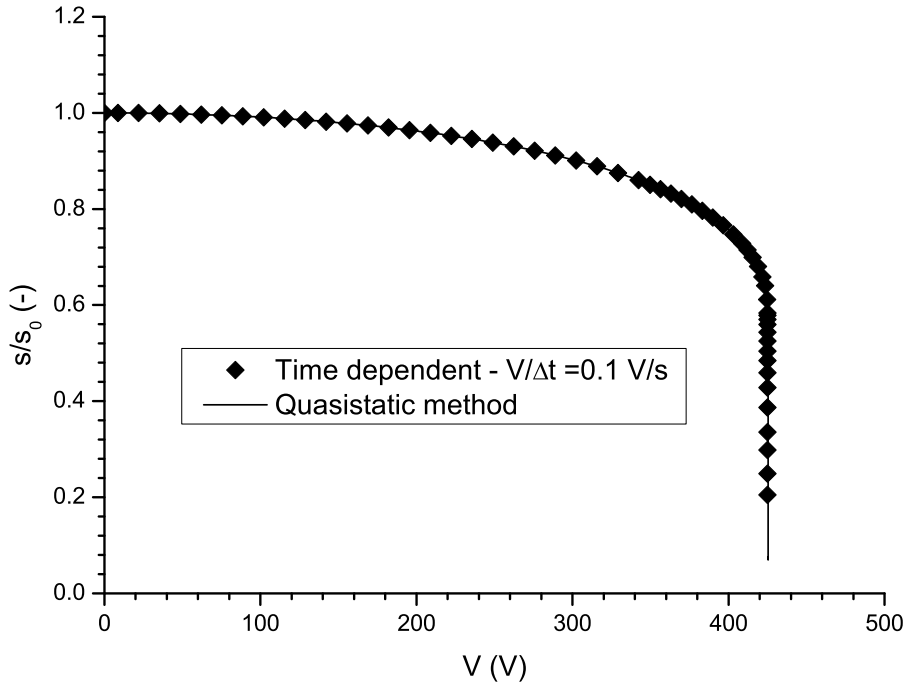

Figure 2.10: *Quasi-steady relative spacing s/s_0 vs increasing applied potential difference ΔV. Simulation parameters: $\theta_m = 90°$, $R_0 = 279\ \mu m$, $\psi = s_0/R_0 = 0.717$, $\gamma = 0.025\ N.m^{-1}$, $\epsilon_{r_o} = 2.3$, $V_{Crit} = 425.3\ V$, $s_{Crit}/s_0 = 0.6$.*

Both experimentally and numerically, values of s_0, R_0 and V_{Crit} were then used to build a critical electric Bond number Be_{Crit} and to investigate its variation as a function of the relative initial spacing ψ, for different values of the anchorage angle θ_m.

2.3.2.3 Results

As seen on Figure 2.11, simulations agree well with the asymptotic treatment, giving very similar results for a wide range of relative initial menisci spacing. As expected, the shift between the curves belonging to different approaches increases with ψ and becomes significant above $\psi = 0.1$. Oppositely to the rigid sphere - deformable interface configuration, the asymptotic treatment predicts here Be_{Crit} higher than that calculated by the numerical model. Since the simulations use the same problem formulation (i.e. equations, boundary conditions and relative domain sizes), such behavior is believed to result from the approximations made in the theoretical analysis and especially from their consequence on the electric field calculation at the water-dielectric fluid interface. Indeed, as already discussed in section 2.3.1.2, whereas the sphere surface was estimated by a paraboloid in the former configuration, an exact expression was retained here to describe the anchored menisci interface. Therefore, the electric field at the interface $V/\Delta z$ assumed in the asymptotic treatment should be lower than that computed in the simulations and lead to slightly higher critical applied voltage. Both approaches show consistently a decrease of

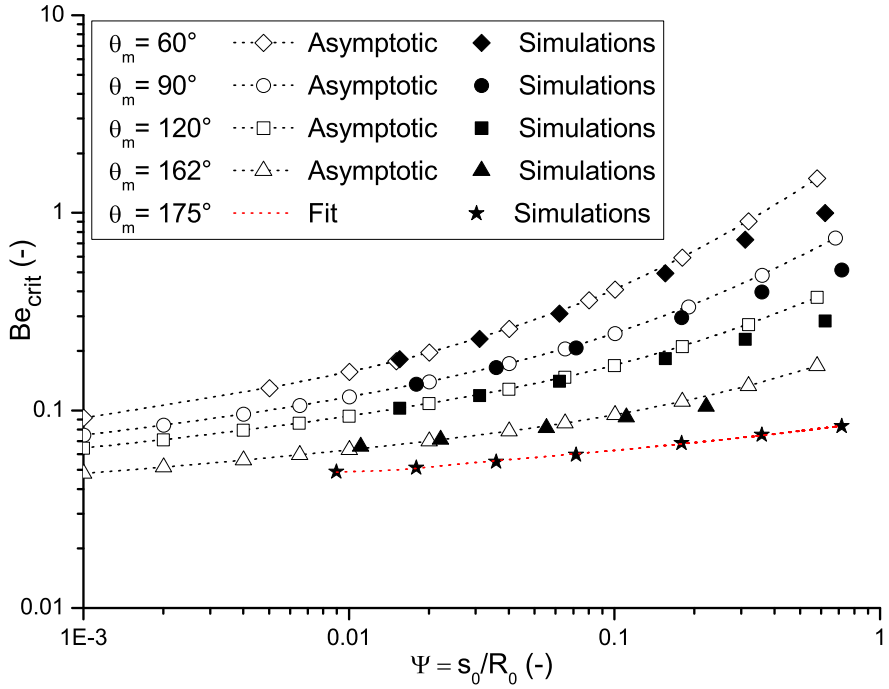

Figure 2.11: *Critical value of the electric Bond number Be_{crit} as a function of the relative initial spacing ψ for four values of the angle θ_m. Asymptotic (analytical) and numerical results.*

the critical electric Bond number with the relative initial "drops" spacing ψ. Nevertheless, finding a law governing the variation of Be_{Crit} appears very difficult since it must additionally consider the non-trivial dependency on the anchorage angle θ_m. For a given ψ, Be_{Crit} decays with the augmentation of θ_m as more interfacial area is allowed to elongate which straightforwardly lowers the applied voltage required to reach instability. Curves with values θ_m close to 180° should give rough approximations of the critical conditions for the quasistatic coalescence of two free drops suspended in a viscous insulating liquid. Among many others, a possible law in the interval $\psi \in [0.01, 1]$, extracted through a fit of data points computed for $\theta_m = 175°$, is:

$$Be_{Crit} \cong 0.46\,(\psi - 0.012)^{0.341} + 0.043 \qquad \text{with} \qquad R^2 = 0.99631. \tag{2.20}$$

It should also be noted that the critical separation distance s_{Crit} follows a similar evolution, being greater than the value found empirically by Taylor (1968) and later justified by Atten et al. (2006), i.e. $s_{Crit}/s_0 \cong 0.5$, at large ψ and small θ_m (see caption from Figures 2.9 and 2.10) and converging towards it as the latter parameters tend to satisfy the condition of very close interfaces.

Figure 2.12 indicates that measured values are generally lower but still close to those determined by the numerical simulations. Noticeable deviations arise at the smallest relative initial spacings ψ (see data points for $\theta_m = 130°$), i.e. when s_0 is deduced from

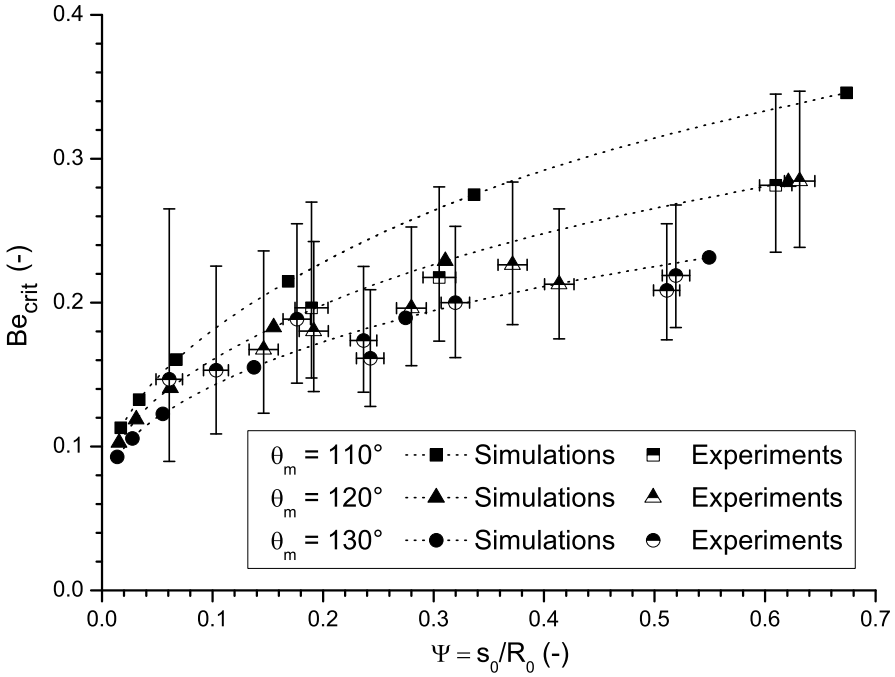

Figure 2.12: *Critical value of the electric Bond number Be_{crit} as a function of the relative initial spacing ψ for three values of the angle θ_m. Numerical and experimental results. Horizontal error bars correspond to an indeterminacy of 2 pixels on the value of the initial separation distance between the drops s_0 calculated from digitized photographs. Vertical error bars account for its influence, cumulated with 0.002 $N.m^{-1}$ uncertainty on the measured IFT coefficient, on Be_{Crit}.*

only a few pixels on the photographs, and generally as the anchorage angle decrease. Such phenomenon might be interpreted in terms of elongation ability of the menisci: the greater θ_m and thus the radius of the "drops", the more deformation of the interface will prevail over increase of the volume (this was often observed when air bubbles were trapped in the syringes). Still, as the numerical curves lie within the domain defined by the error bars of the corresponding experimental data and given their size, these explanations will remain assumptions. Finally, the anchorage angle being known a posteriori, the accuracy of $\pm 5°$ on the value used to plot Figure 2.12, definitely contributes to the dispersion of the results.

2.4 Conclusion

The approach proposed in this chapter, consisting in the joint use of simulations and experiments, had proven so far to be truly powerful and well able to characterize the electrically induced quasistatic deformation of interfaces between perfectly conductive and insulating liquids. The developed numerical scheme, though based on simple physical models, was confirmed accurate by the good agreement found with results from asymptotic analytical treatments in their validity range and from experiments. The latter, additionally, high-

lighted the strong influence of relatively low indeterminacy at such scales and thus the need for improved measurement techniques with higher spatial resolution. The approach further enabled to extend previously existing asymptotic criteria, that predict the critical conditions for the appearance of a quasistatic instability at the interface between facing even and "infinitely" uneven drops, to a wider range of parameters. Those relating the critical electric Bond number to the initial geometrical configuration gave interesting tools and insights to address the problem of electrocoalescence. Still, some of the assumptions made in the theoretical analysis, e.g. constant applied potential difference between the drops, were not representative of the actual mechanism and many more aspects should be considered. Among them, a good description of the dynamics and especially of the electrically induced film thinning occurring in between approaching droplets appeared mandatory.

Chapter 3

Dynamic electrocoalescence of two water drops in oil

3.1 Introduction

In the turbulent flows of state-of-the-art dewatering technologies, electrocoalescence of droplets is promoted by the combined action of the hydrodynamic and electric forces. Therefore, as mentioned in chapter 1, a striking fact about the related literature available in 2007, was the lack, even in the case of model fluids, of a simple criterion relating the time of close proximity of two drops in a flowing emulsion and that required for the formed intervening film to thin down to its critical thickness. Whereas the former can straightforwardly be approximated from the local shear rate and drop spacing, very few was, and still is, known on the latter in the presence of electric fields. Indeed, the phenomenon of film thinning between drops suspended in an immiscible liquid had been extensively investigated in hydrodynamic and buoyant forces driven configurations (Liao and Lucas, 2010) in which it represents the time-determining step of the whole coalescence process (Rommel et al., 1992) and has a great impact on emulsions stability (Sanfeld and Steinchen, 2008). An impressive number of different analytical expressions had thus been established depending on the nature and behavior of the interfaces. However, the characteristic properties and results found were not applicable to the electrocoalescence case because of the strongly different pressure distribution in the film induced by electric forces and of the absence of the dimple formation. Filling in this lack seemed therefore of primary importance while attempting to build a criterion, before, e.g., looking at the possible factors able to prevent the film rupture to occur (surfactants, trapping of solid particles). Sticking with the previously proven approach, both computational and experimental works were conducted. However, since the latter has not reached operational

phase and produced results yet, this chapter is organized differently from chapter 2. The first section provides an estimation of the time of close proximity of droplets with regards to the industrial context (polydisperse water-in-crude oil emulsions under turbulent flow conditions). The second section introduces a model, based on the developed numerical scheme, implemented to simulate the electrocoalescence of two perfectly conductive drops of even and uneven radii in a perfectly dielectric liquid. Initial results are used to illustrate the limitations of the existing theoretical approaches and to elaborate an order of magnitude approximation for the drainage time as a function of the initial configuration. The validity of the new expression is then assessed through systematic comparison with a parametric computational study. Owing to the gained understanding, an electrocoalescence criterion is proposed and its applicability to the actual conditions experienced by water-in-crude oil emulsions is discussed. Finally, the last section deals with the design and assembly of a semi-automated experimental setup achieved to study the electrocoalescence mechanism of two conductive water drops suspended in a shear flow of insulating oil and improve the relevance of the former criterion.

3.2 A time based criterion

A prerequisite for the determination of a criterion predicting the drainage of the intervening film between two colliding drops is a clear description of their relative motion while they are in close proximity. Under turbulent flow conditions, droplet trajectories are governed by two different mechanisms: isotropic turbulent shear and turbulent inertia (Urdahl et al., 2001, Less, 2008). In order to assess which one is most likely to occur, it is convenient to use the dimensionless Kolmogorov Stokes number St defined by

$$St = \frac{\tau_d}{\tau_\eta}. \tag{3.1}$$

In the above relation, τ_d and τ_η are the droplet response time and the Kolmogorov time scale, respectively expressed as

$$\tau_d = \frac{1}{18}\frac{\rho_w \left(2R_d\right)^2}{\mu_o} \tag{3.2}$$

and

$$\tau_\eta = \left(\frac{\nu_o}{\zeta}\right)^{1/2} \tag{3.3}$$

where ζ stands for the turbulent energy dissipation rate per unit mass (Melheim and Chiesa, 2006). If $St \ll 1$, i.e for very small droplets in a relatively viscous continuous phase, isotropic turbulent shear dominates and collisions result from the small scale motion

due to spatial variations (velocity gradients) in the flow. Inversely, for $St \gg 1$[1], the motion of large drops is barely affected by the turbulence and providing they have different radii, R_1 and R_2, collisions emanate from their relative movement (inertia) in the surrounding fluid. Using $\zeta = 0.22\ m^2.s^{-3}$, corresponding to an intermediate value used by Melheim and Chiesa (2006) in their turbulent electrocoalescence simulations, a typical drop radius of $R_d = 10\ \mu m$ and water and polybutene oil properties (Table 2.2) for the dispersed and continuous phase give $St \sim 0.0003$. Therefore, in the following study and, generally, in the problem of crude-oil dehydration, the trajectory of droplets in the approaching stage is mostly due to the action of the local shear $\dot{\gamma} = \tau_\eta^{-1}$ (Chesters, 1991) as represented on Figure 3.1. From there, assuming parallel flow streamlines allows to calculate a typical

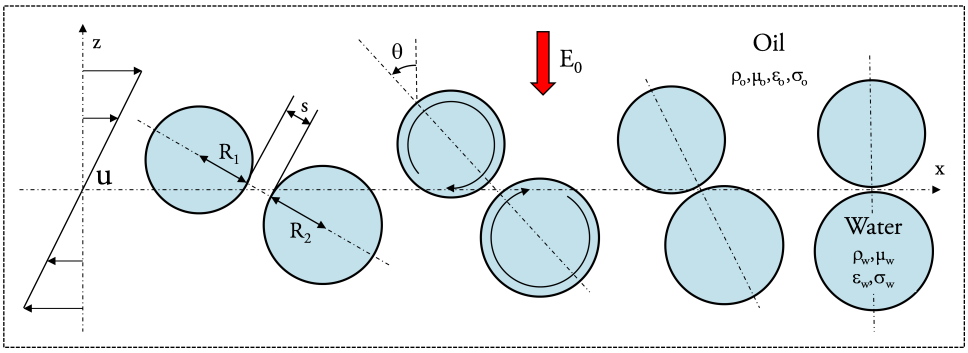

Figure 3.1: *Schematic representation of the electrocoalescence mechanism in a state-of-the-art dewatering device: water drops collide due to local shear flows inside the oil turbulent mainstream and then approach each other under the effect of strong electric attraction forces. Bridging of interfaces may or may not occur depending on the different parameters involved. θ characterizes the angle between the direction of the field and the line passing through the drops center.*

order of magnitude for the time available to achieve a complete thinning of the intervening film t_{Prox} and eventually promote coalescence. For two drops of relative velocity $w_2 - w_1 \sim \dot{\gamma}(z_2 - z_1) \sim \dot{\gamma}(R_2 + R_1 + s)$ being in close proximity while $|x_2 - x_1| < R_2$, t_{Prox} writes

$$t_{Prox} \sim \frac{2R_2}{\dot{\gamma}(R_2 + R_1 + s)}. \tag{3.4}$$

Obviously, in the case $R_1 \sim R_2 \gg s$, t_{Prox} mainly depends on the intensity of the local shear $\dot{\gamma}$. Denoting the drainage time by $t_{Drainage}$, the "(electro)coalescence efficiency" or probability of merging resulting from a collision is then stated[2] as (Coulaloglou and

[1]Readers should be aware that both Urdahl et al. (2001) and Less (2008) contain respectively a typesetting and a mixed up error in the definition of these inequalities.

[2]The starting point of this model is the work from Ross (1971) in which the author applied the *probability density function of a normal distribution* for the computation of coalescence efficiency. Simplification was later made by Coulaloglou and Tavlarides (1977) by assuming that the drainage time is not distributed. Despite a few criticisms regarding the validity of this model have been formulated, it remains, to date, the most popular one. In view of some other assumptions made in this chapter, the

Tavlarides, 1977):

$$p_d = \exp\left(-\frac{t_{Drainage}}{t_{Prox}}\right) \tag{3.5}$$

It is also noteworthy that for $1 < R_2/R_1 < 2$, an approximation for the collision frequency N_c $(m^{-3}.s^{-1})$, that can further be used to estimate the (electro)coalescence rate, was proposed by Saffman and Turner (1956)[3] and yields:

$$N_c = 2.3\,(R_1 + R_2)^3\, n_1 n_2 \left(\frac{\zeta}{\nu_o}\right)^{1/2} \tag{3.6}$$

where n_1 and n_2 are the number densities of droplets having radii R_1 and R_2 (m^{-3}).

3.3 Numerical simulation of the electrocoalescence of two water drops in stagnant oil

3.3.1 Configuration and relevant parameters

The time-dependent problem of film thinning associated with the motion and deformation of two perfectly conductive water drops, suspended in a initially quiescent dielectric oil, triggered by the application of a uniform background electric field, is considered here. Owing to computational power restrictions, investigations were limited to the axisymmetric geometry depicted on Figure 3.2. Such configuration can be viewed as the asymptotic case of fine droplets flowing side by side in a local velocity gradient and passing at a finite interfacial distance s_0 while becoming aligned with the field direction. It is notably a typical example where coalescence would not occur without the field assistance and should therefore provide an upper bound for the drainage time. Indeed, in other situations, such as that depicted on Figure 3.1, the compressional force (section 1.5.1.5) exerted by the flow would positively contribute to the intervening film thinning.

Preliminary simulations were performed with evenly sized drops ($R_1 = R_2 = R_0$) to illustrate the different behaviors that may be observed in industrial separators. Again, tap water and polybutene oil, the properties of which are documented in Table 2.2, were respectively used as the conductive and insulating phase. A wide range of initial electric Bond numbers ($Be_0 = \frac{1}{2}\epsilon_0\epsilon_{r_o}V^2R_0/(\gamma s_0^2)$, V being the potential difference between the drops) were tested by varying the drop radius while keeping both the interfacial tension coefficient and electric field intensity constant. Moreover, in order to stick closely to

author considers that the present model is accurate enough and provides a clear picture of the involved time scales.

[3]The original factor in equation (3.6)was 1.3. It was later found to be incorrect by Pearson et al. (1984).

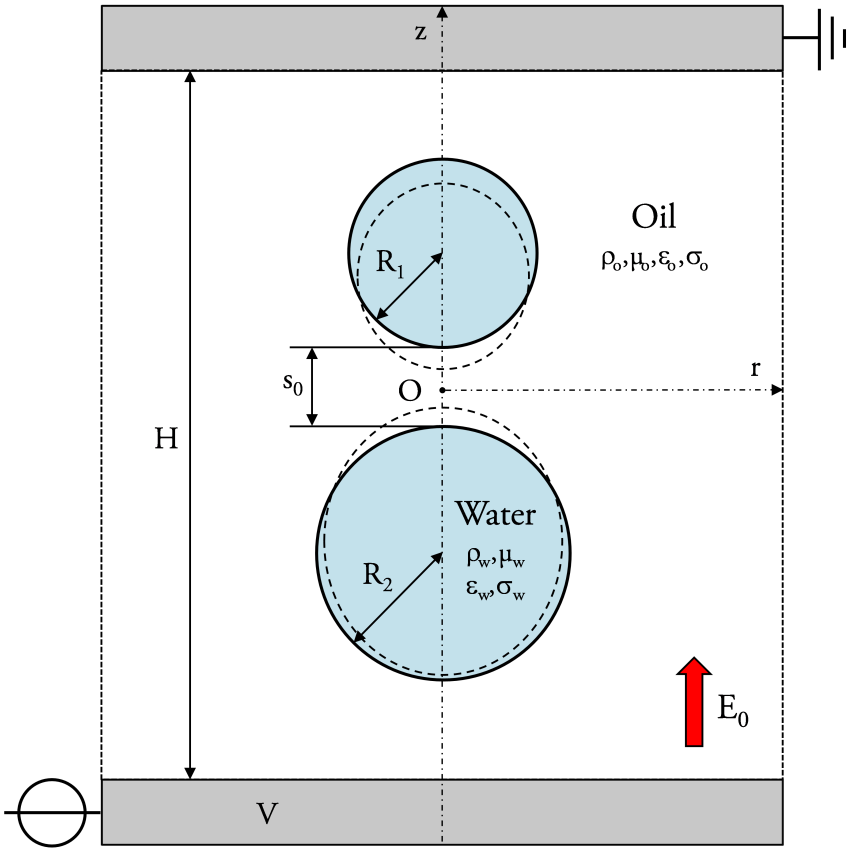

Figure 3.2: *Pair of perfectly conductive water drops freely suspended in a stagnant insulating oil and aligned with a uniform electric field. Axisymmetric geometry and relevant parameters. Electrode spacing is* 10 *times greater than the larger drop diameter, i.e.* $H = 20R_2$.

reality and distinguish, at least in the first stage of approach, both the motion of the deforming drops and the instability of the interfaces, special attention was made on the choice of the initial separation distance. That was therefore adjusted, in each computation to $s_0 = R_1 + R_2$, i.e about twice the spacing at which the electrostatic pressure p_E significantly increases due to the drops reciprocally influencing their polarization. Results are presented on Figure 3.3 in the form of the temporal evolution of the relative oil film thickness and of the drop axial elongation.

A first interesting trend is highlighted by looking at the contact times of even drops having an identical ratio of the initial separation distance s_0 to the radius R_0. According to the similarity observed in the computed values, this latter parameter could somehow be a scaling factor for the drainage mechanism (this question is further addressed in the following section). That being said, numerical results clearly show one of the complex feature of the film drainage mechanism: the scale limitation (Aryafar and Kavehpour, 2009).

For rather large Be_0, here corresponding to drops radii about one or two order of magnitudes greater than that usually found at the inlet of electrocoalescers (but still

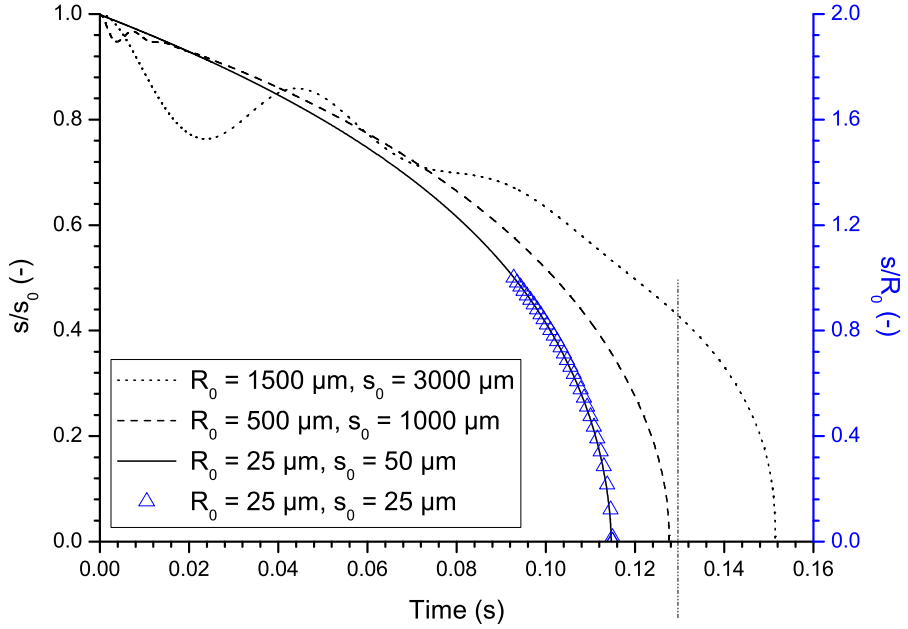

(*a*)

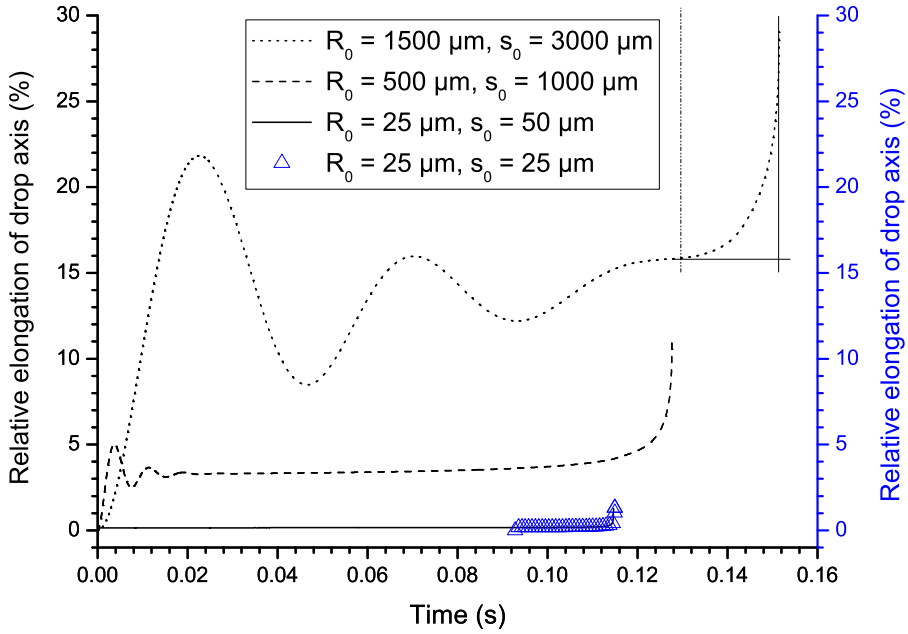

(*b*)

Figure 3.3: *Approach of two neutral water drops, suspended in a stagnant dielectric oil, under the influence of a background electric field. Temporal evolution of the relative oil film thickness s/s_0 (lines), s/R_0 (lines+marks) (a) and drop axial elongation (b) for different drop radii R_0 and initial separation distances s_0. Initial time in the computation $R_0 = 25\ \mu m, s_0 = 25\ \mu m$ was adjusted to $t = 0.0928$ to match that at which the same interfacial spacing is reached in the case $R_0 = 25\ \mu m, s_0 = 50\ \mu m$. Simulation parameters: $\rho_w = 1000\ kg.m^{-3}$, $\rho_o = 824\ kg.m^{-3}$, $\mu_w = 0.001\ Pa.s$, $\mu_o = 0.0102\ Pa.s$, $\gamma = 0.025\ N.m^{-1}$, $\epsilon_{r_o} = 2.3$ and $E_0 = 3\ kV.cm^{-1}$.*

sometimes formed in the process), electric stresses dominate over the restoring capillary forces and cause dramatic deformation of the drops, even at a moderate background electric field (3 $kV.cm^{-1}$). Interfacial disruption, indicated by the sharp increase of the relative elongation of the drops, tends to occur at a non-negligible separation distance ($s/s_0 \sim 0.44$ for $R_0 = 1500\ \mu m$) thus complicating the drainage modeling by including a variable critical thickness parameter[4]. Moreover, additional modifications of the drag force and characteristic length of the oil film, due to the substantial deformation of the interfaces, should also be considered.

On the opposite, for low Be_0, i.e. for radii in the scale of interest (tens of micrometers (Kokal, 2006)), water droplets remain nearly spherical during the overall drainage stage, the relative axial elongation hardly exceeding 0.25% except during the final instants when disruption occurs. Such a result offers many practical advantages. Among those, the possibility to approximate both the time required to reach the critical film thickness by that of contact and the deformed radius by its initial value R_0 is particularly handy. Indeed, these are typical assumptions found in classical problems of solid or liquid particles collision in two-phase flows (Davis et al., 1989). For instance, Atten (1993) gave the expression,

$$t_{Contact} = \frac{8}{15}\frac{\mu_o}{\epsilon_0 \epsilon_{r_o} E_0^2}\left[\left(\frac{s_0 + R_1 + R_2}{R_1 + R_2}\right)^5 - 1\right], \tag{3.7}$$

for the time to contact of spherical droplets flowing in another liquid (with a viscosity ratio $\lambda = \mu_w/\mu_o \ll 1$) based on Stokes' formula and on the point-dipole approximation for drag (equation (1.16)) and electrostatic (equation (1.10)) forces respectively. Despite disregarding the lubrication effect, relation (3.7) predicts, here ($R_0 = 25\ \mu m$), times to contact close to those determined by simulations for large relative initial separation distances (Figure 3.4). In the case $s_0 = 2R_0$, the difference is very small (0.092 instead of 0.114). An explanation lies in the fact that the retained forces formulation is globally valid over the longest part of the oil film thinning (down to an interfacial separation distance $s \sim R_0$, see Berg and Ingebrigsten (2005) and appendix A.4). Nevertheless, since an even finer match is obtained when starting with $s_0 = R_0$ (0.0196 s instead of 0.0221 s), another phenomenon, trickier, is expected to also play a role. Indeed, the underestimation of the electrostatic attraction while $s < R_0$ seems to be fairly well compensated for, up to a certain point, by the neglect of the contribution of the increasing pressure in the film as oil is expelled from the facing interfaces region. Unexpectedly, the latter effect renders Atten (1993)'s expression quite accurate down to an initial relative separation

[4]According to recent experimental works (Hellesø et al., 2009, Ristenpart et al., 2009), the tendency to conical interface formation at such electric Bond number seems to negatively affect the bridging and full merging stage and so to be detrimental to the electrocoalescence efficiency.

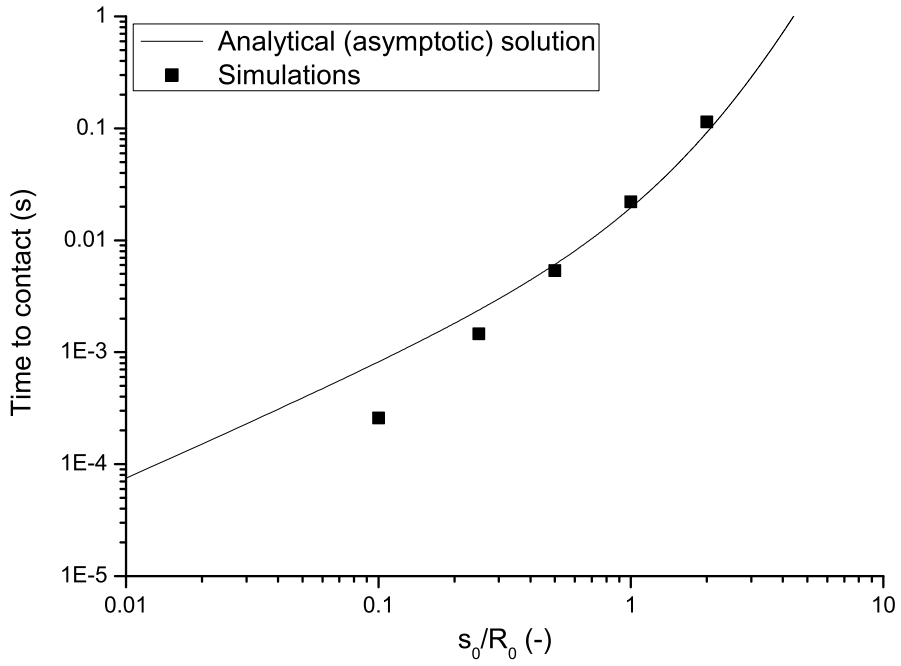

Figure 3.4: *Approach of two small neutral water droplets, suspended in a stagnant dielectric oil, under the influence of a background electric field. Variation of the time to contact as a function of the relative initial separation distance as computed through numerical simulation and predicted by Atten (1993)'s analytical asymptotic solution. Simulation parameters:* $R_0 = 25\ \mu m$, $\rho_w = 1000\ kg.m^{-3}$, $\rho_o = 824\ kg.m^{-3}$, $\mu_w = 0.001\ Pa.s$, $\mu_o = 0.0102\ Pa.s$, $\gamma = 0.025\ N.m^{-1}$, $\epsilon_{r_o} = 2.3$ *and* $E_0 = 3\ kV.cm^{-1}$.

distance $s_0/R_0 \sim 0.3$. Though, when s_0/R_0 is further reduced, simulations showed that the adequacy of equation (3.7) becomes poor. Unfortunately, this corresponds to a range much more relevant to the industrial problem since actual times to contact should be considerably lower than those of close proximity estimated around $t_{Prox} \sim 0.001 - 0.01\ s$ (equation (3.4)) for typical[5] shear rates $\dot{\gamma} \sim 100 - 500\ s^{-1}$ in the turbulent flow conditions of electrocoalescers. These results confirmed the need for a modeling of the drainage process, including more accurate electric forces approximations like that of Davis (1964) (see appendix A.4), and implied the use of smaller initial relative separation distances s_0. Concerning the latter, the very weak inertia experienced by the micrometer scale droplets, supported here by the superposition of curves representing different s_0 in Figure 3.3 is, again, a crucial asset.

3.3.2 Film drainage: existing models and order of magnitude

Benefiting from the preliminary investigations, a set of liquid and geometric properties relevant to the industrial electrostatic demulsification was defined (see Table 3.1) to serve as a basis for a parametric study on the drainage mechanism. Prior to that, results

[5] Melheim and Chiesa (2006)'s intermediate value for the turbulent energy dissipation rate $\zeta = 0.22\ m^2.s^{-3}$ gives $\dot{\gamma} = 133.3\ s^{-1}$.

Table 3.1: *Set of parameters retained for the reference case*

Geometric properties	
Drop radius	$R_1 = R_2 = R_0 = 10\ \mu m$
Initial spacing	$s_0 = 1\ \mu m$
Physical properties	
Water density	$\rho_w = 1000\ kg.m^{-3}$
Water viscosity	$\mu_w = 0.001\ Pa.s$
Oil density	$\rho_o = 824\ kg.m^{-3}$
Oil viscosity	$\mu_o = 0.0102\ Pa.s$
IFT	$\gamma = 0.025\ N.m^{-1}$
Relative permittivity	$\epsilon_{r_o} = 2.3$

computed with the reference case were used to evaluate the ability of some classical theoretical lubrication models to reproduce the temporal evolution of the oil film thickness in the presence of electric forces. Emphasis was placed, here, on those, older and less sophisticated, that assume unperturbed drop shape during the approaching stage and viscous dominated flows. Indeed, to the author's knowledge, most of the recent treatments were developed in relation with the DLVO theory (Sanfeld and Steinchen, 2008) in which the time determining step of the thinning process, preceding drop coalescence, is controlled by the combined effects of van der Waals attraction and double layer repulsion. Hence, taking into account the interfaces deformation through, e.g., the popular parallel film model (Liao and Lucas, 2010) has inevitably led to equations stating either the proportionality (Coulaloglou and Tavlarides, 1977, Chesters, 1991) or the independence (Chesters, 1975) of the drainage time versus a potential driving external force. As strange as it may appear, the former type stems from the flattening of the drops in the facing zone that increases the film area and consequently slows its thinning (Chesters, 1991). The latter is more trivial and concerns "infinitely" viscous suspending liquids.

Models chosen for comparison purposes were extracted from Davis et al. (1989) and rewritten to express the relative approach velocity W as a function of the external applied force F[6]. Using the lubrication theory to describe the film flow between the droplets and introducing a dimensionless "interface mobility" parameter $m \equiv \lambda^{-1}\sqrt{R_1R_2/(s(R_1+R_2))}$, characterizing the velocity profiles in both the disperse and continuous phase, the authors obtained the following approximations:

$$W_{RS} = \frac{Fs}{6\pi\mu_o \left(\frac{R_1R_2}{R_1+R_2}\right)^2 (1 - 1.31m + 1.78m^2)}\text{[7]}, \tag{3.8}$$

[6]In the original work, F stands for the hydrodynamic resisting force on the drops. Assimilation is possible here, since for negligible inertia, it must balance any external forces.

[7]Only the first three terms of the asymptotic polynomial expansion for the force were kept. For $m \to 0$,

$$W_{PM} = \frac{Fs\,(1 + 1.69m + 0.43m^2)}{6\pi\mu_o \left(\frac{R_1 R_2}{R_1+R_2}\right)^2 (1 + 0.38m)} \tag{3.9}$$

and

$$W_{FM} = \frac{F\sqrt{s}}{16.5\mu_w \left(\frac{R_1 R_2}{R_1+R_2}\right)^{3/2}} \tag{3.10}$$

corresponding to $m \ll 1$, $m \sim 1$ and $m \gg 1$ respectively. It should be noted that the mobility mentioned here is a purely hydrodynamic effect arising from a difference in fluid viscosities ($\lambda = \mu_w/\mu_o \neq 1$). It thus does not account for interfacial Marangoni flows created by gradients of adsorbed species. For $m \ll 1$, drops behave mostly like rigid spheres during their approach. As a consequence from the interface immobility, the expel of the oil volume contained in the interstitial region takes the shape of a radial parabolic flow. Despite requiring viscosity ratios λ much higher than those of actual water-in-crude oils emulsions, equation (3.8) was retained for some[8] relevance to the drainage mechanism of droplets completely covered with surfactants, in which the velocity fields of the disperse and continuous phase are not coupled. On the opposite, for $m \gg 1$, droplets offer relatively little resistance to the radial oil flow. The strong interfaces mobility leads to an almost flat velocity profile in the gap and to a formulation depending, rather astonishingly, on the dispersed phase viscosity only (Davis et al., 1989). Finally, when $m \sim 1$, neither of the former scenarios prevails and a more complex solution was found, reflecting the full coupling of both hydrodynamic problems, i.e. the circulation pattern inside the drop and the oil flow.

In order to further obtain, by integration of the above equations, the temporal evolution of the film thickness, s, as a function of the initial configuration, it is first paramount to express the external or interaction force F. However, whereas the hydrodynamic collision force driving the drainage may simply be assumed constant in the referenced studies, the dependency of the electrostatic attraction F_e on the interfacial spacing s must be considered here. Again, owing to the limited interfacial deformation, a very accurate estimate (in the range of interest ($s/R_0 = 0.1 - 0.001$)) of the force $F_e = 0.92\pi\epsilon_0\epsilon_{r_o}E_0^2R_0^{2.8}s^{-0.8}$ acting between two conducting spheres of even radii R_0 aligned with the field was derived from a power law fitting of Davis (1964)'s bispherical solution (appendix A.4). Since both equations (3.8) and (3.9) include polynomial form of m, only the dominating terms $O(1)$ for $m \ll 1$ and $O(2.26)$ for $m \sim 1$ were taken into account to ease the calculation. After

the well-known rigid sphere solution (Jeffrey, 1982) is recovered.

[8] Flattening of the facing interfaces resulting from the lowering of the IFT coefficient may also play a significant role.

integration, this yielded

$$s_{RS}(t) = \left(s_0^{0.8} - \frac{0.49\epsilon_0\epsilon_{r_o}E_0^2R_0^{0.8}}{\mu_o}t \right)^{1.25}, \tag{3.11}$$

$$s_{PM}(t) = \left(s_0^{0.8} - \frac{1.11\epsilon_0\epsilon_{r_o}E_0^2R_0^{0.8}}{\mu_o}t \right)^{1.25} \tag{3.12}$$

and

$$s_{FM}(t) = \left(s_0^{1.3} - \frac{0.644\epsilon_0\epsilon_{r_o}E_0^2R_0^{1.3}}{\mu_w}t \right)^{1/1.3} \tag{3.13}$$

for rigid, partially and fully mobile interfaces, respectively. Figure 3.5 shows the evolution of the oil film thickness computed through simulation and those predicted by equations (3.11), (3.12) and (3.13) in the reference case. According to computations, the drops

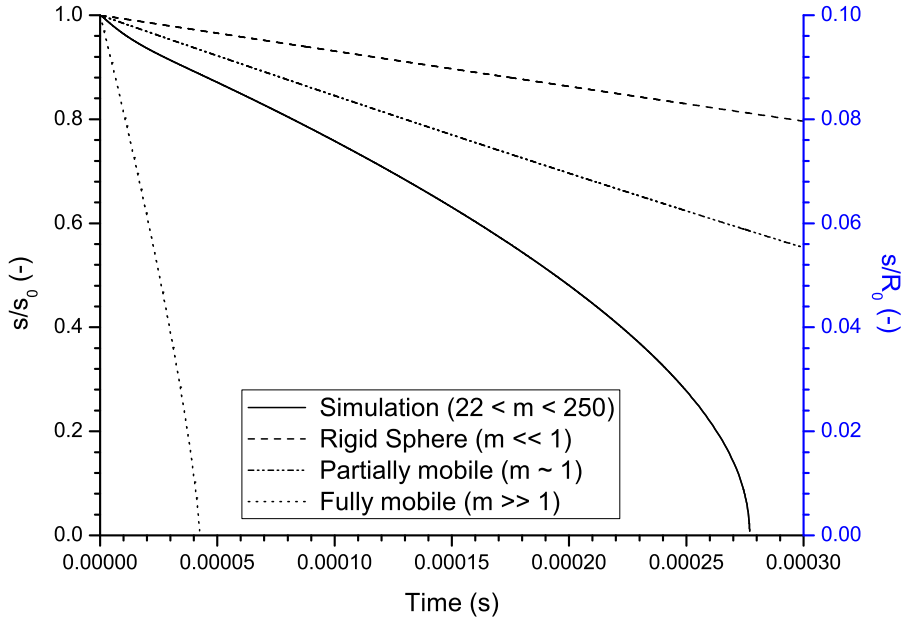

Figure 3.5: *Evolution of the relative oil film thickness s/s_0 between two water drops approaching under the action of electrostatic forces. Results from numerical simulation and asymptotic models developed within the lubrication theory, by Davis et al. (1989), for different value of the "interface mobility" parameter m. The chosen configuration corresponds to the reference case with a background electric field of 3 $kV.cm^{-1}$.*

approach velocity, being nearly constant up to about $s/s_0 = 0.5$, then clearly augments with the decrease of their relative spacing. This is of primary importance from a physical modeling point of view since, by implying a very short duration for the final stage of thinning ($s/s_0 < 0.1$), it confirms the negligible influence of van der Waals attraction and double layer repulsion forces (typically arising below $s = 1000$ Å (Eow et al., 2001)) in practical electrostatic-based dewatering applications. In comparison with those former results, the extremely longer contact time extrapolable in the rigid sphere case was quite expected as the absence of internal circulation and interfacial mobility strongly slows the

expel of the oil and thus the whole drainage process. The large deviation observed from the curve plotted using Davis et al. (1989)' model for fully mobile interfaces (equation (3.13)) is, yet, a bit more confusing, especially considering the relative correspondence in the value of the parameter m. Not criticizing the authors' original results[9], the issue behind the discrepancy was believed to lie in the applicability of the lubrication theory. The latter exploits the disparity in length scale characterizing the film, i.e. thickness and width, and leads to a simplified formulation of the Stokes equations ($Re \ll 1$) for the flow in the gap writing, in the present axisymmetric configuration,

$$\frac{\partial p_o}{\partial r} = \mu_o \left[\frac{1}{r}\frac{\partial}{\partial r}\left(r\frac{\partial u_o}{\partial r}\right) - \frac{u_o}{r^2} + \frac{\partial^2 u_o}{\partial z^2}\right] \sim \mu_o \frac{\partial^2 u_o}{\partial z^2} \tag{3.14}$$

$$\frac{\partial p_o}{\partial z} = \mu_o \left[\frac{1}{r}\frac{\partial}{\partial r}\left(r\frac{\partial w_o}{\partial r}\right) + \frac{\partial^2 w_o}{\partial z^2}\right] \sim 0 \tag{3.15}$$

where r and z are the radial and axial coordinates as introduced in Figure 3.2. p_o and u_o stand respectively for the pressure and radial velocity component in oil. As demonstrated in Raisin et al. (2010)[10], lubrication theory well describes the drainage mechanism between close rigid spheres because the viscous dissipation mainly comes from the axial variation of u_o. However, when dealing with liquid droplets having clean interfaces, the scheme is considerably altered. The circulation pattern inside water deeply modifies the radial velocity profile of the oil flow (Figure 3.6). Due to the low viscosity ratio $\lambda = \mu_w/\mu_o < 0.1$, the tangential velocity at the drop interface appears, to a first approximation, close to the mean radial velocity component $\overline{u}_o$ in the bulk of the gap. An estimation of the latter is obtained by stating mass conservation in the film which implies equality between the flow rate through a cylinder of radius r ($Q_{u_o} = 2\pi \overline{u}_o 2z_s$) and the rate of decrease of the oil volume ($Q_w = \pi r^2 2w_s$) where z_s denotes the height of the upper interface. Taking the osculating paraboloid ordinate $z = (s + r^2/R_0)/2$ for z_s gives:

$$\overline{u}_o = w_s \frac{r}{s + \frac{r^2}{R_0}} \tag{3.16}$$

which takes its maximum value,

$$\overline{u}_{o_{Max}} = \frac{1}{2}\sqrt{\frac{R_0}{s}} w_s, \tag{3.17}$$

at $r = l_{u_o} = \sqrt{R_0 s}$. This distance can thus be viewed as a characteristic length scale for the radial variation of u_o and w_o in the oil film and coincides, as a matter of fact, with

[9] Those were, e.g., found accurate through comparison with treatments using bispherical coordinates.
[10] Readers should know that most of the credits for the asymptotic analytical part belong to P. Atten.

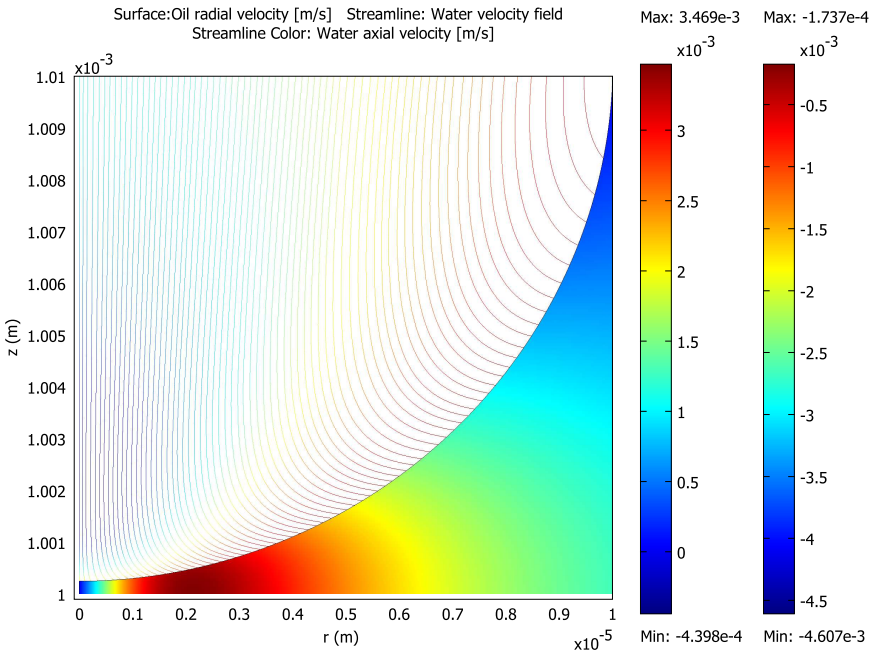

Figure 3.6: *Numerical simulation of the viscous dominated flows between and inside two perfectly conductive drops approaching under the effect of a background electric field. Instantaneous state at $s = s_0/2$ in the reference case. The colored surface plot (left scale) illustrates the radial velocity profile in oil. The streamlines and their associated colors (right scale) represent the velocity field in water and its axial component intensity, respectively.*

that of the electrostatic pressure (Atten et al., 2006). From Figures 3.6 and 3.7, it seems reasonable to assume that $l_{u_o} = 2.23\ \mu m$ also holds for the velocity field within the water drops ($l_{u_w} \sim 2\ \mu m,\ l_{w_w} \sim 1.75\ \mu m$). Thus, using the continuity of viscous stresses that imposes:

$$\mu_o \left.\frac{\partial u_o}{\partial n}\right|_{z=z_s^-} = \mu_w \left.\frac{\partial u_w}{\partial n}\right|_{z=z_s^+} \tag{3.18}$$

the z-derivative of u_o at the interface can be approximated by:

$$\left|\frac{\partial u_o}{\partial z}\right|_{z=\pm z_s} \sim \frac{\mu_w \overline{u}_{o_{Max}}}{\mu_o l_{u_o}}. \tag{3.19}$$

The term retained in the lubrication theory for the radial derivative of the pressure has, consequently, the following order of magnitude:

$$\mu_o \left|\frac{\partial^2 u_o}{\partial z^2}\right| = \mu_o \left|\frac{\partial}{\partial z}\left(\frac{\partial u_o}{\partial z}\right)\right| \sim \mu_o \frac{1}{s}\left|\frac{\partial u_o}{\partial z}\right| \sim \mu_w \frac{w_s}{s^2}. \tag{3.20}$$

Still, in the general case, the contribution from the radial derivatives of u_0, writing

$$\mu_o \left|\frac{1}{r}\frac{\partial}{\partial r}\left(r\frac{\partial u_o}{\partial r}\right) - \frac{u_o}{r^2}\right| \sim \mu_o \frac{\overline{u}_{o_{Max}}}{l_{u_o}^2} \sim \mu_o \frac{w_s}{R_0^{1/2} s^{3/2}}, \tag{3.21}$$

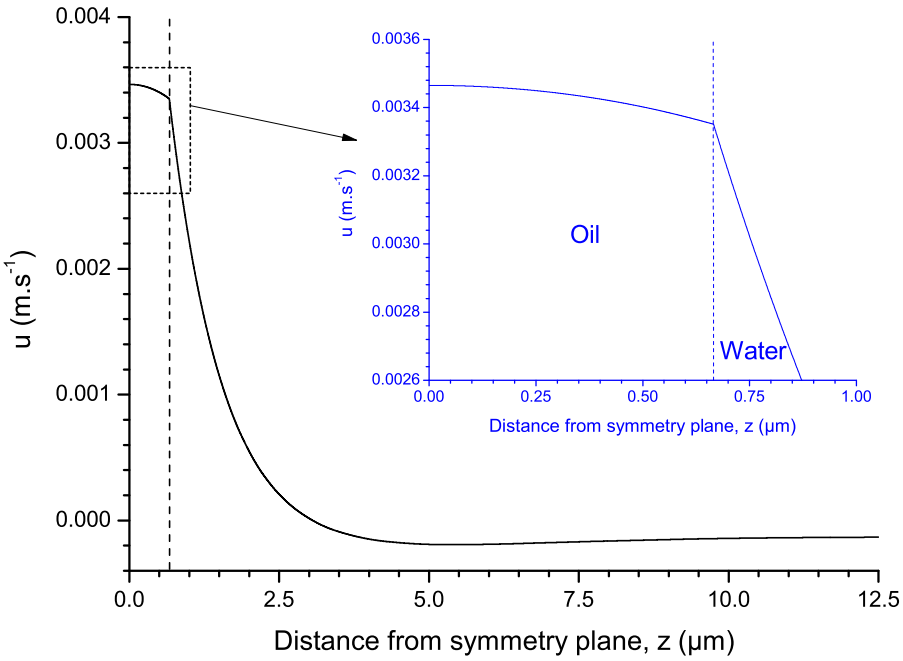

Figure 3.7: *Computed profile of the radial velocity component in both oil and water at* $r = \sqrt{R_0 s} \sim 2.23$ *µm and* $s = s_0/2$ *for the reference case. The vertical dotted line symbolizes the position of the interface.*

must also be taken into account. This yields:

$$\left|\frac{\partial p_o}{\partial r}\right| \sim \mu_o \frac{w_s}{R_0^{1/2} s^{3/2}} \left(1 + \alpha \frac{\mu_w}{\mu_o} \sqrt{\frac{R_0}{s}}\right). \tag{3.22}$$

where α is a numerical constant accounting for the effect of the different assumptions and expected to be on the order of 1. Equation (3.22) reveals something stunning which, on its own, explains the large discrepancy visible on Figure 3.5. Indeed, the lubrication theory is based on the assumption that most of the contribution to the radial pressure gradient comes from the axial derivative of u_0 (see equation (3.14)), or in other words that $\lambda\sqrt{R_0/s} \gg 1$ (equation (3.22)). In practice, with the typical viscosity ratios encountered in water-in-crude emulsions ($\lambda \sim 0.02-0.1$), the first member of equation (3.22) markedly dominates over the longest part of the drainage process. The radial pressure difference (equal to about twice that in the gap) therefore mostly arises from the radial derivatives of u_0, giving:

$$(\Delta p_o)_r = p_o(0,0) - p_{o\infty} \sim 2\left|\frac{\partial p_o}{\partial r}\right| \sqrt{Rs} \sim 2\mu_o \frac{w_s}{s}. \tag{3.23}$$

Similarly, $(\Delta p_o)_z$, exerting between the interface and the plane of symmetry, writes

$$(\Delta p_o)_z = p_o(0, s/2) - p_o(0,0) \sim \left|\frac{\partial p_o}{\partial z}\right| \frac{s}{2} \sim \mu_o \frac{w_s}{2s}. \tag{3.24}$$

Again, unlike anticipated by lubrication theory, $(\Delta p_o)_z$ is, here, on the same order as

$(\Delta p_o)_r$. From there, an estimate for the approach velocity of each drop w_s can be straightforwardly obtained by balancing $(\Delta p_o)_r$ with the mean electrostatic pressure p_E from which it originates. Taking Davis (1964)'s expression $p_E = \epsilon_0 \epsilon_{r_o} (E_3 E_0)^2/2$, corresponding to the maximum intensity reached at the droplets surface (i.e at the facing poles), lowered by a factor β and a fitted power law $1.87(s/R)^{-0.85}$ for the variation of E_3 (see appendix A.4) then leads to:

$$2\mu_o \frac{w_s}{s} = \frac{1}{\beta} \frac{\epsilon_0 \epsilon_{r_o} \left[1.87 \left(\frac{s}{R_0} \right)^{-0.85} E_0 \right]^2}{2} \Rightarrow w_s = \frac{3.50 \epsilon_0 \epsilon_{r_o} s^{-0.70} R_0^{1.70} E_0^2}{4\beta\mu_o}. \tag{3.25}$$

The rate of film thinning, equal to $-2w_s$, is therefore defined as

$$\frac{ds}{dt} = -\frac{1.75 \epsilon_0 \epsilon_{r_o} s^{-0.70} R_0^{1.70} E_0^2}{\beta\mu_o}. \tag{3.26}$$

which after integration, yields the equation for the temporal evolution of the interfacial separation distance:

$$s(t) = \left(s_0^{1.70} - \frac{2.975 \epsilon_0 \epsilon_{r_o} E_0^2 R_0^{1.70}}{\beta\mu_o} t \right)^{1/1.70}. \tag{3.27}$$

The behavior predicted by equation (3.27) is in agreement with that computed through numerical simulation and endorse the rather rough analysis conducted (see Figure 3.8). With $\beta = 8$[11], an almost perfect correspondence in the thinning rate is achieved (the difference in drainage time being due to the slight droplets deformation, particularly visible in the early stage of the approach). Assuming that coalescence occurs at near contact, an approximation for the drainage time is:

$$t_{Drainage} = \frac{\beta\mu_o s_0^{1.70}}{2.975 \epsilon_0 \epsilon_{r_o} E_0^2 R_0^{1.70}} = \frac{\beta\mu_o}{1.7\frac{1}{2} \epsilon_0 \epsilon_{r_o} (E_{3_0} E_0)^2} \tag{3.28}$$

which qualitatively involves the initial maximum electrostatic pressure acting on the drops and the oil viscosity.

3.3.3 Results of simulation for even and uneven droplets

In order to further evaluate the domain of applicability of equation (3.28), a parametric study was conducted using numerical simulation. Influence of the initial interfacial spacing

[11] Although such a value may appear high, readers should note that the parameter β compensates for at least one additional (other than lowering Davis (1964)' expression) source of overestimation of the rate of thinning, not mentioned in the text. The mean electrostatic pressure, used in equation (3.25), contributes, in fact, both to the radial and axial pressure difference.

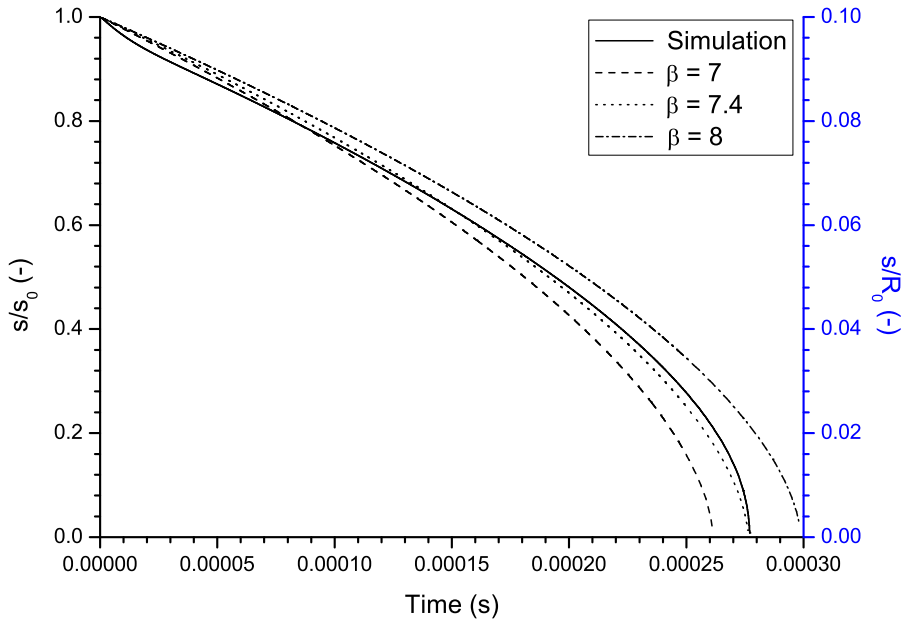

Figure 3.8: *Evolution of the oil film thickness s/s_0 versus time for the reference configuration and $E_0 = 3$ kV as predicted by numerical simulation and equation (3.27) with different values of the factor β.*

s_0, drop radii R_1 and R_2, interfacial tension coefficient γ and continuous phase viscosity μ_o were successively studied by varying each variable separately around its reference value. For each configuration, a series of about eight computations were performed by adjusting the background electric field E_0 in the range $0.5 - 8$ $kV.cm^{-1}$. A systematic analysis of the results confirmed the tendency enlightened by the former theoretical study.

First of all, as clearly shown on Figures 3.9 and 3.10, the drainage time of even and uneven droplets subjected to a given initial maximum electrostatic pressure $p_{E_0} = \frac{1}{2}\epsilon_0\epsilon_{r_o}(E_{3_0}E_0)^2$, is not, to a first approximation, explicitly dependent on their initial spacing s_0 and radii R_1 and R_2. Indeed, providing the influence of different s/R_1 and R_1/R_2 on the field enhancement is taken into account, curves overlap particularly well. Secondly, according to Figure 3.11, the drainage time markedly increases with the continuous phase viscosity μ_o.

Despite being based on a few, some of them strong, hypotheses, equation (3.28) proves accurate over most of the investigated range of p_{E_0}, the largest deviations arising consistently as its different validity conditions stop being fulfilled. This happens, for instance, when the initial relative separation distance s_0/R_0 is increased over 0.1 (validity limit of the retained E_3 approximation) or when the viscosity ratio λ becomes smaller than 0.1. In the latter case, the underestimation of the drainage time comes from the neglect of the term $\lambda\sqrt{R_0/s}$ which supposedly contributes to the lowering of the radial velocity in the film flow. Drawing conclusions on the discrepancy observed for the greater p_{E_0} values is however much more complex. From both Figures 3.9 and 3.11, the onset of

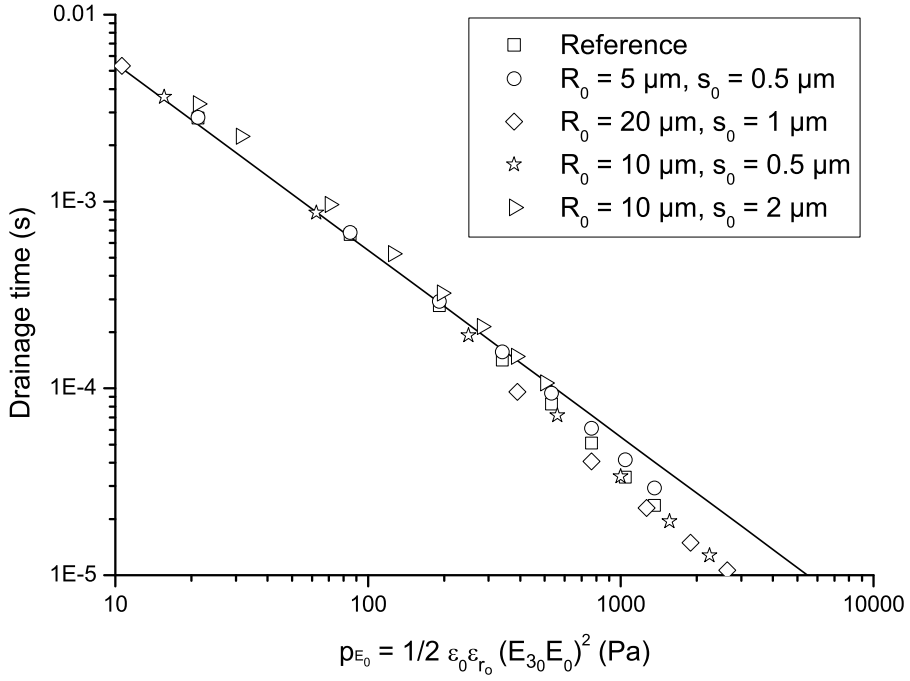

Figure 3.9: *Variation of the drainage time as a function of the initial maximum electrostatic pressure p_{E_0}, estimated using Davis (1964)' formulation, for even droplets. Detailed influence of the undeformed drops radius R_0 and initial spacing s_0. The full line corresponds to equation (3.28) with $\beta = 8$.*

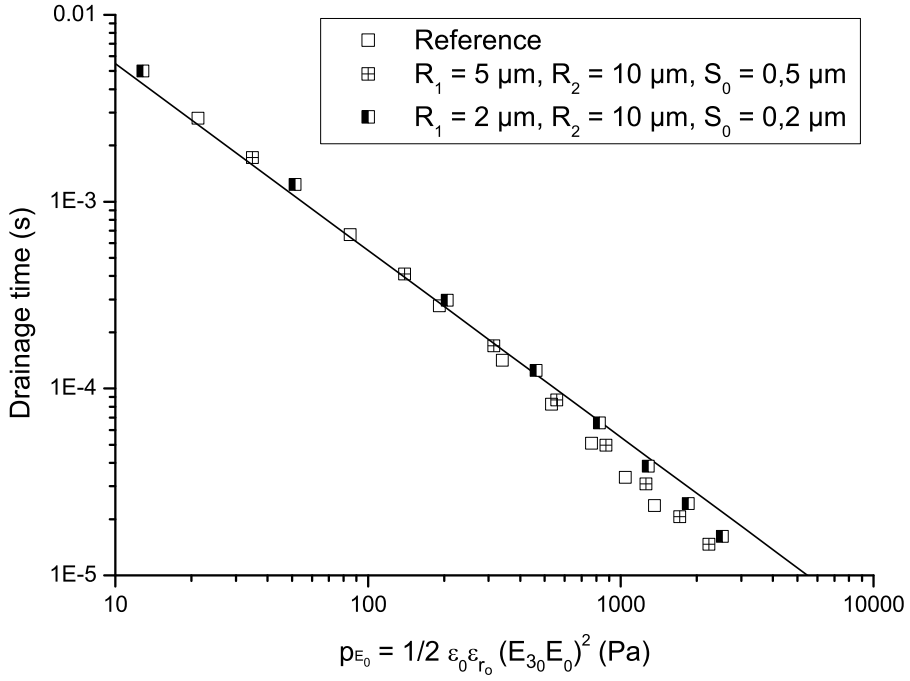

Figure 3.10: *Variation of the drainage time as a function of the initial maximum electrostatic pressure p_{E_0} estimated using Davis (1964)' coefficient, for uneven droplets. Influence of the size ratio R_1/R_2. The full line corresponds to equation (3.28) with $\beta = 8$.*

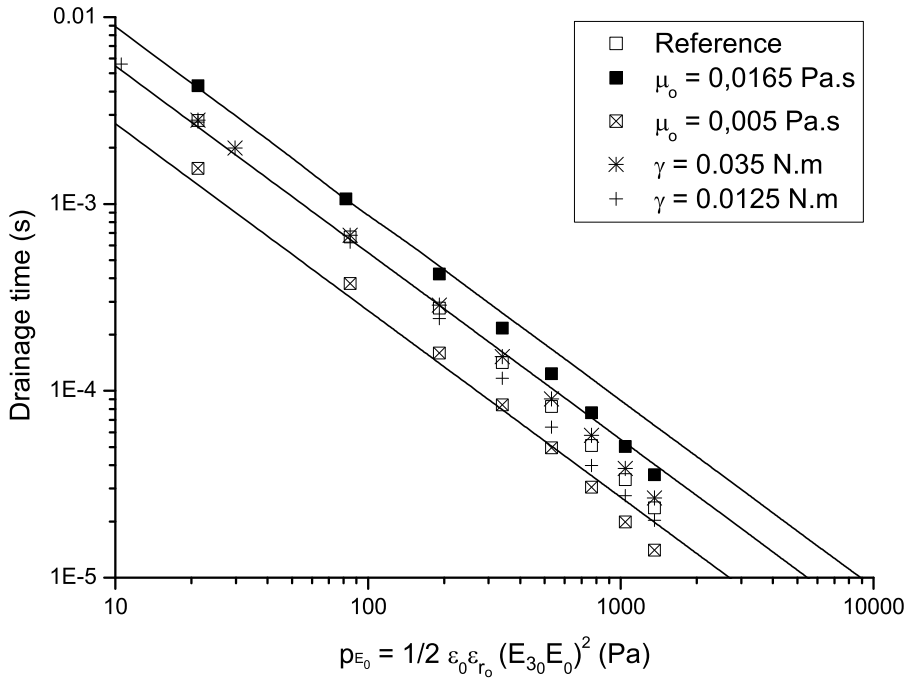

Figure 3.11: *Variation of the drainage time as a function of the initial maximum electrostatic pressure p_{E_0}, estimated using Davis (1964)' formulation, for even droplets. Detailed influence of the interfacial tension coefficient γ and oil viscosity μ_o. The full lines corresponds to equation (3.28) with $\beta = 8$ for each value of μ_o.*

shifting seems to significantly vary with the drop radius and interfacial tension coefficient, implying that it is somewhat connected to the capillary force. This becomes even more obvious when the drainage time is plotted as a function of the electric Bond number $Be_0 = \frac{1}{2}\epsilon_0\epsilon_{r_o}(E_{3_0}E_0)^2R_0/\gamma$ for the various configurations tested. The change in slope visible in Figure 3.12 corresponds to the transition from the drainage in between almost undeformed droplets to a slightly faster, but less pertinent, disruption mechanism. Indeed, above a certain initial electric Bond number $Be_{0_{Crit}}$, as in chapter 2, the water-oil interfaces become instantaneously unstable and film thinning occurs through elongation at the poles without noticeable displacement of the center of gravity. Although defining a threshold value from Figure 3.12 or from the computations appears difficult, it is, nonetheless, interesting to note that the transition seems to take place at a Be_0 (in the interval $0.08 - 0.01$) higher than that, on the order of 0.05, obtained in the static anchored drops problem (see the curve $\theta_m = 175°$ in Figure 2.11). This can be understood by looking at the different "role" played by the electric forces: in the latter case, the electrostatic pressure compensates for the local increase in curvature accompanying interfacial deformation, whereas with free drops, its effect mainly consists in counteracting the viscous force in the film.

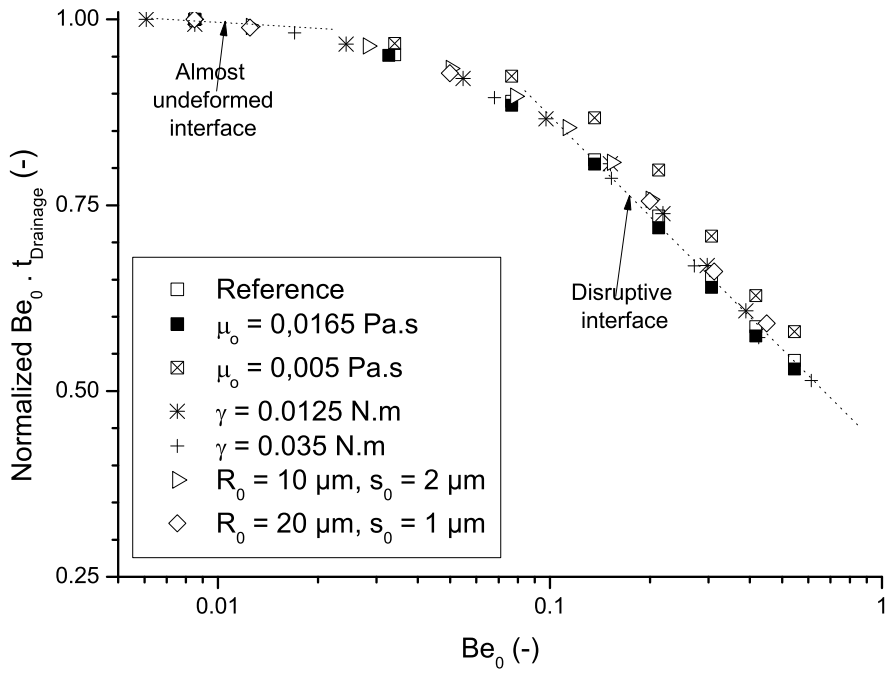

Figure 3.12: *Variation of the normalized product of the electric Bond number* $Be_0 = \frac{1}{2}\epsilon_0\epsilon_{r_o}(E_{3_0}E_0)^2R_0/\gamma$*, estimated using Davis (1964)' formulation, by the drainage time* $t_{Drainage}$ *as a function of* Be_0 *for even droplets.*

3.3.4 Probability of electrocoalescence

In the light of results from the former section, introducing equations (3.28) and (3.4)[12] into (3.5) should give a fair order of magnitude estimate for the probability of electrocoalescence of two water drops colliding in a local shear flow of a clean viscous liquid, writing:

$$p_d \sim \exp\left(-\frac{\beta\mu_o\dot{\gamma}}{0.85\epsilon_0\epsilon_{r_o}\left(E_{3_0}E_0\right)^2}\right) \tag{3.29}$$

Equation (3.29) provides some very interesting insights into what happens, at a larger scale, in industrial devices. First, it supports qualitatively results obtained, within the project, on the destabilization of water-in-crude oil emulsions by stating that both a decrease in oil viscosity μ_o and an increase in applied electric field intensity E_0 favors the separation process (e.g. illustrated on Figure 3.13). All other parameters being kept constant, changes in one of those two can considerably modify the amount of water resolved after treatment, especially for low water cuts emulsions (jump from about 13% to $90-100\%$). Equation (3.29) also enlightens an subtlety that was maybe not so clear a few years back and, as a consequence, misled on the appreciation of the relative contribution of turbulence. Indeed, even if the latter undoubtly speeds up the droplet growth by favoring collisions (see equation (3.6)), its strengthening may not always lead to an improvement of

[12] Assuming $R_1 \sim R_2 \gg s$.

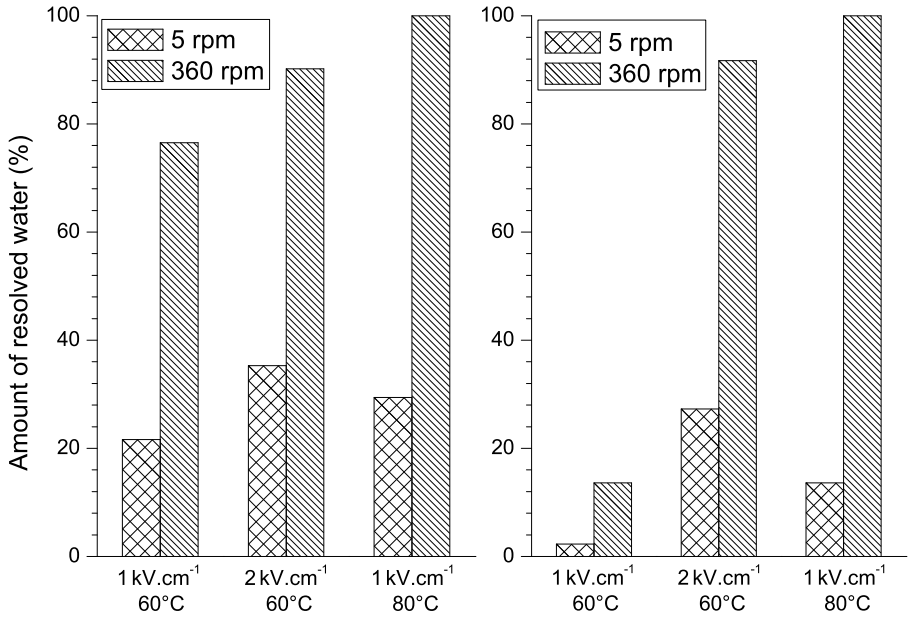

Figure 3.13: *Water resolved after a 15 seconds electrostatic treatment in an electrorheometer of 30 % (left) and 10 % (right) water-in-crude oil emulsions. Influence of the shear rate (here "expressed" in rotations per minute and corresponding to 6.12 s^{-1} and 440 s^{-1}), electric field and temperature. Reproduced with the courtesy of S. Less (Less, 2008).*

the dewatering efficiency. It is expected that above a certain threshold[13] $\dot{\gamma}$, electric fields required to compensate for the shorter time of close proximity t_{Prox} may strongly affect the freshly coalesced drops. For instance, in a highly turbulent flow ($\zeta = 0.73\ m^2.s^{-3}$ from Melheim and Chiesa (2006)) the maximum stable drop diameter, estimated using Hinze (1955)'s formula ($d_{Max} = 0.725(\rho_o/\gamma)^{-0.6}\zeta^{-0.4}$) would be about 1.6 mm. According to (3.29), achieving $p_d = 75\%$ would demand a background electric field $E_0 = 1.354\ kV.cm^{-1}$ that would prevent (either through interfacial disruption or more complex mechanisms (Hellesø et al., 2009, Ristenpart et al., 2009)) electrocoalescence of droplets with diameter above a few hundreds of microns. This is, a priori, what could explain the relatively limited largest diameter observed[14] on Figure 3.14. Optimization of these two double-edged parameters (Urdahl et al., 2001) is and will, therefore, become more and more crucial, especially as for economical reasons, manufacturers and oil companies push toward the progressive reduction of the amount of heating provided to the system.

In its current form, the developed criterion should be well suited to multi-particle CFD codes able to predict the initial relative separation distance s_0/R_1 (and thus E_{3_0}) for each collision. Still, in order to further progress toward the actual conditions in an electrocoalescer, many other aspects should also be considered and included. For

[13] Still low enough not to cause shear driven drop break-ups which, unlike in propulsion or polymer mixing applications, are detrimental here.

[14] The shear rate and electric field intensity, here about $\dot{\gamma} = 440\ s^{-1}$ and $E_0 = 1\ kV.cm^{-1}$, are not so far from those used in the previous calculation.

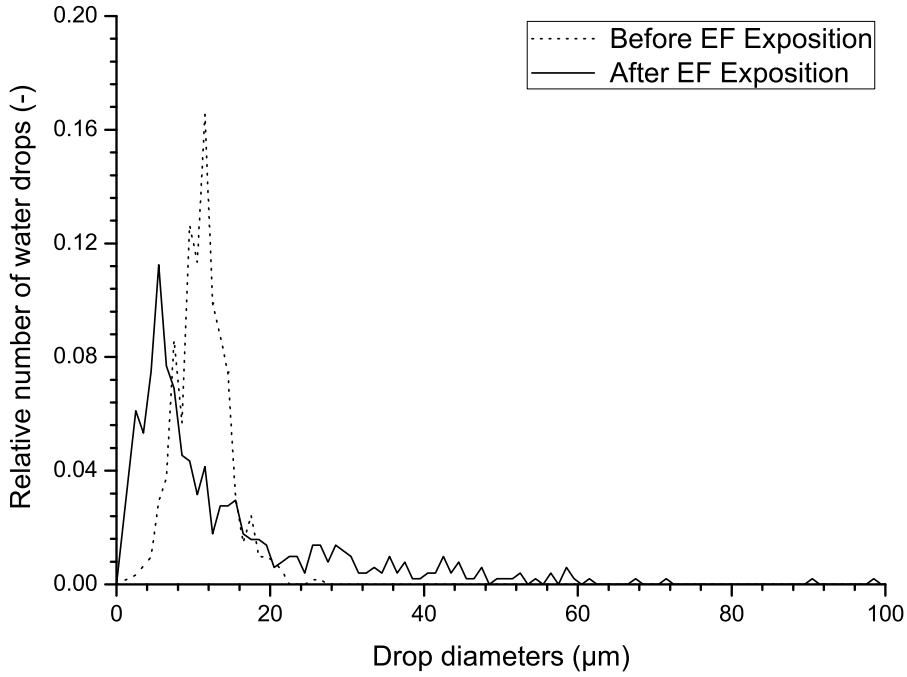

(a)

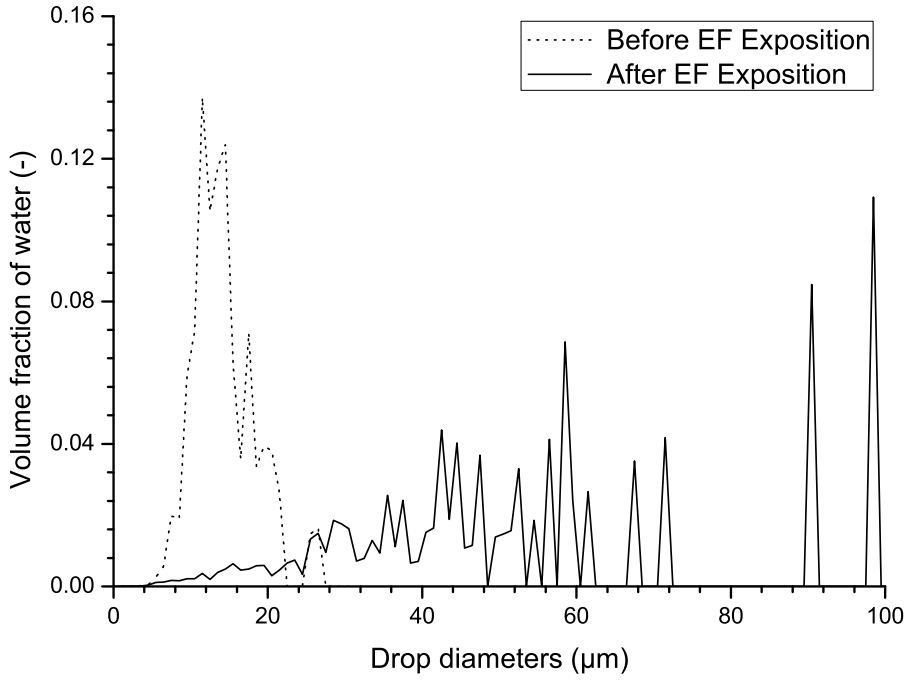

(b)

Figure 3.14: *Drop size distribution in terms of relative number (a) and volume fraction (b) of a 30 % water cut crude oil emulsion before and after a 15 seconds electrostatic treatment in an electrorheometer ($E_0 = 1\ kV.cm^{-1}$, $\dot{\gamma} = 440\ s^{-1}$ and $T = 60°C$). Results reproduced with the courtesy of S. Less (Less, 2008). The total water content of the sample being about 9 times larger after treatment, the shift of the peak in the drop size distribution may primarily comes from the growth of much smaller droplets that the image processing software failed to detect. Even if the retained parameters might not be optimal, (b) clearly shows the strongly beneficial effect of electrocoalescence, i.e. increasing the droplets size so that they sediment much faster under gravity.*

instance, modifications should be made to take into account the transient variation of the electric force intensity with the angular offset θ. Moreover, knowing how the rotation of the droplets and the presence of an interfacial coverage influence the oil film flow also appears mandatory. Concerning the latter, the problem might be very different from that encountered in resting emulsions where surfactants are usually assumed at equilibrium during coalescence. Here, the shear stresses, exerted by the outer viscous fluid during the drops motion, tend to move surfactants along the interface and concentrate them in region with lower velocity gradients, i.e. at the outer poles. Depending on the dynamics involved (surface Peclet number Pe), this might lead to Marangoni flows that can dramatically slow the film thinning.

3.4 Experimental electrocoalescence of two water drops in an oil shear flow

3.4.1 Principle

In order to overcome the inherent limitations of numerical simulation, the main task scheduled within the course of the thesis was the design and assembly of an experimental setup allowing to study the electrocoalescence mechanism at the drop scale through all its different steps. Such a tool would be very handy to improve the relevance of the developed criterion by both increasing the physical knowledge on previously neglected phenomena and quantifying their respective influence. The experiment basically consists in the injection of two calibrated conducting water drops at relatively close positions inside a well established shear flow of a dielectric liquid. Due to the spatial velocity gradients, (see a schematic representation in Figure 3.1), the one initially behind will chase the other and catch up in a region where a background electric field will be applied. The following sections aim at presenting and explaining some of the numerous choices made throughout the building stage with regards to its three main functions: flow establishment, drop injection and data acquisition. Along with specifications that will be further detailed, a few general considerations that ruled the overall design are recalled here:

- Model system to keep a moderate number of parameters and control their evolution;
- Chemical compatibility of all liquids and materials involved;
- Electrical hazards free: absolutely no contact with HV possible;
- Promote automation to reduce the experimentalist's charge.

3.4.2 Design of the setup

3.4.2.1 Flow establishment

Regarding the hydrodynamic part, the first and most important decision, conditioning almost all subsequent others, concerned the choice of the type of flow. Indeed, an ideal Couette flow and a Poiseuille flow were both possible options (Figure 3.15). In the former,

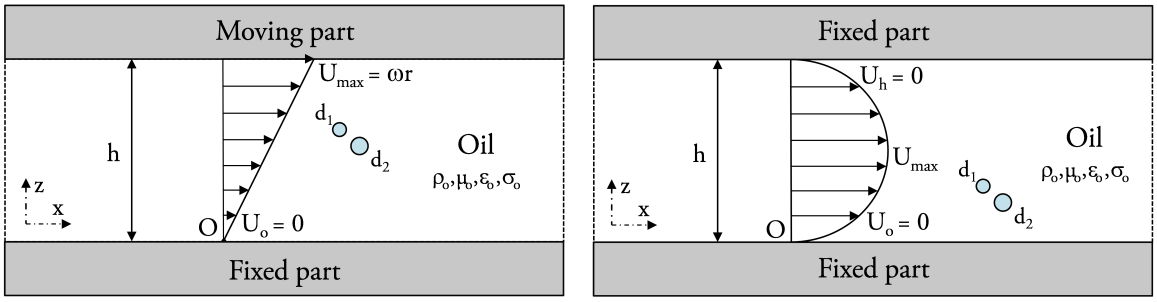

Figure 3.15: *Velocity profiles corresponding to (a) cylindrical ideal Couette and (b) Poiseuille flows.*

fluid motion originates from the action of viscous drag forces and is generated, commonly inside two coaxial cylinders, by the displacement of one surface relatively to the other. The latter refers to the natural flow of fluid between parallel plates or in a pipe. The main advantage of an ideal Couette flow lies in the simplicity of its velocity profile: thanks to the constant shear rate $\dot{\gamma}$, any drops with given longitudinal and transversal initial separations (respectively $|x_{2_0} - x_{1_0}|$ and $|z_{2_0} - z_{1_0}|$), will always collide after the same time of travel. Apart from that, all other arguments support the use of a Poiseuille flow. For instance, on a mechanical viewpoint, having to deal with moving parts imposes tight constraints on the selection of materials and manufacturing techniques to reach high precision adjustments and to avoid vibrations. This usually results in far more complex, prone to failure, expensive and/or heavier mechanisms. Moreover, in most cases, the presence of cylindrical surfaces, even transparent, is detrimental to optical visualizations. Finally, if further needed, the implementation of a linearly translating acquisition system following the droplets motion would be easier than a rotating one.

In this experiment as well as in all the others in the thesis, a polybutene oil (Ineos Oligomers - Indopol Grade L-6) was retained for the dielectric liquid phase for two main reasons: first, its long time use at the G2ELab facilities had never highlighted any significant compatibility issue either with usual cell construction materials or with HV; Moreover, in addition to being an ideal lubricant, it offers a few very interesting assets with respect to the study of the electrocoalescence phenomenon. According to their sup-

plier, Indopol polybutenes are transparent to visible light with a refractive index (1.461) different from that of water (1.333)[15], non-drying, highly resistant to oxidation by UV and moderate heat, hydrophobic, and can easily be emulsified. They are also practically non-toxic and can be washed efficiently through dilution in Cyclohexane. The relatively strong dependency of the Grade L-6 viscosity with temperature (see appendix B) and the unexpected evolution of its IFT coefficient with the storage under ambient conditions are however quite troublesome (see e.g. section 4.4.2). A detailed survey on a replacement candidate might thus be required before starting any test campaign.

The different materials investigated for the build up of the cell walls were Polyvinyl Chloride (PVC)[16], Poly(methyl methacrylate) (PMMA) and glass. Though, the latter was soon discarded due to its greater density and its poorer machinability. As for the polymers, their comparison in terms of price, hardness, light transmittance, dielectric strength and compatibility with polybutene oil failed to break the tie. Since the main parts (corresponding to #3 and #5 in Figure 3.16) needed to be outsourced, the final choice was dictated by the presence of a manufacturer in the surroundings of Grenoble and fell on PMMA. Dimensioning calculations, performed by a master student (Déléonibus, 2008), led to the CAD model depicted on Figure 3.16. The cell is composed of four different subparts, namely, a divergent (#1), two channels (#3 and #5 respectively 500 mm and 600 mm long) and a convergent (#9). The main body (#3 and #5) features a rectangular inner section 20×160 mm^2 with an aspect ratio large enough to ensure a 2D flow in the central zone. At each junction, an impervious sealing is guaranteed by the compression of a rubber gasket partly housed into one of the screwed flanges. After entering the cell, the perturbed oil flow of mean velocity up to $\bar{u} = 0.05$ $m.s^{-1}$ is first smoothed by a Polyester Polyurethane convoluted foam (not represented) held inside the divergent (#1) by an HDPE grid (#2). It then develops completely in #3 before passing through the injection (#6) and electrocoalescence regions (#7, #8) located in #5 and finally exiting through #9.

The filling, isolation and emptying of the cell is controlled by the presence of a valve at each extremity. Those are, in turn, linked through $\varnothing$ 30 mm plastic corrugated tubes (see Figure 3.17) to an upstream and a downstream reservoir, respectively. With its larger capacity (60 liters instead of 20) and opaque walls, the latter (#10) is held fixed and allows to properly store all the oil during long pauses separating campaigns of experiments. Besides, it also features a drain system to dispose of the sedimented water drops. On the contrary, the upstream reservoir (#11) is partially transparent and is mounted on a

[15] Both values are measured at a wavelength of 589.29 nm.
[16] In its transparent declination.

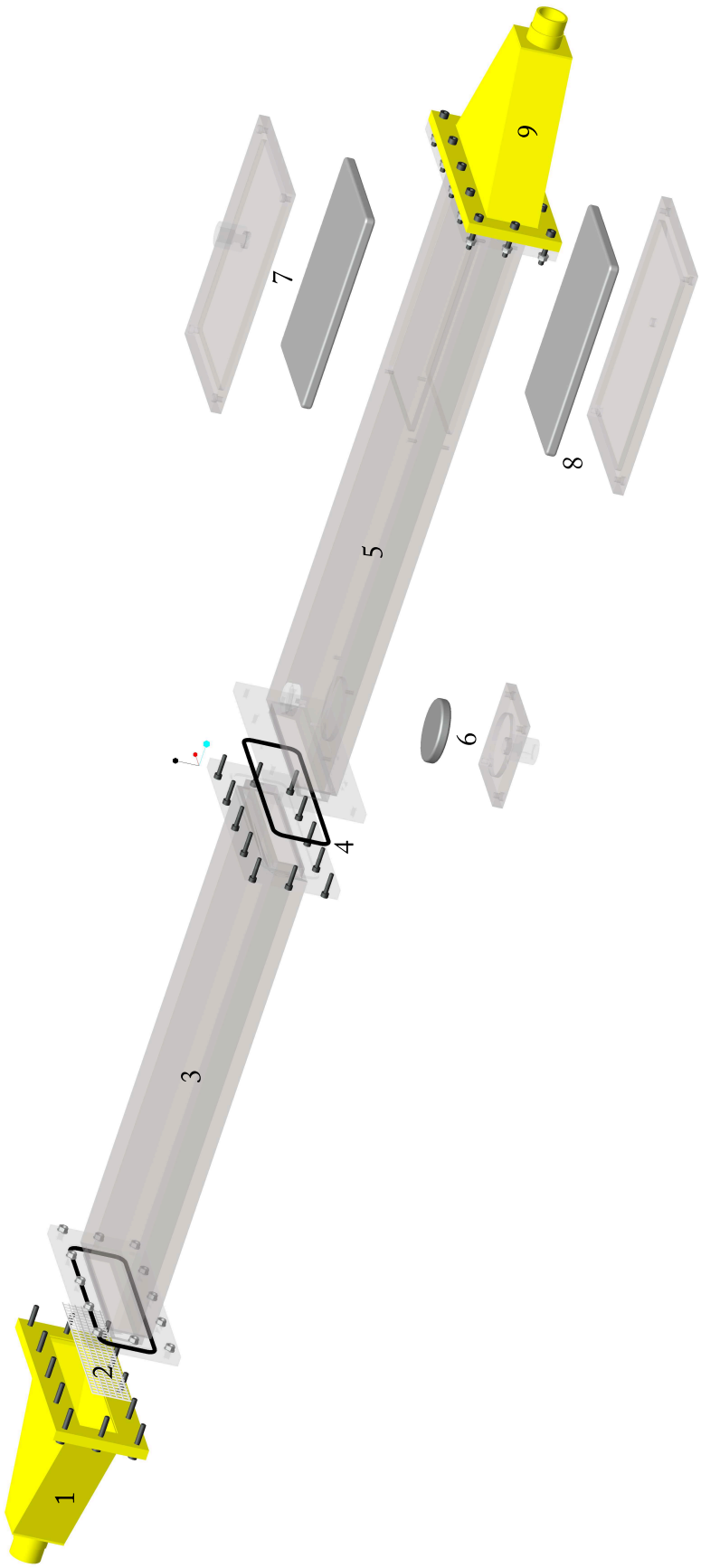

Figure 3.16: *3D CAD model of the "drop-drop electrocoalescence in a shear-flow" experimental cell. Nomenclature:* 1, *Divergent* - 2, *HDPE grid (the Polyester Polyurethane convoluted foam is not represented here)* - 3, *Flow establishment part* - 4, *Rubber gasket* - 5, *Main part* - 6, *Injection region: HV electrode and PMMA holder* - 7 & 8, *Coalescence region: HV and grounded electrodes plus PMMA holders* - 9, *Convergent.*

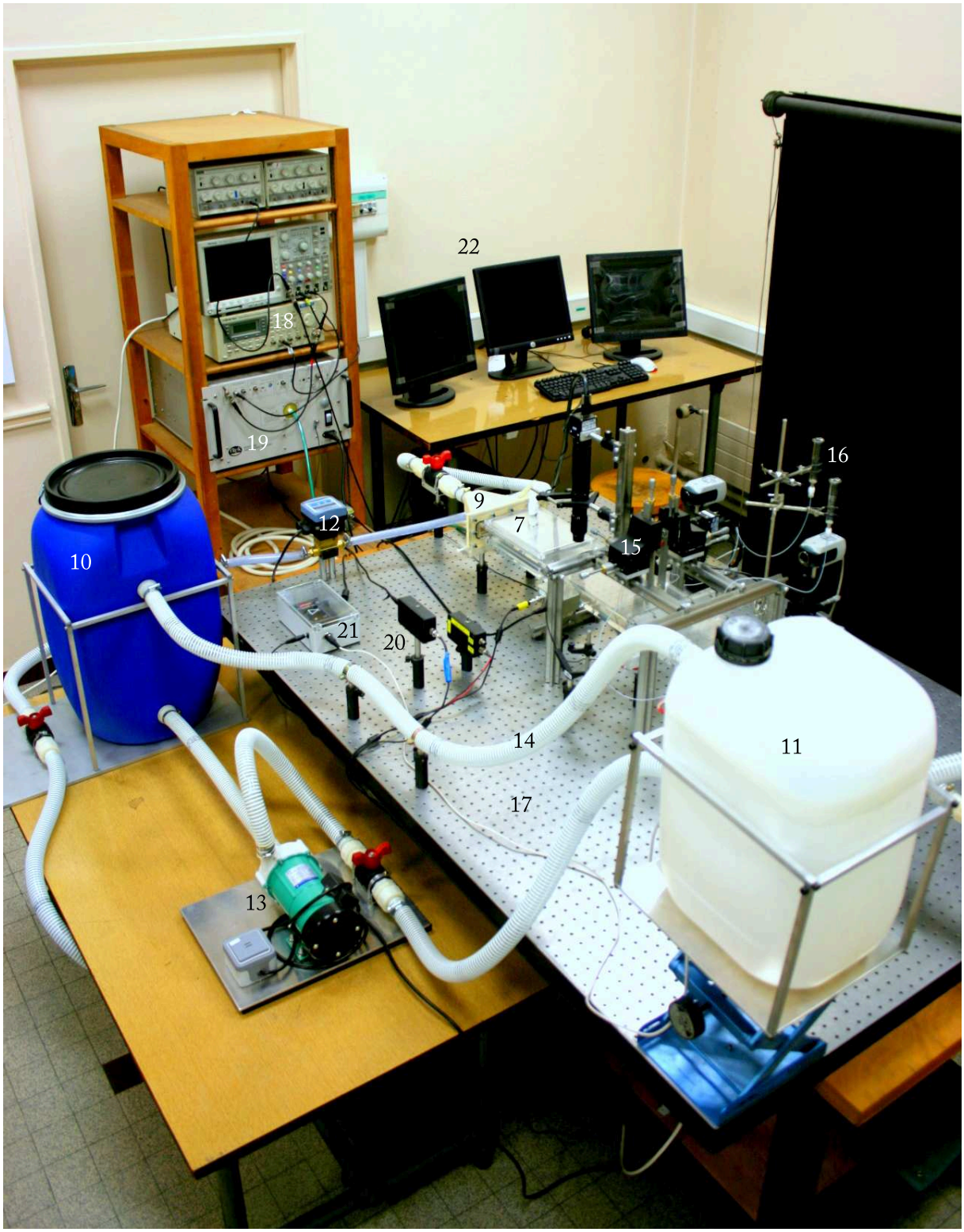

Figure 3.17: *Photograph showing the "drop-drop electrocoalescence in a shear flow" experimental setup: 10, Downstream reservoir - 11, Upstream reservoir - 12, Flowmeter - 13, Magnetic pump - 14, Overflow - 15, XYZ linear stage - 16,* 100 *ml water reservoir - 17, Optical table - 18, Arbitrary wave generator - 19, HV amplifier - 20, Flashable LED light sources - 21, Real-time oil temperature measurement system - 22, Visualization desk.*

vertical lifting table in order to visualize and position the liquid free surface. As a result from the generated height difference and thus pressure gradient, oil will flow at a rate measured by an inline flow meter (Bűrkert - S030/8035) (#12) placed downstream of the cell, and set to the desired value ($Q_c = 0.16\ L.s^{-1}$) by iterative adjustments. A magnetic pump (Iwaki - MD-55R-5) (#13) supplying $Q_r > Q_c$ and an overflow (#14) are used to refill and maintain a constant free surface level in the upstream reservoir. At last, all connexions, including e.g. those between valves or tips and tubes, are sealed with flat rubber gaskets, o-rings and clamps.

3.4.2.2 Synchronized injection of two electrically neutral water drops in oil

The aim of the injection system is to release two electrically neutral water drops at given locations in the Poiseuille oil flow so that they become close when entering the steady electric field region, i.e. after traveling about $L \sim 315\ mm$. Owing to their small size, a very weak influence of gravity on their motion is to be expected. Therefore, drops with either even or slightly uneven radii will most likely follow parallel, nearly linear, flow path (e.g., a simple estimation for $R_0 = 25\ \mu m$ using the terminal fall velocity U_T and $\bar{u} = 0.05\ m.s^{-1}$ predicts a vertical offset of about $0.315\ mm$ at $L = 315\ mm$). Hence, collisions will only occur for initial transversal separation Δz_0 close to $R_1 + R_2$ and will mainly depend on the initial longitudinal separation Δx_0 and relative height in the shear flow z_0/h. According to the aforementioned hydrodynamic calculations (see appendix B.2), the designed cell allows to study drops with diameters ranging from 20 to 240 μm by simply adjusting Δx_0 and z_0/h between $1-3\ mm$ and $0.2-0.4$, respectively. Even if it may seem feasible on paper, achieving such requirements appeared very intricate in view of the common injection techniques' capability. Indeed, as it will be shown in chapter 4, most of them would demand, for instance, frequent changes in the nozzle diameter to produce such a drop diameter distribution. This feature, among others, was hardly compatible with the authors' will to decrease the experimentalist's load and led to the development of a novel actuation technique based on the application of a high electric field pulse on a water meniscus in oil. In addition, the injection system needs to be able to individually and accurately position each nozzle in the three directions, to avoid as much as possible the generation of perturbations in the flow and to prevent any leakage.

The implementation of the retained technical solution is presented on Figure 3.18. A slotted hole ($3 \times 1\ mm^2$) (#28) across the upper PMMA wall allows two metallic needles (#26) of inner radius $R_{Cap} = 231\ \mu m$ to penetrate inside the cell. In order to attain the intended longitudinal spacing and thus overcome a spatial interference at their top extremity, both were angled 90°. Such an arrangement was also favored as, combined

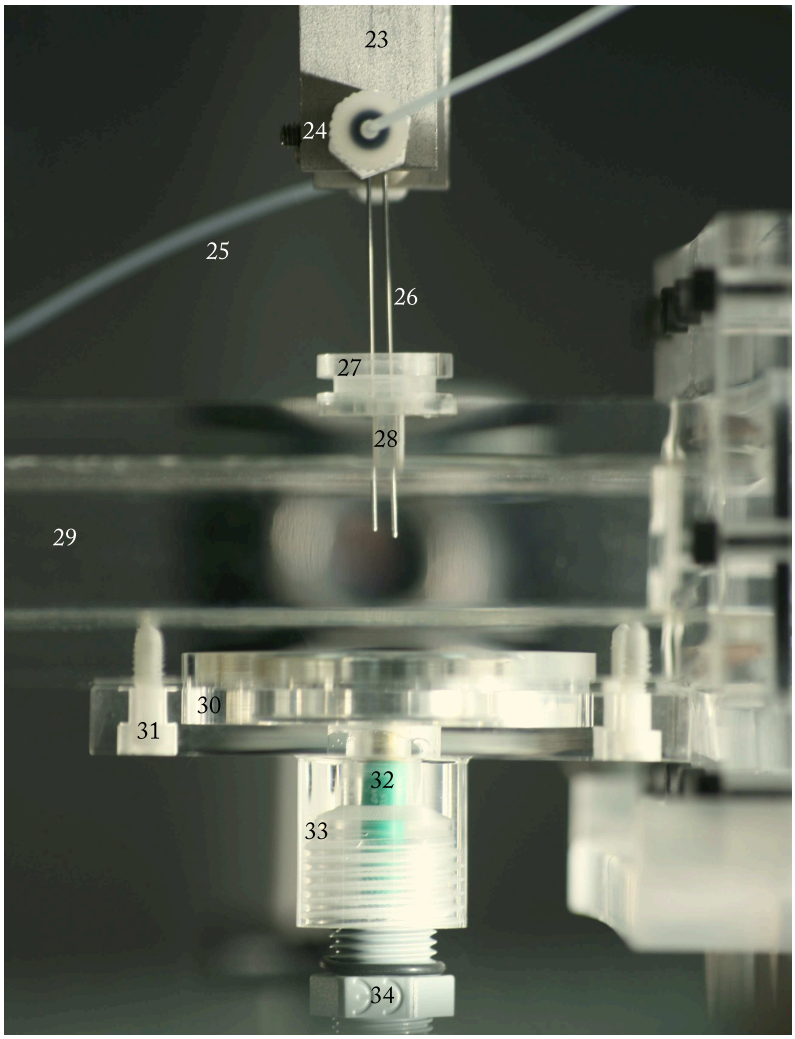

Figure 3.18: *Close-up photograph of the injection zone. From top to bottom: 23, Grounded needle holder - 24, Luer connector - 25, PTFE capillary - 26, Curved metallic needles - 27, Sealing system (neither the thin latex film nor the snap ring are represented) - 28, Slotted hole - 29, PMMA cell - 30, HV electrode - 31, Plastic screw - 32, HV supply cable - 33, HV electrode holder - 34, Cable gland.*

with a pivot mount into their respective holders (23) and a screw block, a quasi perfect parallelism between the needles can be ensured. Their final positioning is then easily managed through two XYZ linear stages (Newport - M-460P-XYZ) (#15) attached on a rigid stainless steel structure (#37) (see Figure 3.19). Efficiently sealing the slotted hole was however quite trickier. Indeed, the system has to be rigid and elastic enough to counteract the impact, yet limited, of the oil pressure and not to alter the needle placement at the same time. A good compromise to address those two problems involves the use of a film of latex, let loose around the needles and compressed, around an annular extension of the cell (#27), by a snap ring. Water supply is accomplished through a one meter long PTFE capillary (#25) of inner radius 400 μm connected to a reservoir (#16) of about 100 ml capacity. The former advantageously increases the inertial and viscous effects experienced by the fluid column and thus prevents volumetric changes in

the meniscus during the injection. The latter helps to keep the back pressure constant and consequently to almost restore the initial meniscus height, afterwards. If necessary, corrections can be made by adjusting the vertical location of the water free surface. Drops release, resulting from the action of an electrostatic field pulse at the water/polybutene oil interface will be triggered by the application of a potential difference between the needles #26 and a planar electrode (#30). As all other conducting components potentially in direct contact (needle holder, stainless steel structure, optical table plate (#17)...), #26 was grounded while #30 was set to receive the driving signal created by an arbitrary wave generator (Wavetek - 395) (#18) and multiplied (1000 times) by a High Voltage amplifier (Trek - 5/80) (#19). Finally, a PMMA holder (#33) and a cable gland (#34) were added to the system to lock both #30 and #32 in position and avoid any electrical hazard.

3.4.2.3 Detection and image acquisition of flowing drops

Once both electrically neutral water drops could correctly be injected in the well established oil flow, arose the question of relevant data acquisition. Indeed, for each experiment, not less than 8 parameters (recalled as the interfacial tension coefficient γ, oil viscosity μ_o, background electric field type (AC sine/triangular/square or DC) and intensity E, undeformed drop radii R_1 and R_2 as well as the interfacial separation distance s_0 and angular offset θ when entering the coalescence region (#8)) need to be measured without interference on the studied phenomenon, i.e. preferably using indirect techniques. Concerning drop related parameters, acquisition will therefore rely on ombroscopic imaging as in all the other experiments of the thesis. For that matter and learning from previously faced experimental difficulties, two new CMOS cameras (Dalsa - Falcon 1.4M100) (#35) with improved resolution (1400×1024 *pixels*) and PC remote control ability were purchased. Those were equipped with optical zooms (#36) enabling to focus on 1×1 mm^2 windows (about five to twenty times the predefined drop diameters) and so guaranteeing a satisfactory definition for accurate shape detection in further post-treatments. As seen on Figure 3.19, cameras were respectively mounted on horizontal and vertical 3D positioning systems and focused on a small region of the oil flow near the coalescence electrodes. To complete the visualization system, the combination of two green[17] emitting LED light sources (#20), converging lenses and mirrors provide strong back illumination in the two directions. In addition, since oil viscosity is mostly dependent on temperature (see Figure B.1), a real-time monitoring device, consisting in a PT100 sensor immersed in the upstream reservoir and connected to a converter (#21), was added to the setup. Finally, IFT coefficient and electric field related data will be deduced externally: the former through

[17] To maximize the quantum efficiency of the camera (see Figure B.4).

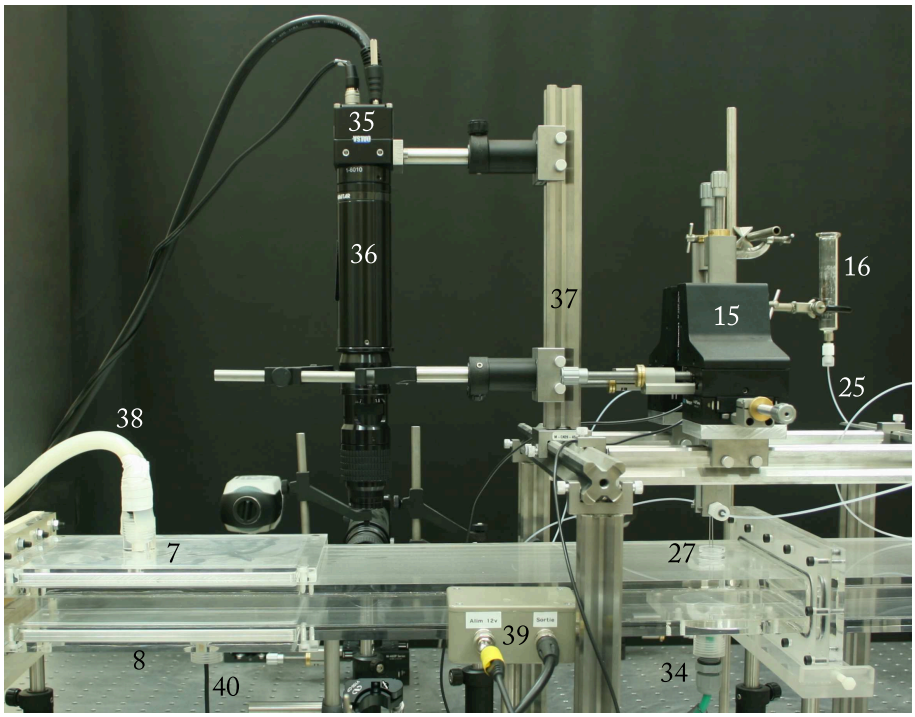

Figure 3.19: *Photograph of the experimental setup illustrating the drop detection and frame acquisition hardware assemblies. Again, from top to bottom: 35, Falcon 1.4M100 camera - 36, Optical zoom - 37, Stainless steel structure - 38, HV supply cable - 39, Drop detection system (the photocathode is visible in the foreground while the laser is hidden on the opposite side of the cell) - 40, Grounded Copper cable.*

tensiometer measurements on samples taken from the cell, the latter straightforwardly as a user defined parameter.

In order to drive each of those hardware subsets and efficiently store their collected data without overloading the experimentalist, the "full" automation of the process seemed very appropriate. A software[18] based on the graphical programming language NI LabVIEW was therefore developed to control the whole sequence as described on Figure 3.20. Once launched, it loads the camera configuration, temporarily store the manually inputted (and importantly constant) parameters in memory and waits for the reception of a trigger signal. The latter originates from the detection, by a photocathode[19] (#39), of a fluctuation in the density of light emitted by a continuous laser (located on the other side of the cell) as droplets cross its $1 \times 2\ mm^2$ wide beam path. The software then stores the temperature of the oil and, after a certain delay corresponding to the travel time up to the border of the camera windows, initiates the frame acquisition. A defined number of images (most probably between 2 and 4 in view of the oil flow velocity, maximum frame

[18]Implementation was partly accomplished by an intern and finalized by a technician. The author only defined the specifications and checked the compliance of the final version.

[19]Compared to others (e.g. magnetic), such a system also offers the great advantage of discarding any situations in which drops do not flow inside the camera window, due to improper injections or else, and thus considerably simplifies the post-treatment stage.

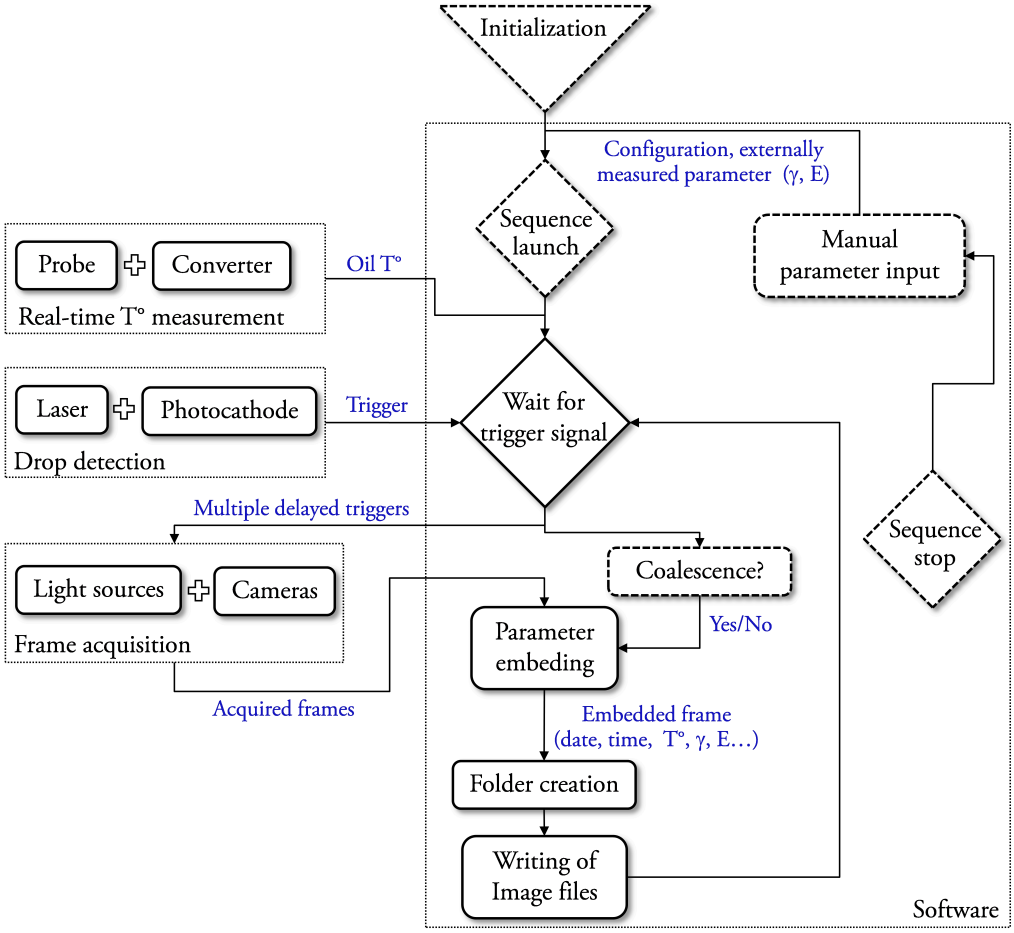

Figure 3.20: *Schematic diagram of the automated data acquisition system (ADAS) in its current form: nature (in blue) and flow of data between the successive software and hardware subassemblies actions. Dashed lines represent steps where a user input is required.*

rate and possible use of a portion of the CMOS sensor) are captured, each being synchronized with a flash[20] of adjustable duration. At the same time, the user is prompt to enter whether electrocoalescence was observed or not on the screens (#22) through a 25 fps CCD camera. Finally, after being embedded with all the stored experimental parameters, images are automatically saved in folders created and labeled by the software. It then remains on hold until the next drop detection and can be stopped if new adjustments become necessary.

Despite being operational, some work is still underway to improve the automation of the experimental setup. For instance, a first task consists in modifying the Automated Data Acquisition System (ADAS) so that it allows to set the type and intensity of the electric field through the software interface. This was already partly accomplished and only awaits the purchase of a GPIB interface card enabling communication between the computer and the generator. Another task concerns the inclusion, into the ADAS, of an

[20] A stroboscopic technique was favored as, for a given exposure time, it allows to supply the LEDs with currents greater than nominals and therefore obtain more light intensity.

image treatment procedure handling the calculation of the undeformed drops radii R_1 and R_2, initial separation distance s_0 and angular offset θ on the fly. As originally planned, the idea was to benefit from the NI LabVIEW environment to directly implement the algorithm using pre-existing routines. Though, it might as well be performed externally through the adaptation of the software suite created, in the framework of the thesis (see chapter 2), to cope for the delayed availability of the NI IMAQ vision library at the laboratory (around mid 2011). Further decision should be based on accuracy comparisons between both solutions.

3.5 Conclusion

This third chapter aimed at pushing forward the estimation of efficiency in industrial dewatering devices by addressing the question of probability of electrocoalescence resulting from a shear flow induced collision of two water droplets. A well established formulation, based on the comparison between the time of close proximity and that required for the intervening oil film to thin down to its critical thickness, was retained. An axisymmetric model was therefore implemented, using the numerical scheme previously introduced in chapter 2, to investigate the influence of electrostatic forces on the drainage mechanism and to further identify the dominant parameters. Preliminary results pointed out large differences with predictions given by some classical theoretical lubrication models. An order of magnitude analysis confirmed the strong singularity of the present problem and led to an approximation for the drainage time stating proportionality with the continuous phase viscosity and inverse proportionality with the initial maximum electrostatic pressure. Using Davis (1964)' very accurate solution for the field enhancement at the facing poles of the droplets, the developed expression proved well able to reproduce behaviors deduced through simulation, providing the validity conditions (a large viscosity ratio and a very low interfacial deformation) were fulfilled. In light of those findings, an electrocoalescence efficiency criterion was proposed and discussed with respect to experimental results obtained, within the "Electrocoalescence II" project, on the resolution of water-in-crude emulsions. In combination with already existing functions determining collision frequencies, it was found to offer interesting new insights into the optimization of industrial devices. Finally, in order to improve its relevance, factors that may also significantly contribute to the film drainage mechanism were underlined. As a starting point, the design and assembly of an experimental setup allowing to study the complete electrocoalescence process between two calibrated charge free water drops injected in an oil shear flow was presented.

Chapter 4

Synchronized injection of two electrically neutral water drops in oil

4.1 Introduction

At this point, any reader familiar with drop formation or manipulation might be skeptical about the interest of dedicating a full chapter to the on-demand injection of two electrically neutral water drops in oil and would be right, in a way, as a few methods have already been reported in the literature. The first section aims at showing how, however, a comparison between their respective features and the requirements defined in the design of the "water drops electrocoalescence in an oil shear flow" experiment (detailed in section 3.4.2.2) highlighted a major compatibility issue. In order to address this matter, a new drop-on-demand technique able to inject a charge free conducting liquid drop into an insulating liquid, and relying on the application of a high electric field pulse, was developed thanks to the laboratory knowledge on electrohydrodynamics. The purpose of the second and third sections is to present such a technique and investigate the influence of the different parameters, both geometric and pulse related, on the diameter of the produced drop. Based on an analysis of the meniscus deformation dynamics, an improved pulse shape is proposed and tested. The new pulse is then used, in a configuration very close to that of the previously mentioned experiment, to simultaneously inject two electrically neutral water drops in polybutene oil. Finally, the applicability of the technique in other scientific or industrial domains is discussed.

4.2 Review of the available techniques

Since the first detailed study on the formation of droplets resulting from the manipulation of liquids (Savart, 1833, Plateau, 1863, Rayleigh, 1878)[1] during the nineteenth century, the field of drop generation has grown tremendously under the driving demand of both science and industry. Applications can now be found in various domains such as optics, drug delivery, analytical chemistry, biotechnologies, electronics manufacture and many others. Bulk drop dispense[2] technologies are divided in two groups depending on their operating mode, which are either continuous streaming (CS), also known as continuous jetting, or drop-on-demand (DoD)[3]. Both kinds of techniques have their own assets and liabilities, which are discussed hereafter regarding our application. Those relying on electric forces will be deliberately omitted, for now, as to the author's knowledge, none has ever been used to produce charge free drops. Any reader interested in becoming a seasoned practitioner in the field of microdrop generation is greatly advised to read the book of Lee (2003) and the review paper from Ben-Tzvi and Rone (2010) which were both used to compose the following sections.

4.2.1 Continuous streaming

In CS generators, a train of monodisperse drops is formed: i) in liquid-gas systems, by the destabilization of a liquid jet flowing out of a nozzle. This phenomenon was first characterized by Lord Rayleigh — and is consequently often referred to as the Rayleigh instability — who showed back in 1878, through a linear analysis, that all disturbances with wavelength longer than the circumference of the circular jet will grow and lead to its break-up. Such a destabilization is generally promoted by a mechanical or acoustical excitation in up-to-date devices (Lee, 2003). ii) in liquid-liquid systems, through the action of hydrodynamic shear forces exerted by a flowing continuous phase or carrier fluid on a "disperse phase".

Continuous streaming is the oldest of both drop generation techniques. First large-scale implementations of CS generators appeared in the 1950s in the inkjet printing industry. Their use in this field expanded until the 1970s and the introduction of DoD generators, by which they were progressively replaced. Following the industrial desire for continuous improvement of the ejection process, many scientific studies, both experimental and numerical, were conducted on the dynamics of liquid drop formation in a

[1] The fascinating early developments and findings of Savart and his contemporaries are very well told in French by Clanet (2000) and in English by Eggers (2006).

[2] As opposed to contact drop dispense.

[3] Some devices can actually function in both modes based on their setup (Meacham et al., 2005, Castrejon-Pita et al., 2008).

surrounding gas, first at high flow rates (jetting Bogy (1979)) and later at lower flow rates (dripping[4] Zhang and Basaran (1995)). A particular focus was put on the understanding of satellite drop formation (Mansour and Lundgren, 1990, Schulkes, 1994, Zhang and Basaran, 1995, Zhang, 1999), highly undesirable in printing applications since it results in irregular patterning. Producible drop sizes are predictable (Cooley et al., 2001) because closely tied to the diameter of the ejector aperture (about two times greater).

Continuous streaming of liquid in liquid applications emerged at the beginning of the 21st century, with the development of microfluidics, especially in biotechnologies and chemistry. In the segmented flow and digital microfluidics, the confinement of reactive materials, cells or small particles, in droplets in an immiscible carrier fluid helped overcoming contamination and evaporation problems respectively, arising with the downscaling of devices (Link et al., 2006). CS generation of drops is obtained by two types of shear-flow-driven techniques: T-Junction and flow focusing. In T-Junction generation, drops are created by the confluence of two liquid streams at a perpendicular channel intersection. As the disperse phase (i.e. the phase to be dispersed) enters the main channel, a droplet is formed and detached under the shearing effects of the carrier liquid flow. By adjusting the respective phase flow velocity, Nisisako et al. (2002) were able to vary the diameter of monodisperse water drops, injected in oil, over a wide range. Moreover, drops much smaller than the carrier fluid channel width and height can be produced, which makes these drop generation devices extremely competitive in terms of manufacturing complexity and price. In flow focusing geometry, the flowing disperse phase is forced into a narrow gap (of rectangular (Anna et al., 2003) or circular (Yobas et al., 2006) section) by two flanking carrier fluid streams. As observed experimentally by Yobas et al. (2006) and shown through numerical simulations by Suryo and Basaran (2006), three non-coexisting kinds of flow can develop, namely slug flow, dripping and tip-streaming, depending on the phase flow rate and viscosity ratios and on the capillary number. Flow focusing geometry generators are thus able to achieve a wide range of drop sizes (from tenths to tens of times the orifice diameter) and injection frequencies.

Despite being constantly challenged by DoD, continuous streaming remains widely used in applications where high throughput is required, e.g. emulsification (Yobas et al., 2006), as it can achieve production rates on the order of a few MHz, that is two order of magnitudes greater than the best drop-on-demand generators. However, when the injection of only a discrete number of drops is required, as in our experiment, DoD techniques are almost always preferred.

[4]Dripping is often illustrated by a drop falling from a leaking tap under its own weight.

4.2.2 Drop-on-Demand

In DoD generators, a single or a finite quantity of drop release is targeted. Either way, it results from the application of an external stimulus to a liquid meniscus, directly at its surface (e.g. EHD and focused ultrasound actuation (Amemiya et al., 1999)) or indirectly through bulk transmission (e.g. piezoelectric actuation)[5].

In some early inkjet printing applications (e.g. character printing), based on CS drop generation, it was necessary to prevent, controllably, some of the droplets from being deposited. This was most often accomplished by adding an electrostatic deflector to the printing system. In such devices, unwanted ejected drops are successively charged by the actuation of an electric field and deflected under the action of the Coulomb force, while flowing through two separated sets of electrodes. The deflection path, directly controlled by the drop induced charge and potential difference applied between the latter set of electrodes, generally leads to a receptacle where collected droplets are either discarded or recirculated back into the fluid reservoir (Le, 1998). CS printing systems were, at that time, complex, size consuming and expensive and the first Drop-on-Demand device was thus invented, by Zoltan (1972) and the Clevite corporation in 1972, in a attempt to overcome all the aforementioned drawbacks. It consisted of a piezoceramic element designed to fit around a capillary tube and squeeze it, when electrically excited, causing a volumetric change in the tube and forcing out a drop. Such a technique, known as the squeeze mode, constitutes, along with three others (each representing a different type of piezo deformation), i.e. the push-mode, the bend mode and the shear mode, the family of piezoelectric direct DoD generators. Due to its inherent way of applying pressure, piezoelectric actuation places very few constraints on the liquids that can be ejected (e.g. chemicals, fragile payloads such as living cells, DNA) and has consequently become the most popular DoD drop production technology. In addition to inkjet printing (Dong et al., 2006), applications of liquid-in-gas and liquid-in-liquid dispensing can be found in domains as diverse as inhalation drug therapy (de Heij et al., 2000), manufacturing of liquid crystal displays (Fan et al., 2008) and microfluidics (Xu and Attinger, 2008, Bransky et al., 2009). Moreover, the large tuning possibilities of the driving electric signal allowed both suppression of satellite droplets (Dong et al., 2006, Fan et al., 2008) and ejection of drops much (about two times) smaller than the generator orifice (Chen and Basaran, 2002). The latter was a major achievement as, during decades, the decrease in produced drop diameters was tied to that of the orifice from which they were issued, and many

[5]Some liberties have been taken, here, by the author. The definition is, indeed, a little more specific than that of Ben-Tzvi and Rone (2010) and thus does not include very particular processes such as evaporation instability and channel-geometry-driven drop generation.

problems arose, in the micron scale, due to clogging and breaching.

Other common technologies for production of electrically neutral drops rely on thermal, pneumatic, acoustic and mechanical/ultrasonic actuations. In thermal DoD generators, drop release emanates[6] from a pressure impulse produced by the formation and collapse of a gas bubble, near the ejection aperture nozzle, obtained by the vaporization of a small amount of fluid. Two types of thermal actuation can be further distinguished depending on the mechanism used to induce vaporization: thermal bubble and spark bubble, in which the local heating of the liquid is respectively performed by heating elements (Chen et al., 1997) and by the circulation of a current between two wire electrodes (Dadvand et al., 2009). As the process tends to disturb the chemical composition of the fluid to be ejected, applications have been, up to now, restricted to inkjet printers, notably developed by Hewlett Packard (Vaught et al., 1984) and Canon (Endo et al., 1979). Thermal bubble actuation represents the largest share of thermal DoD generators, despite being unable to eject drop smaller than the nozzle orifice. This advance feature was recently established in spark bubble actuation, by Dadvand et al. (2009) (by closely adjusting the orifice size and bubble ignition position, drop diameters of about one-fourth the orifice size were obtained) and is also present in up-to-date pneumatic DoD actuators (Amirzadeh Goghari and Chandra, 2008). In pneumatic actuation, drop emission is triggered by the application of a gas pulse to the liquid contained in a chamber, itself connected to a pressurized gas tank through a solenoid valve. The ejection process is directly controlled by the gas pressure and the opening and closing of the valve, which determine the pulse duration. Since free from moving parts, very robust pneumatic DoD generators can be manufactured, making them particularly ideal in applications where high temperatures are required, as for instance in material deposition (Cheng et al., 2005), to decrease the fluid viscosity. Acoustic actuation was developed as a cheap, reliable substitute to piezoelectric actuation, capable of both Drop-on-Demand and continuous streaming generation (see section 4.2.1). Castrejon-Pita et al. (2008) reported successful DoD drop ejection of liquid-in-gas and liquid-in-liquid, using a loudspeaker to apply pressure pulses and identified satellite free conditions (in the former configuration). Finally, sometimes called indirect DoD production, as drop formation is most often[7] caused by the cumulative action of vibrations (with frequency ranging from tens of kilohertz up to hundreds of megahertz) — as opposed to a single pulse — mechanical/ultrasonic actuation is one of the mainstays of MEMS technology (Cabal et al., 2005). In "mechanical" DoD generators, either a membrane containing the nozzle or

[6] The author sticks here with the classification proposed by Lee (2003) and considers thermally actuated bimetallic cantilever developed by Cabal et al. (2005) as one of the possible technique for the mechanic flextentional aperture plate actuation.

[7] Meacham et al. (2005) observed, at steady state, ejection of a new drop at each cycle corresponding to the frequency of the ac voltage signal driving the piezoelectric transducer.

a paddle (behaving like a cantilever) is vibrated at its resonant frequency, by the excitation of a contacting piezoelectric material (Percin et al., 1998) or by the exploitation of the difference in thermal expansion of two metals from which, in that case, it is constituted (Jarrold and Lebens, 2003, Cabal et al., 2005). Drop release occurs if, at some time during the actuation cycle, the pressure rise induced in the liquid, at the vicinity of the interface, overcomes inertia and surface tension restoring forces. The range of operable liquids is thus tightly constrained by their properties, especially as the resonant frequency and process efficiency decrease with the increase in the surrounding liquid viscosity. In "ultrasonic" DoD generators, sound waves are generated by the vibration of piezoelectric elements and can either be geometrically focused at the liquid/gas interface (Elrod et al., 1989, Meacham et al., 2005) to eject drops in a similar fashion as "mechanical" generators or be used to weaken the cohesive force among liquid molecules, enabling flow in a capillary and subsequent dripping of a large drop (Tan et al., 2008). As based on the same physical mechanism, "ultrasonic" actuators also suffer from the previously mentioned limitations.

Some interesting features of the presented DoD techniques regarding our requirements, extracted from experimental studies, are summarized chronologically in Table 4.1. The first conclusion drawn was that of all techniques, only those based on direct pressure pulse, i.e. piezoelectric, pneumatic and acoustic actuations, had proven able to either eject viscous liquid drops in gas or inject liquid drops in another liquid (with at least one of the phase viscosity above 10 $mPa.s$). Moreover, the three above can "or at least might" (pneumatic and acoustic actuation are still in their infancy), produce droplets smaller than the generator nozzle diameter, which is convenient and can become compulsory when working in the micron scale. However, none of them seemed capable of achieving the desired drop diameter range, i.e. one order of magnitude or more, without repeatedly changing the nozzle size. So far, the combination of all these features had only been demonstrated in electrohydrodynamically actuated microfluidic DoD generators. For example, Link et al. (2006) applied external electric fields[8] of different intensity to assist, in a flow focusing device, the shear driven injection of charged water drops in oil. Diameter ranging approximately between 15 μm and 100 μm were achieved from an elongated meniscus, passing through a 30 μm orifice. Even more interesting is the work from He et al. (2005) in which a wide range of charged water drops were release (see Table 4.1), though with chaotic trajectories[9], in silicone oil, by using electrostatic pulses alone. Furthermore, the authors observed, in certain cases, formation of drops at a finite time

[8] Malloggi et al. (2007) introduced, in a analogous configuration, electrowetting as an alternative drop aided detachment technique but did not, unfortunately, discuss obtainable drop sizes.

[9] Probably due to the poor accuracy of their manufactured non-axisymmetric geometry and to the influence of a mist of very fine charged drops atomized from an expanding conical interface, prior to the main drop injection (also encountered in Atten et al. (2008a)).

Table 4.1: *Characteristic features of drop-on-demand techniques found in Bransky et al. (2009), Dadvand et al. (2009), Castrejon-Pita et al. (2008), Amirzadeh Goghari and Chandra (2008), Xu and Attinger (2008), Fan et al. (2008), Dong et al. (2006), Meacham et al. (2005), Cheng et al. (2005), He et al. (2005), Chen and Basaran (2002), Ulmke et al. (2001), de Heij et al. (2000), Percin et al. (1998) and Chen et al. (1997).*

Actuation Mechanism	**Application**	**Interface type**	**IFT** ($N.m^{-1}$)	**Drop** D_d **diameter** (μm)	**Orifice** D_{Cap}	**Production rate** (kHz)
Piezoelectric, push	Microfluidic	DI Water/Oleic Acid	-	80-280	80	-
Thermal, spark	Inkjet printing	Water/Air	72	$\approx$ 0.25 D_{Cap}	-	-
Acoustic	Inkjet printing	Water-glycerol/Air[a]	63-72	2600-2900, 1800	2200, 1000	-
Pneumatic	-	Water-glycerin/Air	65	147	204	$0.5\,10^{-3}$
Piezoelectric, bend	Microfluidic	Water/Hexadecane	52.5	42.5-83	50	0.0062-2.5
Piezoelectric, bend	Material deposition	Liquid Crystals/Air[b]	-	535-675	300	0.05
Piezoelectric, push	Inkjet printing	Water, GW and, GWI/Air[c]	73, 68, 35	46.5-51, 43, 39.5	53	0.02
Ultrasonic	-	Water/Air	72.7	7.2	5.93	952
Pneumatic	Material deposition	Tin/Air	-	600	254	$2.5\,10^{-4}$
Electric Field pulse[d]	Microfluidic	Water/Silicone oil	-	3-25[d]	20x20	-
Piezoelectric, squeeze	Inkjet printing	GW/Air	65	16[e]	35	-
Piezoelectric, -	Biotechnologies	Double-distilled W/Air	72	$0.5 < D_d/D_{Cap} < 1.35$	60	-
Piezoelectric, bend	Medicine, IDT[f]	Liquid/Air	-	4.5, 65	5, 70	250-300[f], 45
Mechanic	Material deposition	Water/Air	72.7	49.2	60	-
Thermal, bubble	Inkjet printing	Water based ink/Air	-	26.2-32.2	25	1

[a] A photographic sequence of a water-glycerol drop injection in paraffin oil is also briefly presented to illustrate possible focus for further works. Despite missing parameter data, it is noticeable that the drop diameter is again larger than the nozzle orifice.

[b] Liquid crystals do not behave as a Newtonian fluid but are interesting for having a viscosity close to that of the Grade L-6 Indopol polybutene oil.

[c] GW and GWI stands respectively for Glycerin-Water and Glycerin-Water-Isopropanol. Glycerin was added to increase the dynamical viscosity from 1 to 5 $mPa.s^{-1}$ while Isopropanol was used to dramatically decrease the interfacial tension coefficient.

[d] The paper is included here as, in the author's opinion, a few electrically neutral drops might have unexpectedly been obtained among all the produced drops. Diameter of these drops is however unknown and stands somewhere in the overall reported range.

[e] The study references eight additional papers on DOD production, dating back to the nineties, where drops have a diameter of the same order as the nozzle orifice.

[f] IDT are initials for Inhalation Drug Therapy. At such high frequencies (250-300 kHz), deviations on the drop diameter can exceed 100%.

(on the order of a few hundreds microseconds) after the voltage was switched off. Without much information on the aqueous phase conductivity and thus on the time needed by the charges to relax, electroneutrality of their injected drops could hardly be concluded. Yet, neither could it certainly be excluded and it had seemed worthy to start looking into this direction.

4.3 Electric field pulse based injection

The choice of using electrostatic forces to inject charge free drops of a conducting liquid into a dielectric fluid might be surprising and confusing at first but, as mentioned by Wright et al. (1993), they have the remarkable asset of being inherently surface forces — thus allowing far more control on the drive of the interface deformation compared to traditional pressure pulses — and of being able to directly oppose surface tension. Moreover, they scale in somewhat the same way as capillary forces[10], increasing as objects shrink and become sharply curved. Another main reason is the long-lasting experience accumulated in the electrostatic manipulation of liquids. Indeed, the ability of electric forces to draw liquid from surfaces has been known since the pioneering work of Zeleny (1915, 1917) on the determination of the conditions leading to the instability of electrified liquid meniscus. Long after his experimental observations and the reference theoretical work of Taylor (1964), an extensive activity was devoted to the characterization of the various spraying modes (Cloupeau and Prunet-Foch, 1990, Jaworek and Krupa, 1999b,a) and sprayable liquids (Grace and Marijnissen, 1994). Most of the efforts were spent on the understanding of the cone-jet mode (Hayati et al., 1986, Gañán-Calvo et al., 1997, Collins et al., 2008), the most commonly used mode of EHD liquid atomization in industrial applications such as, for example, spray coating (Hines, 1966) or crop spraying (Inculet, 1985) and on the identification of the parameters leading to continuous generation of discrete charged drops. Still, with the development of DoD applications, researchers started investigating addition of direct electrostatic pulse to traditional pressure pulse to gain some additional control on the drop emission process. In this context, Wright et al. (1995) first reported the electric field pulse based ejection of a charged ethanol drop in air, in 1995, establishing the basis for the present study.

[10]The assertion is, however, only valid from a qualitative viewpoint as both forces have different radius exponent dependency (see section 1.5.1.2).

4.3.1 Principle

As schematized on Figure 4.1, the developed on-demand EHD injection technique consists in the application of an electric field pulse to a meniscus of a conductive liquid immersed into a dielectric one. Due to the action of the induced electrostatic pressure, the water-oil interface, initially in equilibrium under the effects of gravity and capillary pressure, deforms and eventually becomes unstable, leading to the release of one or more drops.

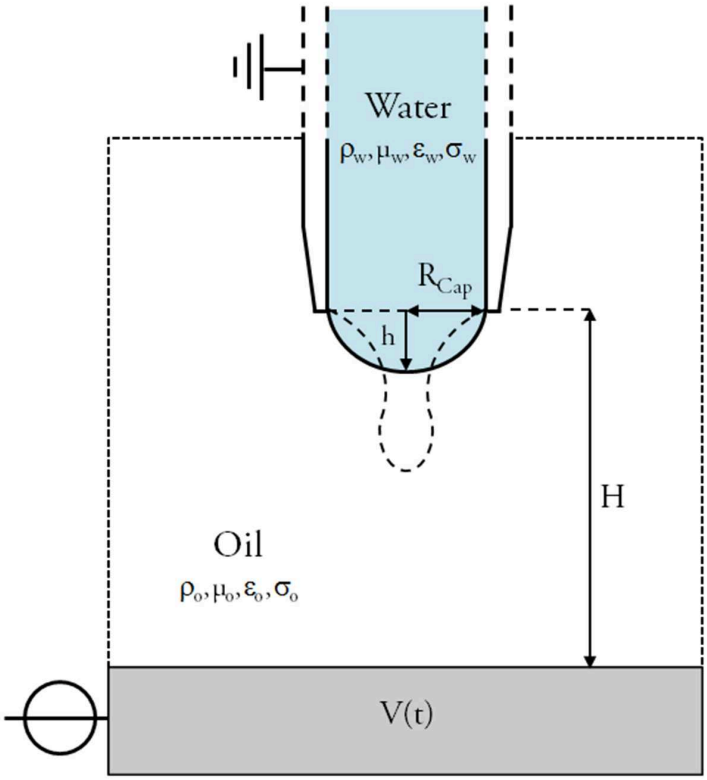

Figure 4.1: *Electric field pulse based injection of a charge free water drop in oil from a meniscus. Geometry, in the meridian plane, and associated parameters.*

However, unlike conventional referenced studies, tight constraints are here placed on the process. Indeed, in order to achieve the charge free condition, the electric pulse has to be finished before the last stage of the meniscus elongation, i.e. the appearance of a liquid filament between the drop and the meniscus and its break-up. A thorough knowledge of the different physical mechanisms involved in the injection process and of their relative influence is thus essential to set the key parameters which were identified by Atten et al. (2008a) as the relative meniscus height h/R_{Cap} and the duration, lead/trail times and amplitude defining the pulse. As seen on Figure 4.1, other involved parameters include the electrodes distance H and the fluids respective densities, viscosities, conductivities and permittivities.

4.3.2 Process calibration

4.3.2.1 Amplitude

Again following the pioneering work of Zeleny (1915), several papers including Joffre et al. (1982), Harris and Basaran (1993), Wright et al. (1993) have dealt with the static equilibrium of a conductive liquid meniscus influenced by an electric field. In their work, the authors related the instability, leading to the release of a drop, to an imbalance between the capillary, hydrostatic and electrostatic pressures, denoted p_{Cap}, p_0 and p_E respectively, acting at the meniscus surface. By further neglecting the gravitational effects ($Bo = (\rho_w - \rho_o)gR_{Cap}^2/\gamma$ being smaller than 0.005) and considering a hemispherical shape for the water-oil interface, the above condition becomes:

$$p_E > p_{Cap} \Rightarrow \frac{1}{2}\epsilon_r\epsilon_0 E^2 > \frac{2\gamma}{R_{Cap}}. \tag{4.1}$$

Instability is therefore most likely to occur in the highest electric field region which is located at the axial tip of the water meniscus, in the configuration described in Figure 4.1. An approximation of its intensity E_{Max}, calculated for a hyperboloidal surface having the same radius of curvature, is (Coelho and Debeau, 1971):

$$E_{Max} = \frac{2V}{R_{Cap}\ln\left(\frac{4H}{R_{Cap}}\right)}. \tag{4.2}$$

The threshold applied potential difference leading to the quasistatic injection of a charged drop, V_{low}, can thus be estimated by substituting equation 4.2 in 4.1, giving:

$$V_{low} = \sqrt{\frac{\gamma R_{Cap}}{\epsilon_r\epsilon_0}}\ln\left(\frac{4H}{R_{Cap}}\right). \tag{4.3}$$

With the particular dimensions (see section 4.3.4) and liquids properties (Table 2.2) retained for all the experiments, one obtains $V_{low} = 2785\ V$. However, readers should bear in mind that the developed technique is purely dynamic and consequently differs from the afore static condition which only gives a rough order of magnitude. As seen in the previous section, the electric field pulse based injection of a charge free drop requires the supply of a large amount of energy in a very limited time to the water meniscus. Applied potential differences V higher than V_{low} might thus be necessary depending on the pulse duration Δt.

4.3.2.2 Duration

The determination of a pulse duration range is even less straightforward as most of the studies addressing the dynamics of DoD generation dealt with liquid/gas interfaces. Influence of the surrounding fluid was consequently neglected in the determination of the governing dimensionless groups[11] which are, depending on the applications, either the capillary Ca (Zhang and Basaran, 1995) or the Weber We (Eggers, 1997) number and the Ohnesorge[12] number Oh. The latter, comparing the relative influence of the viscous force over the inertial and capillary forces, is defined as:

$$Oh = \frac{\mu}{\sqrt{\rho L \gamma}} \tag{4.4}$$

where, μ, ρ and L are the dynamic viscosity and density of the liquid and the characteristic length, respectively. Moreover, the Ohnesorge number can also be viewed as the ratio of the capillary time t_{Cap} and the viscous time t_μ which can be used to estimate (Chen and Basaran, 2002) the required duration of the process that drives the injection, i.e. the effective electric field pulse width t_E, over which the fluid momentum is changed. In order to account for the influence of the surrounding fluid and similarly to Stone et al. (1986) in their work on the transient deformation of viscous drops, Oh was calculated here with the sum of viscosities $\mu_o(1+\lambda)$ where λ is the viscosity ratio μ_w/μ_o. It is noteworthy that when the outer fluid viscosity is large compared to that of the inner fluid, Oh becomes close to the Morton number[13]. In the present conditions, taking $L = R_{Cap}$ leads to $Oh \sim 0.16$ implying that neither inertial and capillary nor viscous effects are predominant. A rough estimate of the maximum value of t_E lies, thus, within the range defined by:

$$\left[t_{Cap} = \sqrt{\frac{\rho_w R_{Cap}^3}{\gamma}}, t_\mu = \frac{\rho_w R_{Cap}^2}{\mu_o \left(1+\lambda\right)} \right] \Rightarrow \; 0.785 \; ms < t_E < 4.76 \; ms \tag{4.5}$$

Another relevant time scale is given by the charge relaxation time, $\tau_E = \epsilon_w/\sigma_w$, which represents the time needed by the charges to relax inside the water phase. Indeed, for the electroneutrality requirement to be fulfilled, the break-up of the water filament forming between the drop and the meniscus should appear with a delay t_D, at least, one order of

[11] A fair description on how those are obtained from the Navier-Stokes equations of mass conservation and of linear momentum is available in Dreyer (2007).

[12] The Ohnesorge number is named after W. von Ohnesorge. It was first introduced in Ohnesorge (1936) and progressively replaced the Reynolds number Re in the description of free surface flows issuing from capillaries as it conveniently depends on geometry and fluid properties alone.

[13] The Morton number can be seen as a Ohnesorge number (Dreyer, 2007) computed with the capillary length $L_C = \sqrt{\gamma/\rho g}$ and is widely used in two-phase flows to characterize the shape of bubbles or drops moving in a surrounding fluid or a continuous phase.

magnitude greater than τ_E after the end of the pulse (particularly, as the relation does not consider the increase in resistance occurring in the water bridge during the necking and therefore underestimates the actual charge relaxation time). In our study, t_D is negligibly small ($\approx 0.15\ \mu s$) due to the high conductivity of tap water. However, in the presence of less conductive liquids, the dielectric relaxation time would be of primary importance (e.g. with typical deionized water of conductivity 0.1 $\mu S.cm^{-1}$, the charge relaxation time increases up to about one hundred microseconds).

4.3.3 Multi-stage pulses

As briefly presented in section 4.2.2, under certain circumstances, drops generated through the application of an electric field pulse to a conductive liquid meniscus into a surrounding dielectric liquid most often have non-axial and non-reproducible trajectories. This phenomenon, highly influencing reproducibility, was first reported by He et al. (2005) and also observed, later, by Atten et al. (2008a), in preliminary experiments on the injection of an electrically neutral water drop in oil[14]. An explanation for its occurrence was found by further investigating the dynamics of the drop formation process, both experimentally and through simulations. Again, computations were performed with COMSOL MULTIPHYSICS^{TM}, using the mathematical scheme and boundary conditions described in chapter 2. Both approaches agreed well (see Figure 4.2) and proved that, when improperly scaled, square electric pulses (of lead and trail times $t_L = t_T = 10\ \mu s$) tend to severely distort the water-oil interface and cause spraying of fine charged water droplets that perturb but not necessarily prevent the following main drop injection. Two modes of combined transient EHD spraying (Jaworek and Krupa, 1999a) and drop injection were identified, depending mainly on the applied voltage: above an upper threshold, inertial effects are so important that the meniscus takes a blunt-tipped shape (firstly referred to by Wright et al. (1995) in methanol drop injection in air), due to a faster shrinking of the sides compared to the tip displacement. Highest curvatures, located away from the axis of symmetry, are then amplified by local electric field reinforcements (Figure 4.2a), until destabilization of the interface and atomization of charged droplets in a multi-jet mode (Figure 4.2c). As voltage is decreased, the blunt-tipped shape progressively disappears with the weakening of inertial effects, and below a lower threshold, a cone forms at the extremity of the elongated meniscus (Figure 4.2b) and emits charged droplets, in a micro-dripping mode (Figure 4.2d). Numerical simulations and experiments additionally showed that these two modes, respectively generating relatively large and small drops only, bound and thus strongly limit the range of operable parameters. Outside this range,

[14] Those were actually conducted in a configuration identical to that described in Figure 4.1.

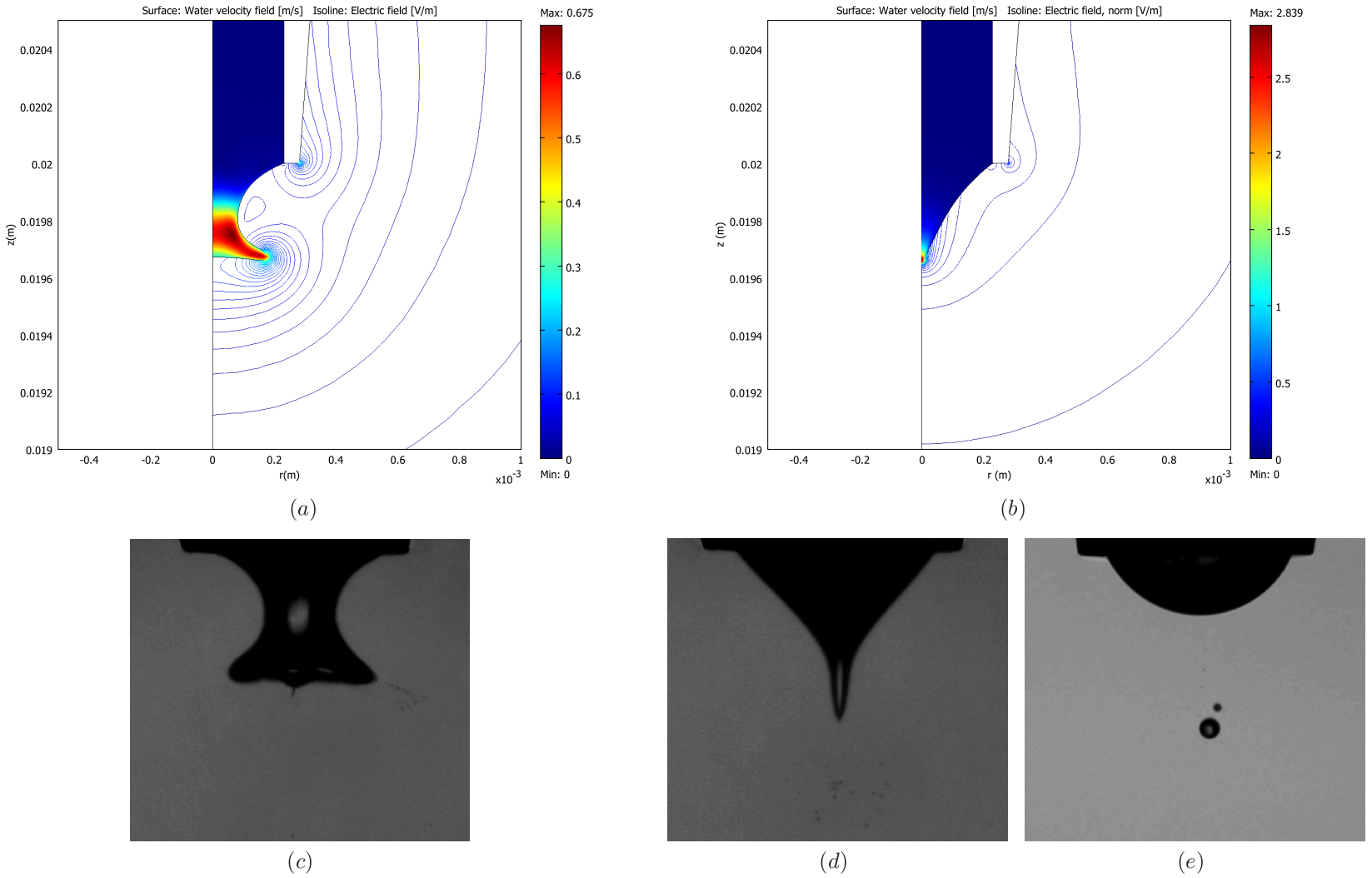

Figure 4.2: *Numerical simulations and experiments illustrating the formation of multi-jet (a,c) and micro-dripping spraying modes (b,d,e) from meniscus subjected to improperly scaled square electric pulses. Last converged computed water velocity field and electric field isoline densities in (a) and (b) both suggest impending interfacial instabilities. Experimental photographs (d,e) confirm that the main injected drop can experience a non axial trajectory, despite being released after the end of the pulse. Simulation and experiment parameters: (a) Computed time is* 864 μs, $\gamma = 0.025\ N.m^{-1}$, $h/R_{Cap} = 0.75$, $\Delta t = 1\ ms$, $t_L = t_T = 0.01\ ms$, $V = 3.00\ kV$; *(b) Computed time is* 1050 μs, $\gamma = 0.022\ N.m^{-1}$, $h/R_{Cap} = 0.65$, $\Delta t = 1.5\ ms$, $t_L = t_T = 0.01\ ms$, $V = 2.20\ kV$; *(c) Frame acquisition time is* 750 μs, $\gamma = 0.022\ N.m^{-1}$, $h/R_{Cap} = 0.78$, $\Delta t = 0.8\ ms$, $t_L = t_T = 0.1\ ms$, $V = 4.2\ kV$; *(d) Frame acquisition time is* 1700 μs, $\gamma = 0.022\ N.m^{-1}$, $h/R_{Cap} = 0.59$, $\Delta t = 1.5\ ms$, $t_L = t_T = 0.1\ ms$, $V = 2.85\ kV$; *(e) Main injected drop diameter* $D_d = 25.7\ \mu m$.

shifts in the trajectory of the main injected drop were found to increase with the applied voltage, independently of the spraying mode.

The low efficiency of square pulses, in producing a wide variety of drop diameters, lies in their poor degrees of freedom. In order to address this matter, a new type of pulse was developed, based on the work from Wright et al. (1995). In their paper, the authors proposed an improved pulse shape which, despite necessarily releasing charged drops, offers a few interesting assets corresponding roughly to its each distinct part: first, the rising edge and plateau of a trapezoidal pulse provide a fast and controlled deformation of the meniscus mandatory to avoid the aforementioned cone formation. Then, the voltage intensity decrease during the trailing edge prevents the multi-jet spraying and lets interfacial tension bring back the maximum elongation at the axis. Finally, a DC offset is applied so that electric forces overcome interfacial tension forces and detach a drop. From there and according to numerical simulations[15] (Figure 4.4), the inertia-based injection of an electrically neutral drop should be achieved by replacing the last part by a second short trapezoidal pulse, to obtain what will now be referred to as a Multi-Stage Pulse (MSP). As seen on Figure 4.3 five to seven durations and two to three amplitudes are

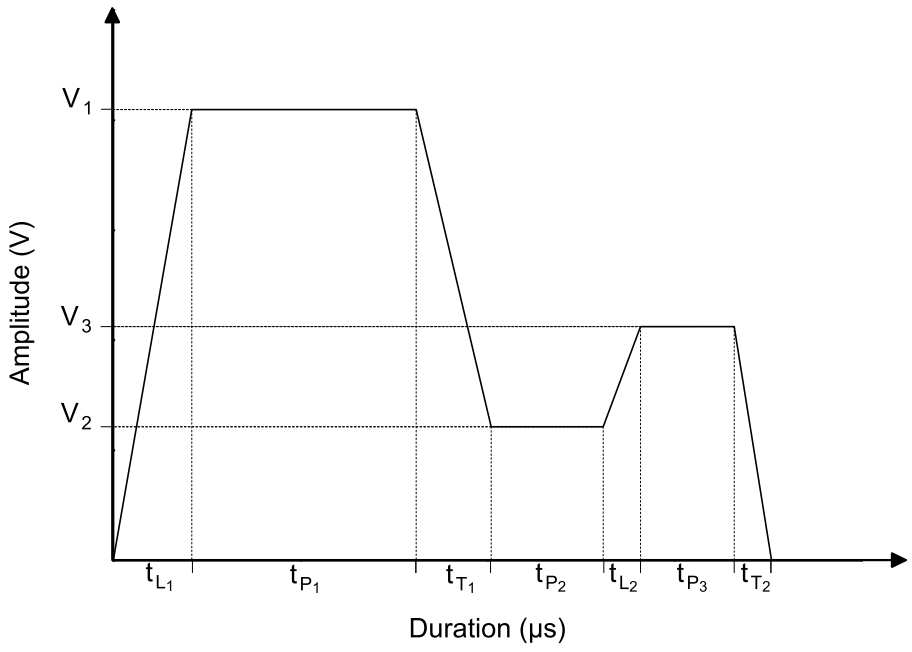

Figure 4.3: *Multi-Stage pulses.*

involved in the definition of MSPs, allowing tremendous new tuning possibilities.

[15] A sequence representing a full simulated injection will be presented and compared to experiments in section 4.4.2 to discuss the model accuracy.

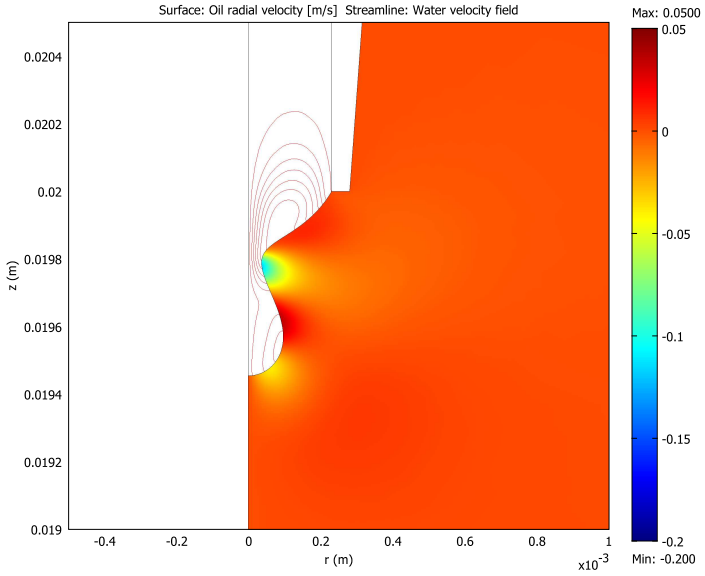

2100 μs

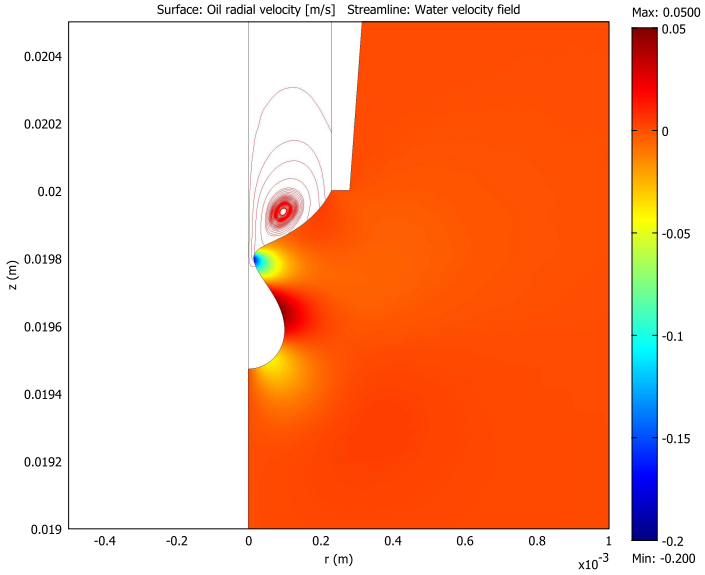

2270 μs

Figure 4.4: *Last stages of a MSP-based water drop injection in polybutene oil. Simulation parameters:* $h/R_{Cap} = 0.85$, $\gamma = 0.02\ N.m^{-1}$, $\Delta t = 1760\ \mu s$, $t_{L_1} = 210\ \mu s$, $t_{P_1} = 600\ \mu s$, $t_{T_1} = 200\ \mu s$, $t_{P_2} = 300\ \mu s$, $t_{L_2} = 100\ \mu s$, $t_{P_3} = 250\ \mu s$, $t_{T_2} = 100\ \mu s$, $V_1 = 2.9\ kV$, $V_2 = 0.429\ kV$, $V_3 = 1.504\ kV$. *From top to bottom, images show a strong increase in oil radial velocity in the necking region (reaching typical values an order of magnitude greater than in the surrounding bulk) and indicate an imminent interface break-up, more than* 500 μs *after the end of the pulse ensuring electroneutrality of the produced drop. Water velocity field at* 2270 μs *suggests that the volume contained in the lower part of the meniscus should remain approximately constant, during the final moments of bridge thinning, since water flows only back into the upper part. A fair estimation of the produced drop volume can therefore be calculated from the last converged simulation time step. Here* $D_d \approx 222\ \mu m$.

4.3.4 Experimental setup

Injection experiments were performed in a cell (#4) manufactured mainly out of PMMA to allow visualization in two perpendicular horizontal directions (Figure 4.5) and in compliance with the technical choices, explained in section 3.4.2.2. A water meniscus was anchored on the inner radius[16] $R_{Cap} = 231\ \mu m$ of a grounded metallic needle, hanging at a distance $H = 2\ cm$ above a high-voltage electrode and immersed in polybutene oil. In the absence of an oil flow, injected drops are here collected in a small hole drilled at the top of the lower electrode and periodically disposed of. Apart from that, all other features, including, for instance, the water and electric pulses supply systems corresponded exactly to those already described in chapter 3.

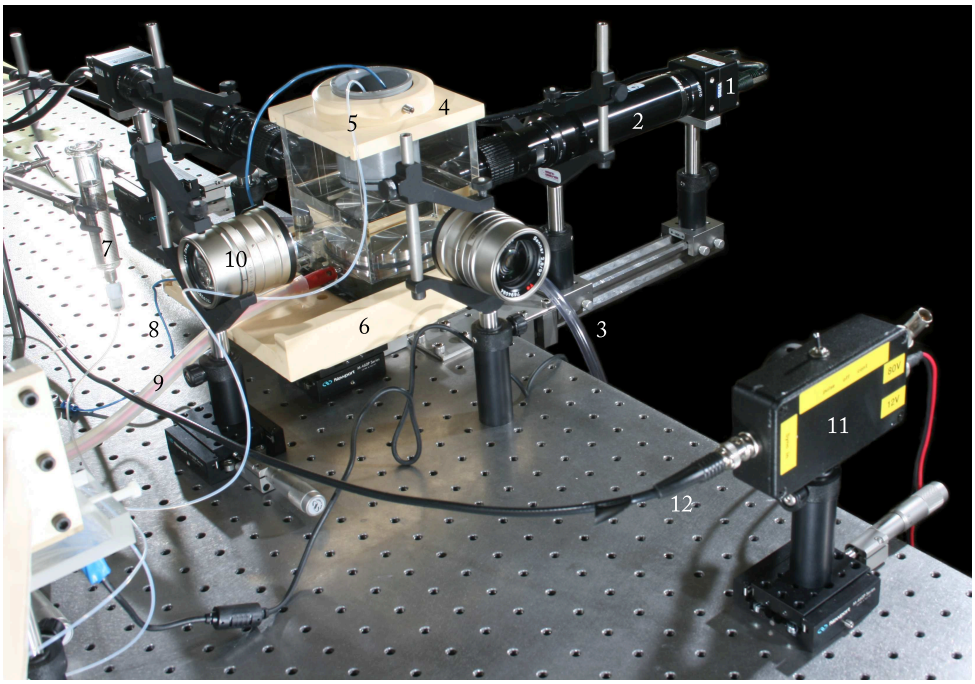

Figure 4.5: *EHD drop injection experimental setup. From back to front: 1, Falcon 1.4M100 camera - 2, Optical zoom - 3, Drain - 4, Cell - 5, PTFE capillary - 6, XY translating support - 7,* 100 *ml water reservoir - 8, Ground - 9, HV cable - 10, Light focusing lens - 11, Flashable green LED light source - 12, PC connection.*

Since the duration of the whole injection process is much shorter than the minimum interframe time (10 *ms* at full resolution) of the Falcon 1.4M100 camera and thus could not be recorded, a hybrid setup was assembled to acquire the minimum amount of information necessary to characterize the technique. These are the initial meniscus size, defined by h, and the injected drop diameter D_d, trajectory and electroneutrality. The setup contained the two Falcon cameras (#1) and LED light sources (#11) functioning as focused back illuminators. A first couple operated in real-time display (mandatory while

[16] According to reproducibility tests, inner anchorage offers much more stability and thus better results than outer anchorage.

setting the initial water meniscus height to the desired value) and was used to capture two photographs (before the pulse and after the injection, once the drop has reached terminal velocity) from which h, the drop diameter D_d and trajectory were deduced. A "stroboscopic" method was retained for the second couple, as in Dong et al. (2006). The frame acquisition of the camera was synchronized with a light flash of controllable duration and triggered (#12) at any time during the injection, allowing tremendous possibilities: on the one hand, electroneutrality of the released drop could easily be verified by looking at the meniscus shape at a preset instant (based on the charge relaxation time τ_E) after the end of the electric pulse. On the other hand, dynamics of the injection could be investigated, providing the phenomenon is reproducible, by varying the trigger delay in repeated experiments. Accuracy of the signals (delays, durations) was checked using a 4 channel oscilloscope (Tektronix - DPO4104). Photographs were post treated using the software suite detailed in chapter 2. Light flash duration was set to 30 μs and resulted from a compromise between minimizing the motion-blurred region and keeping a sufficient contrast on the frames. Both trapezoidal pulses, which can be viewed as a generalization of previously experimented square pulses (Atten et al., 2008a), and MSPs were used. For the latter, in order to keep a moderate number of parameters in the study, times were fixed using numerical simulation results and correspond to those given in Figure 4.4, while amplitude ratios were varied. Moreover, for MSPs, the voltage set in the arbitrary wave generator was applied to the highest plateau, the other parts being automatically scaled. It should finally be noted that injections in which atomization of charged droplets was detected prior to the main drop release, were not reported in the results presented in the upcoming section.

4.4 Results on single drop injection

4.4.1 Trapezoidal electric pulses

Experiments using trapezoidal pulses were conducted with two different relative meniscus heights $h/R_{Cap} = 0.52$ and 0.75 and the following pulse durations, lead and trail times ($\Delta t = 0.8, 1, 1.2$ and 1.5 ms; $t_{L/T} = 0.01, 0.05, 0.1, 0.2$ and 0.3 ms). Along with the influence of the main parameters on the injected droplet diameter D_d, the reproducibility and dynamics of the phenomenon were also investigated. Examples of the transient electrically driven deformation of the water-oil interface are shown on Figures 4.6 and 4.7 for both relative meniscus heights with a temporal resolution of two hundred microseconds. In both cases, the meniscus splitting occurred a few hundred microseconds after the

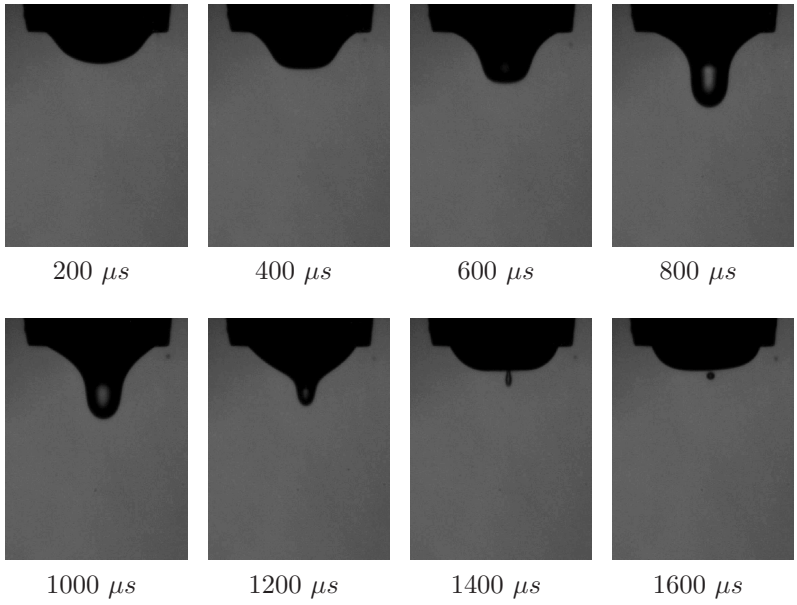

Figure 4.6: *Photographs of water drop injections in polybutene oil using a trapezoidal electric pulse ($\Delta t = 0.8\ ms, t_L = t_T = 0.1\ ms$ and $V = 3.70\ kV$) with $h/R_{Cap} = 0.54$ and $\gamma = 0.022\ N.m^{-1}$. Mean injected drop diameter is about 36 μm.*

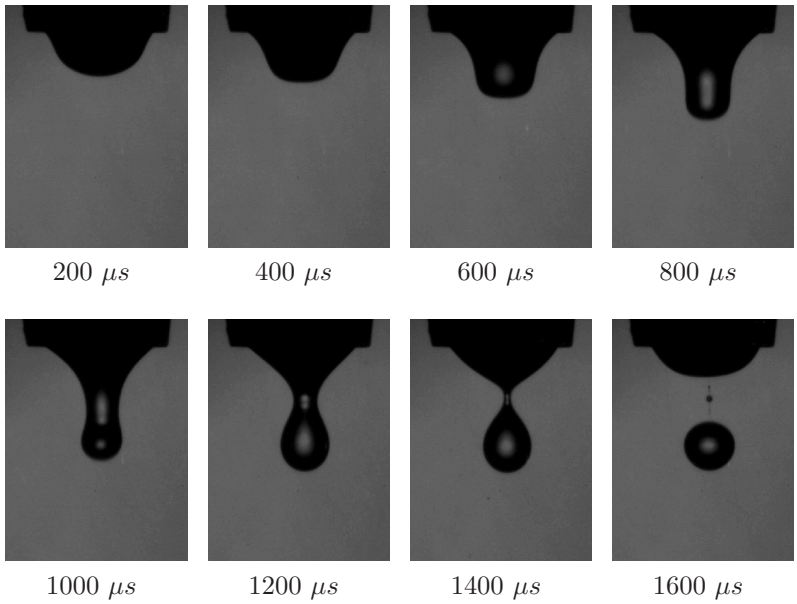

Figure 4.7: *Photographs of water drop injections in polybutene oil using a trapezoidal electric pulse ($\Delta t = 1\ ms, t_L = t_T = 0.05\ ms$ and $V = 3.38\ kV$) with $h/R_{Cap} = 0.75$ and $\gamma = 0.024\ N.m^{-1}$. Mean injected drop diameter is about 215 μm.*

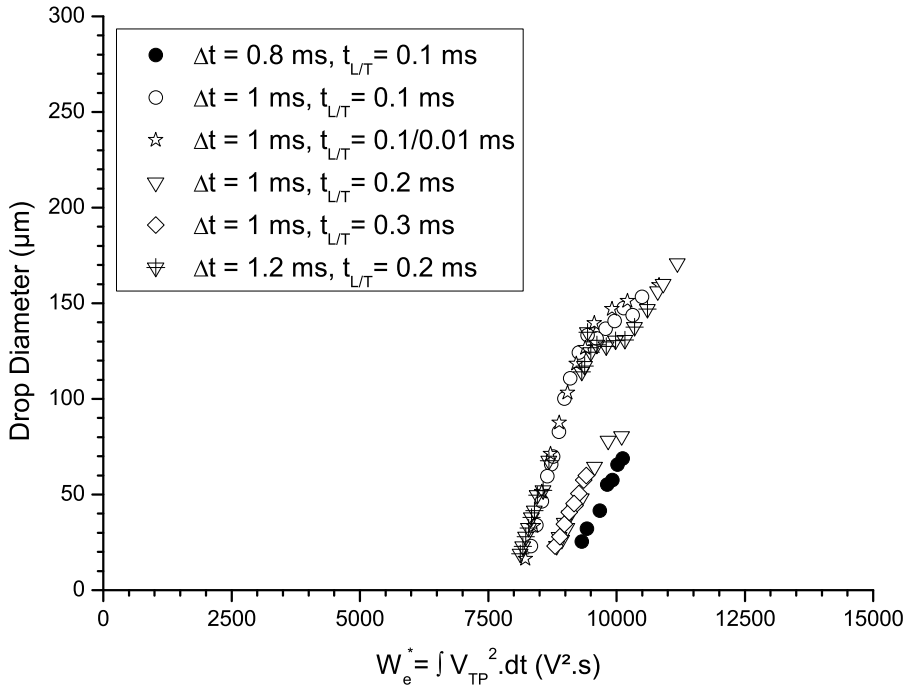

Figure 4.8: *Variations of the injected drop diameter as a function of* W_e^*. *Average relative meniscus height* $h/R_{Cap} = 0.52 \pm 0.02$ *and IFT coefficient* $\gamma = 0.023 \pm 0.02$ $N.m^{-1}$. *All drops generated using a pulse duration of* $\Delta t = 1.5$ ms *were either identified as charged or accompanied by atomized charged droplets.*

end of the pulse (between frames 7 and 8), leaving enough time for the charges to relax and ensuring the electroneutrality of the drop. Trajectory of the main drop was axial. Small satellites, resulting from the break-up of the water ligament, were observed, most frequently after injections of relatively large drops (Figure 4.7). These two sequences of photographs perfectly illustrate the results obtained with trapezoidal electric pulses and presented on Figures 4.8 and 4.9 in the form of the injected drop diameter as a function of:

$$W_e^* = \int V\,(t)^2 \cdot dt \tag{4.6}$$

where $V(t)$ is the temporal shape of the applied voltage pulse. Expression (4.6) represents the lead term of the work of the electrostatic forces acting on a non-deformable meniscus and was first introduced by Atten et al. (2008a) to compare water drop injections using square voltage pulses of different durations and amplitudes. Two modes of injection were identified through both the discontinuity in the produced drop diameters and the change in slopes. The gap between the two ranges became even clearer as the relative height and thus the volume of the meniscus was increased. Interestingly, He et al. (2005) also noticed a bimodal drop size distribution in a close configuration. However, a few uncertainties in their article rendered quite difficult further comparisons: i) first of all and most importantly, it is unclear whether the authors were aiming toward charged or electrically neutral

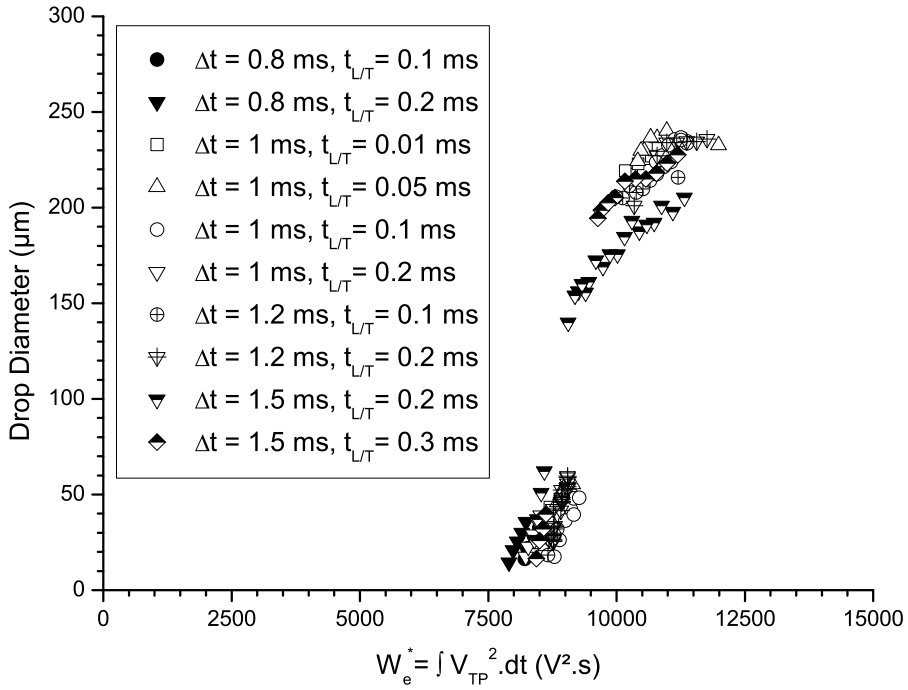

Figure 4.9: *Variations of the injected drop diameter as a function of* W_e^*. *Average relative meniscus height* $h/R_{Cap} = 0.76 \pm 0.02$ *and* $\gamma = 0.023 \pm 0.02\ N.m^{-1}$.

drop injections even though, as said in section 4.2.2, they might had obtained both; ii) Secondly, they did not report any discontinuity in the produced drop diameters which is striking, especially when dealing with different injection modes. Though, it might be due to a plotting artifact; iii) Finally, they suggested that the range of small drops (where typical diameters are approximately two times smaller than in the larger one) was constituted by satellites which is conflicting with our experiments, where the primary drop is always at least one order of magnitude in diameter greater than the eventual satellites (see e.g. Figure 4.7). In the absence of additional data, finding an explanation for this difference seemed very intricate and was thus considered out of the thesis scope. Figures 4.8 and 4.9 also show an important result that validates the conclusions drawn after the dynamical analysis performed to understand the trajectory issue encountered by Atten et al. (2008a) and presented in section 4.3.3. Indeed, "square" pulses, i.e. with very small lead/trail times (primarily lead times of $0.01 - 0.05\ ms$) completely failed at injecting electrically neutral drop for relative meniscus heights averaging around $h/R_{Cap} = 0.52$. Furthermore, even at higher h/R_{Cap} (averaging around 0.76), extremely short drop diameter ranges were produced, confirming their poor efficiency and limited range of operable parameters. On the opposite, pulses with longer lead/trail times were able to generate wider drop size distributions in a fairly accurate way, as evidenced by reproducibility tests presented in Table 4.2. The slope of the curves, steep in the small drop diameter range and flatter in the larger one, explains (along with the difference in spatial resolution) the higher repro-

Table 4.2: *Injection reproducibility of three different trapezoidal pulses. Mean diameters and standard deviations are average of sixteen values*

Meniscus and pulse parameters (ms, kV)	**Mean drop diameter** (μm)	**Standard deviation** (%)
$h/R_{Cap} = 0.53,\ \Delta t = 0.8,\ t_{L/T} = 0.1,\ V = 3.70$	36.0	6.45
$h/R_{Cap} = 0.75,\ \Delta t = 1,\ t_{L/T} = 0.05,\ V = 3.38$	215.3	2.56
$h/R_{Cap} = 0.75,\ \Delta t = 1.2,\ t_{L/T} = 0.2,\ V = 3.17$	48.1	5.22

ducibility achieved in the latter (standard deviation of 2.55% in Figure 4.7 versus 6.45% in Figure 4.6). Greater initial meniscus heights offered wider ranges of achievable drop diameters (the ratio of the largest produced drop volume V_d over the meniscus volume V_{Men} is 0.4 for $h/R_{Cap} = 0.75$ compared to 0.22 for $h/R_{Cap} = 0.52$) and gave optimum results when combined with pulse parameters lying in the middle of the operable range. Still, the technique's inability to release medium sized drops, between 80 μm and 140 μm, remained a major drawback.

4.4.2 Multi-stage electric pulses

For comparison purposes and in light of the former findings, experiments using Multi-stage pulses were conducted with three different relative meniscus heights $h/R_{Cap} = 0.52,\ 0.75$ and 0.86. In addition, seven different temporal shapes (see Figure 4.10) were tested to study the relative influence of the second and third amplitude on the injected drop diameter. The main motivation for the development of a new type of pulse was to improve

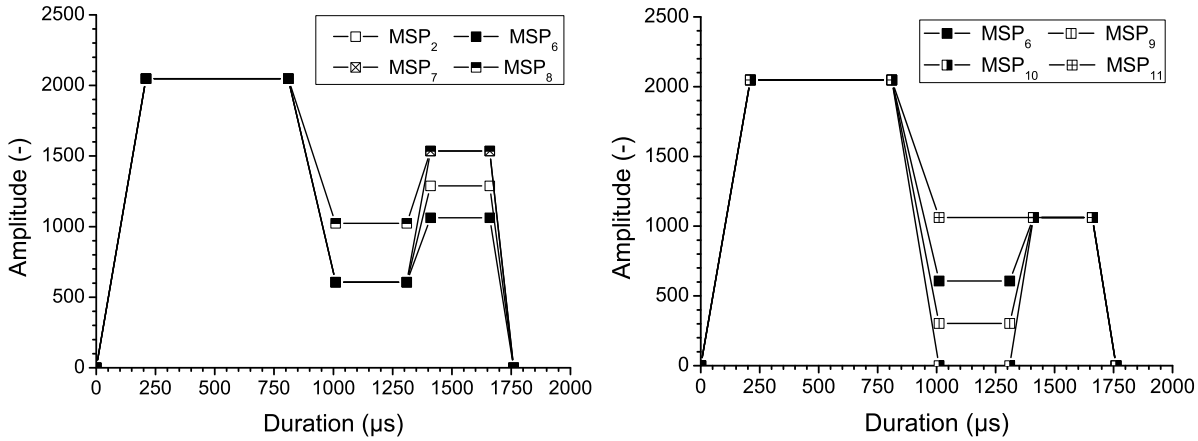

Figure 4.10: *Temporal shapes of the Multi-stage pulses tested.*

the adaptability and the control of the meniscus deformation. The benefits were directly visible either for producing medium sized drops (Figure 4.11) where a small amount

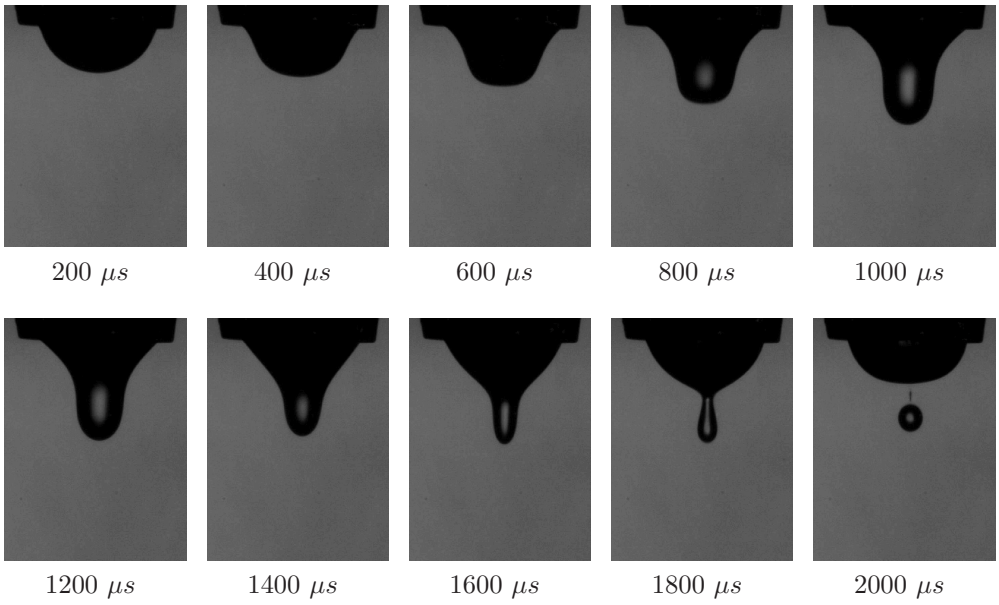

Figure 4.11: *Photographs of water drop injections in polybutene oil using the Multi-stage pulse MSP_6 with $V = 3.15\ kV$, $h/R_{Cap} = 0.75$ and $\gamma = 0.021\ N.m^{-1}$. Injected drop diameter is about 92 μm.*

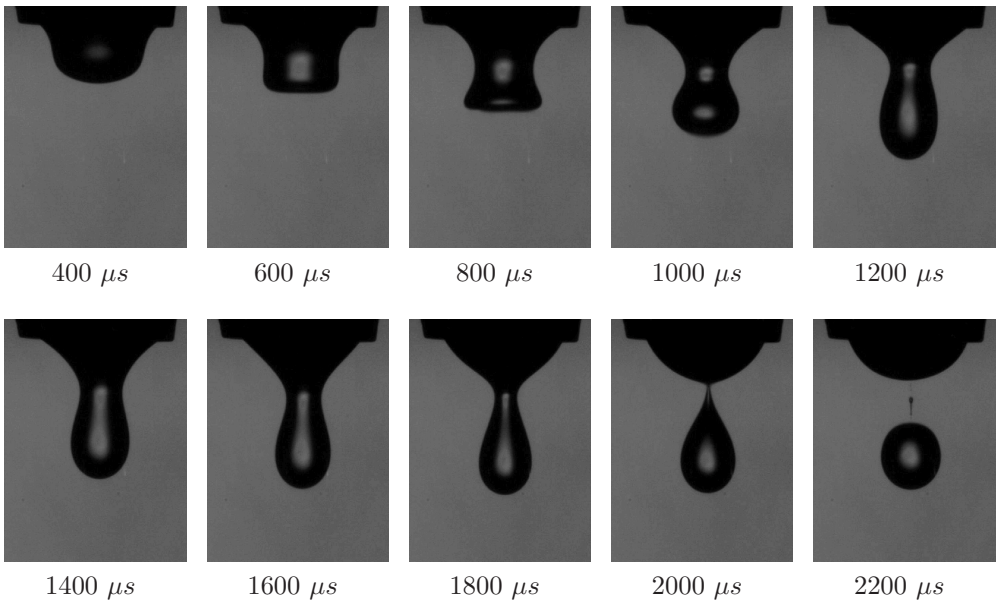

Figure 4.12: *Photographs of water drop injections in polybutene oil using the Multi-stage pulse MSP_9 with $V = 3.64\ kV$, $h/R_{Cap} = 0.86$ and $\gamma = 0.021\ N.m^{-1}$. Injected drop diameter is about 238 μm.*

of water is drained from the retracting meniscus by the third part of the pulse or for producing large drops where an off-axis atomization is avoided (Figure 4.12, frames 3-4) by the voltage decrease in the second part. Similarly to trapezoidal pulse injections, the meniscus break-up occurred a few hundred microseconds (approximately 200 μs in Figure 4.11 (frames 9-10) and 300 μs in Figure 4.12 (frame 9)) after the voltage shutdown.

Reproducibility of the Multi-stage pulse was also investigated: results are presented on Figure 4.13 for four different sets of parameters including those used to plot Figures 4.11 and 4.12. Calculated standard deviations decreased, as expected, with the increase of the produced drop diameters and were slightly lower than those obtained with trapezoidal pulses (respectively 1.08 % and 2.55 % for a drop diameter of 215 μm). Another

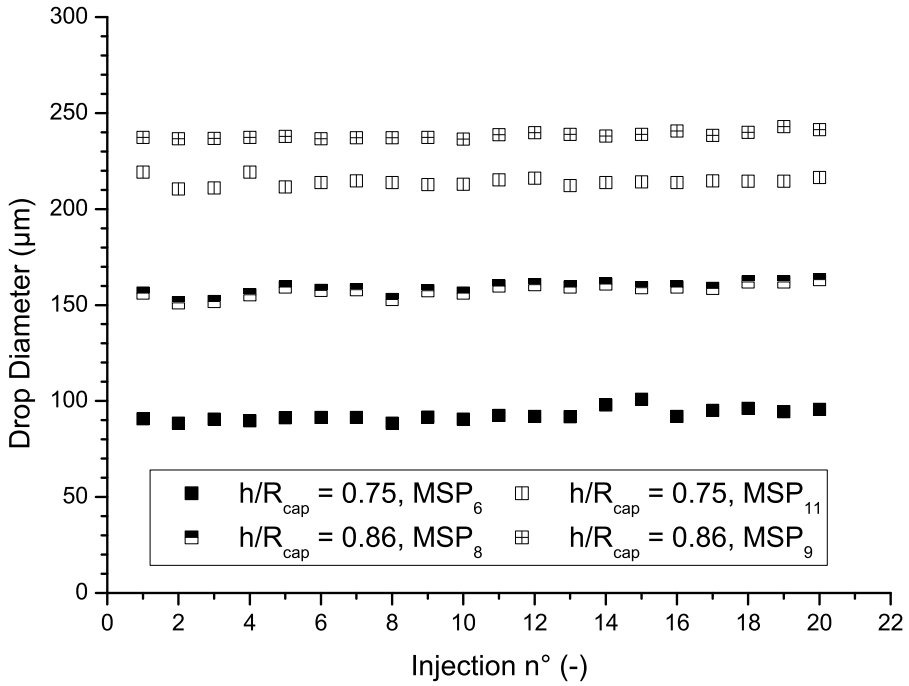

(*a*)

Meniscus and pulse parameters (ms, kV)	**Mean drop diameter** (μm)	**Standard deviation** (%)
$h/R_{Cap} = 0.75,\ MSP_6,\ V = 3.15$	92.6	3.44
$h/R_{Cap} = 0.75,\ MSP_{11},\ V = 3.45$	214.2	1.08
$h/R_{Cap} = 0.86,\ MSP_8,\ V = 3.17$	158.6	2.28
$h/R_{Cap} = 0.86,\ MSP_9,\ V = 3.64$	238.4	0.74

(*b*)

Figure 4.13: *Injection reproducibility of four different Multi-stage pulses. Experimentally obtained drop diameters (a) and corresponding means and standard deviations (b).*

difference, more fundamental, was enlightened by the comparison of the dynamics: while two modes of injection, respectively producing small and large drops, had been identified with trapezoidal pulses, only one seemed to be found for the Multi-stage pulses. It was, in fact, confirmed by looking at the variation of the produced drop diameter as a function of the applied voltage, on Figure 4.14 and 4.15. Most curves (except for the MSP_{10} and MSP_{11} in Figure 4.15) exhibit a continuous behavior. For a relative meniscus height $h/R_{Cap} = 0.75$, the drop diameter increased linearly with the applied voltage. The

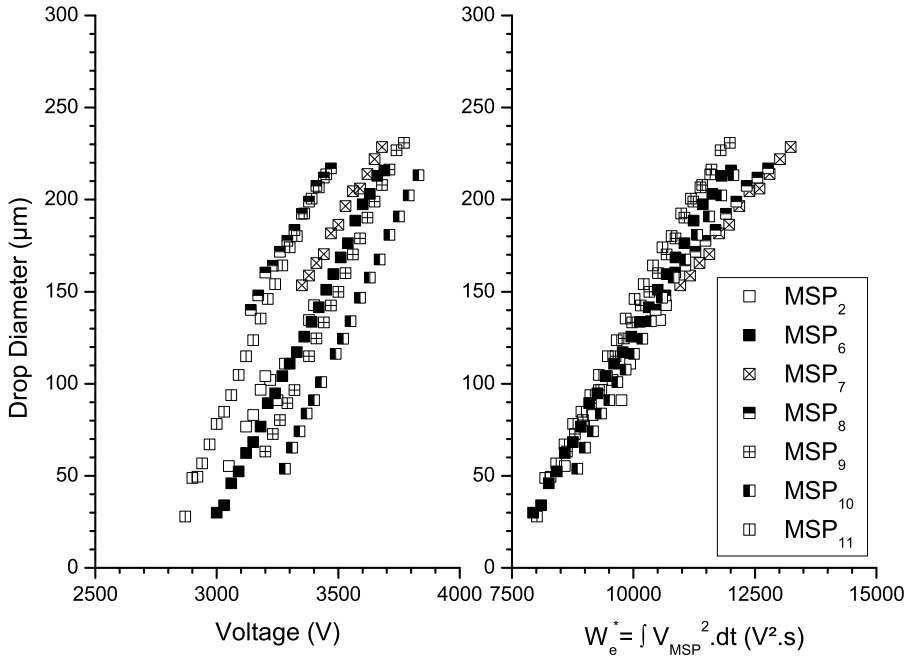

Figure 4.14: *Variations of the injected drop diameter for different MSPs as a function of applied voltage (left) and W_e^* (right). Average relative meniscus height $h/R_{Cap} = 0.76 \pm 0.02$ and IFT coefficient $\gamma = 0.021 \pm 0.001$ $N.m^{-1}$.*

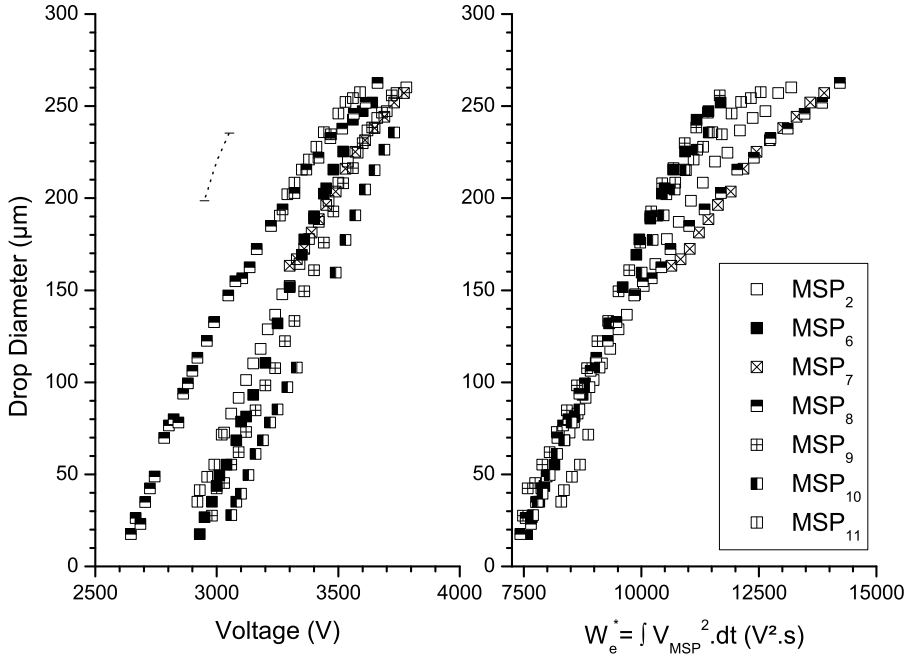

Figure 4.15: *Variations of the injected drop diameter for different MSPs as a function of applied voltage (left) and W_e^* (right). Average relative meniscus height $h/R_{Cap} = 0.86 \pm 0.02$ and IFT coefficient $\gamma = 0.021 \pm 0.001$ $N.m^{-1}$. The dotted curve represents numerically computed results with MSP_9, for $h/R_{Cap} = 0.85$, $\gamma = 0.025$ $N.m^{-1}$ and different applied voltages (see section 4.4.3).*

widest range was achieved with the MSP_6 which is thus used as a reference in the rest of the discussion. Largest drops had a ratio $V_d/V_{Men} = 0.37$ which is a little smaller than that attained with the trapezoidal pulses. Roughly similar results were obtained with

$MSPs_{2,9,10,11}$. MSP_7 and MSP_8, though, gave significantly narrower drop size distributions implying that the efficiency of the pulse is here mostly determined by the amplitude of its third part. For a relative meniscus height $h/R_{Cap} = 0.86$, drop diameter versus voltage curves converge toward an upper limit corresponding to a ratio $V_d/V_{Men} = 0.45$. Again, the MSP_6 produced the widest drop size distribution along with the MSP_8 that offers, in addition, higher control due to a less steep curve. However, efficiency of the pulse appeared here to be mainly controlled by the amplitude ratio between its second and third parts: obtained drop diameter ranges shortened as the ratio deviated from 0.5. For a relative meniscus height $h/R_{Cap} = 0.52$, as with trapezoidal pulses of duration $\Delta t = 1.5\ ms$, all the injected drops were charged. Adjusting the different durations composing the Multi-stage pulses would have probably solved the problem but the resulting produced drop diameter ranges would still be limited by the smaller initial meniscus volume. Figures 4.14 and 4.15 also show a very interesting trend: for both $h/R_{Cap} = 0.75$ and $h/R_{Cap} = 0.86$, curves, representing the evolution of the injected drop diameter as a function of We^*, overlap surprisingly well in their lower part. The lead term of the work of the electrostatic force accounts, in that case, quite accurately for the influence of the different amplitude ratios and can be used to reduce the number of pulse related parameters. Though, above a threshold released drop diameter, deviations between the curves become significant and increase with We^*, especially for the greatest initial meniscus volume. This is most likely due to the implicit assumption of non-deformable meniscus made in the definition of We^* which thus fails at considering the consequence of large interface deformation on the electrostatic pressure and to higher hydrodynamic effects as more fluid is set into motion.

4.4.3 Comparisons with numerical simulations

Through its reproducible nature, the present experimental study constituted an interesting benchmark in view of the improvement of the numerical scheme regarding surfactants modeling. Computations were therefore performed, as a starting point, to get a better insight into their influence. Figure 4.16 shows a series of pictures representing the computed deformation of the water-oil interface at different time steps, matching some of those on Figure 4.12, during an injection using the same electrical pulse. In this example, both the interfacial tension coefficient and the applied voltage were adjusted[17] in the computation

[17] As temperature was roughly kept constant in experiments, variations on the liquids intrinsic properties should remain small and have very little influence on the injection process (e.g. in the configuration simulated here, an increase in polybutene oil viscosity of about 10 %, corresponding to a temperature fall of about $3°C$ (see Figure B.1), resulted in a drop diameter increase of 2.1 %. A modification of the prescibed IFT coefficient, even small, has, on the other hand, a much stronger impact and a probable

to obtain a correspondance in drop release time and produced diameters between simulation and experiment (deviations were respectively of about 2.5 % and 1.26 %). Despite requiring appreciably different input parameters (γ was about 20 % higher while V was approximatively 16 % lower), the numerical model proved well able to reproduce the actual injection dynamics (the maximum meniscus tip elongation was about 10 % smaller in the simulation). In order to further understand the observed deviations and, in particular, discriminate between contributions from surfactants and from any other unexpected phenomenon (explaining e.g. the significant voltage difference), additional simulations were carried out. Results, plotted on Figure 4.15, confirmed doubts of the author. Indeed, the monotonic increase of the shift led to think that the electric field and thus the driving electrostatic pressure were slightly overestimated in the simulations. An explanation is believed to lie here in the nightmarish complexity of the electrostatic problem and of the choice of boundary conditions. The validity of the far-field assumption (see Table 2.1), guaranteed, in all the former numerical models, by a very small ratio between the spacing of interfaces and their distance to the outer domain boundaries, and also retained here, is questionable. The subsequent improper distribution of electric field streamlines along with the neglect of the polarization at the relatively close oil-PMMA and oil-air interfaces could have noticeably affected the electric potential (consequently even more the electrostatic pressure). This artifact[18] quite complicated further interpretation of the results, but still, the higher IFT coefficient required in the computations appeared consistent with the presence of surfactants[19]. Although, this may appear unusual, those might have had here an influence much more complicated than in the case of the electrocoalescence of two small water drops in oil (see section 3.3.4). Over the few minutes between each injection, soluble surfactants adsorbed[20] from the bulk to the water-oil interface, reaching a quasi-steady equilibrium concentration and lowering the IFT coefficient down to values close to that measured using the tensiometer. On the opposite, during the process, the rate of surfactant exchange became largely negligible compared to interfacial dilatation (Biot numbers $Bi \ll 1$) and surfactants behaved as insoluble. Thus, the increase in interfacial area occurring with the stretching of the meniscus might have resulted in local reinforcement of the IFT coefficient and allowed withstanding of higher applied voltages. Furthermore,

cause is discussed hereafter.

[18] A common trick, to ease comparison without redesigning the whole cell, would consist in turning the upper electrode into a metallic plate in order to force electric field streamlines into verticals in the vicinity of the cell walls, as in a capacitor (Notz and Basaran, 1999).

[19] Besides, in large concentrations, as reflected by the break-up of the liquid thread at a secondary neck (Jin et al., 2006), away from the forming drop (see, for example, the last frame in Figure 4.12 and appendix B.4 for enhanced details).

[20] Without much information on the type of surfactants, its adsorption/desorption and interfacial diffusion rate, maximum surface concentration and solubility, most of the deductions that follow are hypothetical.

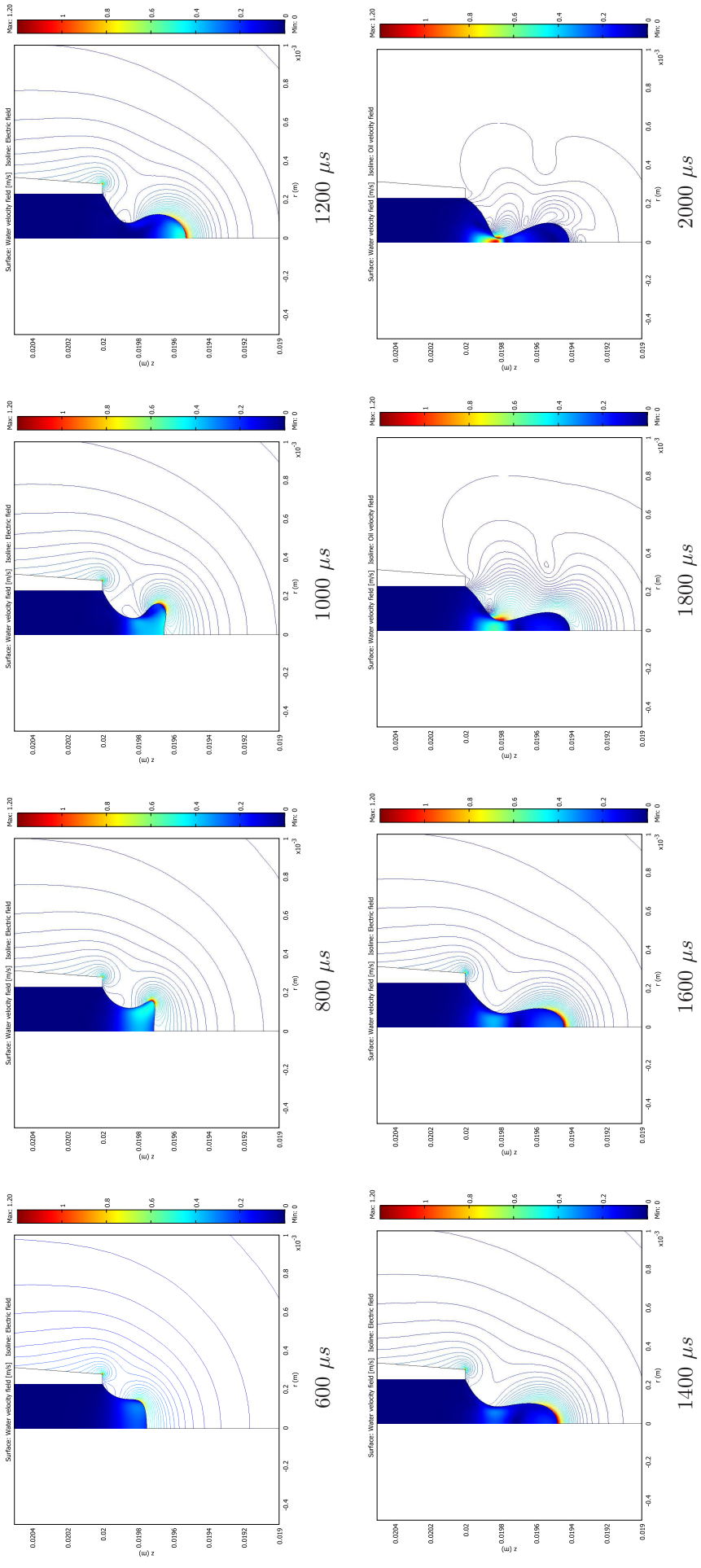

Figure 4.16: *Numerical simulation of an electrically neutral water drop injection in polybutene oil from a meniscus defined by* $h/R_{Cap} = 0.85$ *using* MSP_9, $V = 3.05\ kV$ *and* $\gamma = 0.025\ N.m^{-1}$. *Injected drop diameter, deduced from the last converge time steps* $t = 2.05\ ms$ *is about* $235\ \mu m$. *Image times match those of the experimental frames presented in 4.12.*

surfactants might also have concentrated in the necking region and altered its dynamics as interfacial convection predominated over interfacial diffusion (surface Peclet numbers $Pe \gg 1$) due to the influence of the outer viscous oil (Jin et al., 2006).

4.5 Results on dual drop injection

So as to evaluate the ability of the developed Multi-stage pulse to fulfill the requirements of the dynamic electrocoalescence experiment, i.e. the simultaneous injection of two charge free water drops in a polybutene oil shear flow, modifications were made in the test cell to include a second needle. Two menisci of individually controllable volume (see Figures 4.17a and 4.22a), formed at the tip of the needles, spaced by a center distance of 1.5 mm — i.e. on the order of that determined for the injected drops to meet in the desired location of the shear flow (see section 3.4.2.2) — and again hanging at $H = 2$ cm above the HV electrode, were then subjected to the same electric field pulse.

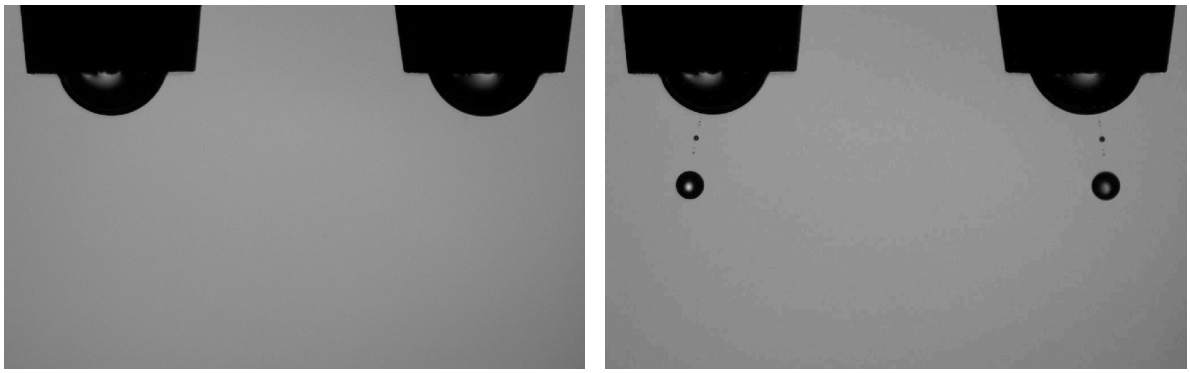

(a) (b)

Figure 4.17: *Synchronized injections of two electrically neutral even water drops in polybutene oil using MSP_2 with $V = 3.57$ kV and $\gamma = 0.018$ $N.m^{-1}$. (a) Initial menisci with respective relative heights: left $h/R_{Cap} = 0.76$, right $h/R_{Cap} = 0.77$. (b) Released drops and satellites. Measured drops diameters and angular offsets: left $D_d = 104.8$ μm and $\alpha = 14°$, right $D_d = 105.1$ μm and $\alpha = 16°$.*

First experiments were conducted, using even initial relative meniscus heights and two different MSPs, to investigate possible modifications induced by the new geometry on the obtainable drops diameter ranges and quantify the technique accuracy in terms of drops uniformity. Results, presented on Figures 4.18 and 4.19 for $h/R_{Cap} = 0.75$ and $h/R_{Cap} = 0.86$ respectively, allowed to draw the following conclusions: first of all, the technique is clearly capable of producing couples of highly identical drops, independently of the initial relative menisci sizes, pulse type and applied voltage. It is, for instance, perfectly illustrated in Figure 4.17b, as the number and sizes of drop and satellites that

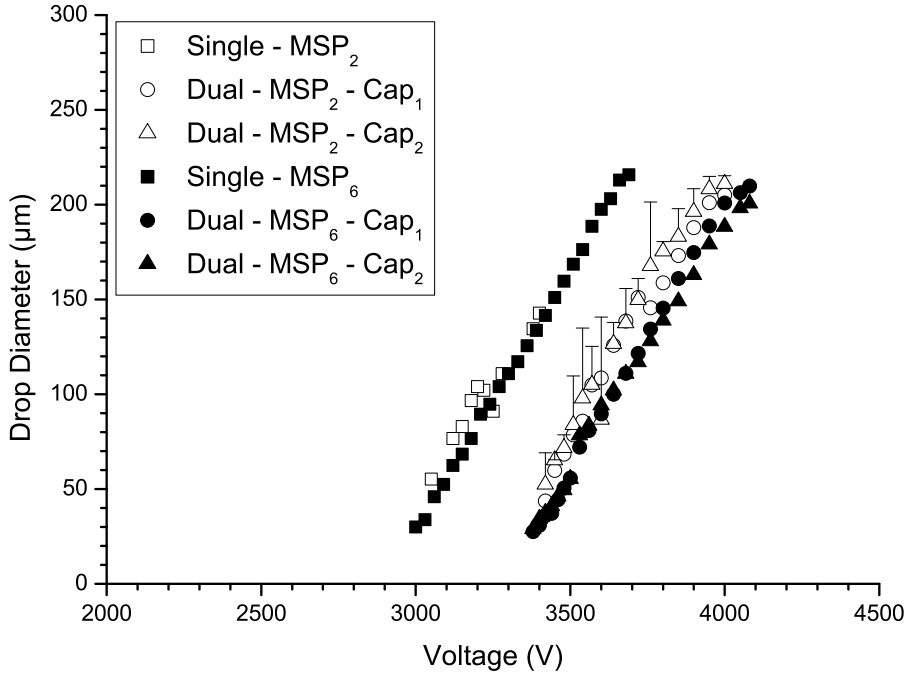

Figure 4.18: *Evolution of produced drops diameters as a function of applied voltage in dual injections using two different MSPs. Comparison with single drop injections. Relative menisci heights* $h/R_{Cap} = 0.75$ *and IFT coefficient* $\gamma = 0.018\ N.m^{-1}$*. Error bars represent the difference in relative initial meniscus height in ‰ for each injection performed with* MSP_2*.*

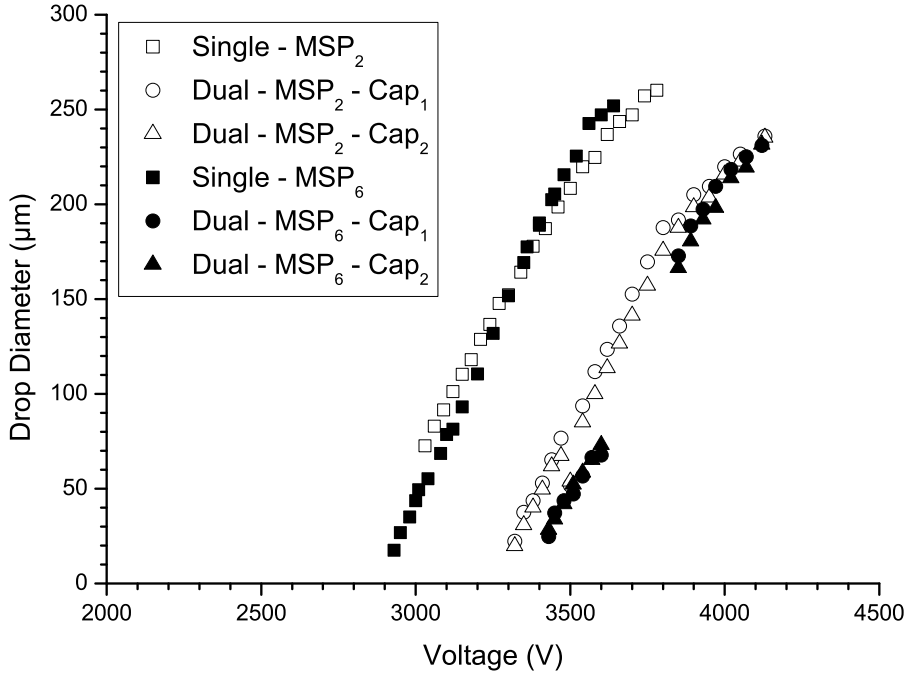

Figure 4.19: *Evolution of produced drop diameters as a function of applied voltage in dual injections using two different MSPs. Comparison with single drop injections. Relative menisci heights* $h/R_{Cap} = 0.86$ *and IFT coefficient* $\gamma = 0.018\ N.m^{-1}$*.*

issued from each meniscus match extremely well on the photograph. Deviation on the primary drops diameter was here less than 0.5 % and evolved along with differences in initial menisci volume (Figure 4.18). Secondly, no obvious alteration of the widest

producible drop diameter range was observed in comparison to single injections. Still, the MSP_6 was no longer optimal and exhibited a discontinuous behavior for an initial relative menisci height $h/R_{Cap} = 0.86$. Furthermore, despite having analogous slopes, curves representing the variation of the injected drops diameter as a function of the applied voltage in dual injections are significantly shifted from those obtained, for corresponding pulses, in single injections. Finally, water drops were here released with a non-axial and outward initial velocity and followed symmetric curved trajectories as they were slowed by the surrounding viscous oil until falling vertically at their terminal velocity under gravitational effects.

The need for higher applied voltages to achieve comparable (to those produced in single injections) drops diameter in dual injections as well as the trajectory difference were directly related to the modification of the electric field distribution induced by the new geometry. Indeed, as shown by numerical simulation[21] (Figure 4.20), the two grounded needles and conductive menisci electrostatically influenced each other, resulting in a lessening of the electric field intensity E in between them and disturbing its former axisymmetric distribution. Similar computations (with the same level of accuracy,

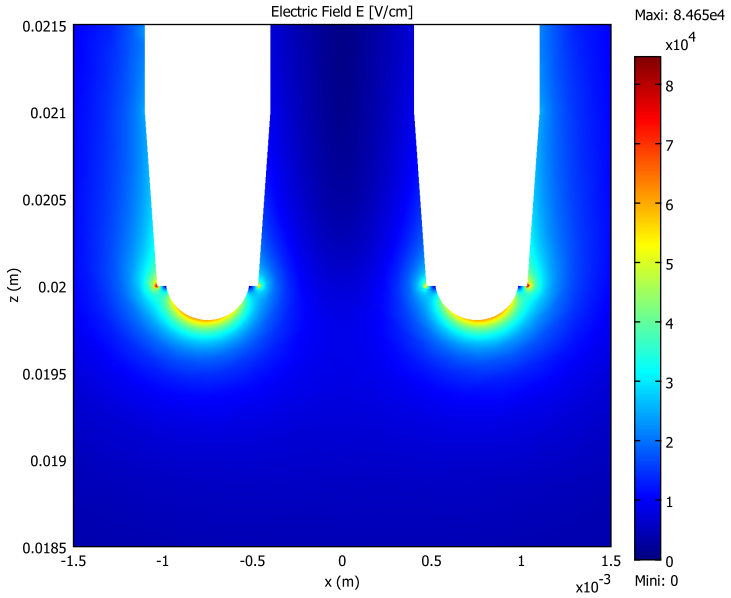

Figure 4.20: *Numerical simulation of the electric field distribution created by a steady applied potential difference $V = 3.50\ kV$ around two undeformed menisci defined by $h/R_{Cap} = 0.85$. Surface plot in the meridian plane of the dual drop injection experiment. Boundary elements sizes are $1.25\ 10^{-5}\ m$ and $4\ 10^{-5}\ m$ on the meniscus and on the needles beveled part, respectively.*

relative meniscus height and applied voltage) were performed, in the single injection configuration, to estimate this decrease. Matching either the maximum local value of the

[21] Because of the 3D nature of the problem and its subsequent very high computational power requirement (even when considering symmetries), simulations were here restricted to electric field calculations only and thus undeformed menisci.

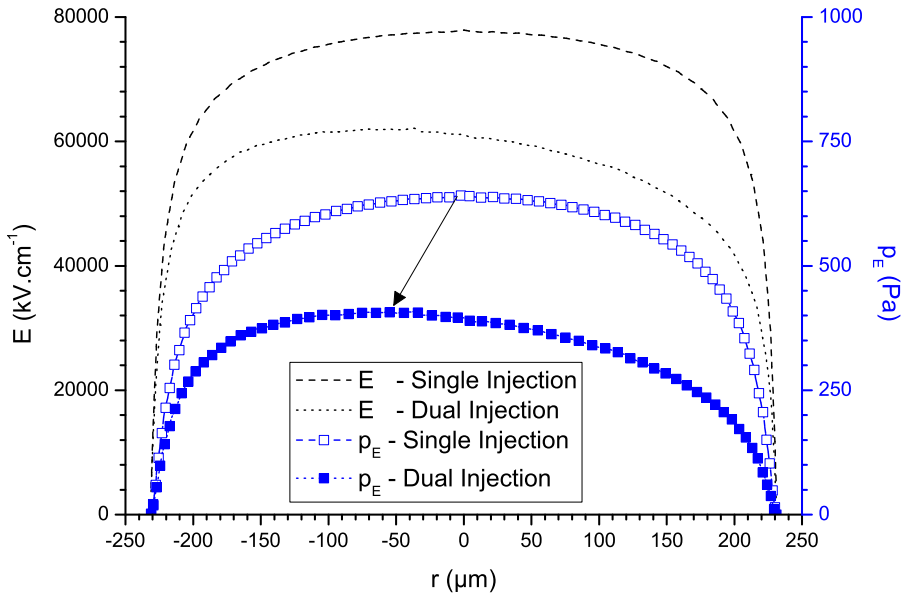

Figure 4.21: *Comparison of the electric field E and associated electrostatic pressure p_E acting at undeformed water/oil interfaces in single and dual drop injections for $h/R_{Cap} = 0.85$ and $V = 3.50\ kV$. The arrow points out the displacement of the maximum intensity of p_E.*

electrostatic pressure p_E or its integral on Figure 4.21 gave applied voltage differences of 800 V and 700 V respectively. Interestingly, those were quite close to the experimental value of 500 V, deduced from Figure 4.19, taking into account the lower interfacial tension coefficient ($\gamma = 18\ mN.m^{-1}$) in the dual injections due to a longer aging of the oil. Figure 4.21 also shows a clear displacement of the maximum electrostatic pressure intensity, along the interface, characterized by the angle α_E formed with the capillary axis. In the absence of a full 3D simulation, α_E can be used to extrapolate the initial trajectory of the injected drop by approximating the experimental angular offset α between the vertical and the normal to the interface orienting the water ligament in its vicinity. The latter was measured from the position of the satellite closest to the meniscus in photographs (see e.g. on Figure 4.17b. Here, numerical results predicted an angle $\alpha_E = 11°$ which corresponds exactly to the α values of the smallest injected drops. However, unlike α_E which only depends on the needles spacing, α was found to augment with the applied electric field (up to about 25° for the configurations tested). This considerably limits the interest of the extrapolation to relatively small deformations of the interface and thus to the release of small and medium sized drops. It is, nonetheless, noteworthy that these angular deviations could have been reduced by introducing modifications in the electrodes geometry design to restore the axisymmetric distribution of the electric field. Yet, the increase in distance between produced drops remained small compared to the needle spacing and was not troubling regarding our application.

By extending the results on the generation of even water drops in oil, an important

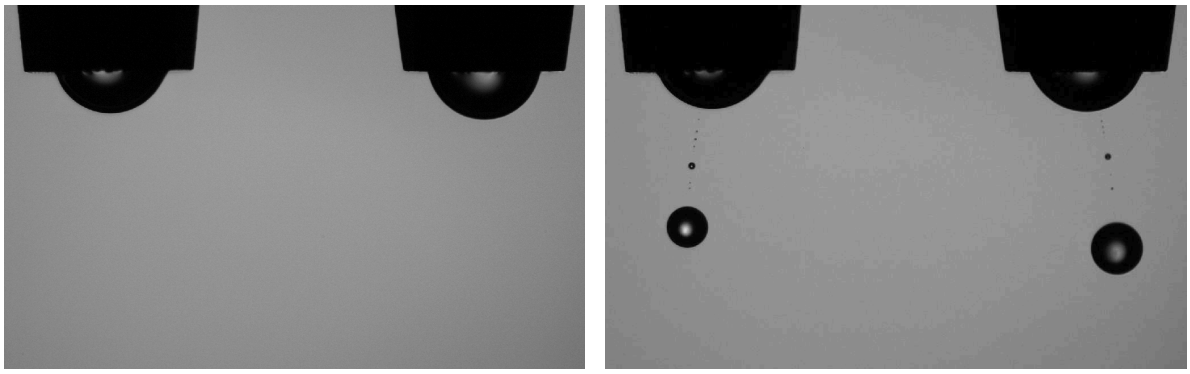

(a) (b)

Figure 4.22: *Synchronized injections of two electrically neutral uneven water drops in polybutene oil using MSP_2 with $V = 3.80\ kV$ and $\gamma = 0.018\ N.m^{-1}$. (a) Initial menisci with respective relative heights: left $h/R_{Cap} = 0.74$, right $h/R_{Cap} = 0.87$. (b) Released drops and satellites. Measured drops diameters and angular offsets: left $D_d = 164.9\ \mu m$ and $\alpha = 18°$, right $D_d = 207.2\ \mu m$ and $\alpha = 17°$.*

feature of the complete injection setup, i.e. allowing the possibility to "easily" study the influence of the drop diameter ratio in the electrocoalescence process, appeared achievable by working with different initial menisci volumes. Another set of experiments was thus conducted with two uneven menisci defined by $h/R_{Cap} = 0.75$ and $h/R_{Cap} = 0.86$ (Figure

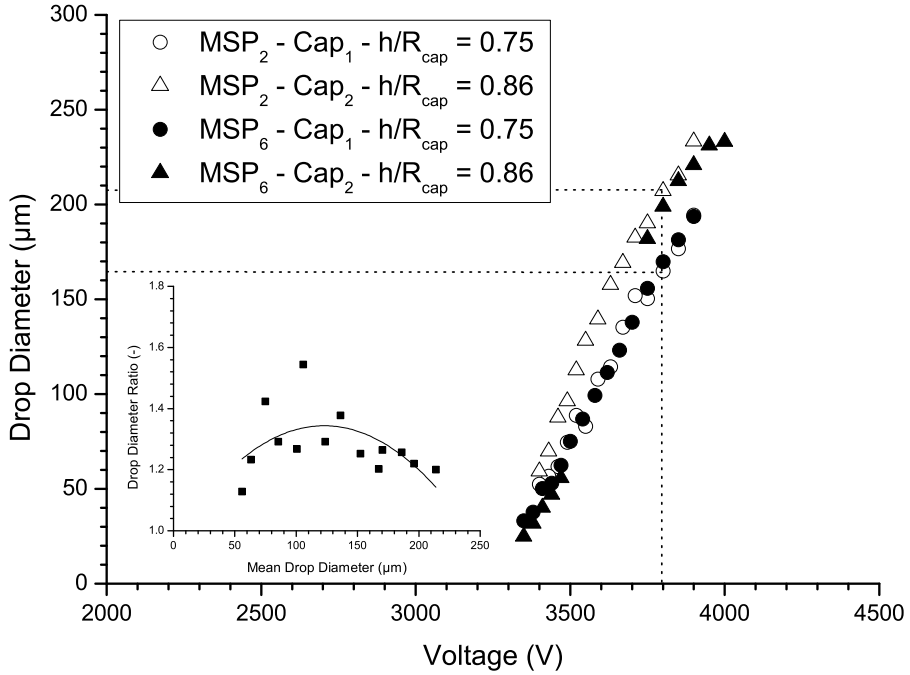

Figure 4.23: *Variations of produced drops diameters and drop diameter ratio respectively as a function of applied voltage and mean drop diameter in dual injections using two different MSPs for relative menisci heights $h/R_{Cap} = 0.75$ and $h/R_{Cap} = 0.86$ and IFT coefficient $\gamma = 0.018\ N.m^{-1}$. Dashed lines correspond to the experimental values deduced from the photograph of Figure 4.22b*

4.22a), the two previously used MSPs and varying applied voltages. Results, depicted on Figure 4.23, were roughly similar to a superimposition of those obtained, with different initial menisci, in even drop injection. Nevertheless, some discrepancies emerged when looking more closely at the curves: MSP_2 generated narrower drop size distributions owing to the decrease in largest diameter produced from the smaller meniscus (from 215 μm to 200 μm) while MSP_6 underwent a broadening of its non-injecting range of applied voltage, indicating an overall, still moderate, lowering of the pulses efficiency. Achieved drop diameter ratios varied from 1.15 up to around 1.35, increasing with the applied voltage until reaching its maximum for medium sized drops and then decreasing due to the limited volume available to be drawn from the water meniscus. From there, it is straightforward to expect that, providing an adequate pulse, greater relative initial menisci height differences give larger drop diameter ratios.

4.6 Transversal applications

In order to assess the applicability of the developed injection technique in other scientific or industrial domains, it was necessary to evaluate and discuss some additional intrinsic and conventionally used characteristics. Those are the range of injectable liquids, the process maximum repetition rate and its ability to perform satellite free drop releases. Concerning the former and as demonstrated throughout the chapter, the technique seems particularly suited, but not restricted, to the generation of conductive aqueous drops in relatively low viscous insulating oil. It might therefore be of particular interest in microfluidic applications where the presence of ionic species is tolerated. In fact, the choice of the fluids is mostly dictated by a high ratio of the drop detachment delay to the dielectric relaxation time ($t_D \gg \tau_E$) (see section 4.3.2.2), rather than by any single property such as disperse and continuous phase conductivities, viscosities, densities or interfacial tension. Another crucial factor is the partial discharge inception voltage (PDIV) of the continuous phase as it can considerably limit the available electrostatic pressure (Wright et al., 1993). For instance, following the work of Wright et al. (1995), EHD ejection of charge free drops of conductive water in air should only be possible through chemical lowering of the surface tension. Any kind of classification may include combinations of ethanol, air, sunflower and transformer oils, water-isopropanol mixtures and many others. Secondly, in the absence of experimental data, the process maximum repetition rate can be roughly represented by the minimum time needed for the meniscus to return to its original shape and for the liquid column to become at rest. Here, numerical simulations with conditions closely below the injection threshold showed that complete damping of the free interfacial oscillations,

occurs in about 5 ms. However, in experiments, hydrostatic forces often required longer delays to refill the extracted meniscus volume, due to the strong inertial and viscous effects experienced by the fluid column inside the PTFE capillary. The actual maximum repetition rate should be on the order of tens of hertz and should compare quite well with that of other techniques, summarized in Table 4.1. Finally, in many applications, the co-generation of satellites, resulting from the break-up of the liquid thread forming during the necking of the meniscus, along with the main drop is highly unwanted. First results (Figure 4.24) indicated obviously that a connection exists between the pulse shape and the number and size of the satellites and subsatellites: basically, they both tended to vanish as the ratio of the second and third amplitude of the pulse (V_2/V_3) converged toward unity, eventually disappearing completely as in Figure 4.24f. According to Tjahjadi et al. (1992), such behavior can be related to the variation of the wavenumber of the optimal parasitic disturbance since the predominant factor affecting the production of satellites, i.e. the viscosity ratio λ, was kept constant. Indeed, the wavenumber decreased with the ratio V_2/V_3 and, up to a certain value, the liquid thread elongated until it pinched successively from the meniscus and from the primary drop, releasing satellites in a non-

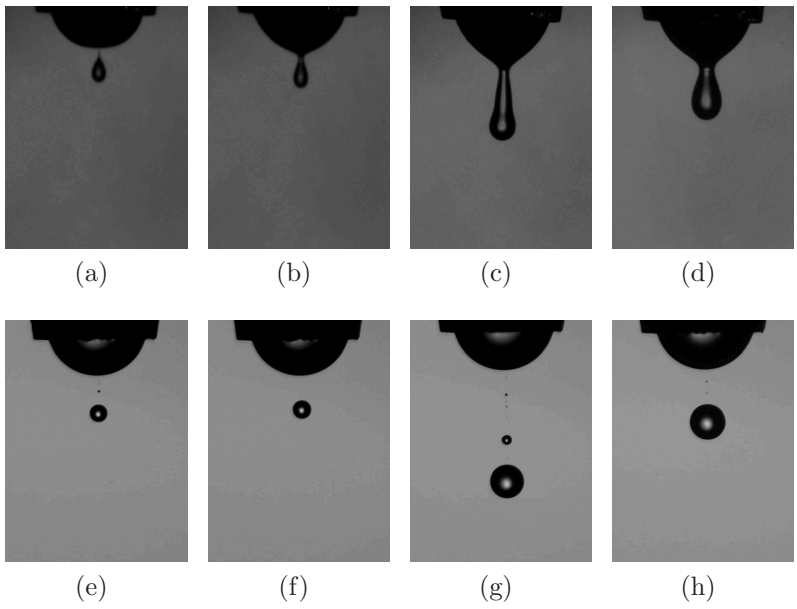

Figure 4.24: *Influence of the MSP shape on the satellite formation in injections of single water drop in polybutene oil for two different configurations (h/R_{Cap} and D_d). Photographs of the interface deformation* 1900 μs *after the beginning of the pulse (a)-(d) and of the corresponding produced drops and satellites (e)-(h). Injection parameters: average IFT coefficient* $\gamma = 0.021 \pm 0.001\ N.m^{-1}$, *(e)* $h/R_{Cap} = 0.75$, $D_d = 84.8\ \mu m$, MSP_9 *and* $V = 3.26\ kV$; *(f)* $h/R_{Cap} = 0.73$, $D_d = 80.3\ \mu m$, MSP_{11} *and* $V = 3.03\ kV$; *(g)* $h/R_{Cap} = 0.84$, $D_d = 163\ \mu m$, MSP_7 *and* $V = 3.30\ kV$; *(h)* $h/R_{Cap} = 0.82$, $D_d = 169.3\ \mu m$, MSP_6 *and* $V = 3.35\ kV$

linear self repeating process (Figures 4.24e and 4.24h). When the wavenumber was further lowered, the meniscus got more sensitive to parasitic disturbances which concentrated at nodes along the interface (Lee, 2003) and led to multiple thread formation, thus increasing the number and volume of satellites (Figure 4.24g). No direct correspondence was found between the production of satellites and the range of achievable drop diameters. Still, further optimization of the pulse shape should yield to very good compromises as MSP_6 already behaved well in both categories (see section 4.4.2 and Figure 4.24h).

4.7 Conclusion

The developed DOD actuation technique is able to generate, simultaneously, two drops of diameter ranging from 50 to 250 μm with respective size varying from 1 to 1.35 by simply tuning two of the key parameters — the relative menisci height and applied voltage — and fulfills all the requirements defined in the design of the "water drops electrocoalescence in an oil shear flow" experiment. Despite being based on the application of a high electric field pulse to a conductive meniscus surrounded by a dielectric liquid, injections of charge free water drops in polybutene oil were achieved thanks to an advanced control of the interface deformation dynamics allowed by the in-house invention of an improved pulse shape. The technique also offers an unprecedented feature, i.e. the possibility to produce drops of volume spanning from hundreds of femtoliters to tens of nanoliters without modifying the nozzle geometry, which might be of great interest in the fast expanding field of microfluidics. The combination of experiments and simulations has helped to establish a strong basis for the operation of the technique and has given a thorough insight into the different aspects that should be further investigated.

Conclusion

The thesis aimed toward the establishment of a criterion predicting the efficiency of the electrocoalescence process on the destabilization of water-in-crude oil emulsions.

In order to progressively study the complex and various mechanisms involved, a consequent work was devoted to the development of a multiphysics simulation tool. A numerical scheme, coupling fluid dynamics (Navier-Stokes) and electrostatics (Laplace) equations as well as interfacial tension effects, was therefore implemented. The latter was then integrated in a commercial software (COMSOL MULTIPHYSICS^{TM})and used, with a Finite Element Arbitrary Lagrangian-Eulerian method, to solve problems of motion and deformation of interfaces (droplets) between perfectly conductive and dielectric liquids. After preliminary accuracy assessments, quasistatic simulations were performed in model configurations relevant to the electrocoalescence of water drops in oil. Those proved well able to both reproduce experimental measurements and extend asymptotic stability criteria given by former analytical treatments.

One of the main contributions concerned the modeling and analysis of the mechanism of film thinning between conductive droplets approaching, in a quiescent dielectric liquid, under the effects of an applied electric field. Results from simulations highlighted the strong singularity of the present problem and, as a consequence, the inadequacy of existing theoretical lubrication models usually employed to represent coalescence events in two phase flows. Assuming negligible droplets deformation, an order of magnitude analysis led to an estimate for the drainage time, stating proportionality with the suspending liquid viscosity and inverse proportionality with the initial maximum electrostatic pressure (acting at the facing poles of the droplets). Validity of the obtained expression was then investigated and confirmed through systematic comparison with a parametric computational study. From there, a criterion predicting the probability of electrocoalescence resulting from a shear flow induced collision was proposed by balancing the time of drainage and that during which droplets are in close proximity. Despite being based on a few assumptions (as e.g. model liquids), it still provides some interesting insights into what happens at larger scales in industrial devices and qualitatively supports obser-

vations made in real-crude oil systems by project coworkers. In parallel, a sophisticated experimental setup was designed and assembled to cope for the inherent limitations of numerical simulations and to investigate the electrocoalescence of water droplets conveyed in a dielectric oil shear flow.

Another important effort, quite unexpected, was finally dictated by the necessity to overcome a technological bottle-neck enlightened during the design of this last experimental setup. It consisted in the development of a novel actuation technique for the synchronous on-demand injection of two charge free conductive droplets in an insulating viscous liquid, relying on the application of a high electric field pulse. Once again, the joint use of numerical simulation and experiments was crucial. The former gave the opportunity to closely look at the phenomenon dynamics, thereby helping to make a big step forward in the understanding of a trajectory issue, recurrently encountered in former experiments with traditional (square) pulses. Based on simulation results, an optimized pulse shape was introduced along with viable starting parameters. An extensive campaign of experiments then clearly demonstrated the effectiveness of the newly developed Multi-Stage pulses either for injecting single or pairs (of even and uneven) droplets, as required.

As for the possible continuations of the thesis, almost every single study has opened up for tantalizing research leads. For obvious reasons, the exploitation of the assembled experimental setup should be the top priority within the crude oil dewatering context. Great feedback is expected, enabling further improvements of the criterion relevance to the actual conditions of industrial electrocoalescers. In this perspective, the implementation of additional physical/chemical mechanisms, such as adsorption/desorption and interfacial transport of surfactants, in the numerical scheme would be of particular use (Tenno and Pohjoranta, 2008). At last but definitely not least, the unprecedented ability to produce controlled drop volume distributions spanning over almost 5 decades without any modifications of the nozzle geometry exhibited by the injection technique may find potential applications in other fields.

Bibliography

Aakre, H., Solbakken, T., Schüller, R. B., 2005. An in-line nir/endoscope technique for observations in real hydrocarbon multiphase systems. Flow Measurement and Instrumentation 16 (5), 289–293, optical Techniques for Multiphase Flow Measurement. 35

Ahmed, T., 2001. Reservoir Engineering Handbook (2nd Edition). Elsevier. 18

AkerSolutions, 2011. http://www.akersolutions.com. 34

Allan, R. S., Mason, S. G., 1961. Effects of electric fields on coalescence of liquid+liquid systems. Transactions of the Faraday Society 57, 2027–2040. 36

Altamirano, J. J., Flores, M. A., Pie, O., Panivino, N., Arzate, C., Kapellmann, G., Lopez, M. T., Espinosa, S., Rosales, S., 1986. Caracterizacion fisico-quimica de asfaltenos procedentes de los crudos maya e itsmo. Revista del Instituto Mexicano del Petroleo 18 (2), 32. 16

Alvarado, V., Manrique, E., 2010. Enhanced oil recovery: An update review. Energies 3 (9), 1529–1575. 19

Amemiya, I., Yagi, H., Mori, K., Yamamoto, N., Saitoh, S., Tanuma, C., Hirahara, S., 1999. IS&T's Recent Progress in Ink Jet Technologies II. Society for Imaging Science and Technology, Ch. Ink jet printing with focused Ultrasonic beams, pp. 275–279. 96

Amirzadeh Goghari, A., Chandra, S., Jan. 2008. Producing droplets smaller than the nozzle diameter by using a pneumatic drop-on-demand droplet generator. Experiments in Fluids 44 (1), 105–114. 97, 99

Anna, S. L., Bontoux, N., Stone, H. A., 2003. Formation of dispersions using "flow focusing" in microchannels. Applied Physics Letters 82 (3), 364–366. 95

Armstrong, J., Sams, G. W., 2008. New challenges in oil dehydration improved by dual frequency® electrostatic process. www.c-a-m.com. 31

Aryafar, H., Kavehpour, H. P., 2009. Electrocoalescence: Effects of dc electric fields on coalescence of drops at planar interfaces. Langmuir 25 (21), 12460–12465, pMID: 19817472. 36, 65

Aske, N., Kallevik, H., Sjöblom, J., 2001. Determination of saturate, aromatic, resin, and asphaltenic (sara) components in crude oils by means of infrared and near-infrared spectroscopy. Energy & Fuels 15 (5), 1304–1312. 15

Atten, P., 1993. Electrocoalescence of water droplets in an insulating liquid. Journal of Electrostatics 30, 259–269. 21, 23, 35, 67, 68

Atten, P., Aitken, F., 2006. Mécanisme de base du phénomène d'électrocoalescence. In: Proc. of the 5th Conference of the French Society of Electrostatics. pp. 155–160. 47, 48, 49

Atten, P., Aitken, F., 2007. Electrocoalescence criterion for two close water drops. In: 42nd IAS Annual Meeting Industry Applications Conference Record of the 2007 IEEE. pp. 452–456. 46, 52

Atten, P., Aitken, F., Koulova-Nenova, D., 2005. Field-induced deformation and disruption of a planar water-oil interface under the influence of a conducting sphere. In: Proc. IEEE International Conference on Dielectric Liquids ICDL 2005. pp. 165–168. 47, 50

Atten, P., Lundgaard, L., Berg, G., 2006. A simplified model of electrocoalescence of two close water droplets in oil. Journal of Electrostatics 64 (7-9), 550–554. 36, 46, 58, 73

Atten, P., Ouiguini, A., Raisin, J., Reboud, J.-L., 2008a. Drop-on-demand extraction from a water meniscus by a high field pulse. In: Proc. IEEE International Conference on Dielectric Liquids ICDL 2008. pp. 1–4. 98, 101, 104, 109, 111, 112

Atten, P., Raisin, J., Reboud, J.-L., 2008b. Field induced disruption of a planar water-oil interface influenced by a close metallic sphere. In: Proc. IEEE International Conference on Dielectric Liquids ICDL 2008. pp. 1–4. 47

Bailes, P., Larkai, S., 1981. An experimental investigation into the use of high voltage d.c. fields for liquid phase separation. Chemical Engineering Reasearch and Design 59a, 229–237. 22, 26, 35

Bailes, P. J., Stitt, E. H., 1987. Column liquid contacting with vigorous agitation balanced by electrostatic coalescence. i: Intensified coalescence-redispersion 65 (6), 514–523. 22

Basaran, O. A., Scriven, L. E., 1989. Axisymmetric shapes and stability of charged drops in an external electric field. Physics of Fluids A 1 (5), 799–809. 40, 149

Becker, E., Hiller, W. J., Kowalewski, T. A., 1991. Experimental and theoretical investigation of large-amplitude oscillations of liquid droplets. Journal of Fluid Mechanics 231, 189–210. 147

Ben-Tzvi, P., Rone, W., Mar. 2010. Microdroplet generation in gaseous and liquid environments. Microsystem Technologies 16 (3), 333–356. 94, 96

Berg, G., Ingebrigsten, S., 2005. Electrostatic forces between charged and uncharged water drops in dielectric liquids. In: Proc. of the 19th Nordic Insulation Symposium : NORD-IS 05. Tapir Akademisk Forlag. 67

Berg, G., Lundgaard, L., Becidan, M., Sigrnond, R., 2002. Instability of electrically stressed water droplets in oil. In: Proc. IEEE 14th International Conference on Dielectric Liquids ICDL 2002. pp. 220–224. 24

Berg, G., Lundgaard, L., Hansen, F. K., 2005. Elongation of water drops in oil during transient electric fields. In: Proc. of the 2005 IEEE International Conference on DIelectric Liquids, ICDL 2005. pp. 189–192. 24

Bogy, D. B., 1979. Drop formation in a circular liquid jet. Annual Review of Fluid Mechanics 11 (1), 207–228. 95

Brackbill, J. U., Kothe, D. B., Zemach, C., Jun. 1992. A continuum method for modeling surface tension. Journal of Computational Physics 100 (2), 335–354. 41

Bradski, G., Kaehler, A., 2008. Learning OpenCV: Computer Vision with the OpenCV Library. O'Reilly Media. 55

Bransky, A., Korin, N., Khoury, M., Levenberg, S., 2009. A microfluidic droplet generator based on a piezoelectric actuator. Lab on a Chip 9 (4), 516–520. 96, 99

Brazier-Smith, P. R., 1971. Stability and shape of isolated and pairs of water drops in an electric field. Physics of Fluids 14 (1), 1–6. 40

Brazier-Smith, P. R., Jennings, S. G., Latham, J., Nov. 1971. An investigation of the behaviour of drops and drop-pairs subjected to strong electrical forces. Proc. of the Royal Society of London A 325 (1562), 363–376. 149

Brown, P., Hindmarsh, A., Petzold, L., 1994. Using krylov methods in the solution of large-scale differential-algebraic systems. SIAM Journal of Scientific Computing 15 (6), 1467–1488. 45

Cabal, A., Ross, D. S., Lebens, J. A., Trauernicht, D. P., 2005. Thermal actuator with optimized heater for liquid drop ejectors. Sensors and Actuators A: Physical 123-124, 531 – 539. 97, 98

Cameron, 2011. www.c-a-m.com. 30, 31

Castrejon-Pita, J. R., Martin, G. D., Hoath, S. D., Hutchings, I. M., 2008. A simple large-scale droplet generator for studies of inkjet printing. Review of Scientific Instruments 79 (7), 075108. 94, 97, 99

Charles, G. E., Mason, S. G., 1960. The mechanism of partial coalescence of liquid drops at liquid/liquid interfaces. Journal of Colloid Science 15 (2), 105–122. 22, 36

Chen, A. U., Basaran, O. A., 2002. A new method for significantly reducing drop radius without reducing nozzle radius in drop-on-demand drop production. Physics of Fluids 14 (1), L1–L4. 96, 99, 103

Chen, P.-H., Chen, W.-C., Chang, S. H., 1997. Bubble growth and ink ejection process of a thermal ink jet printhead. International Journal of Mechanical Sciences 39 (6), 683 – 695. 97, 99

Cheng, S. X., Li, T., Chandra, S., 2005. Producing molten metal droplets with a pneumatic droplet-on-demand generator. Journal of Materials Processing Technology 159 (3), 295–302. 97, 99

Chesters, A. K., 1975. The applicability of dynamic-similarity criteria to isothermal, liquid-gas, two-phase flows without mass transfer. International Journal of Multiphase Flow 2 (2), 191–212. 69

Chesters, A. K., 1991. The modelling of coalescence processes in fluid-liquid dispersions: a review of current understanding. Chemical Engineering Research and Design 69, 259–270. 21, 63, 69

Cho, A. Y. H., 1964. Contact charging of micron-sized particles in intense electric fields. Journal of Applied Physics 35 (9), 2561–2564. 25

Clanet, C., 2000. Les nappes d'eau de félix savart. Bulletin National de la S. F. P. 125, 11–15. 94

Cloupeau, M., Prunet-Foch, B., 1990. Electrostatic spraying of liquids: Main functioning modes. Journal of Electrostatics 25 (2), 165–184. 100

Coelho, R., Debeau, J., 1971. Properties of the tip-plane configuration. Journal of Physics D: Applied Physics 4 (9), 1266–. 102

Collins, R. T., Jones, J. J., Harris, M. T., Basaran, O. A., Feb. 2008. Electrohydrodynamic tip streaming and emission of charged drops from liquid cones. Nature Physics 4 (2), 149–154. 100

Cooley, P. W., Wallace, D. B., Antohe, B. V., 2001. Applications of ink-jet printing technology to biomems and microfluidic systems. Vol. 4560. SPIE, pp. 177–188. 95

Cottrell, F. G., 1911. Process for separating and collecting particles of one liquid suspended in another liquid. US Patent 987,114. 22, 31

Cottrell, F. G., Speed, J. B., 1911. Separating and collecting particles of one liquid suspended in another liquid. US Patent 987,115. 22

Coulaloglou, C. A., Tavlarides, L. L., 1977. Description of interaction processes in agitated liquid-liquid dispersions. Chemical Engineering Science 32 (11), 1289–1297. 29, 63, 69

Dadvand, A., Khoo, B., Shervani-Tabar, M., 2009. A collapsing bubble-induced microinjector: an experimental study. Experiments in Fluids 46 (3), 419–434. 97, 99

Davis, M. H., Nov. 1964. Two charged conductors in a uniform electric field: Forces and field strength. The Quarterly Journal of Mechanics and Applied Mathematics 17 (4), 499–511. 27, 28, 68, 70, 75, 77, 78, 79, 92, 151, 152, 166, 167

Davis, R. H., Schonberg, J. A., Rallison, J. M., 1989. The lubrication force between two viscous drops. Physics of Fluids A 1 (1), 77–81. 67, 69, 70, 71, 72

Davis, T. A., 2004. Algorithm 832: Umfpack v4.3—an unsymmetric-pattern multifrontal method. ACM Transactions on Mathematical Software 30 (2), 196–199. 45

de Heij, B., van der Schoot, B., Bo, H., Hess, J., de Rooij, N. F., 2000. Characterisation of a fl droplet generator for inhalation drug therapy. Sensors and Actuators A: Physical 85 (1-3), 430–434. 96, 99

Decroocq, S., Casserino, M., 2005. Synthetics, mineral oils, and bio-based lubricants: chemistry and technology. Vol. 10. CRC/Taylor & Francis, Ch. Polybutenes. 49

Déléonibus, T., 2008. Électrocoalescence de fines gouttelettes d'eau dans le pétrole. Master's thesis, ENSMM. 84

Donea, J., Huerta, A., Ponthot, J., Rodríguez-Ferran, A., 2004. The Encyclopedia of Computational Mechanics. Vol. 1. John Wiley & Sons Inc., New York, Ch. Arbitrary Lagrangian-Eulerian Methods. 43

Dong, H., Carr, W. W., Morris, J. F., 2006. An experimental study of drop-on-demand drop formation. Physics of Fluids 18 (7), 072102. 96, 99, 109

Dreyer, M., 2007. Free Surface Flows under Compensated Gravity Conditions. Springer Berlin / Heidelberg, Ch. Basic Equations and Dimensionless Numbers, pp. 7–12. 103

Dubash, N., Mestel, A. J., 2007. Behavior near critical for a conducting drop in an electric field. Physics of Fluids 19 (7), 073104. 24

Eggers, J., Jul. 1997. Nonlinear dynamics and breakup of free-surface flows. Reviews of Modern Physics 69 (3), 865–. 103

Eggers, J., 2006. Nonsmooth Mechanics and Analysis. Ch. A brief history of drop formation, p. 163. 94

Elrod, S. A., Hadimioglu, B., Khuri-Yakub, B. T., Rawson, E. G., Richley, E., Quate, C. F., Mansour, N. N., Lundgren, T. S., 1989. Nozzleless droplet formation with focused acoustic beams. Journal of Applied Physics 65 (9), 3441–3447. 98

Endo, I., Sato, Y., Saito, S., ans S. Ohno, T. N., 1979. Liquid jet recording and apparatus therefor. UK Patent 2,007,162. 97

Eow, J. S., Ghadiri, M., 2002. Electrostatic enhancement of coalescence of water droplets in oil: a review of the technology. Chemical Engineering Journal 85 (2-3), 357–368. 21

Eow, J. S., Ghadiri, M., 2003a. The behaviour of a liquid-liquid interface and drop-interface coalescence under the influence of an electric field. Colloids and Surfaces A: Physicochemical and Engineering Aspects 215 (1-3), 101–123. 36

Eow, J. S., Ghadiri, M., 2003b. Motion, deformation and break-up of aqueous drops in oils under high electric field strengths. Chemical Engineering and Processing 42 (4), 259–272. 24

Eow, J. S., Ghadiri, M., Sharif, A. O., Williams, T. J., 2001. Electrostatic enhancement of coalescence of water droplets in oil: a review of the current understanding. Chemical Engineering Journal 84 (3), 173–192. 20, 21, 22, 71

Fan, K.-C., Chen, J.-Y., Wang, C.-H., Pan, W.-C., 2008. Development of a drop-on-demand droplet generator for one-drop-fill technology. Sensors and Actuators A: Physical 147 (2), 649–655. 96, 99

FEMLAB, G., 2006. Comsol multiphysics user's guide (comsol 3.3). Göttingen: FEMLAB GmbH. 45

Feng, J. Q., Jun. 1999. Electrohydrodynamic behaviour of a drop subjected to a steady uniform electric field at finite electric reynolds number. Proc. of the Royal Society of London A 455 (1986), 2245–2269. 40

Førdedal, H., Schildberg, Y., Sjöblom, J., Volle, J.-L., 1996. Crude oil emulsions in high electric fields as studied by dielectric spectroscopy. influence of interaction between commercial and indigenous surfactants. Colloids and Surfaces A: Physicochemical and Engineering Aspects 106 (1), 33–47. 35

Gañán-Calvo, A., Dávila, J., Barrero, A., 1997. Current and droplet size in the electrospraying of liquids. scaling laws. Journal of Aerosol Science 28 (2), 249–275. 100

Grace, J., Marijnissen, J., 1994. A review of liquid atomization by electrical means. Journal of Aerosol Science 25 (6), 1005–1019. 100

Hamworthy, 2011. http://www.hamworthy.com. 32, 33, 163

Hannisdal, A., Ese, M.-H., Hemmingsen, P. V., Sjöblom, J., 2006. Particle-stabilized emulsions: Effect of heavy crude oil components pre-adsorbed onto stabilizing solids. Colloids and Surfaces A: Physicochemical and Engineering Aspects 276 (1-3), 45–58. 15, 20

Harpur, I. G., Wayth, N. J., Bailey, A. G., Thew, M. T., Williams, T. J., Urdahl, O., 1997. Destabilisation of water-in-oil emulsions under the influence of an a.c. electric field: Experimental assessment of performance. Journal of Electrostatics 40-41, 135–140. 35

Harris, M. T., Basaran, O. A., 1993. Capillary electrohydrostatics of conducting drops hanging from a nozzle in an electric field. Journal of Colloid and Interface Science 161 (2), 389–413. 40, 102

Harris, M. T., Basaran, O. A., 1995. Equilibrium shapes and stability of nonconducting pendant drops surrounded by a conducting fluid in an electric field. Journal of Colloid and Interface Science 170 (2), 308–319. 40

Hayati, I., Bailey, A. I., Tadros, T. F., Jan. 1986. Mechanism of stable jet formation in electrohydrodynamic atomization. Nature 319 (6048), 41–43. 100

He, M., Kuo, J. S., Chiu, D. T., 2005. Electro-generation of single femtoliter- and picoliter-volume aqueous droplets in microfluidic systems. Applied Physics Letters 87 (3), 031916. 98, 99, 104, 111

Hellesø, S. V., Lundgaard, L., Berg, G., 2009. Experimental study of electrocoalescence of water drops in crude oils with and without emulsion breakers. In: Proc. of the Internationational Symposium on Electrohydrodynamics. 35, 36, 67, 80

Hines, R. L., 1966. Electrostatic atomization and spray painting. Journal of Applied Physics 37 (7), 2730–2736. 100

Hinze, J. O., 1955. Fundamentals of the hydrodynamic mechanism of splitting in dispersion processes. AIChE Journal 1 (3), 289–295. 80

Hølto, J., 2009. Electrocoalescence II progress reporting December 2008. Tech. rep., SINTEF Energy Research. 23, 162

Hughes, T. J. R., Liu, W. K., Zimmermann, T. K., 1981. Lagrangian-eulerian finite element formulation for incompressible viscous flows. Computer Methods in Applied Mechanics and Engineering 29 (3), 329–349. 43

IEA, 2011. www.iea.org. 9, 159

Inculet, I., 1985. Industrial applications of static electricity. Journal of Electrostatics 16 (2-3), 287–298. 100

Jarrold, G. S., Lebens, J. A., 2003. Thermal actuator. Patent US6561957. 98

Jaworek, A., Krupa, A., 1999a. Classification of the modes of ehd spraying. Journal of Aerosol Science 30 (7), 873–893. 100, 104

Jaworek, A., Krupa, A., Jun. 1999b. Jet and drops formation in electrohydrodynamic spraying of liquids. a systematic approach. Experiments in Fluids 27 (1), 43–52. 100

Jeffrey, D. J., 1982. Low-reynolds-number flow between converging spheres. Mathematika 29 (01), 58–66. 29, 70

Jin, F., Gupta, N. R., Stebe, K. J., 2006. The detachment of a viscous drop in a viscous solution in the presence of a soluble surfactant. Physics of Fluids 18 (2), 022103. 118, 120, 157, 158

Joffre, G., Prunet-Foch, B., Berthomme, S., Cloupeau, M., 1982. Deformation of liquid menisci under the action of an electric field. Journal of Electrostatics 13 (2), 151–165. 40, 102

Knupp, P. M., 1998. Winslow smoothing on two-dimensional unstructured meshes. In: Proceedings of the Seventh International Meshing Roundtable, Park City, UT. pp. 449–457. 44

Kokal, S., 2005. Crude oil emulsions: A state-of-the-art review. SPE Production & Facilities 20 (1), 5–13. 22

Kokal, S. L., 2006. Petroleum Engineering Handbook, Volume I: Engineering. SPE, Ch. Chapter 12: Crude Oil Emulsions, pp. 533–570. 19, 67

Lamb, H., 1932. Hydrodynamics, 6th Edition. Cambridge University Press. 147

Latham, J., Roxburgh, I. W., 1966. Disintegration of pairs of water drops in an electric field. Proc. of the Royal Society of London A 295 (1440), 84–97. 36, 46

Le, H. P., 1998. Progress and trends in ink-jet printing technology. Journal of Imaging Science and Technology 42, 49–62. 96

Lee, E. R., 2003. Microdrop Generation. CRC Press. 94, 97, 127

Lesaint, C., Glomm, W. R., Lundgaard, L. E., Sjöblom, J., 2009. Dehydration efficiency of ac electrical fields on water-in-model-oil emulsions. Colloids and Surfaces A: Physicochemical and Engineering Aspects 352 (1-3), 63–69. 35

Lesaint, C., Spets, ., Glomm, W. R., Simon, S., Sjöblom, J., 2010. Dielectric response as a function of viscosity for two crude oils with different conductivities. Colloids and surfaces. A. Physicochemical and engineering aspects 369 (1-3), 7. 17

Less, S., 2008. Mechanisms of water-in-crude oil emulsions formation, stabilization and resolution by electrostatic means. Ph.D. thesis, Norvegian University of Science and Technology (NTNU). 17, 22, 30, 62, 63, 80, 81

Liao, Y., Lucas, D., 2010. A literature review on mechanisms and models for the coalescence process of fluid particles. Chemical Engineering Science 65 (10), 2851–2864. 35, 61, 69

Lightford, S. T., Pitoni, E., Mauro, L., Armesi, F., 2008. Development and field use of a novel solvent/water emulsion for the removal of asphaltene deposits in fractured carbonate formations. SPE Production & Operations 23 (3), 301–311. 16

Link, D. R., Grasland-Mongrain, E., Duri, A., Sarrazin, F., Zhengdong, C., Cristobal, G., Marquez, M., Weitz, D. A., 2006. Electric control of droplets in microfluidic devices. Angewandte Chemie 45 (16), 2556–2560. 95, 98

Lundgaard, L., Berg, G., Ingebrigsten, S., Atten, P., 2006. Emulsions and emulsion stability. Vol. 132. CRC Press, Ch. Electrocoalescence for oil-water separation: Fundamental aspects, pp. 549–592. 21, 22, 23, 26, 28

Macky, W. A., Oct. 1931. Some investigations on the deformation and breaking of water drops in strong electric fields. Proc. of the Royal Society of London A 133 (822), 565–587. 24

Malloggi, F., Vanapalli, S. A., Gu, H., van den Ende, D., Mugele, F., 2007. Electrowetting-controlled droplet generation in a microfluidic flow-focusing device. Journal of Physics: Condensed Matter 19 (46), 462101–. 98

Mansour, N. N., Lundgren, T. S., 1990. Satellite formation in capillary jet breakup. Physics of Fluids A 2 (7), 1141–1144. 40, 95

Marshall, A. G., Rodgers, R. P., 2008. Petroleomics: Chemistry of the underworld. Proc. of the National Academy of Sciences 105 (47), 18090–18095. 15, 20

Meacham, J. M., Varady, M. J., Degertekin, F. L., Fedorov, A. G., 2005. Droplet formation and ejection from a micromachined ultrasonic droplet generator: Visualization and scaling. Physics of Fluids 17 (10), 100605. 94, 97, 98, 99

Melheim, J. A., Chiesa, M., 2006. Simulation of turbulent electrocoalescence. Chemical Engineering Science 61 (14), 4540–4549. 62, 63, 68, 80

Miksis, M. J., 1981. Shape of a drop in an electric field. Physics of Fluids 24 (11), 1967–1972. 24, 40

Mohammed, R., Bailey, A., Luckham, P., Taylor, S., 1993. Dewatering of crude oil emulsions 1. rheological behaviour of the crude oil–water interface. Colloids and Surfaces A: Physicochemical and Engineering Aspects 80 (2-3), 223–235. 35

Nierstrasz, V. A., Frens, G., 1998. Marginal regeneration in thin vertical liquid films. Journal of Colloid and Interface Science 207 (2), 209–217. 21

Nisisako, T., Torii, T., Higuchi, T., 2002. Droplet formation in a microchannel network. Lab on a Chip 2 (1), 24–26. 95

Noik, C., CHEN, J., Dalmazzone, C. S., 2006. Electrostatic demulsification on crude oil: A state-of-the-art review. In: International Oil & Gas Conference and Exhibition in China. SPE. 10, 22

Notz, P. K., Basaran, O. A., 1999. Dynamics of drop formation in an electric field. Journal of Colloid and Interface Science 213 (1), 218–237. 40, 118

Ohnesorge, W., 1936. Formation of drops by nozzles and the breakup of liquid jets. Zeitschrift für Angewandte Mathematik und Mechanik 16, 355–358. 103

Pearson, H. J., Valioulis, I. A., List, E. J., 1984. Monte carlo simulation of coagulation in discrete particle-size distributions. part 1. brownian motion and fluid shearing. Journal of Fluid Mechanics 143 (-1), 367–385. 64

Pedersen, A., 2008. Forces acting on water droplets in electrically energized oil emulsions. Ph.D. thesis, Norvegian University of Science and Technology. 27

Percin, G., Lundgren, T. S., Khuri-Yakub, B. T., 1998. Controlled ink-jet printing and deposition of organic polymers and solid particles. Applied Physics Letters 73 (16), 2375–2377. 98, 99

Piasecki, W., Florkowski, M., Fulczyk, M., Sipowicz, J., Sundt, H. K., 04 2004. Vessel internal electrostatic coalescer (VIEC). ABB Review. 32

Plateau, J. A. F., 1863. Experimental and theoritical researches on the figures of equilibrium of a liquid mass withdrawn from the action of gravity. Annual report of Board of Regents of the Smithsonian Institution, 207–285. 94

Prosperetti, A., 1980. Free oscillations of drops and bubbles: the initial-value problem. Journal of Fluid Mechanics 100 (02), 333–347. 148

Raisin, J., Reboud, J. L., Atten, P., 2010. Field induced coalescence of two water drops suspended in a dielectric fluid. In: Proc. of the 7th Conference of the French Society of Electrostatics SFE 2010. 72

Rayleigh, L., 1878. On the instability of jets. Proc. of the London Mathematical Society s1-10 (1), 4–13. 94

Rayleigh, L., 1882. On the equilibrium of liquid conducting masses charged with electricity. Philosophical Magazine 14, 184–186. 40

Richards, J. R., Beris, A. N., Lenhoff, A. M., 1995. Drop formation in liquid–liquid systems before and after jetting. Physics of Fluids 7 (11), 2617–2630. 41

Ristenpart, W. D., Bird, J. C., Belmonte, A., Dollar, F., Stone, H. A., Sep. 2009. Non-coalescence of oppositely charged drops. Nature 461 (7262), 377–380. 36, 67, 80

Rommel, W., Meon, W., Blass, E., 1992. Hydrodynamic modeling of droplet coalescence at liquid-liquid interfaces. Separation Science and Technology 27 (2), 129–159. 61

Ross, S. L., 1971. Measurements and models of the dispersed phase mixing process. Ph.D. thesis, University of Michigan, Ann Arbor. 63

Saffman, P. G., Turner, J. S., 1956. On the collision of drops in turbulent clouds. Journal of Fluid Mechanics 1 (01), 16–30. 64

Saksono, P. H., Peric, D., Aug. 2006. On finite element modelling of surface tension variational formulation and applications - part i: Quasistatic problems. Computational Mechanics 38 (3), 265–281. 45

Sanfeld, A., Steinchen, A., 2008. Emulsions stability, from dilute to dense emulsions – role of drops deformation. Advances in Colloid and Interface Science 140 (1), 1–65. 20, 21, 61, 69

Sartor, J., 1959. The mutual attraction of cloud droplets in the electrostatic field of the atmosphere. RAND Corporation Publication, P–1824. 36

Savart, F., 1833. Ann. de. Chim. et de Phys. Vol. 53. Ch. Mémoire sur la constitution des veines liquides lancees par des orifices circulaires en mince paroi, pp. 337–386. 94

Schulkes, R. M. S. M., 1994. The evolution and bifurcation of a pendant drop. J. Fluid. Mech. 278, 83–100. 40, 95

Setiawan, E. R., Heister, S. D., 1997. Nonlinear modeling of an infinite electrified jet. Journal of Electrostatics 42 (3), 243–257. 40

Sherwood, J. D., 1988. Breakup of fluid droplets in electric and magnetic fields. Journal of Fluid Mechanics 188, 133–146. 40

Sjöblom, J. (Ed.), 2006. Emulsions and Emulsion Stability: Second Edition. 132. 20

Sjöblom, J., Aske, N., Auflem, I. H., Øystein Brandal, Havre, T. E., Øystein Sæther, Westvik, A., Johnsen, E. E., Kallevik, H., 2003. Our current understanding of water-in-crude oil emulsions: Recent characterization techniques and high pressure performance. Advances in Colloid and Interface Science 100-102, 399–473. 14, 15, 20

Souli, M., Zolesio, J., 2001. Arbitrary lagrangian–eulerian and free surface methods in fluid mechanics. Computer Methods in Applied Mechanics and Engineering 191 (3-5), 451–466. 43

Speight, J. G., 2006. The Chemistry and Technology of Petroleum, Fourth Edition. CRC Press. 9, 14, 18, 19, 20, 159

Statoil, 2011. http://www.statoil.com. 32

Stein, H. N., 1993. The drainage of free liquid films. Colloids and Surfaces A: Physicochemical and Engineering Aspects 79 (1), 71–80. 21

Stewart, M., Arnold, K., 2008. Emulsions and Oil Treating Equipment: Selection, Sizing and Troubleshooting. Gulf Professional Publishing, Ch. Chapter 1: Crude Oil Treating Systems, pp. 1–80. 30

Stone, H. A., Bentley, B. J., Leal, L. G., 1986. An experimental study of transient effects in the breakup of viscous drops. Journal of Fluid Mechanics 173, 131–158. 103

Supeene, G., Koch, C. R., Bhattacharjee, S., 2008. Deformation of a droplet in an electric field: Nonlinear transient response in perfect and leaky dielectric media. Journal of Colloid and Interface Science 318 (2), 463–476. 40

Suryo, R., Basaran, O. A., 2006. Tip streaming from a liquid drop forming from a tube in a co-flowing outer fluid. Physics of Fluids 18 (8), 082102. 95

Tan, Z. W., Teo, S. G. G., Hu, J., 2008. Ultrasonic generation and rotation of a small droplet at the tip of a hypodermic needle. Journal of Applied Physics 104 (10), 104902. 98

Taylor, G., 1964. Disintegration of water drops in an electric field. Proc. of the Royal Society of London A 280 (1382), 383–397. 24, 40, 46, 100, 149, 150

Taylor, G., 1966. Studies in electrohydrodynamics. i. the circulation produced in a drop by electrical field. Proc. of the Royal Society of London A 291 (1425), 159–166. 40

Taylor, G., 1968. The coalescence of closely spaced drops when they are at different electric potentials. Proc. of the Royal Society of London A 306 (1487), 423–434. 36, 46, 58

Taylor, S. E., 1988. Investigations into the electrical and coalescence behaviour of water-in-crude oil emulsions in high voltage gradients. Colloids and Surfaces 29 (1), 29–51. 22

Tenno, R., Pohjoranta, A., 2008. An ale model for prediction and control of the microvia fill process with two additives. Journal of the Electrochemical Society 155 (5), D383–D388. 130, 174

Tjahjadi, M., Stone, H. A., Ottino, J. M., 1992. Satellite and subsatellite formation in capillary breakup. Journal of Fluid Mechanics 243, 297–317. 126

Tomar, G., Gerlach, D., Biswas, G., Alleborn, N., Sharma, A., Durst, F., Welch, S., Delgado, A., 2007. Two-phase electrohydrodynamic simulations using a volume-of-fluid approach. Journal of Computational Physics 227 (2), 1267–1285. 41

Ulmke, H., Mietschke, M., Bauckhage, K., 2001. Piezoelectric single nozzle droplet generator for production of monodisperse droplets of variable diameter. Chemical Engineering and Technology 24 (1), 69–70. 99

Urdahl, O., Wayth, N., Førdedal, H., Williams, T., Bailey, A., 2001. Encyclopedic Handbook of Emulsion Technology. CRC Press, Ch. Compact Electrostatic Coalescer Technology, pp. 679–689. 29, 62, 63, 80

Vaught, J. L., Cloutier, F. L., Donald, D. K., D.Meyer, J., Tacklind, C. A., Taub, H. H., 1984. Thermal ink jet printer. Patent US4490728. 97

Wang, S. S., Lee, C. J., Chan, C. C., 1994. Demulsification of water-in-oil emulsions by use of a high voltage ac field. Separation Science and Technology 29 (2), 159–170. 35

Waterman, L. C., 1965. Electrical coalescers. Chemical Engineering Progress 61 (10), 51–57. 27, 35

Woodson, H. H., Melcher, J. R., 1968. Electromechanical Dynamics. John Wiley and Sons 1968. 42

Wright, G., Krein, P., Chato, J., 1993. Factors affecting dynamic electrical manipulation of menisci. IEEE Transactions on Industry Applications 29 (1 Part 1), 103–112. 100, 102, 125

Wright, G., Krein, P., Chato, J., 1995. Self-consistent modeling of the electrohydrodynamics of aconductive meniscus. IEEE Transactions on Industry Applications 31 (4), 768–777. 100, 104, 106, 125

Xu, J., Attinger, D., 2008. Drop on demand in a microfluidic chip. Journal of Micromechanics and Microengineering 18 (6), 065020–. 96, 99

Yobas, L., Martens, S., Ong, W.-L., Ranganathan, N., 2006. High-performance flow-focusing geometry for spontaneous generation of monodispersed droplets. Lab on a Chip 6 (8), 1073–1079. 95

Yu, K. W., Wan, J. T. K., 2000. Interparticle force in polydisperse electrorheological fluids. Computer Physics Communications 129 (1-3), 177–184. 27, 151

Yuen, H. K., Princen, J., Illingworth, J., Kittler, J., 1990. Comparative study of hough transform methods for circle finding. Image and Vision Computing 8 (1), 71–77. 55

Zdravkov, A. N., Peters, G. W. M., Meijer, H. E. H., 2003. Film drainage between two captive drops: Peo-water in silicon oil. Journal of Colloid and Interface Science 266 (1), 195–201. 21

Zeleny, J., 1915. On the conditions of instability of electrified drops with applications to the electrical discharge from liquid points. Proc. of the Cambridge Phylosophical Society 18, 71–83. 100, 102

Zeleny, J., Jul. 1917. Instability of electrified liquid surfaces. Physical Review 10 (1), 1–8. 100

Zhang, X., 1999. Dynamics of growth and breakup of viscous pendant drops into air. Journal of Colloid and Interface Science 212 (1), 107–122. 41, 95

Zhang, X., Basaran, O. A., 1995. An experimental study of dynamics of drop formation. Physics of Fluids 7 (6), 1184–1203. 95, 103

Zoltan, S. I., 1972. Pulsed droplet ejecting system. Patent US3683212. 96

Appendix A

Additional details regarding numerical simulation

A.1 Free oscillations of liquid drops in air

As a preliminary test for the validation of the hydrodynamic model including the implementation of interfacial tension, the transient relaxation of an initially elongated liquid drop in air was investigated. Under the effects of both the capillary and viscous forces, a transient evolution toward spherical shape is observed, with progressive damping of the oscillations. Simulations were performed with a computational domain defined by half of an elliptic disk in the meridian plane (r-z plane) and containing about 4500 triangular elements. Numerical results for the frequency Ω^* and decay time τ of the oscillations are presented in Table A.1 and compared with analytical expressions (Becker et al., 1991) obtained in the particular case of low viscosity liquids and relatively large droplets ($R_0 \geq 50\ \mu m$) in dynamically inactive surroundings, with the irrotational approximation proposed by Lamb (Lamb, 1932). For the second mode of drop surface deformation, i.e. ellipsoidal-spherical oscillation, Ω^* and τ are given by

$$\tau = \frac{\rho_w R_0^2}{5\mu_w}, \tag{A.1}$$

$$\Omega^* = \Omega\sqrt{1-(\Omega\tau)^{-2}}, \tag{A.2}$$

where Ω is the frequency of the second oscillation mode of the inviscid liquid droplets in vacuum or air:

$$\Omega = \frac{8\gamma}{\rho_w R_0^3}. \tag{A.3}$$

The initial amplitude of oscillation was set to 10 % which is the upper limit for the validity of linear analysis (Becker et al., 1991). A very fine correspondence is obtained

Table A.1: Comparison between numerical and analytical results for characteristic frequency and damping time of oscillation of a single water drop in air. Simulation parameters: $\gamma = 0.07\ N.m^{-1}$; mass density $\rho = 1000\ kg.m^{-3}$; drop volumes $Vol_d = 0.31 - 310\ mm^3$ (corresponding to sphere equivalent radii R_0 of 4.2 mm and 0.42 mm) and viscosity μ_w of 0.01 $Pa.s$ and 0.001 $Pa.s$.

Volume (mm^3) Vol_d	310		0.31	
Dynamic viscosity $(Pa.s)$ μ_w	0.01	0.001	0.01	0.001
Analytical damping (s) τ	0.345	3.45	0.0034	0.034
Numerical damping (s) τ	0.346	3.4	0.0032	0.035
Analytical frequency (Hz) Ω^*	14.09	14.09	443.3	445.6
Numerical frequency (Hz) Ω^*	14.08	14.08	441.8	447.1
Damping error (%)	0.4	1.1	6.1	2.3
Frequency error (%)	0.01	0.06	0.3	0.3

between computational and analytical oscillation frequencies. The viscous damping of the oscillations, quantified by the decay times, is in good agreement with theory, the relative error being smaller than 2.5 %, except for the small drop with large viscosity, where the non dimensional viscosity $\mu_w/\sqrt{\rho_w \gamma R_0} = 0.06$ approaches the limit of validity of the linear irrotational approximation (Prosperetti, 1980).

A.2 Transient elongation of a conductive drop in oil under electrostatic stimulation

Further validations of the model were accomplished by computing the transient evolution and final elongation of a water drop freely suspended in a dielectric liquid and subjected to a step electric field imposed by two parallel electrodes (as in Figure 2.1). The computational domain was, here, reduced to one fourth of a disk in the meridian plane to speed up the calculation and to prevent any drifting of the drop, toward one of the electrodes, due to numerical approximations. Simulations were performed using the boundary conditions described in section 2.2.2 and Table 2.1. Two dielectric liquids were considered: toluene, the viscosity of which is close to that of water ($\mu_{Toluene} = 0.0006\ Pa.s$), and polybutene oil ($\mu_{Polybutene} = 0.0102\ Pa.s$). Prescribed IFT coefficients γ were varied from 0.025 $N.m^{-1}$ up to 0.032 $N.m^{-1}$.

Examples of computed drop oscillations are represented on Figure A.1. The three curves illustrate the influence of interfacial tension and viscosity on the transient regime of drop elongation and exhibit damped oscillations fully consistent with the results presented in the former section. Indeed, a stronger interfacial tension decreases both the pseudo-period of oscillations and the amplitude of the first overshoot while a greater viscosity of

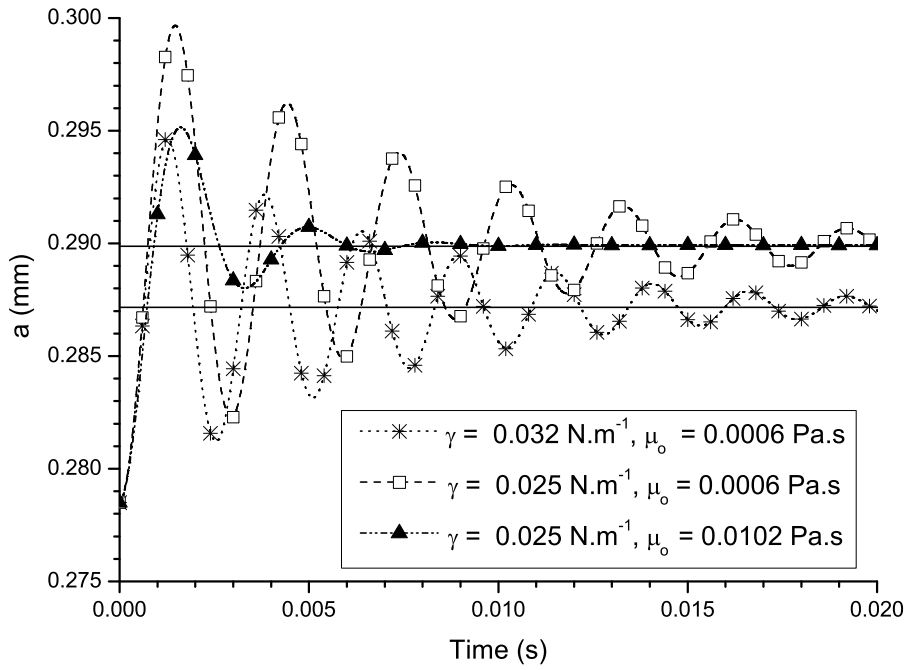

Figure A.1: *Oscillations of a conductive water drop suspended in a dielectric oil and subjected to a step electric field. Influence of the interfacial tension coefficient and of the suspending fluid viscosity. Simulation parameters:* $\rho_w = 1000\ kg.m^{-3}$, $\rho_o = 824\ kg.m^{-3}$, $\mu_w = 0.001\ Pa.s$, $R_0 = 278.5\ \mu m$, $\epsilon_{r_o} = 2.393$, *and* $E_0 = 4.5\ kV.cm^{-1}$. *Horizontal full lines symbolize the final elongations predicted by Taylor's model (steady state).*

the suspending liquid increases damping and slightly augments the pseudo-period.

Assuming an ellipsoidal shape for the deformed drop, Taylor (1964) related the static elongation of the ellipsoid a/b (where a is the semi-major axis, perpendicular to the electrodes, and b is the semi-minor axis) to the dimensionless electric field $E_0(2R_0\epsilon_0\epsilon_{r_o}/\gamma)^{1/2}$, and found the stability limit for a value of 0.648. At low to moderate stabilized elongation, an almost perfect match between computed values and Taylor (1964)'s solution was obtained (Figure A.2). Deviations arose near the critical conditions (i.e. E_{crit}) where the validity of the assumption of ellipsoid shape for the deformed drop is questionable. Using the "quasistatic method" (see section 2.2.4), the static limit of stability was obtained for a dimensionless uniform electric field $E_0(2R_0\epsilon_0\epsilon_r/\sigma)^{1/2} = 0.638$ corresponding to an aspect ratio $a/b = 1.832$. The good agreement found with (0.64, 1.83) from Brazier-Smith et al. (1971) and (0.644, 1.82) from Basaran and Scriven (1989), which are both reference studies in the literature, again confirmed the accuracy of the numerical scheme.

A.3 Remeshing procedure

A very annoying computational issue was inevitably encountered while simulating the electrocoalescence between freely suspended droplets (Chapter 3). Indeed, it was observed that, once the interfacial distance was reduced past a critical value, the Winslow smooth-

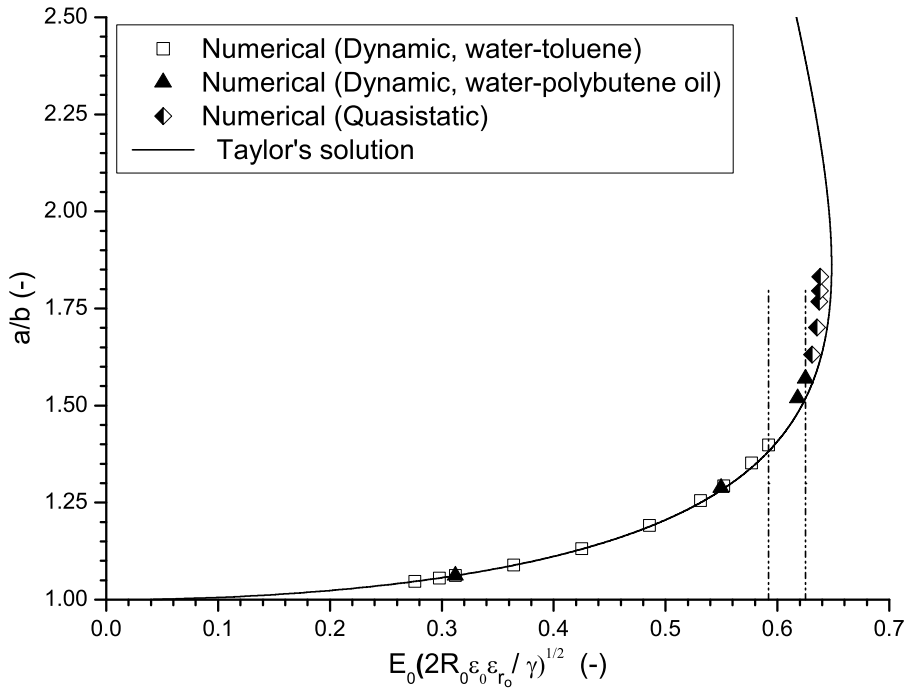

Figure A.2: *Stabilized elongation of a conductive water drop suspended in a dielectric oil and subjected to a step electric field. Comparison between results from simulations and Taylor (1964)'s model. Simulation parameters:* $\rho_w = 1000\ kg.m^{-3}$, $\rho_o = 824\ kg.m^{-3}$, $\mu_w = 0.001\ Pa.s$, $R_0 = 278.5\ \mu m$ *and* $\epsilon_{r_o} = 2.393$. *The vertical dotted lines illustrate the stability limits respectively observed for an oscillating water drop in toluene and polybutene oil. Values smaller than Taylor (1964)'s result from the transient behavior: disruption of the drop may occur prematurely depending on the amplitude of the first overshoot. Highest stable elongations were obtained using the "quasistatic method" (section 2.2.4).*

ing method's regularizing effect was not strong enough to cope for the great stretching of some mesh elements. This led, in the best case scenario, to large discrepancy or worst to a complete stop of the calculation. In order to overcome this phenomena, a remeshing procedure based on the minimum mesh quality (MMQ), handled by COMSOL MULTIPHYSICS, and composed of the following steps was developed:

1. Create an initial mesh with a quality around or above 0.7 (typical value most often obtained through automatic software generation with version 3.4 and 3.5).
2. Turn the "Allow remeshing" option ON.
3. Set the output times according to the problem nature.
4. Set MMQ to a value in the range 0.1-0.3 (computation stops once the condition is fulfilled).
5. Create a new geometry from the deformed mesh (usually best to use the solution from one or two time steps before the last stored).
6. Remesh. If quality goes below 0.5-0.6, try adjustments on the meshing options (maximum number/size of elements, curvature factor...). Restart.

7. Repeat 4 and 5 until MMQ conditions becomes reach without storage of any additional time step.
8. Remove MMQ and restart to let the simulation run up to the final stage of non-linear solver convergence.
9. Beware of the physical significance of those final results.

Note that this procedure holds independently of the mesh types (unstructured triangular, quadrilateral, hybrid) and that it proved also very handy to simulate water drop injections in oil (Chapter 4).

A.4 Models for the electrostatic interaction force

In order to accurately approximate the attractive force F_e acting during the electrocoalescence of conductive droplets freely suspended in a dielectric liquid (chapter 3), behaviors predicted by different theoretical models (introduced in section 1.5.1.4) were analyzed and compared with results computed through numerical simulation. As shown in Figure A.3, all three models give similar values down to an relative interfacial spacing $s/R_0 \sim 1$. When s/R_0 is further reduced, using the point-dipole approximation leads to a strong underestimation of the actual force F_e. The DID model, developed by Yu and Wan (2000), remains globally valid down to 0.1 and may be regarded as accurate enough from a qualitative point of view. Though, for relative interfacial spacing in the range $0.2 - 0.001$, as those considered in this thesis, only Davis (1964)' analytical solution appeared satisfactory. In view of the correspondence obtained with simulation results, approximate expressions for the force F_e and for the field enhancement parameter E_3, writing

$$F_e = 0.92\pi\epsilon_0\epsilon_{r_o}E_0^2R_0^{2.8}s^{-0.8}$$
$$\text{and} \qquad E_3 = 1.87(s/R)^{-0.85},$$

were deduced from allometric power fits in Figures A.3 and A.4, respectively.

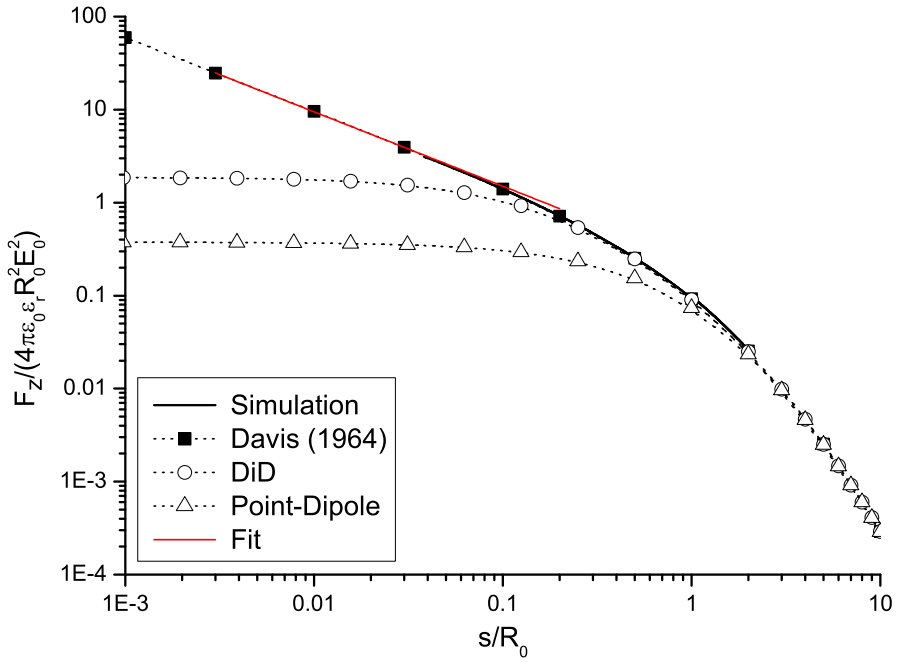

Figure A.3: *Variation of the electrostatic attraction force between two even spherical (conductive and uncharged) droplets as a function of the relative spacing between their interface* s/R_0. *Comparison between predictions from theoretical models and simulations. Simulation parameters:* $\rho_w = 1000\ kg.m^{-3}$, $\rho_o = 824\ kg.m^{-3}$, $\mu_w = 0.001\ Pa.s$, $\mu_o = 0.0102\ Pa.s$, $\gamma = 0.025\ N.m^{-1}$, $\epsilon_{r_o} = 2.3$, $R_0 = 10\ \mu m$, $s_0 = 2\ \mu m$ *and* $E_0 = 0.5\ kV.cm^{-1}$.

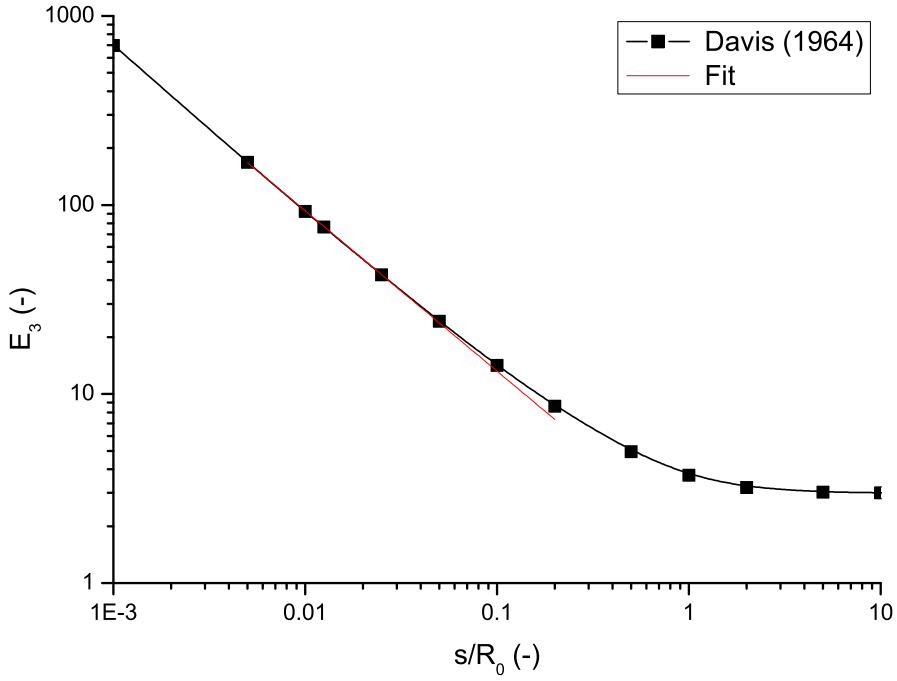

Figure A.4: *Variation of Davis (1964)' parameter* E_3 *predicting the electrostatic field enhancement at the facing poles of two perfectly conducting spherical drops as a function of the relative spacing between their interface* s/R_0.

Appendix B

Additional details regarding experiments

B.1 Oil viscosity versus temperature

The temperature dependence of the viscosity of the Indopol Grade L6 polybutene was investigated with a falling ball viscometer (HAAKE - Type C) on two different samples, both taken from a 100 *Liters* barrel. One (denoted "fresh") was characterized immediately after sampling while the other was first aged for a few weeks through storage under ambient conditions. Measurement results, reported on Figure B.1, show very small differences between the two samples implying that unlike for interfacial tension, aging has here a

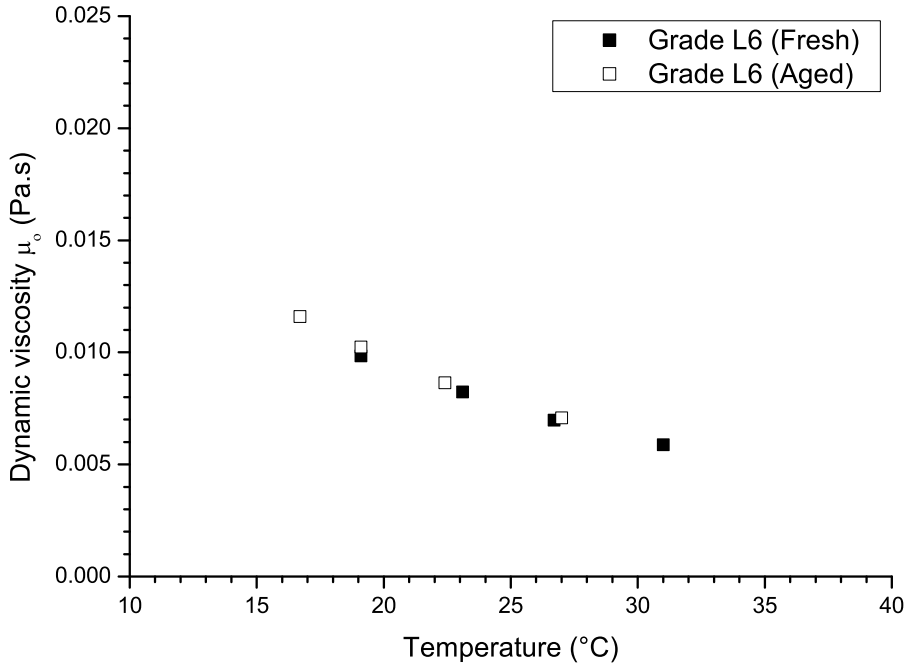

Figure B.1: *Variation of the oil viscosity as a function of temperature for fresh and aged (Indopol Grade L-6) polybutene oil samples.*

very limited impact. The rather strong influence of the temperature on the viscosity of the oil (reduction of almost 50% for a $15°C$ increase) was and remains however of much more concern. Indeed, on an experimental basis, either the injection of water droplets or their acqusition in the poiseuille flow may be strongly affected by uncontrolled variation of viscosity. Concerning the former and as mentioned in chapter 4, special care was therefore taken to ensure a fairly constant operating temperature.

B.2 Hydrodynamic calculations

Once a Poiseuille velocity profile was chosen to experimentally study the electrocoalescence of water droplets in an oil shear flow, calculations were performed to size the main part of the cell (referred to as #5 in section 3.4.2) in the configuration presented on Figure B.2. Assuming that droplets are negligibly affected by gravity and strictly follow the surrounding oil flow, their velocities and position can respectively be expressed as

$$u(z) = 4U_{Max}\frac{z}{h}\left(1-\frac{z}{h}\right) = 4U_{Max}Z(1-Z) \tag{B.1}$$

$$x(t) = 4U_{Max}Z(1-Z)t + x_0 \tag{B.2}$$

where $Z = z/h$ represents the injection height with respect to the cell walls. Denoting $\Delta Z = Z_1 - Z_2$ the transversal (constant) spacing between the droplets, equation (B.2) further allows to determine the temporal evolution of their longitudinal spacing $\Delta x(t)$ writing

$$\Delta x(t) = x_2(t) - x_1(t) = \Delta x_0 - 4U_{Max}\Delta Z(1-2Z_1+\Delta Z)t. \tag{B.3}$$

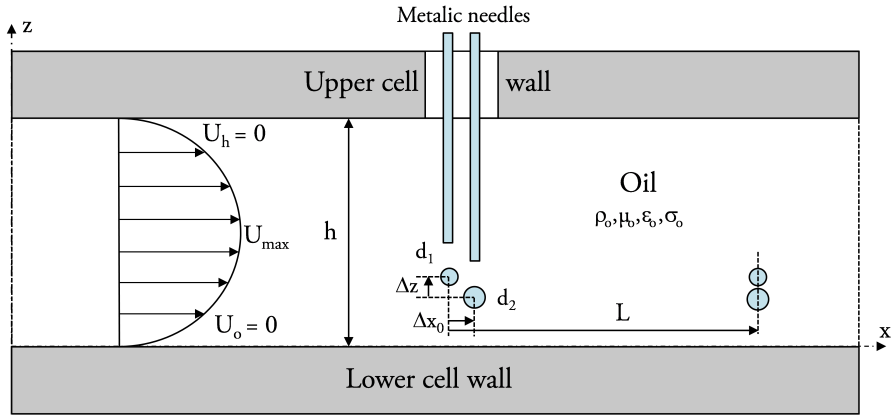

Figure B.2: *Injection and meeting of water droplets in a Poiseuille oil flow.*

From there, an estimation for the time between droplets injection and meeting comes straightforwardly as:

$$t_M = \frac{1}{4U_{Max}} \frac{1}{1 - 2Z_1 + \Delta Z} \frac{\Delta x_0}{\Delta Z}. \tag{B.4}$$

Taking the initial position of the "chasing" droplet (d_1) as a reference, the corresponding traveled distance is then given by:

$$L = [x_1(t_M) - x_1(t = 0)] = Z_1 \frac{1 - Z_1}{1 - 2Z_1 + \Delta Z} \frac{\Delta x_0}{\Delta Z}. \tag{B.5}$$

which is interestingly independent of U_{Max}. The variation of L is plotted on Figure B.3 as a function of the initial parameters Z, and ΔZ for a given $\Delta x_0 = 2\ mm$. For a meeting distance $L \sim 315\ mm$, initial relative transversal spacing varying from 0.002 up to about 0.008 can be used by adjusting the injection height in the Poiseuille oil flow. By considering $\Delta Z \sim R_1 + R_2 + s$ (with $R_2 \geq R_1 \gg s$), so that droplets retain approximately their linear trajectory while becoming in close proximity (i.e without rolling onto each other), an estimate for the range of operable diameters D_d is $[40\ \mu m, 160\ \mu m]$. In order to further broaden this range, the injection system to be developed should also allow to adjust the longitudinal positioning of the injectors (e.g. for $\Delta x_0 \in [1\ mm - 3\ mm]$ $D_d \in [20\ \mu m, 240\ \mu m]$).

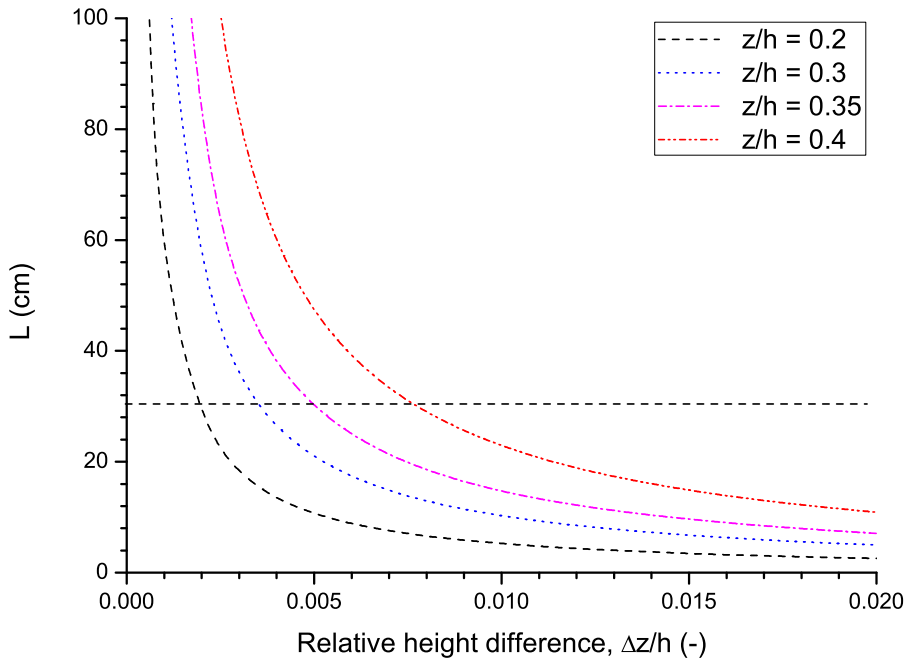

Figure B.3: *Variation of the distance at which drops becomes vertically aligned L as a function of their initial relative transversal spacing $\Delta z/h$ and position in the Poiseuille flow z/h for a fixed initial longitudinal spacing $\Delta x_0 = 2\ mm$.*

B.3 Quantum efficiency of the Falcon cameras

During the design of the "water drops electrocoalescence in an oil shear flow" experimental setup, a particular attention was paid to the illumination system. In order to avoid "long" exposure times, detrimental to the accurate measurement of moving and deforming objects, it is essential to optimize the amount of light provided to the Falcon 1.4M100 camera and that effectively converted by its CMOS sensor (in electron–hole pairs). As already mentioned in chapter 3, the former was achieved by using flashes over which the light sources can be supplied with currents greater than nominals. The latter implies to take full advantage of the CMOS sensor's quantum efficiency, i.e. its electrical sensitivity

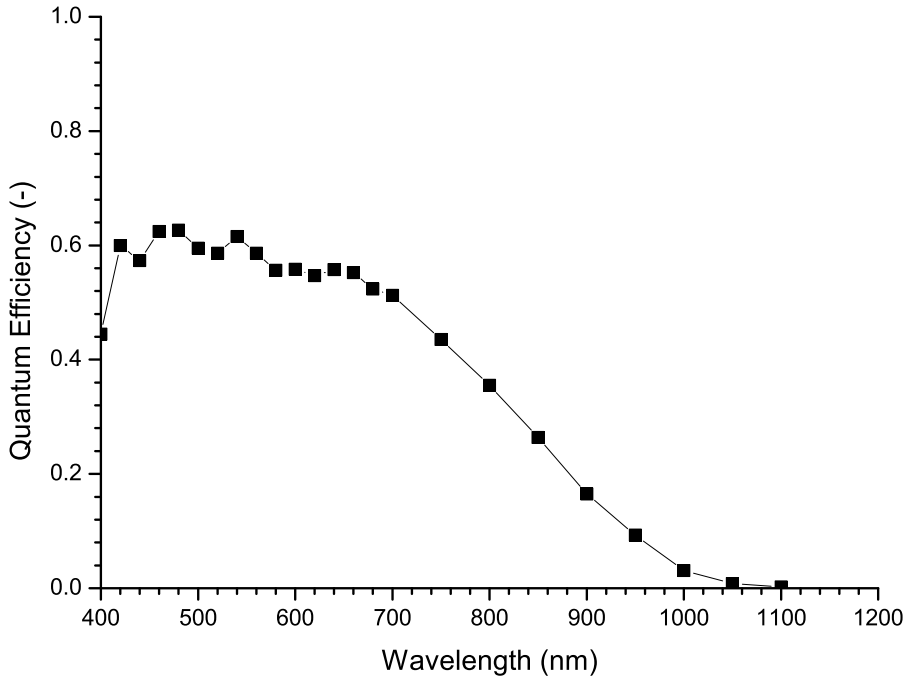

Figure B.4: *Quantum efficiency of the Falcon 1.4M100 camera as a function of the light signal wavelength.*

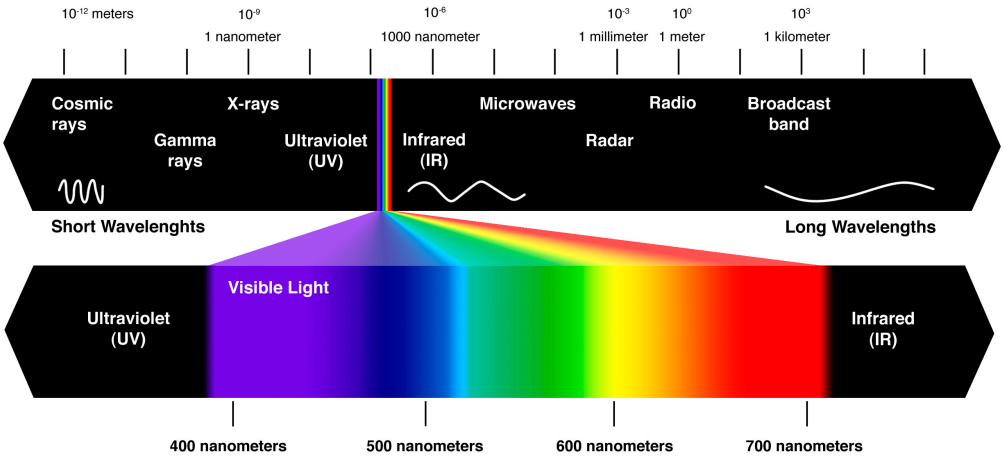

Figure B.5: *Electromagnetic and visible light spectra.*

to light. In this perspective, sources emitting in the range $450 - 550\ nm$ (Figure B.4) corresponding to the green region of the visible light spectrum (Figure B.5) are particularly recommended and were therefore chosen.

B.4 Liquid thread break-up at secondary neck

In addition to the decrease of the measured static IFT coefficient (from 35 $N.m^{-1}$ down to 18 $N.m^{-1}$), another phenomenon indicated the presence of surfactants in the injection experiments described in chapter 4. It consists in the formation of a secondary neck in between the about-to-detach drop and the meniscus, where the first liquid thread break-up is observed (Figure B.6). This phenomenon was well characterized by Jin et al. (2006) through the numerical simulation of buoyancy driven drop injections. According to the author, tangential stresses exerted by the outer viscous liquid, during the early stage of the process, entrain surfactants from the elongated tip to regions with lower velocity gradients where they accumulates. Then, the significant contraction of the water-oil interface arising below the primary neck cause the local concentration to increase (approaching the maximum packing capacity) relatively to that at the neck itself. This result in the appearance of Marangoni stresses that oppose the flow and thus the thinning of the thread. In essence, the same behavior is observed at the secondary neck. Though,

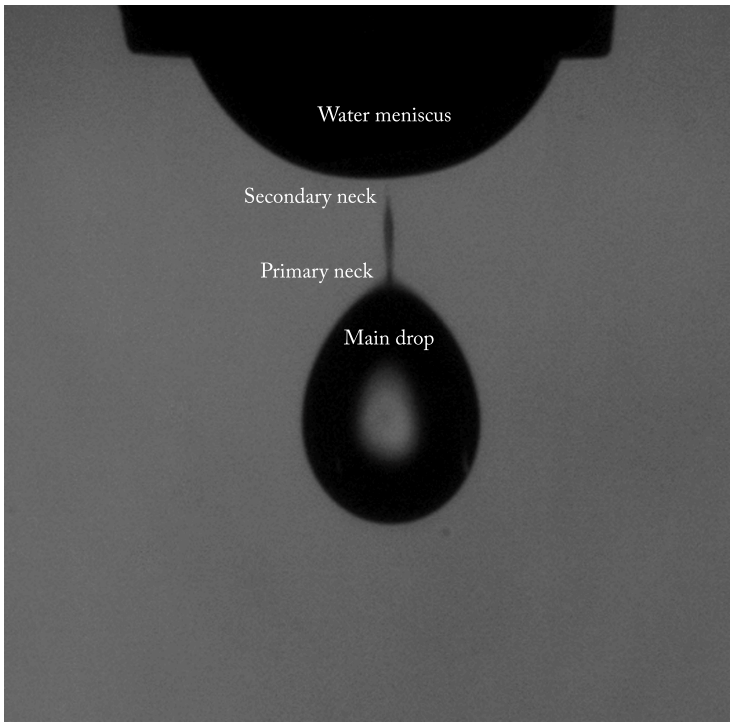

Figure B.6: *Photograph of a water drop injection in polybutene oil illustrating the liquid thread break-up at the secondary neck and corresponding to an acquisition time of* 2100 μs *in Figure 4.12.*

the interface contraction and accumulation of surfactants being far weaker, so is the impeding of the thinning. Jin et al. (2006) reported the transition between primary and secondary necking mode for ratios of adsorbed surfactant concentrations to the maximum packing of such surfactant in a monolayer in the range $0.3 - 0.5$.

Appendix C

Résumé de la thèse en français

C.1 Introduction

Le terme *pétrole*, dérivé du latin *petra* pierre et *oleum* huile, désigne les hydrocarbures majoritairement présents dans les roches sédimentaires sous forme de gaz, liquides, semi-solides ou solides (Speight, 2006). Bien que l'origine de son utilisation se perde dans les ténèbres de l'Antiquité, il a été prouvé que les bâtisseurs de Babylone se sont servi d'*asphaltum* (une substance naturelle proche du goudron provenant de fuites de pétrole sous-marines et s'accumulant sur les rivages) pour lier les pierres à partir desquelles la ville a été construite. L'historien grec, Descorides Pedaners, mentionne également dans ses récits, l'usage de lampes à pétrole par les citoyens d'Agrigente en Sicile bien avant la naissance du Christ. Du pétrole a également été utilisé à diverses fins par les Perses, les Hindous, les Incas, les Aztèques et les Indiens.

Dans les sociétés modernes, le pétrole est devenu incontournable, fournissant non seulement la matière première pour les plastiques et autres produits dérivés mais aussi le carburant nécessaire à l'indutrie, au chauffage, au transport et à la production d'énergie. Pourtant, au vu des baisses de rendement des puits exploités enregistrées ces dernières années (taux annuel moyen de 4.5% selon les prévisions de l'Agence Internationnale de l'Énergie (IEA, 2011)) et de l'augmentation de la consommation énergétique mondiale, l'humanité a progressivement pris conscience que cette ressource viendra à manquer dans un avenir relativement proche. En conséquence, l'industrie pétrolière a radicalement changé d'approche, réouvrant des puits précédemment considérés comme non-rentables, parce que nécessitant une importante stimulation externe pour produire, afin d'en récupérer jusqu'à la dernière goutte de pétrole présente (Speight, 2006). Dans le même temps, les réserves mondiales de bruts légers, plus facile à exploiter, étant presque épuisées, l'extraction de bruts lourds et extra lourds n'a cessé de croître. Du fait de cette transition qualitative du pétrole, les

industriels sont et continueront d'être confrontés à des problèmes extrêmement complexes dont la résolution requiert souvent de solides bases scientifiques.

Cette thèse s'est inscrite dans le cadre d'un projet international de recherche "Electrocoalescence — Criteria for an efficient process in real crude oil systems" focalisé sur l'un de ces problèmes, à savoir l'élimination de l'eau cogénérée avec le pétrole, sous la forme d'émulsions stables, lors des opérations d'extraction et de dessalement. Dans les premiers temps de l'exploitation pétrolière, l'étape de déshydratation tirait uniquement partie de la différence de masse volumique entre les deux phases présentes. A cet effet, le brut extrait était laissé au repos pendant plusieurs jours dans de grandes cuves, particulièrement emcombrantes sur les plate-formes offshore, afin de laisser les gouttelettes d'eau (dont la taille moyenne est de l'ordre de la dizaine de microns) se sédimenter par gravité. Afin d'exploiter pleinement la loi de Stokes (via la dépendance quadratique de la vitesse de sédimentation avec le rayon des gouttelettes) et d'accélérer l'étape de séparation, différentes techniques permettant d'augmenter la taille des gouttes ont par la suite été développées. Parmi elles, l'attraction et la fusion induites par champ électrostatique, aussi connu sous le nom d'*électrocoalescence*, a démontré des performances inégalées. Au fil des années, elle a permis de réduire de manière drastique l'apport de chaleur et l'ajonction de désémulsifiants chimiques, respectivement énergivore et préjudiciable du point de vue environnemental, et s'est par conséquent imposée comme un standard de la plupart des séparateurs de denières générations.

Pourtant, bien que l'effet bénéfique des forces électriques sur le traitement des émulsions eau-pétrole brut soit connu depuis un siècle, de nombreuses zones d'ombre subsistent, notamment sur les questions relatives à l'efficacité du procédé. La majeure partie des études antérieures a été consacré à son amélioration via l'identification de paramètres optimaux (intensité, forme et fréquence du champ électrique). Cependant, ces derniers étant intrinsèquement liés à la nature du brut, de grosses variations en terme d'efficacité de déshydratation ont souvent été observées lors de leur transposition d'un puit à un autre ou tout simplement au fil du temps dans un même puit, avec à la maturation du brut. Les travaux conduits au Laboratoire de Génie Électrique de Grenoble (G2ELab) et résumés dans ce manuscript ont eu pour but de remédier à cette lacune en fournissant un critère prédisant la probabilité d'électrocoalescence de paires de gouttelettes en fonction de différents paramètres clés. L'accent a été mis sur la compréhension et la modélisation des intéractions hydrodynamiques et électrostatiques, les aspects chimiques étant traités en parallèle par des collaborateurs experts en la matière du Norvegian University of Technology (NTNU) - Ugelstad Laboratory.

Le premier chapitre est une brève introduction à la formation, la stabilisation et la

séparation des émulsions eau-pétrole brut. L'accent est mis sur la caractérisation du procédé d'électrocoalescence à travers la description des mécanismes physiques mis en jeu et des forces qui leur sont associées. Quelques-unes des technologies sur le marché sont ensuite présentées et, enfin, les carences qui empêchent une estimation précise de leur efficacité sont soulignées.

Préalablement à l'étude du phénomène d'électrocoalescence, le second chapitre traite de la déformation et de la stabilité d'interfaces eau-huile soumises à des forces électrostatiques. Tout d'abord, un schéma numérique, mis en œuvre pour simuler des problèmes d'électrohydrodynamique faisant intervenir des parois mobiles, est détaillé. Ensuite, il est utilisé en combinaison avec des expériences pour étendre les résultats asymptotiques précédemment obtenus, grâce à des traitements analytiques, dans des configurations de référence.

Le troisième chapitre est divisé en deux parties. Dans un premier temps, des simulations numériques sont utilisées pour étudier l'amincissement du film d'huile entre les gouttelettes lors de leur approche sous l'effet des forces d'attraction électrostatique. Une estimation d'ordre de grandeur pour le temps de drainage est largement validée et mise en balance avec le temps de proximité afin de déduire un critère prédisant la probabilité d'électrocoalescence résultant d'une collision en écoulement. Dans un second temps, l'assemblage d'un dispositif expérimental conçu dans le but d'améliorer la représentativité de ce critère est décrit.

Le quatrième et dernier chapitre constitue une réponse à un point bloquant mis à jour lors de la conception de l'expérience "électrocoalescence de gouttelettes d'eau dans un écoulement cisaillé d'huile". Il présente le développement d'une nouvelle technique pour l'injection de gouttes d'eau conductrice non-chargées, dans une huile diélectrique visqueuse, basée sur l'application d'une impulsion de champ électrique.

C.2 Traitement des émulsions eau-pétrole: aspects physiques, chimiques et technologiques

Dans l'industrie pétrolière, la co-extraction d'eau et de pétrole sous la forme d'émulsions stables est hautement indésirable car susceptible d'engendrer différents effets néfastes en aval de la chaîne de production. Afin d'éviter, par exemple, des problèmes de corrosion des équipements (tuyaux, gaines, vannes, etc), de désactivation des catalyseurs, de hausse des coûts d'exploitation due à l'augmentation significative des pertes visqueuses et au transport de l'eau, une étape de déshydratation est obligatoire. Basé sur une étude bibliograhique, le premier chapitre balaye différents aspects relatifs aux émulsions eau-pétrole brut, de leur formation quasi systématique à leur traitement. Dans cette perspective, la méthode offrant le meilleur compromis des points de vue énergétique et écologique, connu sous le nom d'électrocoalescence, est introduite. Afin de donner une image claire de son principe, une attention toute particulière est porté à la description de ses étapes successsives (Figure C.1) et des interactions hydrodynamiques et électrostatiques. Les autres phénomènes mis en jeu, en particulier ceux expliquant la stabilité des émulsions et lié à la chimie du pétrole, sont brièvement évoqués. Ensuite, les progrès technologiques accomplis au niveau des électrocoalesceurs durant les dernières décennies sont illustrés au travers de quelques exemples marquants, notamment ceux de dernière génération (Figure C.2). Enfin, la question centrale de la thèse, à savoir l'estimation de leur efficacité (Figure C.3) dans les conditions réelles de fonctionnement, est abordée et l'absence de modèles adéquats est soulignée.

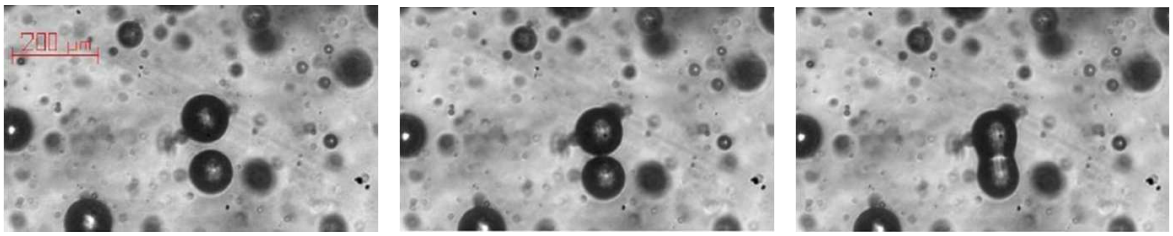

t $t + 24\ ms$ $t + 32\ ms$

Figure C.1: *Électrocoalescence de deux gouttes dans une émulsion constituée de* 1.5 % *d'eau dans de l'huile Nytro 10XN induite par un champ électrique AC vertical* (1 $kV.cm^{-1}$, 100 Hz). *Phases d'approche, de drainage du film d'huile et de coalescence des interfaces. Reproduit de Hølto (2009).*

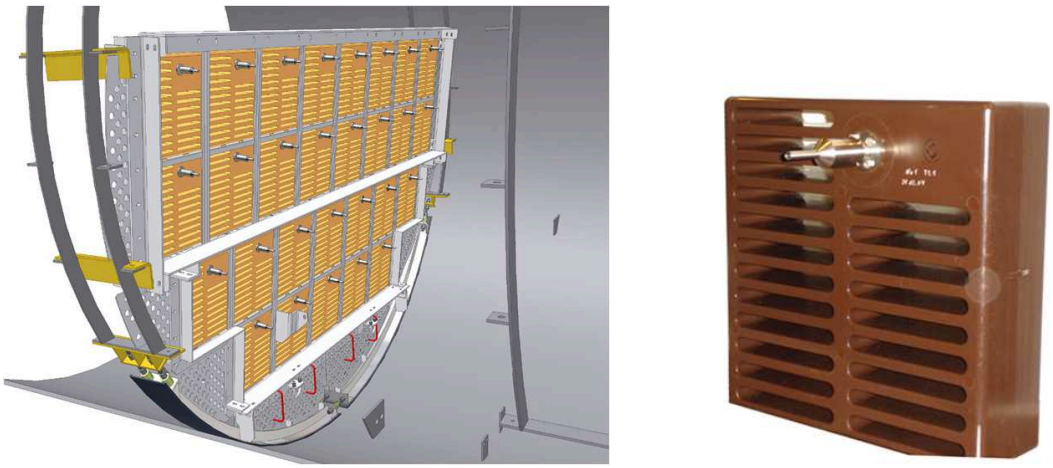

(*a*) (*b*)

Figure C.2: *Modèle CAD 3D d'un séparateur équipé d'un système VIEC® (a) et photographie d'un des 26 modules qui le composent (b) (Hamworthy, 2011).*

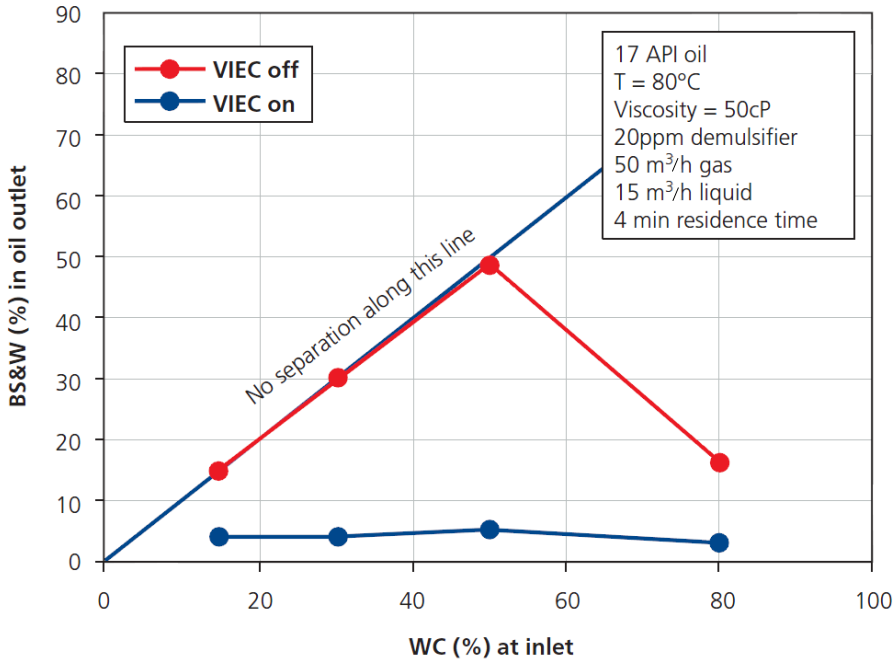

Figure C.3: *Variation de la capacité de déhydratation d'un séparateur haute pression équippé avec un système VIEC en fonction de la teneur en eau du brut en entrée. Données reproduites de Hamworthy (2011).*

C.3 Déformation et stabilité d'interfaces eau-huile soumises à des champs électrostatiques

La difficulté dans la mise en place d'un critère prédisant la probabilité d'électrocoalescence de gouttes entrant en collision provient, en plus de la complexité intrinsèque du mécanisme, des lacunes des différentes techniques permettant son étude. D'une part, en dépit de leur amélioration continue, les résolutions spatiale et temporelle des caméras optiques actuelles demeurent trop faibles pour observer précisément l'évolution des interfaces dans les travaux expérimentaux, en particulier durant les dernières étapes du processus. D'autre part, la simulation numérique, qui permet une discrétisation très fine, est par nature limitée par l'existence de lois décrivant les différents phénomènes physiques mis en jeu et ne représente que rarement des situations réelles. La combinaison des deux est chronophage mais aide à surmonter ces limitations et à identifier les facteurs dominants, parfois sous-jacents, influençant le mécanisme global. Le second chapitre, et plus généralement la thèse, suivent cette démarche. Dans un premier temps, le développement d'un schéma numérique général — implémenté dans un logiciel commercial — permettant de simuler les comportements statiques et dynamiques d'interfaces entre des liquides parfaitement conducteurs et isolants soumises à des forces électrostatiques est présenté. Bien que basé sur des modèles physiques relativement simples, ce nouvel outil s'avère particuliérement adapté à la résolution de problémes quasistatiques d'instabilité. Il est donc, ensuite, utilisé en combinaison avec des expériences dans des configurations typiques du phénomène d'électrocoalescence entre gouttes (Figure C.4) afin d'étendre des critères asymptotiques préalablement établis par des approches analytiques. Ces derniers reliant le nombre de Bond électrique (ratio entre les forces électrostatique et capilaire) aux grandeurs de la

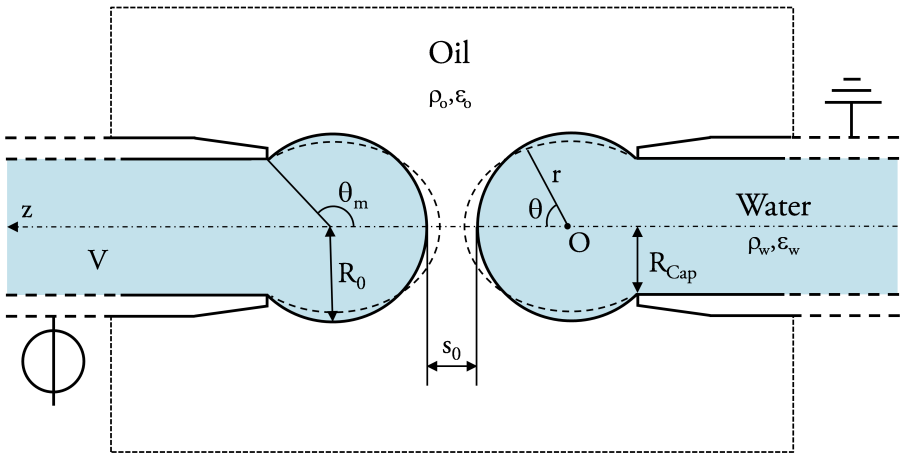

Figure C.4: *Gouttes d'eau anchrées à l'extrémité de cappillaires immergées dans un liquide isolant et soumises à une différence de potentiel. Géométrie axisymmétrique du problème et paramètres associés.*

géométrie initiale (Figure C.5) offre un point de départ interessant pour une étude poussée du phénomène d'électrocoalescence.

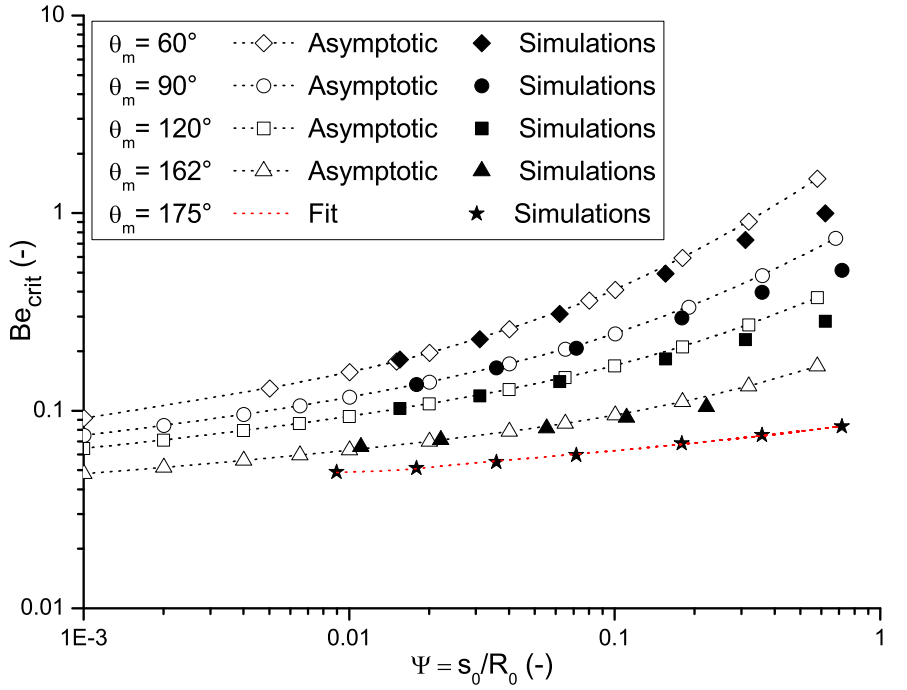

(*a*)

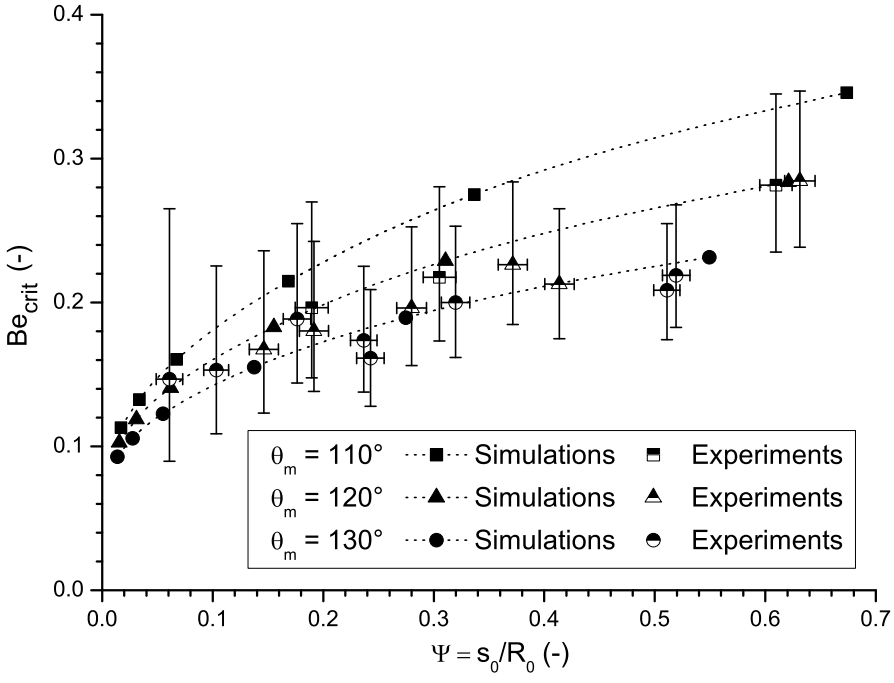

(*b*)

Figure C.5: *Nombre de Bond électrique critique Be_{crit} en fonction de l'espacement relatif initial des interfaces ψ pour différentes valeurs d'angle θ_m. Résultats analytiques (asymptotiques) et numériques (a). Résultats numériques et expérimentaux (cf. thèse pour le calcul des barres d'erreurs) (b).*

C.4 Électrocoalescence de deux gouttelettes d'eau dans de l'huile

Dans les électrocoalesceurs de dernière génération, la fusion des gouttelettes d'eau résulte de l'action combinée des forces hydrodynamiques et électrostatiques (Figure C.6). En l'absence de champ électrique, l'alternative généralement privilégiée dans le but d'estimer la probabilité de coalescence consiste à comparer deux échelles de temps: le temps de proximité de deux gouttes dans l'écoulement et le temps nécessaire pour que le mince film d'huile les séparant soit drainé jusqu'à atteindre son épaisseur critique. Pourtant, bien qu'un tel formalisme soit parfaitement transposable au cas de l'électrocoalescence, aucune expression antérieure à cette thèse n'a, de manière surprenante, pu être identifié dans la littérature. En conservant une démarche numérique et expérimentale, le troisième chapitre a pour objectif de combler ce manque. En premier lieu, des simulations axisymmétriques reproduisant le mécanisme de drainage entre deux gouttelettes d'eau (parfaitement) conductrices en suspension dans une huile (parfaitement) dielectrique mettent en lumière les très grandes modifications engendrées par les forces électrostatiques. A partir de là, une analyse d'ordre de grandeur conduit à une approximation pour le temps de drainage (C.1) faisant intervenir la viscosité du liquide environnant μ_o et la pression électrostatique initiale agissant sur les gouttes p_{E_0}.

$$t_{Drainage} = \frac{\beta \mu_o s_0^{1.70}}{2.975 \epsilon_0 \epsilon_{r_o} E_0^2 R_0^{1.70}} = \frac{\beta \mu_o}{1.7\frac{1}{2} \epsilon_0 \epsilon_{r_o} (E_{3_0} E_0)^2} \tag{C.1}$$

Grâce à l'utilisation de la solution de Davis (1964) donnant la valeur maximale de

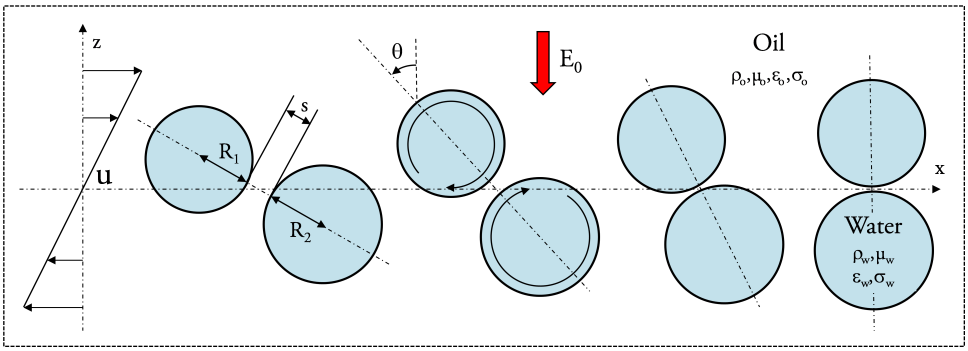

Figure C.6: *Schéma représentatif du mécanisme d'électrocoalescence dans un dispositif de déshydratation de dernière génération: les gouttes d'eau en suspension dans l'écoulement de pétrole entrent en collision à cause des cisaillements locaux engendrés par la turbulence et s'approchent sous l'effet d'intenses forces d'interactions électrostatiques. La fusion des interfaces dépend alors des valeurs prises par les paramètres prédominants. θ caractérise, ici, l'angle entre la direction du champ et l'axe passant par le centre des deux gouttes.*

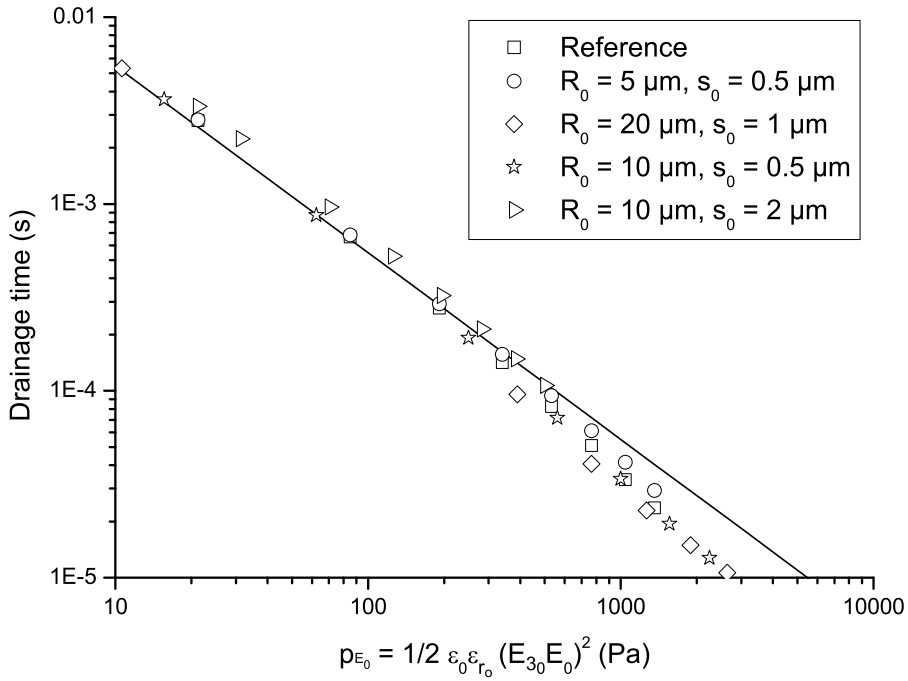

Figure C.7: *Variation du temps de drainage en fonction de la pression électrostatique initiale maximale p_{E_0}, estimée pour des gouttelettes de même taille via la formule de Davis (1964). Étude détaillée de l'influence du rayon des gouttes R_0 et de leur espacement initial s_0. La courbe en trait plein correspond à l'équation (C.1) avec $\beta = 8$.*

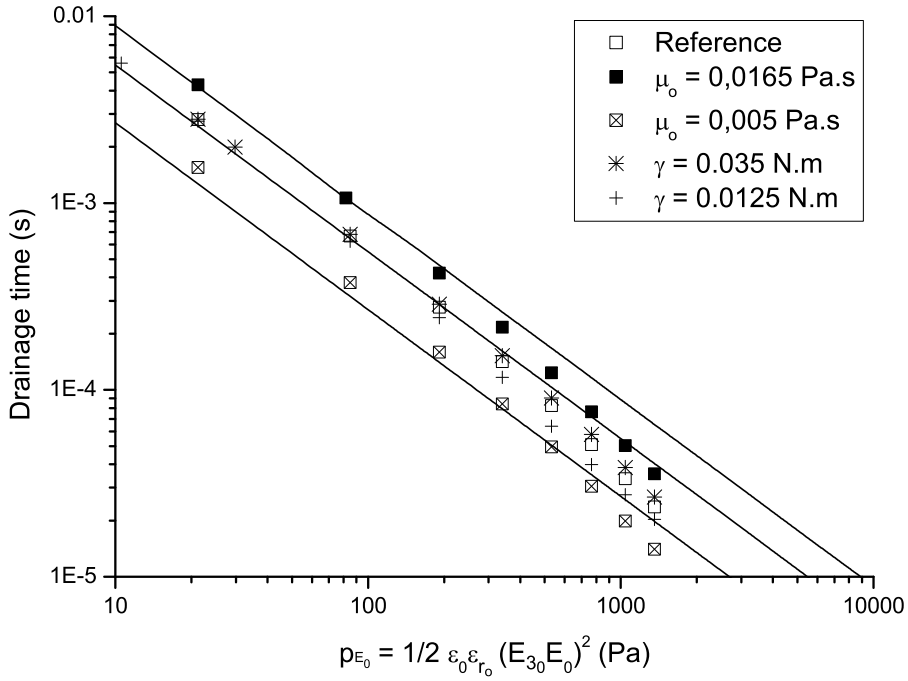

Figure C.8: *Variation du temps de drainage en fonction de la pression électrostatique initiale maximale p_{E_0}, estimée pour des gouttelettes de même taille via la formule de Davis (1964). Étude détaillée de l'influence du coefficient de tension interfaciale γ et de la viscosité de l'huile μ_o. La courbe en trait plein correspond à l'équation (C.1) avec $\beta = 8$.*

$p_{E_0} = \frac{1}{2}\epsilon_0\epsilon_{r_0}(E_{3_0}E_0)^2$ (agissant aux pôles en regard) corrigée d'un facteur β, l'expression developpée reproduit avec précision les comportements déduits des simulations (Figures

C.7 et C.8) dans son domaine de validité (viscosité du liquide environnant très grande devant celle des gouttes et déformation interfaciale négligeable).Au vu de ces résultats, un critère estimant la probabilité d'électrocoalescence entre deux gouttes évoluant dans un écoulement cisaillé est proposé (C.2). Combiné avec des fonctions pré-existantes calculant les fréquences de collision, il constitue un premier outil pour l'optimisation des dispositifs industriels de traitement des émulsions eau-pétrole brut.

$$p_d \sim \exp\left(-\frac{\beta\mu_o\dot{\gamma}}{0.85\epsilon_0\epsilon_{r_o}\left(E_{3_0}E_0\right)^2}\right) \tag{C.2}$$

En outre, dans le but d'améliorer sa représentativité, les autres facteurs susceptibles d'avoir une forte influence sur le mécanisme de drainage sont soulignés. Afin d'élucider ces aspects, un dispositif expérimental (Figure C.9) conçu pour reproduire, observer et caractériser le processus complet d'électrocoalescence entre deux gouttes d'eau non chargées injectées dans un écoulement cisaillé est finalement présenté.

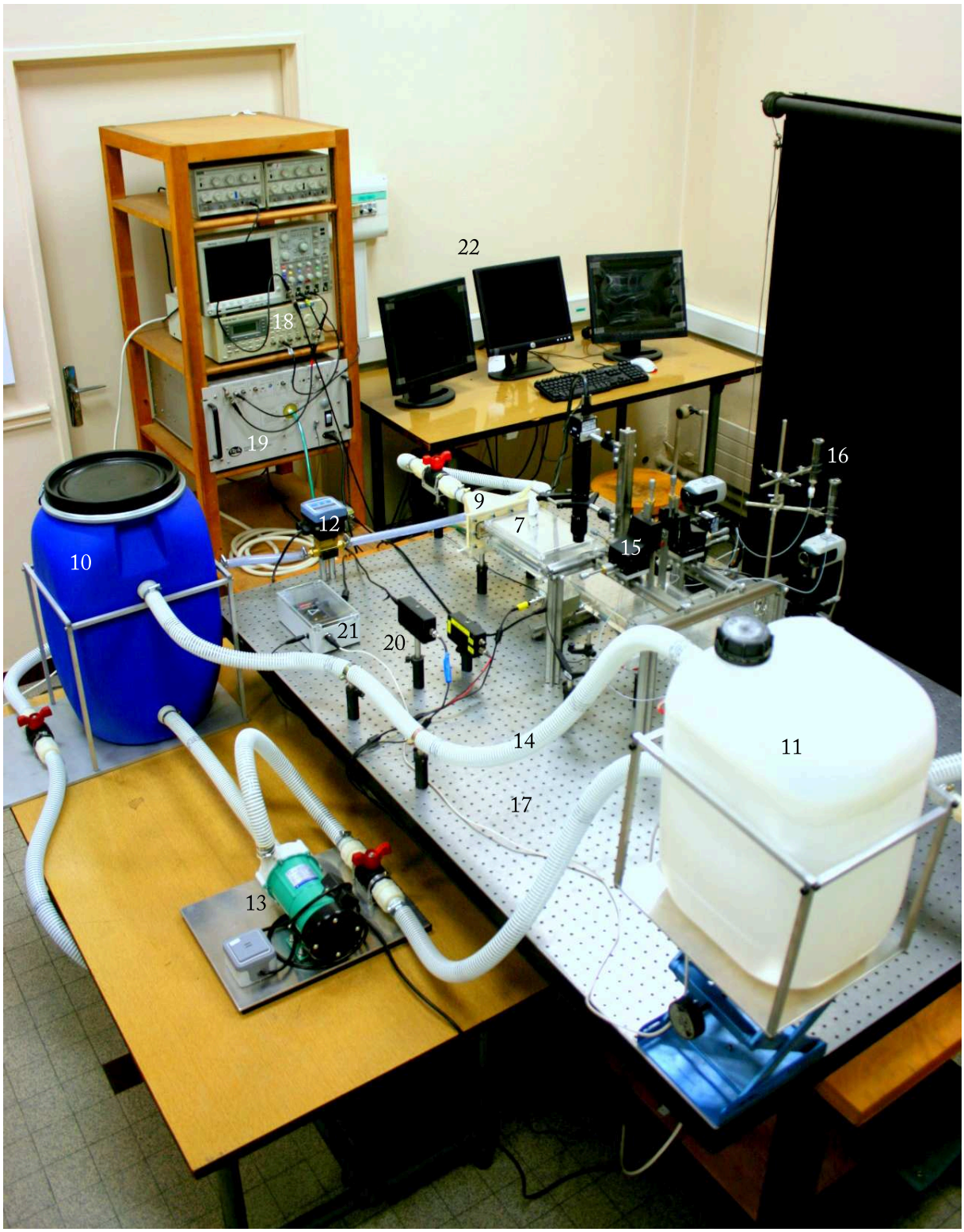

Figure C.9: *Photographie du dispositif expérimental "électrocoalescence de deux gouttes dans un écoulement cisaillé": 10, Réservoir aval - 11, Réservoir amont - 12, Débitmètre - 13, Pompe magnètique - 14, Trop-plein - 15, Système de translation XYZ - 16, Réservoir d'eau de* 100 *ml - 17, Table optique - 18, Générateur de signaux arbitraires - 19, Ampli HT - 20, Sources de lumière LED continue/flash - 21, Système temps-réel de mesure de la température de l'huile - 22, Espace de visualisation*

C.5 Injection simultanée de deux gouttes d'eau non-chargées dans de l'huile

Largement employée dans différents domaines, notamment la microfluidique, l'injection à la demande de gouttes électriquement neutres dans un liquide visqueux est relativement triviale. Pourtant, une étude poussée des différentes techniques de génération disponible montre qu'aucune d'entre elles n'est en mesure de satisfaire aux éxigences définies dans le cahier des charges du dispositif expérimental mentionné précédemment. Le dernier chapitre présente donc le développement d'une nouvelle méthode d'injection capable de produire simultanément et "à la demande" des gouttes, à partir de menisques d'eau conductrice immergés dans une huile polybutene, avec une gamme de diamètre allant de 50 à 250 μm (Figure C.10) et un ratio de taille variant de 1 à 1.35 en réglant simplement deux paramètres clés — la hauteur relative des ménisques (Figure C.11) et l'intensité de l'impulsion de champ életrique appliquée. Bien que basée sur l'utilisation de forces électrostatiques, la génération de gouttes non chargées est accomplie grâce à une maîtrise avancée de la dynamique de déformation de l'interface rendue possible par l'invention d'une nouvelle forme d'impulsion (Figure C.12). Une fois encore, la combinaison d'expériences et de simulations aide à mettre en place une base solide pour le fonctionnement de la technique

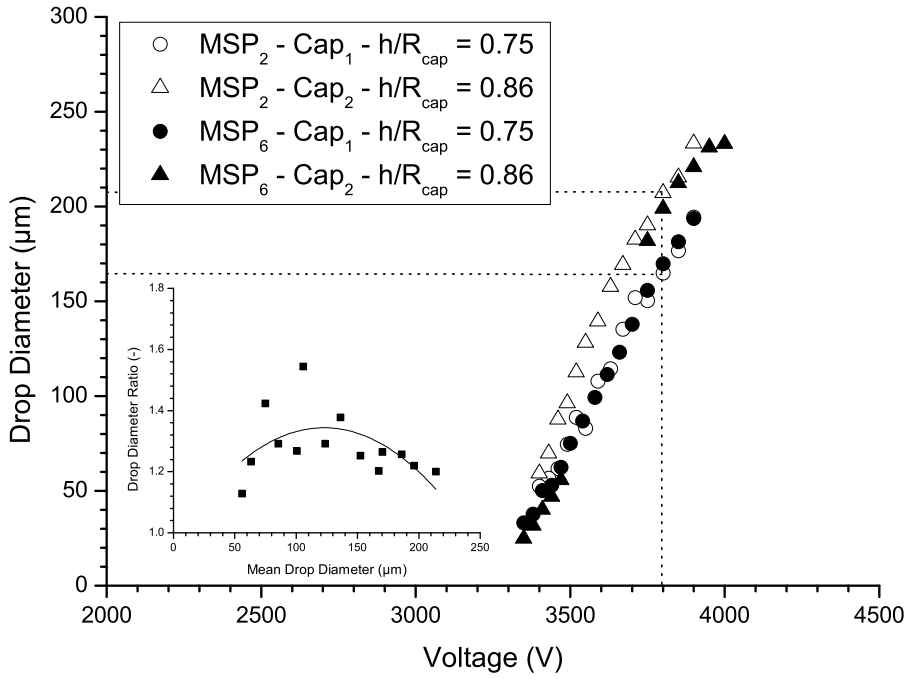

Figure C.10: *Variation du diamètre des gouttes injectées et du rapport de leur taille respectivement en fonction de la différence de potentiel appliquée et du diamètre moyen obtenus lors de doubles injections en utilisant deux impulsions différentes, deux hauteurs relative de ménisques $h/R_{Cap} = 0.75$ et $h/R_{Cap} = 0.86$ pour un coefficient de tension interfaciale $\gamma = 0.018\ N.m^{-1}$*

.

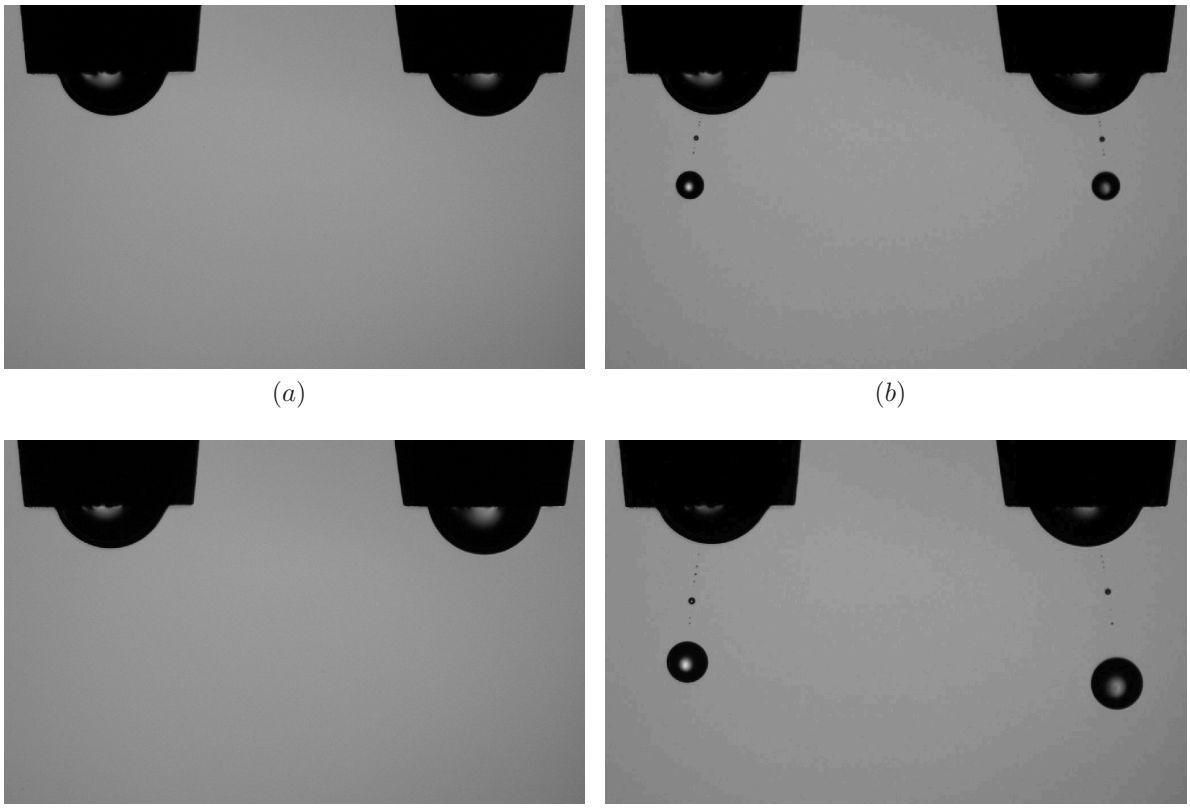

Figure C.11: *Injection synchronisée de deux gouttes d'eau non chargées dans une huile polybutène en utilisant MSP_2 et $V = 3.80\ kV$ pour $\gamma = 0.018\ N.m^{-1}$. (a) Ménisques initiaux identiques. (b) Gouttes injectées et satellites. Diamètres et déviations angulaires mesurés: gauche $D_d = 104.8\ \mu m$ et $\alpha = 14°$, droite $D_d = 105.1\ \mu m$ et $\alpha = 16°$. (c) Ménisques initiaux différents. (d) Gouttes injectées et satellites. Diamètres et déviations angulaires mesurés: gauche $D_d = 164.9\ \mu m$ et $\alpha = 18°$, droite $D_d = 207.2\ \mu m$ et $\alpha = 17°$.*

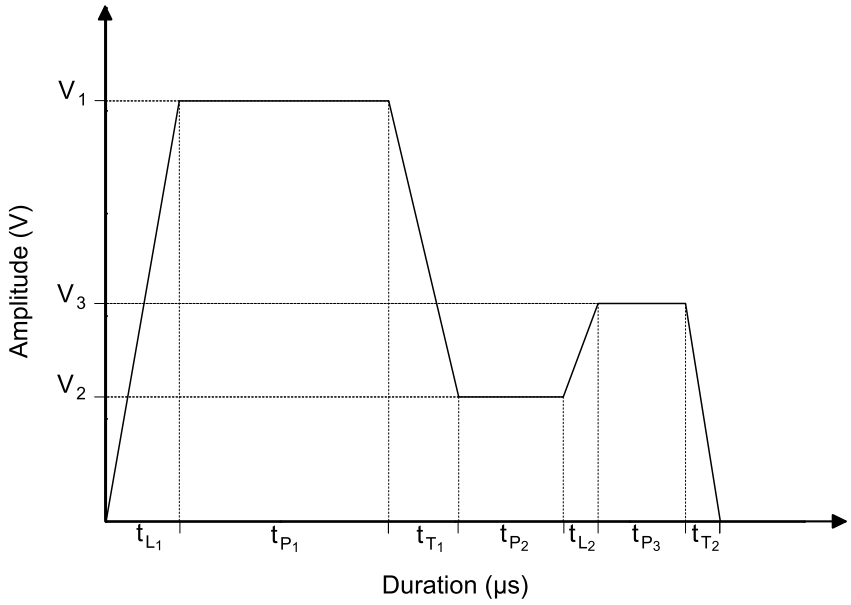

Figure C.12: *Impulsion Multi-Niveaux (MSP).*

et donne une vision claire des aspects à approfondir.

C.6 Conclusion

Cette thèse a eu pour but d'établir un critère prédisant l'efficacité du procédé d'électrocoalescence sur le traitement d'émulsions eau-pétrole brut.

Afin d'étudier progressivement les mécanismes complexes et variés mis en jeu, un travail conséquent a été consacré à l'élaboration d'un outil de simulation multi-physique. Un schéma numérique, couplant des équations de dynamique des fluides (Navier-Stokes) et d'électrostatique (Laplace) et prenant en compte les effets de tension interfaciale, a donc été développé. Ce dernier a ensuite été intégré dans un logiciel commercial (COMSOL MULTIPHYSICS^{TM}) et utilisé, avec une méthode éléments finis et un formalisme Arbitraire Lagrange-Euler, afin de résoudre des problèmes de mouvement et de déformation d'interfaces (de gouttelettes) entre des liquides parfaitement conducteurs et diélectriques.

L'une des principales contributions a concerné la modélisation et l'analyse du mécanisme d'amincissement du film entre des gouttelettes conductrices s'approchant, dans un liquide diélectrique au repos, sous l'effet d'un champ électrique. Les résultats de simulations ont mis en évidence la forte singularité du problème et, par conséquent, l'inadéquation des modèles théoriques de lubrification généralement utilisés pour représenter les cas de coalescence dans les écoulements diphasiques. En supposant négligeable la déformation des gouttelettes, une analyse d'ordre de grandeur a conduit à estimer le temps de drainage comme proportionnel à la viscosité du liquide environnant et inversement proportionnel à la pression électrostatique maximale initiale (agissant aux pôles en regard des gouttelettes). La validité de l'expression obtenue a ensuite été examinée et confirmée via une comparaison systématique avec les résultats d'une étude numérique paramétrique. De là, un critère prédisant la probabilité d'électrocoalescence lors d'une collision induite dans un écoulement cisaillé et reposant sur la confrontation du temps de drainage et de celui au cours duquel des gouttelettes sont proches a été proposé. Bien qu'étant basée sur quelques hypothèses (par exemple l'utilisation de liquides modèles), il fournit néanmoins des indications intéressantes sur ce qui se passe à plus grande échelle dans des dispositifs industriels et appuie qualitativement les observations effectuées, par des collaborateurs norvégiens, sur des émulsions eau-pétrole brut. En parallèle, un dispositif expérimental sophistiqué a été conçu et assemblé pour s'affranchir des limites inhérentes à la simulation numérique et permettre d'étudier l'électrocoalescence de gouttelettes d'eau transportées par un écoulement cisaillé d'huile diélectrique.

Une autre tâche importante, plutôt inattendue, a finalement été engendrée par la nécessité de lever un verrou technique identifié durant la conception de ce dernier dispositif expérimental. Elle a consisté à développer une nouvelle technique pour l'injection syn-

chronisée et à la demande de deux gouttes d'eau conductrice non chargées dans un liquide visqueux isolant, basé sur l'application d'une impulsion de champ électrique. Une fois de plus, l'utilisation conjointe de la simulation numérique et des expériences a été cruciale. La première a permis d'examiner attentivement la dynamique du phénomène, contribuant ainsi à faire un grand pas en avant dans la compréhension d'un problème de trajectoire, rencontré de manière récurrente dans des expériences anérieures avec des impulsions traditionnelles (carrées). Sur la base des résultats de simulation, une forme d'impulsion optimisée a été introduite avec des paramètres de départ viables. Une vaste campagne d'expériences a ensuite clairement démontré l'efficacité de ces nouvelles impulsions Multi-Niveaux pour l'injection d'une ou deux gouttes (de taille identique ou différente) comme spécifié initialement.

En ce qui concerne les suites possibles de la thèse, presque toutes les études menées ont ouvert des pistes de recherche alléchantes. De manière évidente, l'exploitation du dispositif expérimental assemblé devrait constituer une priorité en rapport avec le contexte de déshydratation du pétrole. Un certain nombre de résultats important sont attendus, permettant ainsi d'améliorer la représentativité du critère par rapport aux conditions réelles de fonctionnement des électrocoalesceurs industriels. Dans cette perspective, l'implémentation de mécanismes physique/chimique supplémentaires, telles que l'adsorption/désorption et le transport interfacial de tensioactifs, dans le schéma numérique serait particulièrement utile Tenno and Pohjoranta (2008). Enfin et non des moindres, avec son aptitude sans précédent à produire des gouttes avec une gamme de volume s'étendant sur près de 5 décades sans modification de la géométrie de la buse, la technique d'injection peut potentiellement trouver des applications dans d'autres domaines.

Abstract

The present thesis deals with the electrostatically assisted removal of water coproduced with crude oil in the form of stable emulsions during recovery and desalting operations. This process, referred to as *electrocoalescence*, exploits the ability of electric forces to promote attraction and merging of adjacent water droplets to increase their size and related natural rate of sedimentation under gravity. Still, even one century after the first experimental observations, a lot of gray areas remain, particularly on the optimization of efficiency in state-of-the-art separators. To address this question, an approach combining multi-physics simulation and experiments has been used to investigate the phenomena of motion, deformation and instability of electrically influenced water-oil (droplets) interfaces. The main contribution concerns the modeling and analysis of the mechanism of oil film thinning between droplets approaching under the effect of electrostatic forces. Results from simulations highlight the strong singularity of the present problem and the inadequacy of existing theoretical lubrication models usually employed to represent coalescence events in two phase flows. For the small emulsified droplets, a new asymptotic expression for the drainage time is obtained and allows to deduce a criterion predicting the probability of electrocoalescence resulting from a shear flow induced collision. In parallel, a sophisticated setup, enabling to experimentally investigate the phenomenon and to improve the criterion relevance with regards to the actual processing conditions, has been assembled. At last and as an answer to an otherwise unfulfilled requirement defined in the design of the latter, an innovative actuation technique for the synchronous on-demand injection of two charge free conductive droplets in an insulating viscous liquid, relying on the application of a high electric field pulse, has been implemented.

Keywords: *electrocoalescence*, *crude oil*, *EHD*, *multiphysics numerical simulation*, *film thinning*, *Drop-on-Demand*.

Résumé

Cette thèse porte sur l'utilisation de champs électriques pour faciliter l'élimination de l'eau coproduite avec le pétrole brut, sous la forme d'émulsions stables, lors des étapes d'extraction et de dessalement. Ce procédé, connu sous le nom d'*électrocoalescence*, s'appuie sur la capacité qu'ont les forces électrostatiques à promouvoir l'attraction et la coalescence de gouttelettes d'eau proches afin d'en augmenter la taille et ainsi d'en accélérer la sédimentation par gravité. Bien que les premières observations expérimentales datent dejà d'un siècle, de nombreuses zones d'ombres subsistent, notamment en ce qui concerne l'optimisation de l'efficacité des électrocoalesceurs de dernière génération. Dans ce contexte, une démarche, combinant simulation numérique multiphysique et expérimentation, a été mise en place pour étudier les phénomènes de mouvement, de déformation et d'instabilité d'interfaces eau-huile induit par la présence d'un champ électrique. La contribution la plus marquante concerne la modélisation et l'analyse de l'effet des forces électrostatiques sur le mécanisme d'amincissement du film d'huile séparant les gouttes. Les résultats numériques mettent en évidence la singularité du problème et l'inadaptabilité des modèles théoriques de lubrification classiquement adoptés pour représenter la coalescence dans les écoulements diphasiques. Une nouvelle expression asymptotique pour le calcul du temps de drainage entre les gouttelettes de l'émulsion est proposée et utilisée pour déduire un critère prédisant la probabilité d'électrocoalescence lors d'une collision dans un écoulement cisaillé. En parallèle, un dispositif sophistiqué, permettant de reproduire expérimentalement le phénomène et d'améliorer la réprésentativité du critère, a été construit. Enfin, en réponse à un point bloquant décelé lors de la phase de conception de ce dernier, une technique innovante d'injection à la demande de gouttes conductrices non chargées dans un liquide visqueux isolant, utilisant des impulsions électrostatiques, a été développé.

Mots clés: *électrocoalescence*, *pétrole brut*, *EHD*, *simulation numérique multiphysique*, *drainage de films liquides*, *injection de goutte à la demande*.